Thèse n° 7447

Concurrent multiscale modeling and theory of solute-strengthening for dilute and complex concentrated alloys

Présentée le 25 novembre 2020

à la Faculté des sciences et techniques de l'ingénieur
Laboratoire de modélisation mécanique multi-échelle
Programme doctoral en science et génie des matériaux

pour l'obtention du grade de Docteur ès Sciences

par

Shankha NAG

Acceptée sur proposition du jury

Prof. N. Marzari, président du jury
Prof. W. Curtin, directeur de thèse
Prof. A. Hartmaier, rapporteur
Prof. D. Warner, rapporteur
Prof. P. Derlet, rapporteur

École
polytechnique
fédérale
de Lausanne

2020

Crystals are like people: it is the defects in them
which tend to make them interesting!
— Colin Humphreys

To my parents…

Acknowledgements

The work for this thesis was carried out from 2015 to the time of writing, at the École polytechnique fédérale de Lausanne (EPFL), in the Laboratory for Multiscale Mechanics Modeling (LAMMM). The work was supported by the European Research Council through the ERC/FP Project 339081 entitled "PreCoMet Predictive Computational Metallurgy" and by the Swiss National Science Foundation through the Project #200021_181987 entitled "Harnessing atomic-scale randomness: design and optimization of mechanical performance in High Entropy Alloys". Numerical simulations were performed using the facilities of the Scientific IT and Application Support (SCITAS) Center at EPFL.

Before introducing the subject matter, I would like to thank a few people. First and foremost, I would like to thank my thesis advisor, Prof. William A. Curtin, for his guidance and support. His insight on various problems was very helpful. Weekly meetings with him helped me stay focused. He conducted weekly group meetings and organized annual winter retreats where I learned about various topics in mechanics of materials, outside my own field of research. Prof. Curtin has a unique ability of explaining difficult concepts in very simple words which I find intriguing. I also thank him for granting me the opportunity to visit conferences and summer schools abroad.

I am also grateful to the members of the jury for participating in my PhD oral examination. It was a wonderful discussion which provided me with new perspectives to my PhD work.

Next, I would like to thank the current and former members of LAMMM for their help and support on multiple occasions: Wolfram Nöhring, Binglun Yin, Rasool Ahmad, Ankit Gupta, Abhinav Jain, Alireza Ghafarollahi, Ekin Kubilay, Max Hodapp, Predrag Andric, Ali Tehranchi, Daniel Marchand, Yi Hu, Eleanor Mak, Carolina Baruffi, Ali Falsafi, Marcus Stricker, Xiao Zhou, Céline Varvenne, Wu Zhaoxuan, Varun Rajan, Francesco Maresca, Nikolaos Bouklas, Till Junge, Satish Rao, Mostafa Khosrownejad, Mike Francis, Vladimir Dorodnitsyn and Florian Maurin; as well as a number of visiting professors: Alejandro Strachan, Derek Warner, Ryo Kobayashi and Jun Song. I enjoyed the friendly atmosphere in the lab and the lively discussions. Moreover, I owe a debt of gratitude to the secretary of LAMMM, Géraldine Palaj, for her assistance with numerous administrative issues.

I had insightful discussions on various scientific topics with my colleagues, especially Till,

Rasool, Ankit, Binglun, Alireza, Abhinav and Carol. I would like to thank Till for his CADD mesher and also for the idea of the "Relaxed pad" for the concurrent multiscale project. I am extremely grateful to Wolfram for helping me in resolving various coding-related problems, during the initial years of my PhD. I had many interesting discussions with senior lab members, Wu Zhaoxuan and Satish Rao. And I am very grateful to my colleagues and friends who proof-read parts of my thesis: Eleanor, Ankit, Abhinav, Alireza, Rasool, Max, Charlotte and Mayuri. I would also like to thank Carol, Abhinav, Ankit, Max, Rasool and Xiao for their excellent feedback on my private defense presentation. In the lab, I shared a special bond with Binglun, Rasool, Ankit and Predrag, who helped me through stressful times of my PhD.

I would also like to thank my friends outside LAMMM, who have been a great support: Charlotte Vidal, Venkat Kapil, Nihar Gargava, Mukesh Thakur, Bhushan Hedge, Moulik Choraria, Soumya Basu, Arnab Biswas, Richa Agrawal, Harsh Vardhan, Atri Bhattacharyya, Rishabh Iyer, Siddharth Gupta, Ankita Kayal, Arkopal Choudhury. I have known Charlotte for four years and she and her mother Laurence have been like a family to me. She has always been there for me one call away. Among my other Swiss connections, I would like to mention Sandra Roux, who has also been very helpful and welcoming. My Bengali friends in Lausanne, Soumya and Arnab, are like brothers to me. They introduced me to their friends and I had a great time with them. Venkat is the first person I got to know when I arrived in Lausanne. He welcomed me to stay with him for my first few days in Lausanne until I found an accommodation and showed me around. It was great sharing my office with Ankit and I had insightful scientific discussions with Rasool. Through them, I came to know the other Indian guys living at Livit apartment, Mukesh, Nihar and Bhushan and then some others: Moulik, Harsh and Richa. It was great spending time with them, even when they gave me a hard time! I will never forget their loud knocks on my door, stealing from my fridge, annoying me — but somehow I enjoyed their pranks. They were a great deal of support during the stressful times of my PhD and I am very grateful to them.

Last but not least, I want to thank my parents for always being there for me. I am lucky to have such wonderful parents.

Lausanne, November 4, 2020 S. N.

Abstract

Under common processing conditions, both dilute and complex concentrated alloys are often realized as random alloys, with no correlation in the occupancy of lattice sites by the constituent atom types. The current thesis primary addresses two problems in random alloys, namely (1) the application of concurrent multiscale modeling and (2) solute-strengthening.

For accurate functioning of a forced-based atomistic-continuum (a/c) couple, it is important that the underlying material description of the two domains are the same near the a/c interface. A/c coupling of random alloys violates this criterion since the atomistic domain is inherently inhomogeneous with local fluctuations in atomic configuration and elastic stiffness, while the continuum is defined with the average elastic constants of the alloy. The resulting coupling errors are of the order of 100 MPa in long-range spurious stresses and spurious stress fluctuations near the interface. Two methods of constructing the coupled problem are proposed in this thesis to mitigate coupling errors. In Method 1, the pad atoms are relaxed with respect to the atoms in the atomistics domain in the initial construction of the a/c couple, which eliminates spurious stresses in absence of external loading. Negligible spurious stresses (≈ 5 MPa) arise on loading the coupled problem. Method 2 replaces the random pad atoms with average atoms, thus explicitly eliminating fluctuations in the pad region which causes coupling errors. This methods also yield coupling errors of ≈ 5 MPa, which are negligible relative to stresses arising in realistic mechanical problems of interest.

The latter part of the thesis deals with solute-strengthening in random alloys. In random alloys, strengthening is caused by the pinning of dislocation segments in favourable solute environments. The length scales of dislocation undulation and the energy barrier for unpinning local segments are controlled by solute-dislocation interactions (SDIs) and solute-solute interactions (SSIs). The SDIs are modeled as the interaction of solute misfit volume with dislocation pressure field, under anisotropic elasticity assumption. Comparison of the anisotropic theory with isotropic theory shows that the Voigt-averaged elastic constants best reproduce the anisotropic predictions. SSIs are accounted for in the strengthening theory and it is found to cause significant additional strengthening (≈ 70% at 10% Al) in dilute Ni(Al) alloys with strong Al-Al repulsion, but only a negligible increase in strength (≈ 2%) in bcc MoNbTaW complex alloy with larger solute misfit volumes and lower SSIs. Finally, the thesis also studies the role of short-range order (SRO) on alloy strengthening and predicts the average strengthening due to SRO, in terms of solute pair interaction energies, the well-known Warren-Cowley SRO parameters and alloy composition. The theory accounting for SRO is in progress, however, the theory in its current state lays the groundwork for realizing the most comprehensive strengthening theory for alloys of any compositional complexity.

Keywords: random alloys, atomistic-continuum coupling, dislocations, solute-strengthening, anisotropic elasticity, solute-dislocation interactions, solute-solute interactions, short-range order.

Résumé

Dans des conditions de traitement courantes, les alliages concentrés dilués et complexes sont souvent réalisés sous forme d'alliages aléatoires, sans corrélation dans l'occupation des sites de réseau par le types d'atomes constitutifs. La thèse principale actuelle aborde deux problèmes dans les alliages aléatoires, à savoir (1) l'application de la modélisation simultanée à multiéchelles et (2) le renforcement des solutés.

Pour un fonctionnement précis d'un couple atomistique-continuum (a/c) forcé, il est important que la description matérielle sous-jacente des deux domaines soit la même près de l'a/c interface. Le couplage a/c d'alliages aléatoires viole ce critère car le domaine atomistique est intrinsèquement inhomogène avec les fluctuations locales de la configuration atomique et de la rigidité élastique, tandis que le continuum est défini avec les constantes élastiques moyennes de l'alliage. Les erreurs de couplage qui en résultent sont de l'ordre de 100 MPa en faux stress longue portée et les fluctuations de faux stress près de l'interface. Deux méthodes de construction de problèmes couplés sont proposés dans cette thèse pour atténuer les erreurs de couplage. Dans la méthode 1, le atomes de "pad" sont relâchés par rapport aux atomes dans le domaine atomistique dans la construction initiale du couple a/c, ce qui élimine les faux stress en l'absence de chargement externe. De faux stress négligeables (≈ 5 MPa) surviennent lors du chargement du problème couplé. La méthode 2 remplace les atomes aléatoires par des atomes moyens, éliminant ainsi explicitement les fluctuations de la zone de pad qui provoque des erreurs de couplage. Ces méthodes donnent également des erreurs de couplage de ≈ 5 MPa, qui sont négligeables par rapport aux contraintes résultant de problèmes mécaniques d'intérêt réalistes.

La dernière partie de la thèse traite du renforcement des solutés dans des alliages aléatoires. Dans alliages aléatoires, le renforcement est causé par l'épinglage des segments de dislocation dans des environnements solutés favorables. Les échelles de longueur de l'ondulation de dislocation et la barrière d'énergie pour le détachement des segments locaux sont contrôlées par les interactions soluté-dislocation (ISD) et les interactions soluté-soluté (ISS). Les ISD sont modélisés comme l'interaction du volume de soluté inadapté avec champ de pression de dislocation, sous hypothèse d'élasticité anisotrope. La comparaison de la théorie anisotrope avec la théorie isotrope montre que les constantes élastiques à moyenne de Voigt reproduisent au mieux les prévisions anisotropes. Les ISS sont pris en compte dans la théorie du renforcement et il est constaté qu'elles provoquent un renforcement supplémentaire significatif ($\approx 70\%$ à

10% Al) dans des alliages Ni(Al) dilutés avec une forte répulsion Al-Al, mais seulement une augmentation négligeable de la résistance (≈ 2%) dans un alliage complexe MoNbTaW bcc avec des volumes de soluté inadaptés plus grands et des ISS inférieures. Finalement, la thèse étudie également le rôle de l'ordre à courte distance (OCD) sur le renforcement des alliages et prédit le renforcement moyen dû au OCD, en termes d'énergies d'interaction de paires de solutés, le paramètres connus de Warren-Cowley OCD et composition de l'alliage. La théorie expliquant le OCD est en cours, cependant, la théorie dans son état actuel jette les bases pour réaliser la théorie de renforcement la plus complète pour les alliages de toute complexité compositionnelle.

Mots-clés : alliages aléatoires, couplage atomistique-continu, les dislocations, renforcement de solutés, élasticité anisotrope, interactions soluté-dislocation, interactions soluté-soluté, ordre à courte distance.

Contents

Acknowledgements **i**

Abstract (English/Français) **iii**

List of Figures **xi**

List of Tables **xvii**

Introduction **1**

1 Background **7**
1.1 Concurrent multiscale modeling methods 8
1.2 Solute-strengthening 13

2 Methods **21**
2.1 Atomistic calculations with Classical Potentials 22
2.1.1 Energy minimization 22
2.1.2 Embedded atom method 22
2.1.3 Average-atom approximation for random alloys 23
2.2 Static equilibrium in solid mechanics and Finite Elements Method 25
2.3 Force-based atomistic-continuum coupling 29
2.4 Solute misfit volume 30
2.5 Interaction of two defects in an infinite linear elastic medium 31
2.5.1 Elastic interaction of solute pair 34
2.5.2 Elastic interaction of solute with dislocation 35
2.6 Elastic field of a straight dislocation in elastically anisotropic solid 35
2.7 Solute pair interaction energies 40
2.8 Elementary probability theory 41

I Concurrent multiscale modeling **45**

3 Atomistic continuum coupling of random alloys **49**
3.1 Errors in application of standard a/c coupling to random alloys 52
3.2 Illustration of the problem with 1D array of linear springs and proposed solutions 55

3.3 Methods for accurate 3D a/c coupling of random alloys described by complex interatomic potentials . . . 59
3.3.1 Method 1 . . . 60
3.3.2 Method 2 . . . 64
3.4 Discussion . . . 68

II Theory of Solute Strengthening 71

4 Solute-strengthening in elastically anisotropic fcc alloys 75
4.1 Linear elasticity model . . . 76
4.1.1 Anisotropic elasticity for solute/dislocation interactions . . . 77
4.1.2 Solute/dislocation interactions estimated with average isotropic elastic constants . . . 78
4.1.3 Dislocation core structure parameterization . . . 79
4.2 Results . . . 80
4.2.1 Line tension . . . 80
4.2.2 Error of the isotropic approximation . . . 81
4.2.3 Errors in energy barrier and zero-T strength . . . 82
4.3 Practical application of the theory . . . 87
4.3.1 Normalized results for w_c, ΔE_b and τ_{y0} using isotropic elasticity . . 87
4.3.2 Application using experimental or computational inputs . . . 89
4.4 Discussion and Summary . . . 92

5 Effect of Solute-Solute Interactions on strengthening of random alloys 95
5.1 Solute-strengthening theory accounting for solute-solute interactions . . 97
5.2 Analytical expression for normalized variance $\widetilde{\sigma}^2_{\Delta E_{ss}}$ for multicomponent alloys . . . 103
5.3 Validation of $\widetilde{\sigma}_{\Delta E_{ss}}$ . . . 109
5.4 Strengthening in high entropy and dilute binary alloys due to solute-solute interactions . . . 112
5.4.1 MoNbTaW and NbTaV bcc high- and medium- entropy alloys . . . 112
5.4.2 Dilute Ni-Al fcc solid solution alloys . . . 114
5.5 Summary . . . 119

6 Solute-strengthening in alloys with short-range order 123
6.1 Characterizing short-range order . . . 124
6.2 Properties of pair correlation functions . . . 125
6.3 Superposition approximation for higher-order correlation functions 127
6.4 Solute-strengthening theory: accounting for short-range order (SRO) . . . 128
6.4.1 Average strengthening in alloys with SRO . . . 129
6.4.2 Local strengthening in alloys with SRO . . . 137
6.5 Variance in energy change due to dislocation glide $\sigma^2_{\Delta E_p}$ . . . 141

6.5.1 Contribution due to solute-solute interactions $\sigma^2_{\Delta E_{ss}}$ 141
6.5.2 Contribution due to solute-dislocation interactions $\sigma^2_{\Delta E_{sd}}$ 143
6.5.3 Correlation between the energy changes due to solute-solute (ΔE_{ss}) and solute-dislocation (ΔE_{sd}) interactions 148
6.6 Discussion and Summary 152

7 Summary 155

8 Outlook 159

A Appendix 163
A.1 Slip density in fcc elements 163
A.2 Interaction energies, Effective Pair Interactions and Bond energies 166

Bibliography 171

Curriculum Vitae 183

List of Figures

1 Ashby plot of strength versus fracture toughness showing that NiCoCr-based medium- and high-entropy alloys are among the most damage-tolerant materials on record. (*Extracted from Ref. [1]*) 2

2 Schematic showing decreasing fluctuation in alloy composition with increasing system size. 3

3 Schematic comparison of the energy landscape relative to a gliding dislocation in (a) elements and (b) multicomponent alloys. 4

1.1 Demonstration of a concurrent multiscale strategy in problems with localized deformation; in this example a nanoindentation experiment. Figure (a) highlights the "interesting" atoms in a full atomistics simulation where plasticity has taken place through dislocation motion. Figure (b) shows a concurrent multiscale implementation where the "interacting" atoms are retained while the rest of the problem domain is coarse-grained with finite elements, assuming linear elasticity as constitutive law. Since the percentage of "interesting" atoms is quite small in the entire problem domain, the relevance of a multiscale coupling in such context is overly apparent. *(Adapted from Ref. [2])* 8

1.2 The generic form of the atomistic-to-continuum transition region for concurrent multiscale methods with domain-decomposition. Filled atoms are the atoms right on the interface, which coincide with a set of FE nodes in the continuum. The 'pad' atoms serve only as a neighbour environment to the atoms in the atomistic and interface regions. For many of the methods, some or all of the 'pad' atoms are chosen to coincide with nodes in the mesh. *(Extracted from Ref. [3])* 9

1.3 Schematic of the low-energy wavy configuration of the dislocation as it moves through the random field of solutes in a random alloy *(Extracted from Ref. [4])*. 15

1.4 Burger vector distribution in fcc with split dislocation cores. d_p is the distance between the two Shockley partials and σ is the partial core spreading *(Adapted from Ref. [4])*. 19

2.1 A continuum domain Ω with Dirichlet boundary condition over $\partial\Omega_u$ with specified displacement $\boldsymbol{u}_0$ and Neumann boundary condition over $\partial\Omega_t$ with traction $\boldsymbol{T}^{(\boldsymbol{n})}$. 25

2.2 Illustration of the periodic boundary condition in 1D and the resulting stiffness matrix with nonzero entries. 29

2.3 **Schematic illustration of force-based relaxation of a/c couple.** The problem domain is decomposed into atomistic and continuum sub-domains, $\Omega^{\mathbf{A}}$ and $\Omega^{\mathbf{C}}$ respectively. In the overlap region, the pad atoms derive their displacements $\mathbf{u}^{\mathbf{P}}$ from the underlying continuum nodes and the interface nodes derive their displacements $\mathbf{u}^{\mathbf{I}}$ from the interface atoms. Equilibrium equations for the two sub-domains are solved simultaneously, with traction and displacement boundary conditions ($\mathbf{t}$ over $\partial\Omega_{\mathbf{t}}$ and $\mathbf{u}$ over $\partial\Omega_{\mathbf{u}}$ respectively). 30

2.4 A domain Ω in an infinite linear elastic medium bounded by $\partial\Omega$, which contain two sub-domains Ω_1^* and Ω_2^* with eigenstrains $\varepsilon^{1,*}$ and $\varepsilon^{2,*}$. 31

2.5 Constraints in displacement field and tractions in a problem with an infinite straight dislocation at the origin. The dislocation line vector $\boldsymbol{\xi}$ (not shown) is along $\mathbf{e}_3$ pointing out of the page. b_k is the k^{th} component of the Burgers vector $\boldsymbol{b}$. $\mathbf{F}/L$ is the net force per unit length along the dislocation line acting on the surface of a rod parallel to the dislocation and containing it, as shown in the figure with the contour. 36

2.6 Schematic of two the systems whose energy difference gives the interaction energy for the solute pairs indicated here with red and blue atoms. 41

3.1 **Schematic of an a/c couple under tensile elongation for an infinite slab of random alloy.** For all cases of a/c coupling examined for this study, this geometry has been used. Translucent atoms and nodes in the diagram are the periodic images of the boundary degrees of freedom in the $x-$ and $y-$ directions. The planar a/c interface perpendicular to the thickness of the slab ensures that any coupling-induced spurious stresses propagate through the specimen unattenuated. The thickness of the atomistic and continuum domains are 34 and 17 lattice units respectively, with the atomistic domain being larger so as to achieve converged values for the average lattice constant and elastic constants of the random alloy. The simulation box (with all the opaque atoms and nodes) is 50 lattice units in $x-$ direction and 20 lattice units in $y-$ direction. The thickness of the pad is determined by the cut-off radius of the interatomic potential which is typically one lattice unit in $z-$direction. 53

3.2 **Standard a/c couple with no imposed deformation.** Coupling-induced spurious stresses along coupling direction $\Delta\sigma_{zz}^{m}$ and $\Delta\sigma_{zz}^{std}$ as a function of distance from the a/c interface. Results are for specimens of equicomposition FeNiCr held fixed at z-ends of the specimen (thus no imposed deformation). For each alloy, results for 10 different realizations are shown as indicated by the various colors. 55

3.3 A series of linear spring with same stiffness connected end-to-end, each of which has a different natural length. The average version of this ensemble is another series of linear springs ("average springs") with the same stiffness, where the natural length of every average spring is average of the natural lengths of real springs in the original series. 56

3.4 A standard force-based couple constructed with the random and average ensemble of springs shown in Figure 3.3. 56

3.5 Elimination of spurious force at the interface due to construction by relaxing the pad spring in the random ensemble to its natural length before constructing the coupled problem. 57

3.6 Force-based couple with springs of varying stiffness and average springs with average stiffness $\overline{k}$. 58

3.7 The two solutions to resolve the errors due to coupling that manifest on application of external force. 59

3.8 **A/C coupling for random alloys: Method 1** Ω^A and Ω^C are the atomistic and continuum domains respectively. 60

3.9 **Method 1: results at $\boldsymbol{\varepsilon_{zz} = 0.1}$%** Coupling-induced spurious stresses for the normal component ($\Delta\sigma^m_{zz}$ and $\Delta\sigma^{std}_{zz}$) as a function of distance from the a/c interface, for test specimens of three types of random alloys stretched uniformly by 0.1% along coupling direction. For each alloy, results for 10 different realizations are shown as indicated by the various colors. 63

3.10 **A/C coupling in random alloys: Method 2** The random/homogeneous interface and the atomistic/continuum interface are separated by the introduction of a small buffer zone of A-atoms in the atomistic domain, with the pad atoms being A-atoms. 64

3.11 **Method 2, no imposed deformation** Coupling-induced stress statistics of the normal component of spurious stress along coupling direction ($\Delta\sigma^m_{zz}$ and $\Delta\sigma^{std}_{zz}$) as a function of distance from the a/c interface, for test specimens of three random alloys with z-ends held fixed. For each alloy, results for 10 different realizations are shown as indicated by the various colors. 66

3.12 **Method 2, results at $\boldsymbol{\varepsilon_{zz} = 0.1}$%** Coupling-induced stress statistics of the normal component of spurious stress along coupling direction ($\Delta\sigma^m_{zz}$ and $\Delta\sigma^{std}_{zz}$) as a function of distance from the a/c interface, for test specimens of three random alloys stretched uniformly by 0.1% along coupling direction. For each alloy, results for 10 different realizations are shown as indicated by the various colors. 67

4.1 Non-dimensional total energy of a wavy dislocation in a random alloy as a function of the amplitude, for various Shockley partial separation distances d_p at fixed partial peak width $\sigma/b = 1.5$ as computed assuming isotropic elasticity. For partial separations $> 6b$, there are two minima at $w_{c,1}$ and $w_{c,2}$ while for small partial separations the first minimum is subsumed by the second minimum, resulting in a single minimum label as $w_{c,1}$. 80

4.2 Comparison of μ_{avg} with $\mu_{111/110}$ for the different isotropic averaging schemes as a function of C_{11}/C_{44} and A. 81

4.3 Relative differences in ΔE_b and τ_{y0} estimated with average isotropic elastic constants versus those predicted with full stiffness tensor as a function of anisotropy ratio A (for $C_{11}/C_{44} = 2.7$ and dislocation core parameters being $d_p = 7b$ and $\sigma = 1.5b$). Results are reported for Voigt, Reuss and Hill isotropic averages. Filled circle markers: first minimum solution. Filled star markers: second minimum solution. 82

4.4 Relative differences in ΔE_b and τ_{y0} as estimated with Voigt isotropic elastic constants versus full anisotropy as a function of C_{11}/C_{44} and anisotropy ratio (for dislocation core parameters $d_p = 7b$ and $\sigma = 1.5b$). Marker colors indicate different C_{11}/C_{44} values. Filled circles: first minimum solution; filled stars: second minimum solution. 83

4.5 Relative differences in (a) w_c, (b) ΔE_b and (c) τ_{y0} computed with the Voigt-averaged isotropic elastic constants versus full anisotropic results as a function of the anisotropy ratio A, for the first minimum solution. 85

4.6 Relative differences in (a) w_c, (b) ΔE_b and (c) τ_{y0} computed with the Voigt-averaged isotropic elastic constants versus full anisotropic results as a function of the anisotropy ratio A, for the second minimum solution. *Note that there is no second minimum solution for the wider partial spreads* $\sigma/b = 2, 2.5$ *when the partial separation is* $7b$ *since it is effectively one full dislocation undissociated.* . 86

4.7 (a) Dislocation roughening amplitude w_c, (b) dimensionless ΔE_b, and (c) dimensionless τ_{y0} versus partial separation distance d_p/b, for different partial core spreading σ/b, as computed assuming isotropic elasticity. 88

5.1 Schematic illustration of pair changes across the slip plane due to slip by a lattice vector $\boldsymbol{t}$. Selected atom pairs are indicated by colored lines in both figures. Considering distances only in the two planes just above and below the slip plane for simplicity, upon slip 1st NN pairs become 2nd NN pairs (e.g. red-green), 2nd NN pairs can become 1st NN pairs (e.g. red-red) or 3rd NN pairs (e.g. red-blue), and 3rd NN pairs can become become 2nd NN pairs (e.g. red-blue) or 4th NN pairs (not shown). These changes combine with solute-solute interactions to create the fluctuations in energy upon slip that lead to strengthening. 96

5.2 Dimensionless solute-dislocation energy fluctuation quantity $g(w_c, d_p, \sigma)$ for fcc alloys as a function of the partial dislocatoin separation d_p/b, for different dislocation core structures characterized by partial core spreading σ/b. 99

5.3 Schematic of areas swept during dislocation glide by a distance w. (a) bcc crystal (no dissociation); (b) fcc crystal (dissociated core) with $w < d_p$; (c) fcc crystal (dissociated core) with $w > d_p$. 100

5.4 Lennard-Jones pair potentials U_{mn} versus radial distance r for all pairs among the 5 different atomtypes A, B, C, D, E. Every pair is tabulated alongside labelled by color, with the respective scaling parameters α_{mn} and β_{mn}. 109

5.5 Validation of analytical prediction for $\widetilde{\sigma}_{\Delta E_{ss}}$ derived in Setion 5.2 against simulations. Data corresponding to 10621 different alloy composition with the five atomtypes consisting of binary, ternary, quaternary and quinary alloys, is shown. The dashed line corresponds to exact agreement; deviations arise only due to statistical variations in the simulations due to a finite number of samples studied. 111

5.6 The effective pair potentials V_{mn}^{eff} as a function of normalized nearest-neighbour pair separation d, for bcc MoNbTaW calculated via first principles[5]. 113

5.7 Alloy-specific inputs for strength prediction versus Al concentration: Al-Al interaction energies U_{AlAl}^{int}, solute(n) misfit volume ΔV_n and elastic constants C_{ij}. The Al-Al interaction energies are shown for the first three near-neighbour(NN) distances across the slip plane, only the first NN interaction is significant. Misfit volumes are computed from experimental data[6] on lattice parameter versus composition. 115

5.8 (a) Total energy fluctuations entering the solute-strengthening theory and the contribution of solute-dislocation interactions only, for DFT and EAM potential inputs and for both solutions of w_c; (b) Predicted fractional increase in T=0K yield stress due to the inclusion of solute-solute interactions, for DFT and EAM potential inputs, for both solutions of w_c. 117

5.9 Validation of theory against simulations: characteristic wavelength of dislocation waviness and the yield stress. M04 interatomic potential is used for both predictions and simulations. 119

6.1 Schematic representation of “average” and “local” strengthening in alloys in subfigures (a) and (b) respectively. Average strengthening is related to the stress required to pay for any energy penalty associated with dislocation motion in an alloy. Subfigure (a) shows the glide of average dislocation line from $x = -\eta$ to $x = 0$ — if an energy cost per unit area is associated with the newly created slipped area, then there will be an associated average strengthening. Local strengthening or strengthening due to fluctuations, on the other hand, is related to the stress required to unpin dislocation segments locally from favourable solute environments to resume and sustain unabated glide. Subfigure (b) shows dislocation segments of length ζ in an undulated dislocation line which are pinned by favourable solute environments w distance away from the dislocation mean position. 129

6.2 Schematic illustration of spatial distribution of energy changes due to solute-dislocation and solute-solute interactions when a positive edge dislocation (along z-axis) glides a distance w. The solute-dislocation interactions extends upto infinity but decreases with distance from the core — the bounded regime of solute-dislocation interaction is just for illustration. 138

6.3 Schematic of the distances and indexes used in (a) Equation 6.46 and (b) Equation 6.47, which basically simplifies the 2^{nd} and 3^{rd} terms in Equation 6.44 respectively. 147

A.1 Analysis of the dislocation core: atomistics, Gaussian fit and relative displacement gradient due to the fitted Gaussian core. The blue stars ★ are the $D\Delta\mathbf{u}/Dx$ computed from atomistic displacements near the dislocation core, the dislocations $\perp$ are from bimodal Gaussian fit to the atomistic $D\Delta\mathbf{u}/Dx$ (explained in the text) and the red filled circles • are the $D\Delta\mathbf{u}^{\mathbf{tot}}/Dx$ computed from the anisotropic displacement field due to the dislocations $\perp$ (also explained in the text). 165

List of Tables

3.1 Lattice parameter and elastic constants of true random alloy and those of the corresponding A-atom potential, for the three random alloys studied in this paper. Errors in the A-atom quantities are indicated in parentheses. 51

3.2 Perturbations Δc_X of the A-atom alloy away from the true alloy composition c_X so as to match the lattice constants of the random alloy upto 8 decimal places. The corresponding elastic constants of the A-atom potential are shown but differ negligibly from those at composition c_X; errors relative to the true random alloy are shown in parentheses. 51

5.1 Structure factors $\Theta_{dd'}$ in Equations 5.25 and 5.26 for various fcc and bcc slip systems in terms of pair distances (d, d'). The extended form of the third subtable for partial slip in fcc is provided in Ref. [7]. 108

5.2 Normalized neighbor distance and number of sites at that distance for bcc and fcc crystals. 110

5.3 Role of solute-solute interactions in solute solution hardening of bcc MoNbTaW and NbTaV high-entropy alloys, with inputs from either DFT or interatomic potentials. For each alloy, the characteristic amplitude w_c, solute-dislocation interaction energy parameter $\Delta\widetilde{E}_{\mathrm{p},sd}(w_c)$, solute-solute interaction energy parameter computed from the solute interactions and w_c, and the total energy parameter $\Delta\widetilde{E}_{\mathrm{p}}(w_c)$ are shown. The strengthening with solute-solute interactions is compared to the strengthening with only solute-dislocation interactions, and the increases in strength are negligible. 113

6.1 The structure factors $n_{dd'}$ for every pair of normalized pair distances (d, d') for full slip in fcc and bcc. 135

Introduction

Alloying has been known to mankind since the Bronze Age as a way to improve the properties of metals. The oldest-known alloy Bronze, formed by the addition of tin to copper, is a class of ductile alloys with good thermal and electrical conductivity and corrosion resistance, which has been used extensively by early civilizations to make sculptures and utensils. Brass is another example of a copper-based alloy of high workability which has been used extensively in myriad applications. Over the course of time the Bronze Age gave way to the Iron Age, with the advent of steels, alloys of iron and interstitial carbon, which are stronger than bronze and more durable. During the course of human civilization, alloying has been extensively used to create strong, tough and durable structural materials. The demand for more advanced alloys with other desirable mechanical properties such as creep resistance, resistance to fatigue failure and corrosion keeps increasing, which is fueled by continuing advancements in science and technology. Titanium alloys, nickel- and cobalt-based superalloys, zirconium alloys have been developed for specialized structural applications for example in the blades of gas turbines, in medical implants and in cladding of fuel rods in nuclear reactors.

Until recently, the paradigm of alloying was to add relatively small amounts of secondary elements (*solutes*) to a primary element (*host*) e.g. aluminium to nickel, magnesium to aluminium, chromium to nickel, etc. In contrast to this traditional practice of alloying, the past few decades have seen a surge in research interest for developing alloys with multiple principal elements in relatively high, often equiatomic, concentrations; this class of alloys is called high(or medium)-entropy alloys, complex concentrated alloys, or simply multicomponent alloys. Despite the complex composition, these alloys often form single face-centered cubic (fcc) or body-centered cubic (bcc) phases without precipitates. As there is no one primary element in these alloys, all the atoms can be considered as solutes embedded in an average matrix acting as host, with average elastic and structural properties of the alloys. Notable examples of complex concentrated alloys include the Cantor alloy (equiatomic CrMnFeCoNi) and its variants (e.g. NiCoCr) and the refractory complex alloys (Ti-Zr-Hf-Nb-Ta-Mo-W-V family of high- and medium- entropy alloys). These alloys show superior strength and fracture toughness in comparison to tradition alloys, as evident from the Ashby plot in Figure 1, which shows that the NiCoCr-based medium- and high-entropy alloys are among the most damage tolerant materials on record.

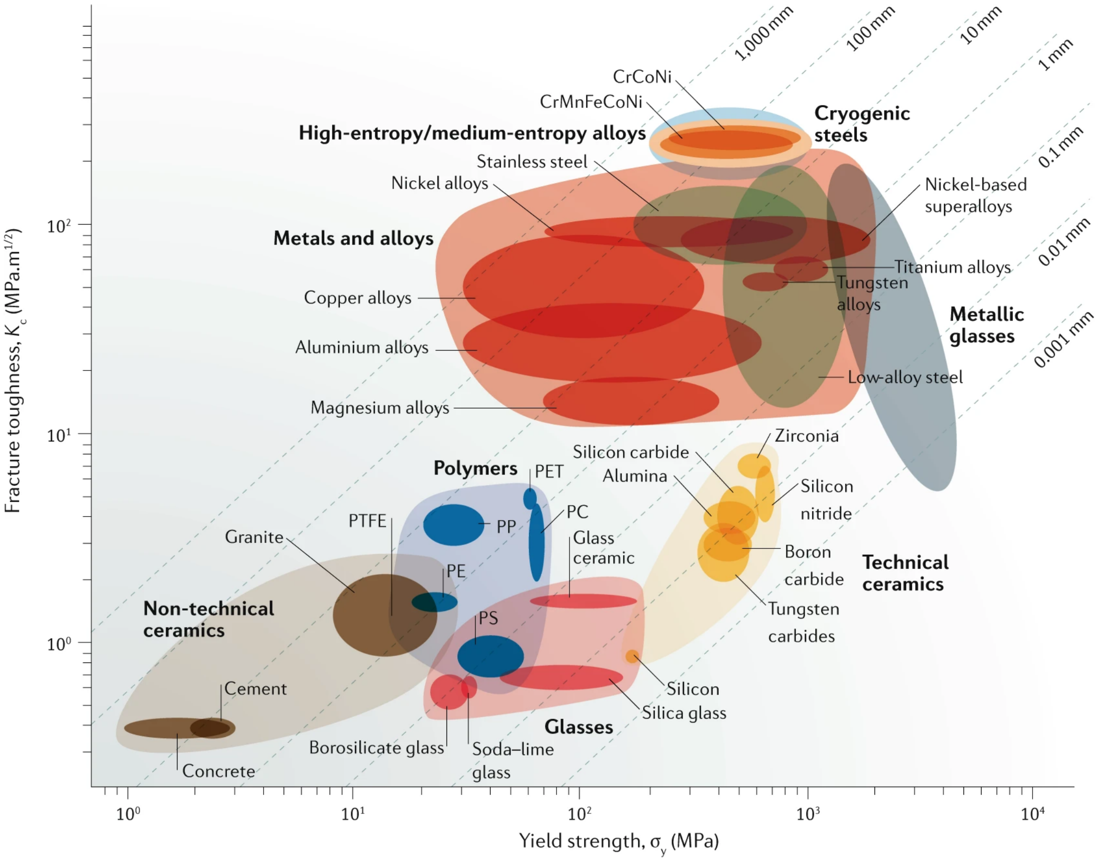

Figure 1 – Ashby plot of strength versus fracture toughness showing that NiCoCr-based medium- and high-entropy alloys are among the most damage-tolerant materials on record. (*Extracted from Ref. [1]*)

Studying complex concentrated alloys can be challenging due to the vast combinatorial possibilities in composition and constituent elements across the periodic table. Theoretical models and efficient computational methods must supplement experiments to probe through the vast combinatorial and compositional space of these complex alloys to find candidates with desirable mechanical properties for various applications. However, modeling alloys, be it dilute or complex concentrated, comes with an unprecedented challenge of dealing with inherent compositional fluctuations in alloys. The general goal of the thesis is to address some of the challenges in modeling alloys by mitigating the errors due to compositional fluctuations in certain computational methods and to develop new theoretical models to predict strength of alloys by carefully treating these fluctuations.

Compositional fluctuations in alloys are associated with length scales. As illustrated in Figure 2b, the concentrations of the constituent atomtypes converge to the ideal concentration for the equiatomic ternary system, i.e. 1/3, with increasing system size following the Law of Large Numbers. However, *locally* the concentration in a solute environment can be far from the ideal alloy composition, e.g. the high compositional fluctuation of the innermost box of atoms in Figure 2a. A line defect in an alloy, for instance a dislocation or a crack front, is subjected to a fluctuating solute environment along its length. The interaction between the defect and solutes mechanically through the pressure field of the defect, and also chemically near the defect core, is associated with length scales dictated by compositional fluctuations. These lengths scales are associated with the undulation along the length of line defects or the spacing of local energy minima encountered by the defect as it moves through the alloy. Any model, whether theoretical or computational, which attempts to model defect behaviour in alloys, e.g. dislocation emission from crack tip or dislocation glide, must consider these length scales.

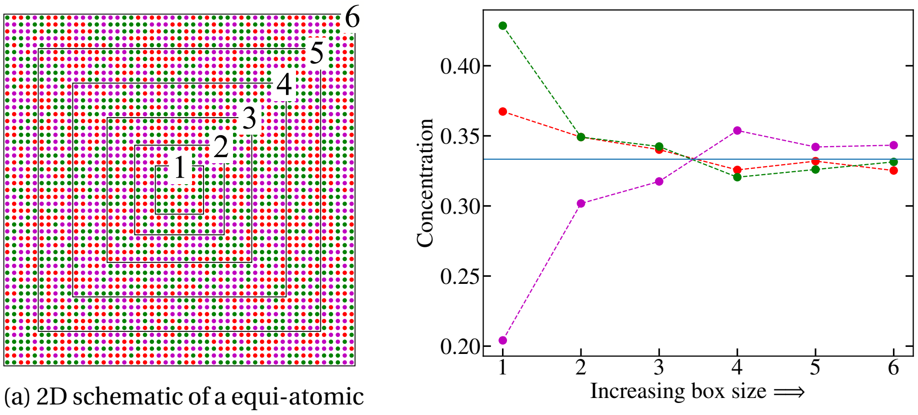

(a) 2D schematic of a equi-atomic ternary alloy

(b) Compositional fluctuations in a ternary alloy

Figure 2 – Schematic showing decreasing fluctuation in alloy composition with increasing system size.

Figure 3 compares the schematic depictions of the energy landscape of a gliding dislocation in monoatomic elements and multicomponent alloys. Due to symmetry, the energy landscape in elements has a corrugated pattern with periodic array of alternating ridges and grooves, commonly known as the Peierls barriers and Peierls valleys respectively. A dislocation resting in a Peierls valley, under stress and/or thermal excitation, makes a transition over a Peierls barrier to the next Peierls valley (Figure 3a). In a multicomponent alloy, the energy landscape is complicated due to the interaction of the dislocation with the surrounding compositional fluctuations. The troughs and crests in the energy landscape are much deeper and elevated, respectively, compared to the elemental landscape and the dislocation undulates in response to the compositional fluctuations so as to have segments lying in the troughs of the energy landscape to minimize total system energy (Figure 3b). More applied stress is required to pull out a relaxed dislocation segment from a deeper tough and glide it over a crest, thereby strengthening the alloy by impeding dislocation motion. The length scales in the compositional fluctuations have translated into length scales associated with the undulations of the dislocation line, which in turns influences alloy strengthening. The underlying fluctuating energy landscape of a dislocation in an alloy (i.e. in Figure 3b) cannot actually be determined without defining some characteristic segment length of the dislocation line to estimate the energy cost/gain of its glide, thus emphasizing the importance of length scales in the mechanics of alloys.

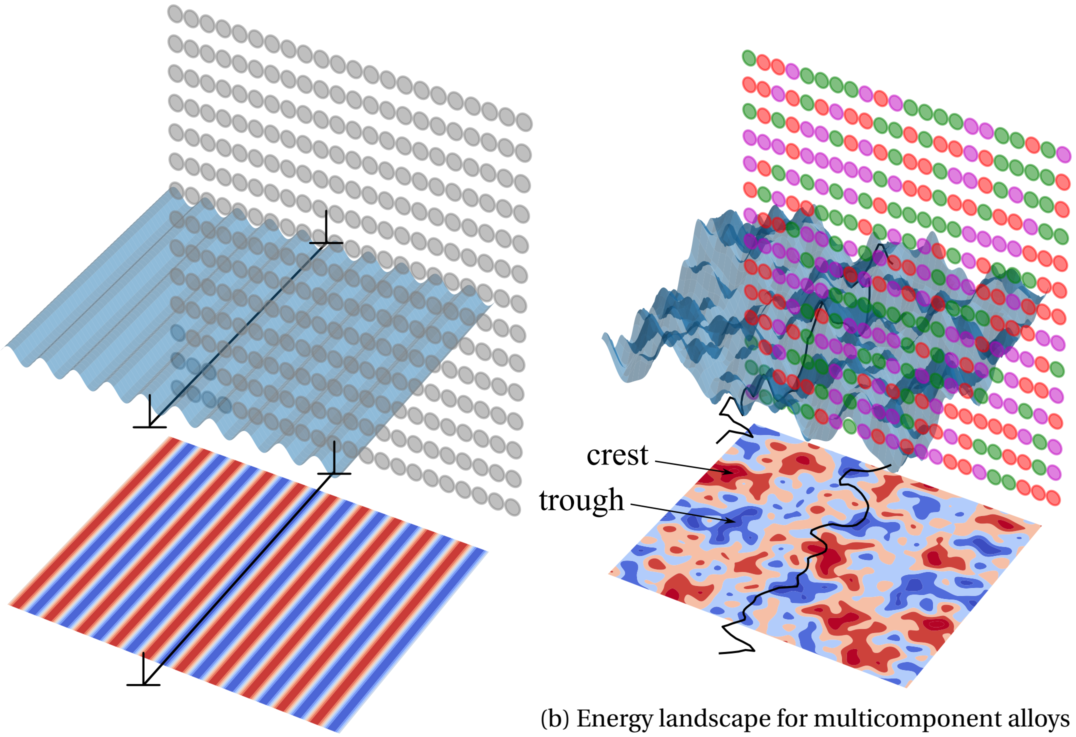

(b) Energy landscape for multicomponent alloys

(a) Peierls valley for elemental crystalline solids

Figure 3 – Schematic comparison of the energy landscape relative to a gliding dislocation in (a) elements and (b) multicomponent alloys.

Another aspect of compositional fluctuation in context of defect behaviour in alloys, concerns the range of influence. Since the pressure field of a dislocation or a crack front extends to infinity, in principle every solute in the system interact with the defect. However, since the elastic fields decay with distance from the defect and depending on the rate of decay, the solute fluctuations no longer have a notable impact on defect behaviour beyond a certain distance from the defect and one can forgo those far-away compositional fluctuations while studying the defect behaviour. This makes it possible to study defects in alloys using concurrent multiscale modeling where the high deformation region around the defect is modeled with atomistics and the far-field deformation is modeled with a less expensive continuum approximation, like Finite Element method, with linear elasticity constitutive law. The fluctuating solute environment around the defect is retained by the atomistics model whereas the far-field continuum model is rid of all compositional fluctuations and is described by the average elastic properties of the alloy. Replacing finer details of a problem with an average description is called *homogenization*; the continuum model mentioned above is one example of homogenization.

This thesis explores certain problems involving fluctuations, length scales and homogenization in alloys. There are two ways to address these problems, viz. (1) computational modeling and (2) theoretical modeling. While simulating defect behaviour in a multicomponent alloy the system size is a limiting factor since it dictates the computational cost. As previously noted, using small system size for simulating defect behaviour will discard compositional fluctuations that might have influence on the defect behaviour. In contrast, a very large system size unnecessarily burdens the simulation with more details with little or no relevance to the defect behaviour of interest. Suitably large domain around the defect is necessary to retain the compositional fluctuations and the rest of the domain may be homogenized; the homogenized domain acts a buffer for load transfer connecting the defect to a much larger external environment. Coupling a homogenous continuum domain to an homogeneous atomistic region of an alloy presents problems which are unseen in the concurrent multiscale modeling of monoatomic crystalline systems. The first part of this thesis addresses these problems and suggest ways to mitigate them.

The other part of this thesis deals with a theoretical framework to predict the strengthening in alloys due to the solute fluctuations around gliding dislocations. The critical length scales associated with an undulated dislocation in an alloy and also the critical energy quantities involved in approximating the rough energy landscape (i.e. in Figure 3b) are identified. The length scales associated with dislocation undulation are then used as inputs for a mesoscale model of solute-strengthening for predicting the critical resolved shear stress for dislocation glide. Such a theoretical framework, albeit rife with assumptions and approximations, captures the physics well, and therefore can help in efficiently scanning through the vast combinatorial and compositional space of high-entropy alloys, and thereby supplement experiments in the search of new alloys with better, more desirable mechanical properties.

The rest of this thesis is organized as follows. Chapter 1 introduces the relevant topics in further detail and existing literature on concurrent atomistic-continuum coupling and theories for solute-strengthening are reviewed. Chapter 2 discusses the methods used in this thesis. The main chapters of this thesis are grouped into two parts: one dealing with concurrent multiscale modeling and the other with the theory of solute-strengthening. Part I has one chapter (Chapter 3) dealing with atomistic-continuum coupling of random alloys. Part II has three chapters — Chapter 4 explores the role of elastic anisotropy on solute-strengthening of random alloys, Chapter 5 modifies an existing solute-strengthening theory for random alloys to incorporate the effect of solute-solute interactions and Chapter 6 proposes a new solute-strengthening theory for alloys with short-range order. Finally, conclusions and open questions and directions for future research are discussed in Chapter 7 and 8 respectively.

1 Background

Structural applications of metal alloys have a long history due to their significant enhancement and control of mechanical properties such as flow strength, ultimate strength, and toughness, as compared to pure elemental metals. Engineering alloys typically fall into two classes. Random or solid-solution alloys have a single-phase crystalline structure but with the alloying elements randomly occupying the lattice sites. Precipitate-strengthened alloys consist of ordered intermetallic precipitates with a well-defined unit cell that are embedded inside a matrix material (which itself is often a dilute random alloy). Intermediate to these two limits are alloys with some short-range order, i.e. not truly random but without long-range order.

The understanding and prediction of the properties of random alloys has seen a resurgence due to the emergence of High Entropy Alloys (HEAs), which are random single-phase crystalline alloys with 5 or more elemental components all at non-dilute concentrations. While some HEAs may be unstable due to precipitate formation, the existence of stable or metastable random phases with high atomic complexity is common. Also, some single-phase HEAs are not entirely random, but show short-range order due to strong underlying solute-solute interactions. Random alloys are nonetheless often obtained because fabrication by annealing at high temperatures in the solid solution state followed by rapid quenching prevents the development of order. The main focus of the thesis is on random alloys, which have applications in, for instance, the automotive (e.g. Al-Mg alloys), aerospace(Ni-Al γ matrix of the Ni-based superalloys), and marine(Cu-Ni alloys) industries and also includes the promising medium and high-entropy alloys with enhanced strength and fracture toughness.

The thesis explores two problems concerning random alloys: (1) atomistic-continuum coupling of these alloys for accurate and efficient study of mechanics boundary value problems where it is essential to capture atomistic phenomena in some localized region of the random alloy, for instance problems involving dislocations and cracks; and (2) the solute-strengthening in random alloys due to pinning of dislocation segments in favourable solute environments which lowers the total potential energy of the alloy.

This chapter will review the relevant existing literature for (1) concurrent multiscale methods and (2) solute-strengthening in random solid solutions. No prior application of any concurrent multiscale method to random alloys is known to the author; so the review of concurent atomistic-continuum coupling will be generic.

1.1 Concurrent multiscale modeling methods

Concurrent multiscale modeling methods aims at reducing the computational cost of modeling a problem with atomistics by resolving only small, strategically chosen sub-domains of the problem with atomistics and coarse-graining/homogenizing the rest of the problem domain; the target is to obtain the same results as classical molecular statics (MS) or molecular dynamics (MD) simulations at a fraction of the computational cost. Figure 1.1 illustrates the strategy using a specific example of nanoindentation.

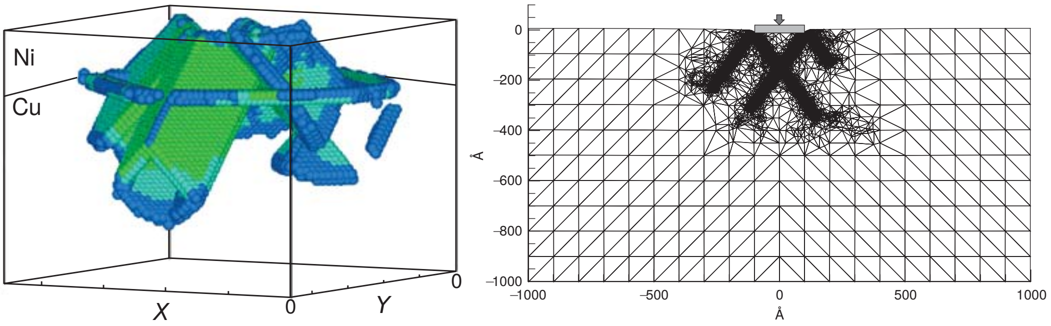

(a) Full atomistics

(b) Atomistics coupled with finite elements

Figure 1.1 – Demonstration of a concurrent multiscale strategy in problems with localized deformation; in this example a nanoindentation experiment. Figure (a) highlights the "interesting" atoms in a full atomistics simulation where plasticity has taken place through dislocation motion. Figure (b) shows a concurrent multiscale implementation where the "interacting" atoms are retained while the rest of the problem domain is coarse-grained with finite elements, assuming linear elasticity as constitutive law. Since the percentage of "interesting" atoms is quite small in the entire problem domain, the relevance of a multiscale coupling in such context is overly apparent. *(Adapted from Ref. [2])*

A number of concurrent multiscale methods has been proposed in the literature, a detailed review of which is beyond the scope and purpose of this thesis; interested readers are recommended the following review articles for a comprehensive understanding of the subject [2, 3, 8–10]. This section aims at introducing the broad classes of concurrent multiscale methods which will provide the readers with a concise overview of this vast field of research and will also help the readers in understanding the references to these methods in the later chapters of this thesis.

A common way to construct a concurrent multiscale problem is domain-decomposition followed by displacement coupling (Figure 1.2), where the problem domain is first decomposed in an atomistics sub-domain and a continuum sub-domain[1]. The continuum domain is generally solved using the method of finite elements (FE). At the interface of the two sub-domains, there is an overlap region called the "*pad*" where information is transferred across the two sub-domains via "*displacement coupling*" (Figure 1.2). In the pad region the atoms and nodes (of FE) are constrained to move together, thus enforcing a displacement coupling across the interface. Since the continuum constitutive deformation law is generally *local*, only a layer of interface nodes is tied to the respective interface atoms. On the contrary, the interatomic potentials dictating the deformation behaviour of the atomistics domain are *non-local* and therefore the pad atoms extend into the continuum domain covering the range of interatomic interactions and are tied to the respective nodes, the continuum degrees of freedom (DOFs). This one-to-one displacement coupling of atoms and nodes in the pad region is referred to as "*strong compatibility*" and requires fine-meshing the continuum in the pad region. To avoid this extra effort, some multiscale methods employ "*weak compatibility*" where the displacement boundary conditions in the pad region are enforced in some average sense or with some type of penalty method approach; however such methods are generally less accurate [8].

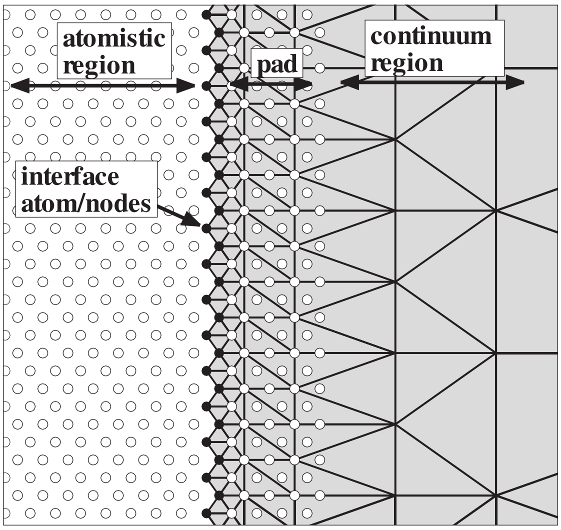

Figure 1.2 – The generic form of the atomistic-to-continuum transition region for concurrent multiscale methods with domain-decomposition. Filled atoms are the atoms right on the interface, which coincide with a set of FE nodes in the continuum. The 'pad' atoms serve only as a neighbour environment to the atoms in the atomistic and interface regions. For many of the methods, some or all of the 'pad' atoms are chosen to coincide with nodes in the mesh. *(Extracted from Ref. [3])*

---

[1] in future the "sub-" of "sub-domain" will be dropped for brevity when referring to atomistics or continuum sub-domains.

The energy of FE region is given by

$$\Phi_{FE} = \sum_{\mu}^{\text{elements}} w_\mu V_\mu W_\mu\Big(\mathbf{F}_\mu(\boldsymbol{p})\Big) - \sum_{i}^{\text{nodes}} \boldsymbol{f}_i \cdot \boldsymbol{p}_i \tag{1.1}$$

where w_μ are weights we will discuss shortly, V_μ is the volume of element μ and W_μ is the strain energy density function. It depends on the deformation gradient $\mathbf{F}_\mu$, which is turn depends on only the displacements of the nodes, $\boldsymbol{p} = \{\boldsymbol{p}_1, \boldsymbol{p}_2, \ldots, \boldsymbol{p}_n\}$, where w_i is the displacement vector of node i. The deformation gradient within element μ is fully determined by the displacements of the nodes defining the element, due to the local nature of the FE formulation. The second sum is the potential of the external forces, $\boldsymbol{f}_i$ applied to the nodes i.

In the atomistic domain, the atoms are presumed to interact via some interatomic potential that can be decomposed into an atom-by-atom contribution to the total potential energy. Only a few studies has attempted to couple atomistics modeled by first principles to FE where decomposition of total potential energy into atom-by-atom contribution is not possible [11, 12]; we will not discuss this case over here. Assuming the decomposition is possible, the energy of the atomistic domain is given by

$$\Phi_A = \sum_{i}^{\text{atoms}} \big(E_i(\boldsymbol{q}) - \boldsymbol{f}_i \cdot \boldsymbol{q}_i\big) \tag{1.2}$$

where $\boldsymbol{q}_i$ is the displacement of atom i and E_i is the potential energy contribution of atom i. The summation is over the atoms which are DOFs, which excludes the pad atoms; however the potential energy contributions E_i of atoms in the vicinity of the atomistic-continuum interface depends on the pad atom displacements.

Concurrent multiscale methods can be broadly classified based on (1) the general formulation of the multiscale problem, which categorizes the methods based on whether or not a well-defined total energy functional exists for the full problem domain and (2) the homogenization strategy, primarily concerning the way in which the energy density functional W_μ is defined.

Broadly, there are two ways to formulate a concurrent multiscale problem which constitutes the (1) the *energy-based methods* and (2) the *force-based methods*. The energy-based methods define a total energy functional, $\Phi_A + \Phi_{FE}$, for the full problem domain and minimize this energy functional in the case of statics problem or derive forces by differentiating the total energy functional with respect to the DOFs and use those forces to evolve the problem's DOFs in time in the case of dynamics problem. The force-based methods prescribe a force scheme for DOFs of the coupled problem that is physically motivated, and then either solve for configuration of atoms and nodes for which the forces are zero (in statics) or evolve the system in time complying to the prescribed scheme of forces (in dynamics). This can be done by obtaining the atomistic forces by differentiating the atomistic energy functional Φ_A with respect to the corresponding atomistic DOFs and by obtaining the nodal forces in the continuum by differentiating the continuum energy functional Φ_{FE} with respect to the corresponding nodal DOFs. In the energy-based methods, the weights w_μ in Equation 1.1 are one except for the elements near the coupling interface, where the weights are positive fractions since part of those elements' energy contribution is accounted for by the interface atoms. For force-based methods, w_μ is taken unity for all elements while calculating nodal forces by differentiating Φ_{FE}.

In the energy-based methods, Newton's third law is violated near the coupling interface if the numerical approximation to continuum deformation behaviour is local, which is often the case. This leads to unphysical deformation near the coupling interface, and the spurious forces responsible are referred to as "*ghost forces*". Ghost force corrections have been attempted by explicitly calculating the spurious forces after constructing the energy-based multiscale problem and deadloads are added to the affected DOFs to nullify the spurious forces [13]. This procedure corrects for the ghost forces explicitly in absence of any deformation; however the ghost forces change under loading, so the ghost force correction with fixed deadloads is associated with an indeterminate error under deformation of the problem domain. One can re-compute the ghost forces and correct for it with deadloads occasionally, however in that case there is no longer a well-defined energy functional for the problem and one has basically moved to the realm of 'force-based methods'. Some implementations have used non-local elasticity theory to model the continuum FE which automatically eliminates the ghost-forces [14]. Also different cluster-based non-local quasicontinuum methods have been developed which either reduces or eliminates the ghost forces [15, 16].

Unlike energy-based methods, the problem of ghost forces does not arise in force-based methods and Newton's third law is satisfied throughout the problem domain since the coupled multiscale problem is constructed as such with a prescribed force scheme. However, unlike energy-based methods there is no well-defined total energy functional in the force-based methods and the system is *non-conservative*. This can lead to unphysical 'equilibrium' solutions which correspond to saddle points or maxima (rather than minima) on some unknown energy surface and the lack of well-defined energy functional can be problematic in dynamic systems. However these methods can be reasonably robust if used carefully.

Different concurrent multiscale methods employs different homogenization strategies. The simplest homogenization technique using FE is to have local constant-strain elements, with linear elasticity as the constitutive law. In coupled atomistic/dislocation-dynamics (CADD) [17–19], assumption of linear elasticity in the continuum domain is instrumental for taking advantage of the principle of superposition for performing dislocation-dynamics. In the energy-based quasicontinuum (QC) method [13], the strain energy density functional W_μ in Equation 1.1 is modeled using the Cauchy-Born approximation — constant-strain elements are used and the energy density of any element μ with deformation gradient $\mathbf{F}_\mu(\boldsymbol{p})$ is given by the potential energy density of an infinite atomistics system deformed with $\mathbf{F}_\mu(\boldsymbol{p})$. Note that with the Cauchy-Born approximation the constitutive law is non-linear but the formulation is *still local.* There are cluster-based non-local quasicontinuum methods [15, 16], which approximates the energy or the forces at any node with clusters of carefully chosen sampling atoms. In these methods, a subset of all the atoms in a fully atomistic problem is chosen which are called *representative atoms* (or *rep-atoms*). Regions where the rep-atoms are chosen to full atomistic resolution are basically the atomistic sub-domains and the rest of the problem domain with sparse population of rep-atoms is for homogenization/coarse-graining — therefore the transition from fully resolved to coarse-grained is seamless for the cluster-based methods. Shape functions associated with the rep-atoms are used to interpolate the atomic displacements with the rep-atom displacements, the latter being the DOFs. Besides the rep-atoms, another subset of atoms is chosen called the *sampling atoms* which may or may not be the same as the set of rep-atoms. There are two approaches to cluster-based formulation. In the one proposed by Knap and Ortiz [15], atomistic forces on the sampling atoms are calculated, they are weighted by appropriate weighting factors, then the shape functions are used to interpolate these weighted atomistics forces of the sampling atoms into the respective rep-atom forces which are then used for statics or dynamics simulation. This approach falls under the “force-based” paradigm since it starts off with a prescription for the rep-atoms forces and therefore doesn’t suffer from spurious forces by construction but lacks a well-defined energy functional[16]. The other cluster-based approach [16, 20] calculates the weighted average of the energies of the sampling atoms using appropriate weights, differentiates it with respect to atomic displacements to get the forces on each atom in the system and then interpolate these forces with shape functions to obtain the respective rep-atom forces. This method has a well-defined energy functional but suffers from force artifacts if the sampling atoms are not carefully chosen [16]. The weight associated with any sampling atom in either method, is related to the number of “missing atoms” in the vicinity of the sampling atom which the latter has replaced, as a part of the coarse-graining protocol. Finally, besides affine interpolation used in the original QC method, a number of other interpolation schemes have been proposed which includes higher-order polynomial shape functions, smoothed-particle-based meshless interpolation schemes and the more recent local maximum-entropy interpolation schemes in a fully nonlocal energy-based formulation [21].

A critical requirement for a general multiscale model is the ability to adapt to an evolving deformation. The QC method and the cluster-based methods allow for adaptive model refinement, allowing the size and shape of the atomistically resolved subdomains to grow and shrink in response to the evolution of the “interesting” microstructural features (see Figure 1.1). In the CADD method, the continuum domain is enhanced by a discrete dislocation (DD) framework, allowing dislocations which nucleate in atomistics to move into the continuum, where they are modeled as computationally less expensive elastic defects which can then evolve under mutual elastic interactions, complying to some phenomenological mobility law [17–19].

As discussed so far, at zero temperature, there are a variety of well-established and reasonably accurate methods of coupling atomistics to a homogenized description. However the move to treating finite temperature leads to additional complications. Nevertheless, any errors or inefficiencies present in the static implementation of a coupled method will remain in the dynamic setting. Indeed some of the multiscale methods may be better suited than others to address the dynamic issues; which is why the implementation of these methods for dynamic problems has been more dependent on the application in mind. Two principle concerns presented by dynamic problem in context of concurrent multiscale implementation are the wave reflections and thermostats [2]. If the system is evolved using forces calculated by differentiating the total energy functional or the individual energy functionals of each domain, the short-wavelength phonons present in the atomistics domain will not be supported by the coarse-grained continuum, causing them to get reflected back at the coupling interface and get trapped in the atomistics. The wave reflection problem is made worse by our explicit goal in multiscale models: to make the atomistic domain as small as possible and to represent the continuum domain as coarsely as we can. Secondly, a thermostatted MD simulation implementated in a multiscale fashion to study near-equilibrium problems, must account for the entropy of the "missing atoms" in the coarse-grained region. Various approaches have been developed to modify the total potential energy functional by taking account of the entropic contribution of the "missing atoms" [22, 23]; these approaches show good agreement to direct MD simulations for studying the temperature-dependence of structural and elastic properties of single-crystal and defect nucleation.

This section reviewed the existing concurrent multiscale techniques. So far, none of the methods have been applied to random multicomponent alloys. Chapter 3 demonstates the problems faced in standard force-based coupling of random alloys using simple toy problem assuming linear elasticity as continuum constitutive law and using constant-strain FE mesh for the continuum domain. Solutions to these problems are proposed, studied and validated against both dilute and medium-entropy alloys. Concepts from this study can be borrowed and extended to other multiscale methods, which has been discussed in Chapter 8.

1.2 Solute-strengthening

Single-phase solid solutions can be broadly classified into substitutional and interstitial alloys. In substitutional alloys, solutes replace the principle element in some lattice sites, for instance, Al in Ni matrix for the γ-phase in Ni-based superalloys. MEAs and HEAs are also substutional alloys in which atoms, considered as solutes embedded in an average matrix, are arranged in a crystal structure. On the contrary, in interstitial alloys the solutes are not on lattice sites, but occupy interstitial voids, for instance, carbon in steels occupies the octahedral voids. In this thesis, we will only focus on solute-strengthening in substitutional alloys.

Theories of solute strengthening in substitutional alloys can be classified into two categories, strong-pinning and weak-pinning, each with its own characteristic scaling with concentration and temperature. The strong-pinning theory (Friedel[24], Fleischer[25, 26]) considers the solute atoms in the plane of the dislocation as independent point obstacles that pin the dislocation, which bows out in the regions between the solutes. On the other hand, the weak-pinning model (Mott [27] and Labusch [28, 29]) considers the interaction of the dislocation with a collective solutes environment surrounding the dislocation, and attributes strengthening to the occurence of favorable statistical fluctuations in the solute configuration, when each individual solute alone would not be strong enough to pin the dislocation at the same stress level.

Strengthening in alloys is controlled by strong-pinning at cryogenic low temperatures and low concentrations of solutes. The transition between the two strengthening mechanisms is a function of temperature, solute concentration and the dislocation core structure. Except for the most highly localized dislocation cores, the Labusch model has been found to control the strengthening in random alloys for concentrations greater than $\sim 10^{-4}$ and temperatures greater than 78K [30]. We would focus on Labusch-type models in the thesis, since at temperatures and concentrations relevant for engineering applications and for most dislocation core structures found in metal alloys, the Labusch model is expected to be the controlling strengthening mechanism.

A Labusch-type model envisions an intially straight dislocation in a random solute environment which is allowed to relax and undulate in the glide plane in order to minimize the potential energy. The undulation causes an increase in dislocation line length which is associated with an elastic energy cost, and so the typical configuration of the dislocation is that which minimizes the total energy as a function of the wavelength ζ and amplitude w of the dislocation roughening/undulation. Such characteristic length scales of dislocation roughening then characterizes the spacing between successive energy minima that the dislocation segments sample while gliding through the alloy (Figure 3b). The temperature and strain-rate dependent flow stress of the alloy is then dictated by the energy barrier that the segments have to overcome to go from one minima to the next.

In his original theory, Labusch developed the strengthening model by considering only the solutes in the glide plane to interact with the dislocation, although the concept is really three-dimensional in nature. If we think of the interaction as the dislocation pressure field times the solute misfit volume, then the solutes near the glide plane interacts weakly with an edge dislocation since the pressure field along the glide plane is zero for elastically isotropic solid. Whereas solutes few layers away from the glide plane in vicinity of the dislocation will interact stronger mechanically. Furthermore, the Labusch's theory assumes an arbitrary cut-off parameter for capturing the spatial range of interaction of solutes with the dislocation. A new parameter-free strengthening model has been developed by Leyson et. al [31, 32] based on the general physical picture of Labusch that predicts the finite-temperature flow stress. This new theory takes into account all the solutes in the system and does not assume any arbitrary interaction cut-off. The theory has been validated against simulations and experiments across many random alloy systems [4, 33]. The solute-strengthening models proposed in this thesis derive concepts from the Leyson's theory for random alloys and therefore this theory will be discussed in further detail in this section.

Leyson's theory of solute-strengthening first envisions a wavy dislocation in a random alloy having a wavelength 4ζ and amplitude w as shown in Figure 1.3.

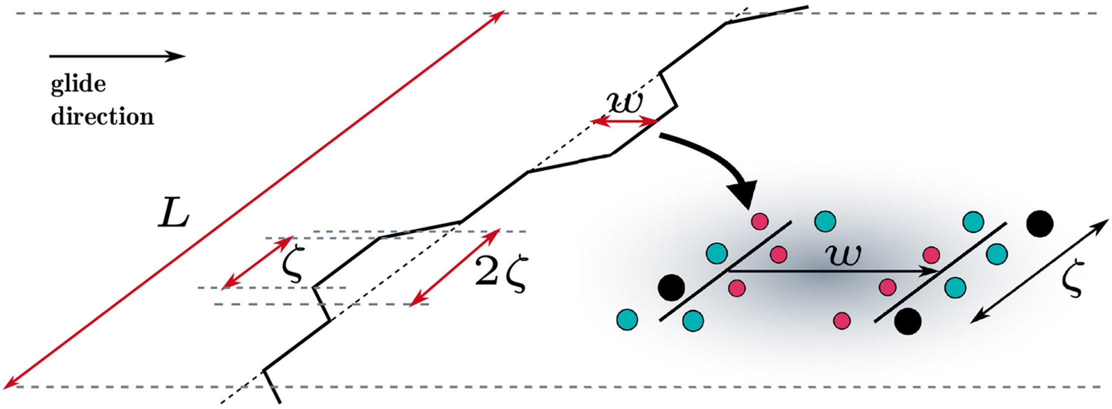

Figure 1.3 – Schematic of the low-energy wavy configuration of the dislocation as it moves through the random field of solutes in a random alloy *(Extracted from Ref. [4])*.

The potential energy change when a straight dislocation segment of length ζ glides a distance w is given by,

$$\Delta E_p(\zeta, w) = \sum_i \sum_n s_i^n \left(U_{sd}^n(x_i - w, y_i) - U_{sd}^n(x_i, y_i)\right)$$
$$\text{where,} \quad i \in \{\text{all lattice sites}\} \quad \text{and} \quad n \in \{\text{all atomtypes}\} \tag{1.3}$$

where s_i^n is the site occupation variable which takes value 1 if site i is occupied by atomtype n and 0 otherwise. $U_{sd}^n(x_i, y_i)$ is the interaction energy of a solute of type n at (x_i, y_i) with the straight dislocation line along z-axis passing through the origin.

In a random alloy, (1) the probability that site i is occupied by atomtype n is c_n, the concentration of type n in the alloy and (2) the occupancy of site i by atomtype n is independent of the occupancy of any other site j by an atomtype m, where m can be same as n. Thus in a random alloy, the average change in potential energy $\Delta E_p(\zeta, w)$ is

$$\begin{aligned}\langle \Delta E_p(\zeta, w)\rangle &= \sum_i \sum_n \langle s_i^n\rangle \left(U_{sd}^n(x_i - w, y_i) - U_{sd}^n(x_i, y_i)\right)\\ &= \sum_n c_n \left(\sum_i U_{sd}^n(x_i - w, y_i) - \sum_i U_{sd}^n(x_i, y_i)\right) = 0\end{aligned} \tag{1.4}$$

since the sum of interaction energies over all lattice sites remains unchanged when the interaction energy map is translated by w. The above result shows that no nett configurational force acts on the dislocation hindering its motion in a random alloy. Then how strengthening in the alloy can be achieved by the fluctuations in solute environment?

Dislocation segments get pinned locally in favourable solute environment while attaining a minimum energy wavy configuration, as idealized in Leyson's theory with wavelength 4ζ and amplitude w of roughening. Then it takes stress and/or thermal activation to unpin the dislocation segments and resume glide. The potential energy decrease when any dislocation segment of length ζ glides a distance w to get pinned at a favourable solute fluctuation is typically $-\sigma_{\Delta E_p}$, the standard deviation in $\Delta E_p(\zeta, w)$. However this glide is associated with a elastic energy cost due to increase in line length of the transition segments (refer Figure 1.3), which is $\Gamma w^2/2\zeta$ for $w \ll \zeta$, where Γ is the dislocation line tension. Therefore the total energy change for a dislocation of length L to undulate from a straight line to a wavy configuration of the fashion depicted in Figure 1.3 is given by,

$$\Delta E_{\text{tot}}(\zeta, w) = \left(\Gamma \frac{w^2}{2\zeta} - \sigma_{\Delta E_p}(\zeta, w)\right)\left(\frac{L}{2\zeta}\right) \tag{1.5}$$

We can extract out from $\sigma_{\Delta E_{\text{p}}}$ the explicit dependence on dislocation segment length ζ by writing $\sigma_{\Delta E_p} = (\zeta \rho_L)^{\frac{1}{2}} \Delta\widetilde{E}_{\text{p}}(w)$ where ρ_L is the density of lattice sites along the dislocation line direction. ρ_L equals $1/(\sqrt{3}b)$ for fcc alloys and $1/(2\sqrt{2}b)$ for bcc alloys. The quantity $\Delta\widetilde{E}_{\text{p}}(w)$ is the standard deviation of the energy change, per periodic length along the dislocation line, when the dislocation glides a distance w. Using the facts that (1) in random alloys the occupancy of site i by atomtype n is independent of the occupancy of any other site j by an atomtype m, where m can be same as n and (2) the sum rule $\sum_n c_n U^n_{sd} = 0$ holds for all sites, one can derive the following form of $\Delta\widetilde{E}_{\text{p}}(w)$,

$$\Delta\widetilde{E}_{\text{p}}(w) = \left(\sum_n c_n \sum_i \left(U^n_{sd}(x_i - w, y_i) - U^n_{sd}(x_i, y_i)\right)^2\right)^{\frac{1}{2}} \tag{1.6}$$

A characteristic wavelength and amplitude (ζ_c, w_c) emerge by minimizing the total energy ΔE_{tot} of the long dislocation with respect to both ζ and w. The length ζ_c is obtained directly as

$$\zeta_c = \left(\frac{4\Gamma^2 w^4}{\rho_L \Delta\widetilde{E}^2_{\text{p}}(w)}\right)^{\frac{1}{3}} \tag{1.7}$$

The amplitude w_c then follows from a second minimization $\frac{\partial \Delta E_{\text{tot}}(\zeta_c(w), w)}{\partial w} = 0$ that reduces to the solution of

$$\frac{\partial \Delta\widetilde{E}_{\text{p}}(w)}{\partial w} = \frac{\Delta\widetilde{E}_{\text{p}}(w)}{2w} \tag{1.8}$$

For split dislocation cores with large partial separation, the above minimization gives two solutions for w_c. One solution has a high zero-T strength and low zero-stress barrier, and controls the strength at lower temperatures. The second solution has a lower strength and higher barrier and controls the strength at higher temperature.

The total reduction in energy per length ζ_c, $\Delta E_c = \Delta E_{\text{tot}}(\zeta_c, w_c)\frac{2\zeta_c}{L}$, then sets an energy scale for pinning of the dislocation. However ΔE_c is not the energy barrier for determining thermally activated motion of the dislocation since it is the typical energy change on moving from one *arbitrary* point to another point w_c glide distance away. On the contrary, the energy barrier is the local maximum in energy which a dislocation pinned in a local minima (typically $-\sigma_{\Delta E_{\text{p}}}$)

has to overcome to reach the next local minimum in a fluctuating energy landscape (Figure 3b). The length scale w_c along the glide plane sets the glide distance between local favorable and unfavorable solute environments. The local potential energy landscape is modeled as a sinusoidal function: with minimum located at $x = 0$ along the glide direction, the energy of the segment of length ζ_c at position x is $E(x) = \Delta E_b'/2\,(1 - \cos(\pi x/w_c))$ with $\Delta E_b' = \sqrt{2}\sigma_{\Delta E_\mathrm{p}}$. The potential energy barrier $\Delta E_b'$ is larger than $\sigma_{\Delta E_\mathrm{p}}$ by $\sqrt{2}$, because the average barrier is the potential energy difference between the average minimum and the average maximum, not the average minimum and the zero energy level. The total energy barrier ΔE_b corresponds to the potential energy cost of moving from a favorable to an unfavorable potential energy fluctuation over a glide distance w_c, minus the gain in the elastic line energy $\Gamma w_c^2/2\zeta_c$, given by

$$\begin{aligned}\Delta E_b &= \Delta E_b' - \Gamma\frac{w_c^2}{2\zeta_c}\\ &= 1.467\left(\rho_L w_c^2 \Gamma \Delta\widetilde{E}_\mathrm{p}^2(w_c)\right)^{\frac{1}{3}}\end{aligned} \tag{1.9}$$

Having determined that the dislocation segments of length ζ_c pinned in typical energy minima with barriers of height ΔE_b over a glide distance w_c away, we can now use standard analyses of thermally activated dislocation motion to determine the finite-T and strain-rate dependent yield stress, as follows. When the material is subjected to an applied resolved shear stress τ, the energy landscape $E(\tau, x)$ must be modified to include the work done by the applied stress, and so becomes

$$E(\tau, x) = \frac{\Delta E_b}{2}\left(1 - \cos\left(\pi x/w_c\right)\right) - \tau\zeta_c b x \tag{1.10}$$

An applied resolved shear stress $\tau = \tau_{y0}$ needed to glide the dislocation at T=0K would be such that the modified energy landscape $E(\tau_{y0}, x)$ will no longer have a minimum or a maximum in $[0, w_c]$ but will have an inflection point at $x = \hat{x}$. To determine the T=0K yield stress, we take the first and second derivatives of $E(\tau, x)$, set both of them to zero and solve the two resulting equations for $(\tau_{y0}, \hat{x})$ as follows,

$$\begin{aligned}\left.\frac{\partial E(x,\tau)}{\partial x}\right|_{(\hat{x},\tau_{y0})} &= \frac{\pi}{2}\frac{\Delta E_b}{w_c}\sin\left(\frac{\pi\hat{x}}{w_c}\right) - \tau_{y0} b\zeta_c = 0 \implies \tau_{y0} = \frac{\pi}{2}\frac{\Delta E_b}{b\zeta_c w_c}\sin\left(\frac{\pi\hat{x}}{w_c}\right)\\ \left.\frac{\partial^2 E(x,\tau)}{\partial x^2}\right|_{(\hat{x},\tau_{y0})} &= \frac{\pi^2}{2}\frac{\Delta E_b}{w_c^2}\cos\left(\frac{\pi\hat{x}}{w_c}\right) = 0 \implies \cos\left(\frac{\pi\hat{x}}{w_c}\right) = 0 \quad \text{(Inflection at } x = \hat{x} = w_c/2)\\ \therefore \tau_{y0} &= \frac{\pi}{2}\frac{\Delta E_b}{b\zeta_c w_c}\end{aligned} \tag{1.11}$$

The T=0K yield stress τ_{y0} can be simplified using Equations 1.7 and 1.9 as follows,

$$\tau_{y0} = 1.45\left(\frac{\rho_L^2 \Delta\widetilde{E}_\mathrm{p}^4(w_c)}{\Gamma b^3 w_c^5}\right)^{\frac{1}{3}} \tag{1.12}$$

The stress-dependent energy barrier height $\Delta E(\tau)$ can be approximated (within 6%) by [34]

$$\Delta E(\tau) \approx \Delta E_b \left(1 - \left(\frac{\tau}{\tau_{y0}}\right)\right)^{\frac{3}{2}} \tag{1.13}$$

In combination with an Arrhenius law for the thermal activation, Equation 1.13 leads to a temperature T and strain-rate $\dot{\varepsilon}$ dependent flow stress given by

$$\tau_y(T, \dot{\varepsilon}) = \tau_{y0}\left(1 - \left(\frac{k_\mathrm{B} T}{\Delta E_b}\ln\left(\frac{\dot{\varepsilon}_0}{\dot{\varepsilon}}\right)\right)^{\frac{2}{3}}\right) \tag{1.14}$$

where $\dot{\varepsilon}_0 \sim 10^4 s^{-1}$ and k_B are a reference strain rate and Boltzmann's constant, respectively. With increasing temperature and at stresses below $\approx 0.5\tau_{y0}$, waviness on multiple scales becomes important [35, 36], but these details are not important for the thesis.

With Equations 1.9, 1.12 and 1.13, Leyson's theory of solute strengthening predicts the zero-stress energy barrier, T=0K yield stress and the temperature/strain-rate dependent flow stress respectively, for random alloys.

The key input to the theory are the solute-dislocation interaction energies for solutes occupying different lattice sites, which enters the theory as the normalized energy fluctuation quantity $\Delta\widetilde{E}_\mathrm{p}(w)$. The solute-dislocation interaction energies can be determined by atomistics using semi-empirical potentials or first-principle methods such as DFT. A less computationally expensive way of calculating these interaction energies is by assuming linear elasticity, which then reduces the interaction energy at any site to the product of the pressure at that site due to dislocation and the solute misfit volume, i.e. $U(x_i, y_i) = p(x_i, y_i)\Delta V_n$. In the seminal works by Leyson et. al [31, 32], Leyson computed solute-dislocation interaction energies by first principles at lattice sites adjacent to the split dislocation core in fcc Al for six solutes. Interaction energies for all other sites were calculated using the linear elasticity assumption. A smooth transition between the DFT-computed interaction energies and the ones computed using the pressure field of uniformly spread dislocation core under linear elasticity assumption, was reported. Inspired by this result, Varvenne et. al [4] developed a reduced model for elastically isotropic solid where linear elasticity is used to compute interaction energies. In the reduced model, the key energy fluctuation quantity $\Delta\widetilde{E}_\mathrm{p}(w)$ take the following form,

$$\Delta\widetilde{E}_\mathrm{p}(w) = g\left(w, \frac{db}{dx}\right)\mu\frac{1+\nu}{1-\nu}\sqrt{\sum_n c_n \Delta V_n^2} \tag{1.15}$$

where $g(w, {}^{db}/_{dx})$ is a structure factor which depends on the dislocation roughening amplitude w and the Burger vector distribution db/dx, which in turn is characterized by a double-Gaussian centered around each Shockley partial in fcc as schematically depicted in Figure 1.4. μ and ν are the shear modulus and Poisson's ratio respectively and ΔV_n is the misfit volume of solute n. Ref. [4] reported that w_c and g for this reduced model does not depend critically on partial core separation for $d_p > 10b$. The yield stress τ_{y0} is sensitive to partial core spreading σ. However, a good agreement was reported [4] between the values of τ_{y0} computed by using the reduced elasticity model with $\sigma = 1.5b$ and those obtained with DFT-computed interaction energies. Therefore it is recommended to use $\sigma = 1.5b$ with the reduced elasticity model.

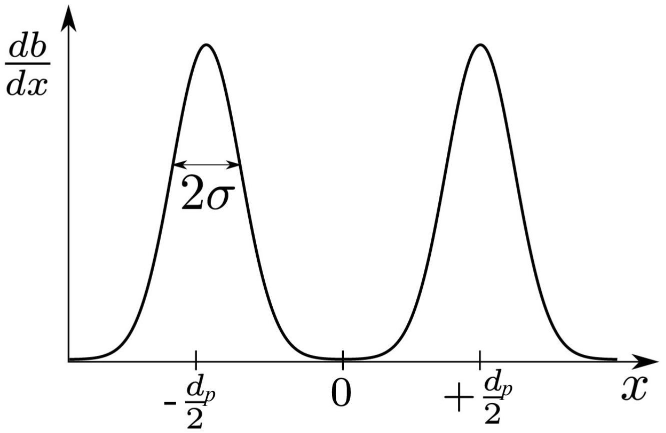

Figure 1.4 – Burger vector distribution in fcc with split dislocation cores. d_p is the distance between the two Shockley partials and σ is the partial core spreading *(Adapted from Ref. [4])*.

The reduced model under elasticity assumption has the advantage that it relies on fundamental material and solute properties: elastic constants C_{ij}, dislocation Burgers vector $\boldsymbol{b}$, stable and unstable stacking fault energies γ_{ssf} and γ_{usf}, dislocation line tension Γ,and the solute misfit strain tensor $\varepsilon_{ij}^{\text{misfit}}$ in the alloy. First-principles methods can compute all of these quantities, even in the highly-complex HEAs [37]. On the other-hand, mechanical tests are often carried out on polycrystals, and supplemented by TEM analyses, to obtain experimental values of properties like the average isotropic elastic constants, Burgers vector (and lattice constant a), and stacking fault width of the dissociated partials that arise in fcc crystals, from which γ_{ssf} can be deduced. The solute misfit volumes $\Delta V = \varepsilon_{ii}^{\text{misfit}} a^3/4$ for fcc alloys can be determined in principle from lattice constant measurements on alloys of varying composition. Thus, if the elasticity approximation is accurate then the theory can be used to rationalize existing experimental measurements and to predict properties of new alloys via the use of first-principles computations on candidate alloys [37, 38]. In Chapter 4 we are going to revisit the reduced model and examine the role of anisotropic elasticity in solute-strengthening of random alloys .

Till now, we have discussed solute-strengthening in alloys, where different alloy constituents are distributed randomly on lattice sites. However there are evidences of local chemical ordering in alloys, due to underlying solute-solute interactions in the alloy [39–42]. It has been claimed that short-range order (SRO) has notable effect on the stacking fault energy and tensile yield strength of alloys [41, 43]. In analogy to the formation of antiphase boundary in ordered stoichiometric phases on passage of dislocation, it has been demostrated by Fisher [44] that high energy planar fault also forms in partially ordered alloys due to destruction of local order, thus giving rise to strengthening. Attempts have been made to estimate this average strengthening effect based on nearest-neighbour (NN) bond energy model [44] and also to relate it to Warren-Cowley SRO parameters for first NN interactions [45] and second NN interactions [46]. According to [45] strengthening due to SRO goes to zero in case of random alloys. However, Leyson's model shows that strengthening due to fluctuating solute environment exists for random alloys due to solute fluctuations over characteristic length scale ζ_c of the dislocation. Recently, Ref. [47] proposed an extension of the Leyson-Varvenne solute-strengthening model to include the effects of SRO, however in their model the statistics of solute-solute interactions across the glide plane has not been correctly accounted for. In Chapter 6, we are going to propose a new solute-strengthening model to predict yield strength of alloys with short-range order. The new theory reverts to the strengthening model for random alloys in absence of short-range order.

2 Methods

This chapter introduces the reader to the methods used in this thesis. Section 2.1 discusses molecular statics calculations with semi-empirical potentials which is used primarily in Chapter 3 for atomistic-to-continuum coupling and in Chapters 4 and 5 for calculating solute misfit volume and interaction energy of a solute pair in an alloy. The semi-empirical potentials used in this thesis are of Embedded-atom (EAM) type, the latter is also discussed in this section. The section also discusses an average-atom approximation which is relevant for calculating solute misfit volume and solute pair interaction energies in a random alloy and has also been used in Chapter 3 for atomistic-continuum coupling of random alloys. Section 2.2 gives a general introduction to Finite Element method (FEM) for solving the equilibrium equation in solid mechanics with Dirichlet and Neumann boundary conditions. Finite elements methods is used in Chapter 3 for atomistic-continuum coupling where the continuum domain is approximated with FEM. Then force-based atomistic-continuum coupling is discussed in Section 2.3. Molecular statics calculation of solute misfit volume is discussed in Section 2.4. Section 2.5 discusses the mechanical interaction of two defects in an infinite linear elastic medium and then discusses the specific cases of solute-dislocation and solute-solute interactions in both elastic isotropic and anisotropic media. The mechanical interaction of a solute with a dislocation depends on the pressure field of the dislocation at the location of the solute. The pressure field of a dislocation in an anisotropic medium does not have a closed form solution for a general dislocation line orientation with respect to the Burgers vector, so Section 2.6 discusses the sextic and Stroh formalism of calculating the pressure field in anisotropic solids. Since the mechanical interaction of a solute pair is negligible, if at all present, the more relevant chemical interaction energy of two solutes needs to be computed using molecular statics, which is discussed in Section 2.7. Finally, Section 2.8 introduces some basic concepts in probability theory which are used quite often in Chapters 5 and 6.

2.1 Atomistic calculations with Classical Potentials

2.1.1 Energy minimization

In molecular statics, an atomistic system is first constructed where atoms are arranged in a simulation cell in an initial configuration of atomic positions and then one solves for the configuration that corresponds to a local minimum in the potential energy landscape of the atomistic system. The optimization problem is equivalent to finding the configuration where the force on every atom is zero. Energy minimization is also referred to as *relaxation* of the atomistic system. In this thesis, we are interested in metallic systems, where the total potential energy of the atomistic system is described by semi-empirical many-body potentials of “Embedded atom method” (EAM) type (discussed in the following section). The EAM potentials are nonlinear and the energy landscape will be complicated with numerous local minima. Therefore the solution of energy minimization depends on the initial configuration of the atomic positions. There are several algorithms for energy minimization, out of which the *conjugate gradient method* and the *Fast inertial relaxation engine (FIRE)* implemented in the open-source molecular dynamics simulator LAMMPS[48, 49] are used in this thesis.

Boundary condition imposed on the simulation cell plays an important role in relaxation. For example, when periodic boundary condition is imposed on any pair of opposite sides of the simulation cell, one can adjust the simulation cell size in that direction to nullify normal pressure in that direction. This is done with the help of the *box/relax* fix implemented in LAMMPS. If periodic boundary condition is imposed in all directions then one can also change the box shape and volume with the help of this fix to nullify all stress components. This fix is useful for the calculation of lattice constant and solute misfit volume which is discussed in Section 2.4.

2.1.2 Embedded atom method

The Embedded atom method (EAM) was developed by Daw and Baskes[50, 51] to create a semi-empirical many-body interatomic potential for metallic systems for studying hydrogen embrittlement in metals and various defects in transition metals. The EAM potential is more accurate than the pair potentials used earlier.

In this method, each atom in the system is viewed as an impurity in a host consisting of all other atoms and the embedding energy of an impurity is determined by the electron density of the host before the impurity is added. It is also assumed that the impurity experiences a locally uniform electron density due to atoms in its surroundings and to a first-order approximation it is taken as the sum of electron density contributed by each of those neighbouring atoms. Thus the local electron density of the host at site i is given by,

$$\overline{\rho}_i = \sum_{j\neq i} \sum_{y} s_j^y \rho_y \left(\|\boldsymbol{r}_{ij}\|\right) \tag{2.1}$$

where the summation is over neighbouring sites j and s_j^y is the occupation variable which is 1 if site j has atomtype y or 0 otherwise. ρ_y is the electron density of atomtype y and $\boldsymbol{r}_{ij}$ is the vector joining sites i and j and $\|\cdot\|$ is the Euclidean norm.

The core-core repulsion is assumed to take the form of a short-range pairwise repulsion between the ion cores which is given by $V_{xy}\left(\|\boldsymbol{r}_{ij}\|\right)$, which is repulsion between atomtypes x and y at sites i and j respectively.

The total energy of the system under the EAM approximation is given by,

$$E_{\text{tot}} = \sum_i \sum_x s_i^x F_x(\overline{\rho}_i) + \frac{1}{2} \sum_{\substack{i,j \\ i \neq j}} \sum_{x,y} s_i^x s_j^y V_{xy}\left(\|\boldsymbol{r}_{ij}\|\right) \tag{2.2}$$

where F_x is the embedding energy of atomtype x which depends on the host electron density at site i.

A related semiempirical potential was proposed by Finnis and Sinclair for transition metals[52], where the local electron density of the host at site i also depends on the atom type occupying site i as follows,

$$\overline{\rho}_i^x = \sum_{j \neq i} \sum_y s_j^y \rho_{xy}\left(\|\boldsymbol{r}_{ij}\|\right) \quad \text{when} \quad s_i^x = 1 \tag{2.3}$$

The embedding energy functional of local electron density $F_x(\overline{\rho}_i)$ is non-linear function which makes these semi-empirical potentials of many-body type. Finnis and Sinclair assumed it to be square-root of the electron density which is indeed a novelty. The square root captures the dependence of atomic interactions on the local density: as the number of neighbors of an atom decreases, the strength of the remaining bonds increases. This immediately predicts an inward relaxation at metallic free surfaces with a tensile surface stress, both of which are widely observed but not predicted by models in which the cohesive energy is just a sum of pair potentials[53]. The assumption of square root for embedding function is inspired by tight-binding theory of metallic cohesion and most semiempirical potential of EAM or Finnis-Sinclair type has square root in their embedding function.

Since the pair potential V and the electron density ρ are radially symmetric, the EAM represents a reasonable approximation for materials without preferred bond angles, such as the FCC metals.

2.1.3 Average-atom approximation for random alloys

Random alloys are multicomponent crystalline solids where the occupancy of any lattice site by an atom type is independent of the atomtypes in the other lattice sites. The average-atom theory is a mean field approximation for random alloys, where a fictituous single-component potential called “average atom” is developed from the multicomponent potential for the random alloy, which approximates the average total potential energy of the random alloy. Therefore this approximation can be used to predict average bulk properties of a random alloy, like lattice constants and elastic constants, while avoiding computationally expensive calculations for these average properties using explicit random alloys with actual atomtypes — the latter needs large simulation cell size for convergence of the bulk properties to an average. This approximation gives good predictions for average defect properties, like surface energy, stable stacking fault energy, misfit volume of a solute in random alloy and solute-solute interaction energy [54]. In this thesis, this approximation is used for atomistic-continuum coupling of random alloys in Chapter 3.

For a random alloy described by EAM potential, the total potential energy of the alloy for any particular arrangement of atomtypes on lattice sites is given by Equation 2.2 in the previous section. The average total potential energy of a random alloy is given by,

$$\langle E_{\mathrm{tot}}(\{s_i^x\})\rangle = \sum_i \sum_x \langle s_i^x F_x(\overline{\rho}_i)\rangle + \frac{1}{2}\sum_{\substack{i,j\\ i\neq j}} \sum_{x,y} \langle s_i^x s_j^y\rangle V_{xy}\left(\|\boldsymbol{r}_{ij}\|\right) \tag{2.4}$$

where $\langle\cdot\rangle$ is the expectation operator.

In a random alloy, the probability of any site i to be occupied by atomtype x is given by c_x which is the concentration of atomtype x in the alloy. Therefore the expectation $s_i^x = c_x$ for all site i and atomtype x. Since the occupancies of different lattice sites by atomtypes are independent, the expectation of the product of occupation variables $\langle s_i^x s_j^y\rangle$ can be decoupled as $\langle s_i^x\rangle\langle s_j^y\rangle$ for all $i \neq j$. Using the above expectation expressions, Equation 2.4 can be simplified as follows,

$$\begin{aligned}\langle E_{\mathrm{tot}}\rangle &= \sum_i \sum_x \langle s_i^x\rangle\langle F_x(\overline{\rho}_i)\rangle + \frac{1}{2}\sum_{\substack{i,j\\ i\neq j}} \sum_{x,y} \langle s_i^x\rangle\langle s_j^y\rangle V_{xy}\left(\|\boldsymbol{r}_{ij}\|\right)\\ &\quad \left(\text{Since the electron density } \overline{\rho}_i \text{ does not have } s_i^x\right)\\ &= \sum_i \sum_x c_x\langle F_x(\overline{\rho}_i)\rangle + \frac{1}{2}\sum_{\substack{i,j\\ i\neq j}} \sum_{x,y} c_x c_y V_{xy}\left(\|\boldsymbol{r}_{ij}\|\right)\end{aligned} \tag{2.5}$$

With the expectation $\langle F_x(\overline{\rho}_i)\rangle$ is approximated as $F_x(\langle\overline{\rho}_i\rangle)$ and the average electron density at site i is given by,

$$\begin{aligned}\langle\overline{\rho}_i\rangle &= \sum_{j\neq i}\sum_y \langle s_j^y\rangle \rho_y\left(\|\boldsymbol{r}_{ij}\|\right) \quad \text{(refer Equation 2.1)}\\ &= \sum_{j\neq i}\sum_y c_y \rho_y\left(\|\boldsymbol{r}_{ij}\|\right)\end{aligned} \tag{2.6}$$

the *average atom* (or A-atom) potential of EAM type is defined as

$$F_A \overset{\text{def}}{=} \sum_x c_x F_x, \quad \rho_A \overset{\text{def}}{=} \sum_y c_y \rho_y \quad \text{and} \quad V_{AA} \overset{\text{def}}{=} \sum_{x,y} c_x c_y V_{xy} \tag{2.7}$$

$$\text{which gives} \quad E_A \overset{\text{def}}{=} \langle E_{\text{tot}} \rangle = \sum_i F_A \left(\sum_{j \neq i} \rho_A \left(\| \boldsymbol{r}_{ij} \| \right) \right) + \frac{1}{2} \sum_{\substack{i,j \\ i \neq j}} V_{AA} \left(\| \boldsymbol{r}_{ij} \| \right)$$

For calculation of defect properties like misfit volume and solute pair interaction energy, it is necessary for the average atom to interact with the real atomtypes. In that case, we define the pair interaction between a real atomtype x and the A-atom as

$$V_{xA} \overset{\text{def}}{=} \sum_y c_y V_{xy} \quad \text{and therefore,} \quad V_{AA} \overset{\text{def}}{=} \sum_x c_x V_{xA} \tag{2.8}$$

The average atom approximation was first proposed by Smith et. al [55] and then validated against true random alloys by Varvenne et.al [54].

2.2 Static equilibrium in solid mechanics and Finite Elements Method

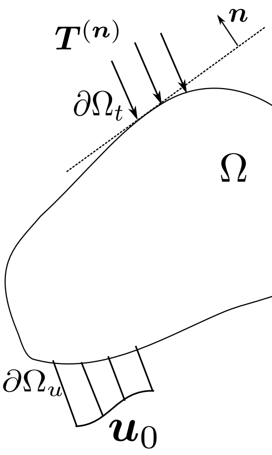

Figure 2.1 – A continuum domain Ω with Dirichlet boundary condition over $\partial\Omega_u$ with specified displacement $\boldsymbol{u}_0$ and Neumann boundary condition over $\partial\Omega_t$ with traction $\boldsymbol{T}^{(\boldsymbol{n})}$.

Let us consider a solid defined by domain Ω and subjected to Dirichlet and Neumann boundary conditions as illustrated in Figure 2.1. In absence of any body force and inertial force over the domain Ω, the solid is said to be under mechanical equilibrium if the following condition is satisfied at every point of the Ω,

$$\sigma_{ij,j} = 0 \qquad \forall i = 1,2,3 \tag{2.9}$$

where σ_{ij} are the components of stress tensor and $,j$ is the partial derivative w.r.t to spatial coordinate x_j. Here, Einstein summation rules for repeated indices applies. The above equation is called the *"equilibrium equation"* and it is a differential form of writing force balance. Static equilibrium is further ensured by Dirichlet (or displacement) boundary condition, which specifies the displacement at the boundary.

Components of stress tensor are functions of the displacement field $\boldsymbol{u}(\boldsymbol{x})$, where $\boldsymbol{x} \in \Omega$. A symmetric strain tensor can be defined in terms of displacement field as follows,

$$\varepsilon_{kl} \overset{\text{def}}{=} \frac{1}{2}(u_{k,l} + u_{l,k}) \tag{2.10}$$

The generalized Hooke's law then relates the components of stress to the components of strain ε_{kl} linearly as follows,

$$\sigma_{ij} = C_{ijkl}\,\varepsilon_{kl} \tag{2.11}$$

where C_{ijkl} are *elastic constants* which form a fourth-rank tensor called the *"elastic modulus tensor"*.

Due to different symmetry considerations, the elastic modulus tensor has the following symmetry properties,

$$C_{ijkl} = C_{jikl} \quad \text{and} \quad C_{ijkl} = C_{ijlk} \quad \text{and} \quad C_{ijkl} = C_{klij} \tag{2.12}$$

which reduces the maximum number of independent elastic constants in the tensor to 21.

Using Equations 2.10 and 2.11 and the symmetry property $C_{ijkl} = C_{ijlk}$, one can rewrite the generalized Hooke's law in terms of displacements as follows,

$$\sigma_{ij} = C_{ijkl}\,u_{k,l} \tag{2.13}$$

The equilibrium equation in Equation 2.9 can be rewritten as,

$$C_{ijkl}\,u_{k,lj} = 0 \quad \forall i = 1,2,3 \tag{2.14}$$

The above second order differential equation can be written in **weak form** which can be then solved numerically for displacements using Finite Element Method (FEM), discussed below.

We first augment Equation 2.14 with test functions $v_i(\boldsymbol{x})$ and then take integral as follows,

$$\int_\Omega C_{ijkl}\,u_{k,lj}\,v_i\,d^3\boldsymbol{x} = 0 \tag{2.15}$$

Using *integration by parts*, the above equation reduces to the weak form,

$$-\int_{\Omega} C_{ijkl}\, u_{k,l}\, v_{i,j}\, d^3\boldsymbol{x} + \int_{\Omega} C_{ijkl}\, (u_{k,l}\, v_i)_{,j}\, d^3\boldsymbol{x} = 0$$

Applying divergence theorem to the second term,

$$\textbf{Weak form} \quad -\int_{\Omega} C_{ijkl}\, u_{k,l}\, v_{i,j}\, d^3\boldsymbol{x} + \oint_{\partial\Omega} C_{ijkl}\, u_{k,l}\, v_i\, n_j\, dS = 0 \tag{2.16}$$

where $\partial\Omega$ is the boundary surface of the domain Ω and n_j is the j^{th} component of the normal to the surface ΔS on the boundary.

The test functions $v_i(\boldsymbol{x})$ are chosen such that they are zero at $\partial\Omega_u$ (See Figure 2.1). So the weak form turns out to be,

$$\textbf{Weak form} \quad -\int_{\Omega} C_{ijkl}\, u_{k,l}\, v_{i,j}\, d^3\boldsymbol{x} + \oint_{\partial\Omega_t} C_{ijkl}\, u_{k,l}\, v_i\, n_j\, dS = 0 \tag{2.17}$$

Applying symmetry property $C_{ijkl} = C_{jikl}$ to the first term in Equation 2.17, the weak form can be expressed in terms of stress and strain and surface traction $T_i^{(\boldsymbol{n})}$ as follows,

$$-\int_{\Omega} \sigma_{ij}(\boldsymbol{u})\, \varepsilon_{ij}(\boldsymbol{v})\, d^3\boldsymbol{x} + \oint_{\partial\Omega_t} T_i^{(\boldsymbol{n})}(\boldsymbol{u})\, v_i\, dS = 0 \tag{2.18}$$

$$\text{where,} \quad T_i^{(\boldsymbol{n})}(\boldsymbol{u}) = \sigma_{ij}(\boldsymbol{u}) n_j$$

The above equation of weak form is consistent with the *Theorem of Minimum potential energy*, if in the sense of variations, the test functions v_i are considered arbitrary small variations in displacements δu_i known as *virtual displacements*.

For solving the weak form with FEM [56], we first mesh (or discretize) the domain Ω in non-intersecting elements. The vertices of elements are called nodes. If there are n nodes we choose n trial functions $\phi^1, \phi^2, \cdots, \phi^n$, one for each node, such that $\phi^k = 1$ at node k and zero at all other nodes (*local* trial functions). We then express the displacement u_i at any point in Ω as a linear combination of the trial functions, as $\sum_{p=1}^{n} U_i^p \phi^p$, where U_i^p are the coefficients which we will be solving using the weak form. We also need to choose n test functions, which we choose to be the same as the trial functions ϕ^p's in the Galerkin method. Following the discretization with trial functions, the weak form in Equation 2.17 turns into a system of $3n$ equations with $3n$ unknowns U_i^p in three-dimensions,

$$-\sum_{p=1}^{n}\sum_{k=1}^{3} U_k^p \underbrace{\int_{\Omega} C_{ijkl}\, \phi^p_{,l}\, \phi^q_{,j}\, d^3\boldsymbol{x}}_{K_{ki}^{pq}} + \underbrace{\oint_{\partial\Omega_t} T_i^{(\boldsymbol{n})}(\boldsymbol{u})\, \phi^q\, dS}_{F_i^q} = 0 \qquad \begin{matrix} q{=}1,2,\cdots,n \\ i{=}1,2,3 \end{matrix} \tag{2.19}$$

Let **U** be a $3n$ size vector with components U_k^p and **K** be a $3n \times 3n$ matrix with elements K_{ki}^{pq}

and **F** be a $3n$ size vector with force components F_i^q. Note that the traction $T_i^{(\boldsymbol{n})}(\boldsymbol{u})$ over the domain boundary $\partial\Omega_t$ is a input to the FEM. In matrix form the discretized form of the weak form can then be written as,

$$K_{ki}^{pq} u_k^p = F_i^q \quad \Longleftrightarrow \quad \mathbf{KU} = \mathbf{F} \tag{2.20}$$

where **K** is known as the *stiffness matrix.* Using symmetry propery $C_{ijkl} = C_{klij}$, one can show that matrix **K** is symmetric; this is also an outcome of using the same trial functions as test functions. Note that Equation 2.20 resembles the equilibrium condition for a system of n nodes in three dimensions, connected by linear springs.

In Chapter 3 constant-strain tetrahedral elements are used to mesh the continuum domain [57]. The matrix **K** will be highly sparse — for any node p the *only* nonzero K^{pq} entries are for nodes q which share a common element will node p. In this thesis, the open-source library DOLFIN [58, 59] has been used to compute the stiffness matrix, and open-source parallel sparse direct solver MUMPS [60, 61] is used to solve the system of linear equations (2.20).

Since the trial functions are *local,* all interior nodes which are not on the domain boundary $\partial\Omega$ will have zero entries in **F**. The entries in the **F** vector for boundary nodes in $\partial\Omega_t$ can be computed with the surface integral in Equation 2.19.

To deal with the Dirichlet boundary condition, the matrix equation (2.20) is representated as follows with partitioned matrices and vectors,

$$\begin{bmatrix} \mathbf{K}' & \mathbf{K}_0 \\ \mathbf{K}_0 & \mathbf{K}'' \end{bmatrix} \begin{bmatrix} \mathbf{U}' \\ \mathbf{U}_0 \end{bmatrix} = \begin{bmatrix} \mathbf{F}' \\ \mathbf{F}_0 \end{bmatrix} \tag{2.21}$$

where $\mathbf{U}_0$ are the prescribed displacements at the nodes on the boundary $\partial\Omega_u$ with Dirichlet boundary condition. We solve for $\mathbf{U}'$ by solving the following system of linear equations,

$$\mathbf{K}'\mathbf{U}' = \mathbf{F}' - \mathbf{K}_0\mathbf{U}_0 \tag{2.22}$$

$\mathbf{F}_0$, corresponding to boundary nodes in $\partial\Omega_u$, can then be computed with the solution of $\mathbf{U}'$, using $\mathbf{F}_0 = \mathbf{K}_0\mathbf{U}' + \mathbf{K}''\mathbf{U}_0$.

Note that boundary nodes cannot have prescribed tractions and prescribed displacements simultaneously, or in other words, $\partial\Omega_u$ and $\partial\Omega_t$ cannot overlap.

In Chapter 3 we have also used periodic boundary condition (PBC). Figure 2.2 demonstrates the situation for a 1D rod discretized with 5 nodes. For finite length, the end nodes has different stiffness compared to the interior nodes. On the contrary, the infinite rod represented with 5 nodes with PBC on the end nodes, shows the all the nodes has the same stiffness; it is in fact expected since in case of PBC there is no real boundary to the overall problem.

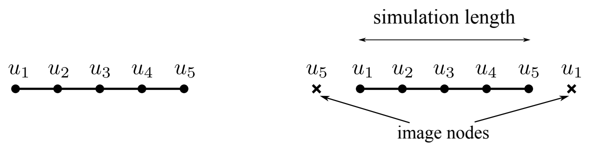
u_1 u_2 u_3 u_4 u_5
simulation length
u_5 u_1 u_2 u_3 u_4 u_5 u_1
image nodes

$$\mathbf{K} = \begin{bmatrix} -\kappa & \kappa & & & \\ \kappa & -2\kappa & \kappa & & \\ & \kappa & -2\kappa & \kappa & \\ & & \kappa & -2\kappa & \kappa \\ & & & \kappa & -\kappa \end{bmatrix} \qquad \begin{bmatrix} -2\kappa & \kappa & & & \kappa \\ \kappa & -2\kappa & \kappa & & \\ & \kappa & -2\kappa & \kappa & \\ & & \kappa & -2\kappa & \kappa \\ \kappa & & & \kappa & -2\kappa \end{bmatrix}$$

(a) Finite rod (b) Infinite rod

Figure 2.2 – Illustration of the periodic boundary condition in 1D and the resulting stiffness matrix with nonzero entries.

2.3 Force-based atomistic-continuum coupling

Force-based a/c coupling is built upon the idea of domain decomposition [62]. A given boundary value problem is decomposed into an atomistic domain where full atomistic resolution is desired and a continuum domain where elastic deformations are deemed sufficiently accurate. Figure 2.3 shows a schematic of the decomposition, with notations described below. The two domains interact mechanically via an overlap region. The atomistic system includes so-called pad atoms that are slaved to the deformation of the continuum. Conversely, the atom positions along the atom/continuum interface define a displacement boundary condition for the deformations in the continuum domain.

The atomistic and continuum domains have independent energy functionals E^A and E^C, respectively. The atomistic energy functional depends on the true atom positions ($\mathbf{r^A}$), including those atoms along the atom/continuum interface and denoted by I with positions ($\mathbf{r^I}$), and the positions of the pad atoms ($\mathbf{r^P}$) that are considered part of the atomistic system. The continuum energy functional depends on the interface atom positions ($\mathbf{r^I}$) as boundary nodes and the nodal positions ($\mathbf{r^C}$) of the (discretized) continuum domain. Any other force and displacement boundary conditions acting on degrees of freedom $\mathbf{r^A}$ or $\mathbf{r^C}$ in each domain can be included in the standard manner discussed in Sections 2.1.1 and 2.2. The equilibrium solution of a given boundary value problem specified on the total domain of the problem is then achieved, in principle, by an iterative process of (i) solving the atomistic problem while holding the pad atoms fixed, which generates new interface positions ($\mathbf{r^I}$), (ii) solving the continuum problem for the nodal degrees of freedom $\mathbf{r^C}$, (iii) computing the pad atom positions $\mathbf{r^P}$ by interpolation of the nodal positions, and (iv) returning to solve the new atomistic problem with the new pad atom positions. In practice, the iterative approach is not necessary [63, 64] but it aids in conceptualizing the solution process.

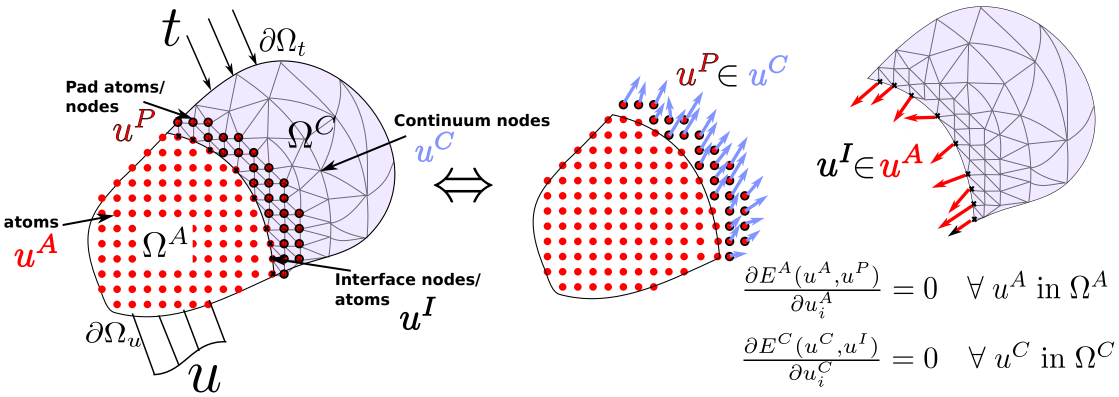
t
$\partial\Omega_t$
Pad atoms/ nodes
u^P
Ω^C
Continuum nodes
u^C
$\Leftrightarrow$
$u^P \in u^C$
$u^I \in u^A$
atoms
u^A
Ω^A
Interface nodes/ atoms
u^I
$\partial\Omega_u$
u
$\frac{\partial E^A(u^A, u^P)}{\partial u_i^A} = 0 \quad \forall\, u^A \text{ in } \Omega^A$
$\frac{\partial E^C(u^C, u^I)}{\partial u_i^C} = 0 \quad \forall\, u^C \text{ in } \Omega^C$

Figure 2.3 – **Schematic illustration of force-based relaxation of a/c couple.** The problem domain is decomposed into atomistic and continuum sub-domains, $\Omega^{\mathbf{A}}$ and $\Omega^{\mathbf{C}}$ respectively. In the overlap region, the pad atoms derive their displacements $\mathbf{u^P}$ from the underlying continuum nodes and the interface nodes derive their displacements $\mathbf{u^I}$ from the interface atoms. Equilibrium equations for the two sub-domains are solved simultaneously, with traction and displacement boundary conditions ($\mathbf{t}$ over $\partial\Omega_{\mathbf{t}}$ and $\mathbf{u}$ over $\partial\Omega_{\mathbf{u}}$ respectively).

In application to elemental crystals having a Bravais lattice, the reference state for both atomistic and continuum domains, including the pad region, is the stress-free perfect lattice structure. Creation of the initial structure is then straightforward where the atoms in the atomistic domain are arranged in a crystalline structure and the surrounding continuum domain is discretized using Finite Elements. It is also common, for accuracy, to refine the discretization of the continuum domain down to the atomic scale in the pad region. Pad atoms then also correspond to continuum nodes, and there is no need to interpolate continuum nodal positions to the pad atom sites.

2.4 Solute misfit volume

In Part II of this thesis dealing with solute-strengthening in alloys, the solute-dislocation interaction energy is estimated using linear elasticity assumption where the solute misfit volume interacts mechanically with the pressure field of the dislocation. The solute misfit volumes, used as inputs, are calculated using molecular statics (performed with LAMMPS) with EAM interatomic potentials and the Average atom method (Section 2.1.3). A simulation cell is first constructed with all the lattice sites occupied by average atoms corresponding to the random alloy. Periodic boundary conditions are imposed on all sides. Care has been taken so that the periodic boundary condition does not create a stacking fault on any face of the simulation cell. Also, the simulation cell size conforms to the average lattice parameter of the random alloy which is also the average atom lattice parameter — so the simulation cell is under zero pressure by construction. One average atom in the centre of the simulation cell is replaced with a solute atom of the random alloy. Energy minimization is performed allowing the simulation cell to change volume in order to attain zero pressure (Section 2.1.1).

The change in volume of the simulation cell as a result of energy minimization and pressure relaxation is noted, which in turn is the misfit volume of the corresponding solute. Misfit volumes of all the solutes (constituents) of the random alloy are computed using the same procedure described above. The relaxation of the simulation cell volume to zero pressure is performed using the "*fix box/relax*" implemented in LAMMPS.

2.5 Interaction of two defects in an infinite linear elastic medium

Part II of this thesis calculates the solute-dislocation and solute-solute interaction energies, which plays an important role in the strengthening of alloys. The interaction of two defects has a mechanical component that can be computed using linear elasticity theory and a chemical/nonlinear component, which decays with increasing distance between the two defects. In this section we will be deriving the expression for mechanical interaction energy of two defects in an infinite elastic medium. Then specific cases of solute-solute and solute-dislocation interaction energies will be discussed.

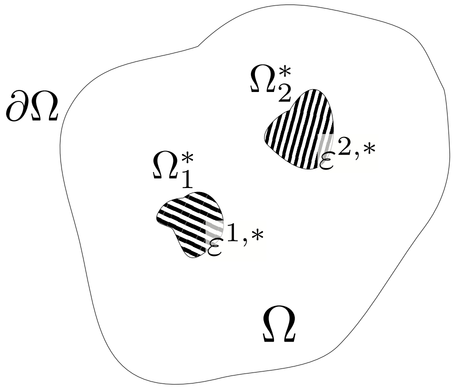

Figure 2.4 – A domain Ω in an infinite linear elastic medium bounded by $\partial\Omega$, which contain two sub-domains Ω_1^* and Ω_2^* with eigenstrains $\varepsilon^{1,*}$ and $\varepsilon^{2,*}$.

A defect is associated with an eigenstrain, which does not arise due to externally applied traction. Figure 2.4 shows two defects in an infinite elastic medium, which are regions Ω_1^* and Ω_2^* with eigenstrains $\varepsilon^{1,*}$ and $\varepsilon^{2,*}$. Each defect in its reference stress-free state is associated with a strain $\varepsilon^{1,*}$ and $\varepsilon^{2,*}$ (which is not an elastic strain), at every point in Ω_1^* and Ω_2^* respectively. When embedded in an elastic matrix, the eigenstrain of the defect induces elastic strain and stress fields at every point inside and outside the defect. The domain Ω in Figure 2.4 is an arbitrary region containing the two defects.

Let $\sigma_{ij}^{1,el}$ be the components of the elastic stress field due to defect 1 in the infinite linear elastic medium if defect 2 didn't exist, that is $\varepsilon_{ij}^{2,*} = 0$; likewise let $\sigma_{ij}^{2,el}$ be the elastic stress field if $\varepsilon_{ij}^{1,*} = 0$. $\varepsilon_{ij}^{1,el}$ and $\varepsilon_{ij}^{2,el}$ are the corresponding elastic strain fields. The total strain is a sum of the elastic strain and the eigenstrain,

$$\varepsilon^{\text{tot}}_{ij} = \varepsilon^{el}_{ij} + \varepsilon^{*}_{ij} \tag{2.23}$$

Using principle of superposition, the total strain energy inside the domain Ω can be decoupled into the strain energies due to defect 1 and 2 individually in absence of the second defect, plus an energy of interaction of the two defects,

$$\begin{aligned} W &= \frac{1}{2}\int_{\Omega} (\sigma^{1,el}_{ij} + \sigma^{2,el}_{ij})(\varepsilon^{1,el}_{ij} + \varepsilon^{2,el}_{ij}) dV \\ &= \frac{1}{2}\int_{\Omega} \sigma^{1,el}_{ij}\varepsilon^{1,el}_{ij} dV + \frac{1}{2}\int_{\Omega} \sigma^{2,el}_{ij}\varepsilon^{2,el}_{ij} dV + \frac{1}{2}\int_{\Omega} (\sigma^{1,el}_{ij}\varepsilon^{2,el}_{ij} + \sigma^{2,el}_{ij}\varepsilon^{1,el}_{ij}) dV \end{aligned} \tag{2.24}$$

where the last term in the second equation is the interaction energy. Using the symmetry relation for elastic stiffness tensor $C_{ijkl} = C_{klij}$ (see Equation 2.12), one can show $\sigma^{1,el}_{ij}\varepsilon^{2,el}_{ij} = \sigma^{2,el}_{ij}\varepsilon^{1,el}_{ij}$.

Therefore the interaction energy of two defects in an infinite linearly elastic medium is given by,

$$E_{\text{int}} = \int_{\Omega} \sigma^{1,el}_{ij}\varepsilon^{2,el}_{ij} dV = \int_{\Omega} \sigma^{2,el}_{ij}\varepsilon^{1,el}_{ij} dV \tag{2.25}$$

We can rewrite the interaction energy in term of eigenstrain using the relation in Equation 2.23 as follows

$$E_{\text{int}} = \int_{\Omega} \sigma^{1,el}_{ij}\varepsilon^{2,\text{tot}}_{ij} dV - \int_{\Omega} \sigma^{1,el}_{ij}\varepsilon^{2,*}_{ij} dV$$

And since $\varepsilon^{2,*}_{ij}$ is zero everywhere outside Ω^*_2,

$$E_{\text{int}} = \int_{\Omega} \sigma^{1,el}_{ij}\varepsilon^{2,\text{tot}}_{ij} dV - \int_{\Omega^*_2} \sigma^{1,el}_{ij}\varepsilon^{2,*}_{ij} dV \tag{2.26}$$

The first term can be further simplified using integration by parts and equilibrium condition as

$$\int_{\Omega} \sigma^{1,el}_{ij}\varepsilon^{2,\text{tot}}_{ij} dV = \int_{\Omega} \sigma^{1,el}_{ij} u^2_{i,j} dV = \int_{\Omega} (\sigma^{1,el}_{ij} u^2_i)_{,j} dV - \int_{\Omega} \cancelto{0}{\sigma^{1,el}_{ij,j}}\, u^2_i dV$$

Using divergence theorem,

$$\int_{\Omega} \sigma^{1,el}_{ij}\varepsilon^{2,\text{tot}}_{ij} dV = \int_{\partial\Omega} \sigma^{1}_{ij} n_j u^2_i dA = \int_{\partial\Omega} T^1_i u^2_i dA$$

where $,j$ in the subscript implies differentiation with respect to j. Note that we have dropped the "*el*" from the superscipt of the stress field due to defect 1 since outside Ω^*_1, the stress field is always elastic.

Therefore, the interaction energy of two solutes in an infinite linearly elastic medium turns out to be,

$$E_{\text{int}} = -\int_{\Omega_2^*} \sigma_{ij}^1 \varepsilon_{ij}^{2,*} dV + \int_{\partial\Omega} T_i^1 u_i^{2,\text{tot}} dA \tag{2.27}$$

Note that the first term is independent of the choice of integration domain Ω as long as it contains the two defects. The second term depends on the choice of the integration domain; however if the domain Ω spans the entire three-dimensional space with no traction at infinity, the second term goes to zero. So we will only consider the first term as the interaction energy.

The stress tensor can be decomposed into hydrostatic and deviatoric components as follows

$$\begin{aligned} \sigma_{ij} &= p\delta_{ij} + (\sigma_{ij} - p\delta_{ij}) \\ \text{where,} \quad p &= \text{ pressure } = -\frac{1}{3}\sigma_{ii} \end{aligned} \tag{2.28}$$

Similarly, the strain tensor can be decomposed into hydrostatic and deviatoric components too as follows,

$$\begin{aligned} \varepsilon_{ij} &= \varepsilon_{\text{vol}}\delta_{ij} + (\varepsilon_{ij} - \varepsilon_{\text{vol}}\delta_{ij}) \\ \text{where,} \quad \varepsilon_{\text{vol}} &= \text{ volumetric strain } = \frac{1}{3}\varepsilon_{ii} \end{aligned} \tag{2.29}$$

Using Equations 2.28 and 2.29, the interaction energy in Equation 2.27 can be further simplified as follows,

$$E_{\text{int}} = \int_{\Omega_2^*} p_1 \varepsilon_{\text{vol}}^{2,*} dV + \int_{\Omega_2^*} (\sigma_{ij}^1 - p_1\delta_{ij})(\varepsilon_{ij}^{2,*} - \frac{1}{3}\varepsilon_{\text{vol}}^{2,*}\delta_{ij}) dV \tag{2.30}$$

If defect 2 is a dilatational solute, which is a relevant case for the thesis, and we assume that the region Ω_2^* is so small that the pressure field p_1 of defect 1 is uniform within Ω_2^*, then we can write the interaction energy as

$$E_{\text{int}} = p_1 \int_{\Omega_2^*} \varepsilon_{\text{vol}}^{2,*} dV \approx p_1 \Delta V_2 \tag{2.31}$$

where ΔV_2 is the misfit volume of solute at Ω_2^*.

Recalling Equation 2.25, one can also express the interaction energy as the product of the pressure field of the second defect and the misfit volume of the first, therefore

$$E_{\text{int}} \approx p_1 \Delta V_2 = p_2 \Delta V_1 \tag{2.32}$$

2.5.1 Elastic interaction of solute pair

Isotropic case

The elastic displacement field due to a centre of dilatation in an infinite isotropic medium [65]

$$\boldsymbol{u} \propto \frac{\boldsymbol{x}}{\|\boldsymbol{x}\|^3} \tag{2.33}$$

Therefore, the volumetric strain $\nabla \cdot \boldsymbol{u}$ is zero everywhere except at the centre of dilatation and so is the pressure. Therefore, recalling Equation 2.31 we can conclude that *two dilatational solute in an infinite isotropic medium do not interact.*

Anisotropic case

The volumetric strain, and therefore the pressure, due to a centre of dilatation in an infinite *anisotropic* medium is not zero outside of the centre of dilatation. Therefore dilatational solutes interact with each other mechanically in an anisotropic medium. Eshelby has derived the expression for the interaction energy of two dilational solutes of misfit volumes ΔV_1 and ΔV_2 in an infinite anisotropic medium of cubic symmetry as follows [66]

$$E_{\text{int}} = \frac{15}{4\pi} f C_{44} \left(1 - \frac{1}{A}\right) \frac{\Gamma}{r^3} \Delta V_1 \Delta V_2 \tag{2.34}$$

where,

$$f = \begin{cases} 1 & \text{for fcc} \\ 1/2 & \text{for bcc} \end{cases}$$

$A = \text{Zener anisotropy ratio} = \dfrac{2C_{44}}{C_{11} - C_{12}}$

r = Distance between the two solutes

$\Gamma = l^4 + m^4 + n^4 - \dfrac{3}{5}$

(l, m, n) = Direction cosines of the line joining the two solutes

It is well-known that Al-Al repulsion in Ni-Al alloys is strong, with $E_{\text{int}} = 0.243$ eV. The misfit volume of Al in Ni is $\Delta V_{\text{Al}} = 1.62\,\text{Å}^3$, lattice parameter of Ni is $a_{\text{Ni}} = 3.518\,\text{Å}$, elastic constants of Ni are $(C_{11}, C_{12}, C_{44}) = (275, 154, 127)$ GPa. All these values are computed using DFT [67]. In fcc, the first nearest neighbour is along $\{110\}$-direction for which $\Gamma = -0.1$ and in Ni the first nearest neighbour is at a distance $r = a_{\text{Ni}}/\sqrt{2} = 2.4876\,\text{Å}$. Substituting the above values in Equation 2.34, we get the interaction energy due to mechanical interaction $E_{\text{int}} = -0.00845$ eV, which is orders of magnitude lower than the DFT-computed value and the sign is opposite. Therefore, we can conclude that elastic interaction between solutes in negligible and one must perform atomistic simulation to accurately determine solute-pair interaction energy. Section 2.7 discusses how to calculate solute pair interaction energy using molecular statics and average-atom method for alloys described by semi-empirical interatomic potentials like the Embedded Atom Method.

2.5.2 Elastic interaction of solute with dislocation

Recalling 2.31, the elastic interaction energy of a dilatational solute with a straight dislocation is the product of the pressure due to the dislocation at the site with the solute and the misfit volume of the solute. Calculation of solute misfit volume using molecular statics and average-atom method for alloy has been discussed in Section 2.4. Using the principle of superposition for linearly elastic solids, the pressure field of a straight dislocation with Burgers vector $\boldsymbol{b}$ along the glide plane can be expressed as a sum of the pressure fields due the edge and screw components.

The pressure due to an edge dislocation of Burgers vector magnitude b_e in an elastically isotropic infinite medium, at a point r distance away from the dislocation which subtends an angle θ with respect to the glide direction is given by

$$p(r,\theta) = \frac{\mu b_e}{3\pi} \frac{(1+\nu)}{(1-\nu)} \frac{\sin\theta}{r} \tag{2.35}$$

where μ and ν are the shear modulus and Poisson's ratio respectively.

The pressure due to a screw dislocation in an elastically isotropic infinite medium is zero everywhere, which is why dilatational solutes do not interact elastically with the screw component of a dislocation.

If the infinite medium is elastically anisotropy, calculation of dislocation stress field becomes involved. In fact, except for certain slip systems meeting certain symmetry requirements, we do not have closed form solution for the dislocation stress field [68]. Section 2.6 discusses the methods for calculating the dislocation stress field in an infinite anisotropic medium for any arbitrary orientation of the dislocation line and Burgers vector.

2.6 Elastic field of a straight dislocation in elastically anisotropic solid

This section reviews the sextic theory and the Stroh formalism for deriving the displacement and stress field of a straight dislocation in an anisotropic media. It is a brief review and interested readers must refer Chapter 13 of Ref. [68] for more details.

Here we will be solving the equilibrium equation 2.14 stated in Section 2.2 with prescribed constraints in displacement and traction as shown in Figure 2.5.

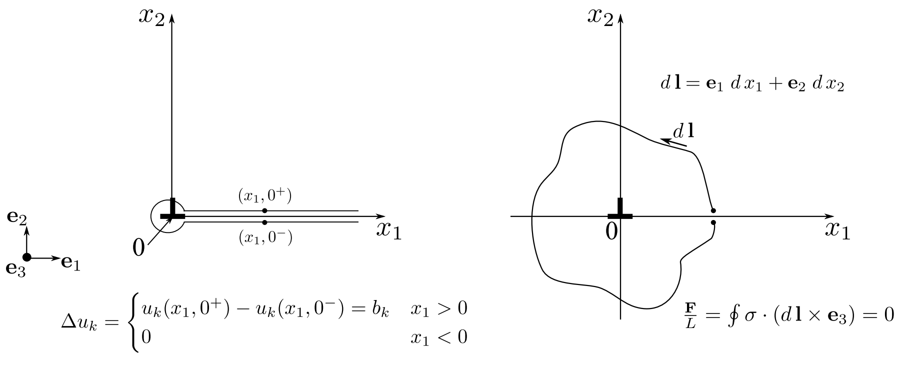
x_2
x_1
$\mathbf{e}_2$
$\mathbf{e}_1$
$\mathbf{e}_3$
0
$(x_1, 0^+)$
$(x_1, 0^-)$
$\Delta u_k = \begin{cases} u_k(x_1,0^+) - u_k(x_1,0^-) = b_k & x_1 > 0 \\ 0 & x_1 < 0 \end{cases}$
$d\mathbf{l} = \mathbf{e}_1\, dx_1 + \mathbf{e}_2\, dx_2$
$d\mathbf{l}$
$\frac{\mathbf{F}}{L} = \oint \sigma \cdot (d\mathbf{l} \times \mathbf{e}_3) = 0$

(a) Constraint in displacement (b) Traction boundary condition

Figure 2.5 – Constraints in displacement field and tractions in a problem with an infinite straight dislocation at the origin. The dislocation line vector $\boldsymbol{\xi}$ (not shown) is along $\mathbf{e}_3$ pointing out of the page. b_k is the k^{th} component of the Burgers vector $\boldsymbol{b}$. $\mathbf{F}/L$ is the net force per unit length along the dislocation line acting on the surface of a rod parallel to the dislocation and containing it, as shown in the figure with the contour.

First the basic steps for solving the equilibrium equation for the straight dislocation will be discussed, following which the Stroh formalism will be introduced.

Step 1: Identification of the general form of the displacement field

The solution of the equilibrium equation (Equation 2.14) for the displacements u_k will be of the form,

$$u_k = A_k f(\eta) \tag{2.36}$$

where

$$\eta = x_1 + p x_2 \tag{2.37}$$

and where p and A_k are constants.

Step 2: Obtaining p and A_k

With the substitution of u_k in Equation 2.14 and cancellation of common factor $\partial^2 f/\partial\eta$, the equilibrium equation reduces to the form,

$$a_{ik} A_k = 0 \tag{2.38}$$

where

$$a_{ik} = c_{i1k1} + (c_{i1k2} + c_{i2k1})p + c_{i2k2} p^2 \tag{2.39}$$

The linear equations (2.38) have a nonzero solution for A_k only when the determinant of the matrix $\{a_{ik}\}$ is zero, which in turn gives a sixth-order equation in p with roots p_α ($\alpha = 1,2,3,4,5,6$).

For each root p_α there is a set of $A_k(\alpha)$ that satisfy Equations 2.38. What is relevant is the ratio of the components of any $\{A_k(\alpha)\}$ vector.

The roots p_α occur in pairs of complex conjugates. $A_k(\alpha)$ also occurs in corresponding pairs of complex conjugates. So one just needs to consider three roots p_1, p_2, p_3 and corresponding $A_k(1), A_k(2), A_k(3)$ and then Equation 2.36 becomes,

$$u_k = \mathrm{Re}\left[\sum_{\alpha=1}^{3} A_k(\alpha) f_\alpha(\eta_\alpha)\right] \tag{2.40}$$

where Re mean the “the real part of”. The f_α are three arbitrary analytic functions.

Step 3: Identification of the general functional form of $f(\eta)$

The stresses involve the derivatives $df/d\eta$; like stresses, the functions $df/d\eta$ are also single-valued and continuous except at the origin. A Laurent series of the form,

$$\frac{df}{d\eta} = \sum_{r=-\infty}^{\infty} a'_r \eta^r \tag{2.41}$$

satisfies such criterion.

Integration of the relation (2.41) gives the functional form of $f(\eta)$ as follows,

$$f(\eta) = \frac{D}{2\pi i}\ln\eta + \sum_{r=-\infty}^{\infty} a_r \eta^r \tag{2.42}$$

The power series terms are not characteristics of a straight dislocation in an infinite medium, so only the logarithmic term is retained in the subsequent discussion.

Step 4: Using the constraints in displacement and traction to find the only remaining unknown D

The complex variable η can be expressed in Euler’s exponential form $\eta = |\eta|e^{i\theta}$, where θ is the argument of η. Then $\ln\eta = \ln|\eta| + i\theta$.

Δu_k in displacement constraint, shown in Figure 2.5, translates into $\ln\eta = i\Delta\theta$. If the imginary part of p, $\mathrm{Im}(p)$ is positive, a counterclockwise path around the dislocation corresponds to a counterclockwise path in the η complex plane. On the contrary, for a negative $\mathrm{Im}(p)$, a counterclockwise path around the dislocation would be a clockwise path in the η plane. Thus across the cut $\ln\eta = \mp 2\pi i$ which implies $\Delta f = \mp D$.

Therefore the constraint on displacement shown in Figure 2.5 becomes,

$$\operatorname{Re}\left[\sum_{\alpha=1}^{3} \mp A_k(\alpha) D(\alpha)\right] = b_k \qquad k = 1,2,3 \tag{2.43}$$

With Equations 2.43, we have three equations for six unknowns, the real and imaginary parts of $D(n)$ for $n = 1,2,3$. The other three equations are provided by the traction boundary condition shown in Figure 2.5, the requirement that there is not net force on the dislocation core. If one carries out the surface integral for the force per unit length and equals it to zero, the following set of three equations can be derived with which we can obtain every $D(n)$,

$$\operatorname{Re}\left[\sum_{\alpha=1}^{3} \mp B_{i2k}(\alpha) A_k(\alpha) D(\alpha)\right] = 0 \qquad i = 1,2,3 \tag{2.44}$$

$$\text{where,} \quad B_{ijk}(\alpha) = c_{ijk1} + c_{ijk2}\, p_\alpha$$

Using Equations 2.43 and 2.45, one can determine the real and imaginary parts of $D(\alpha)$ for $\alpha = 1,2,3$.

Step 5: Obtain expressions for displacement and stress field by substitution

Substituting the expression for $f(\eta)$ in Equation 2.42 (and ignoring the power series terms) in Equation 2.40, we get,

$$u_k = \operatorname{Re}\left[\frac{1}{2\pi i} \sum_{\alpha=1}^{3} A_k(\alpha) D(\alpha) \ln \eta_\alpha\right] \tag{2.45}$$

$$\sigma_{ij} = \operatorname{Re}\left[\frac{1}{2\pi i} \sum_{\alpha=1}^{3} B_{ijk}(\alpha) A_k(\alpha) D(\alpha)\, \eta_\alpha^{-1}\right] \tag{2.46}$$

The steps described above is the sextic theory for solving the equilibrium equation for a infinite system with a straight dislocation.

The Stroh formalism generalizes the sextic theory where the coordinates x_1, x_2 and $\boldsymbol{\xi}$ does not need to align with $\mathbf{e}_1, \mathbf{e}_2, \mathbf{e}_3$. Also it provides an explicit expression for $D(\alpha)$.

First we define an orthonormal basis $(\boldsymbol{m}, \boldsymbol{n}, \boldsymbol{\xi})$ different from $(\mathbf{e}_1, \mathbf{e}_2, \mathbf{e}_3)$, such that coordinates x_1 and x_2 points towards $\boldsymbol{m}$ and $\boldsymbol{n}$ respectively and $\boldsymbol{\xi}$ is the dislocation line direction such $\boldsymbol{\xi} = \boldsymbol{m} \times \boldsymbol{n}$.

For any point $\boldsymbol{x}$ with components defined with respect to $(\mathbf{e}_1, \mathbf{e}_2, \mathbf{e}_3)$, the quantity η will be,

$$\eta = \boldsymbol{m} \cdot \boldsymbol{x} + p\, \boldsymbol{n} \cdot \boldsymbol{x} \tag{2.47}$$

Let the component of the elastic modulus tensor c_{ijkl} be defined with respect to $(\mathbf{e}_1, \mathbf{e}_2, \mathbf{e}_3)$. We define a metric "()" such that $(\boldsymbol{ab})_{jk} = a_i c_{ijkl} b_l$.

Given the above definitions and general set-up, the matrix $\{a_{ik}\}$ in Equation 2.38 becomes $(\boldsymbol{mm}) + [(\boldsymbol{mn}) + (\boldsymbol{nm})]p + (\boldsymbol{nn})p^2$. Till now we have just rewritten quantities in the sextic theory with change of basis.

The departure comes with the definition of a second vector $\boldsymbol{L}$, related to $\boldsymbol{A}(=\{A_k\})$ by

$$\boldsymbol{L} = -[(\boldsymbol{nm}) + p(\boldsymbol{nn})]\boldsymbol{A} \tag{2.48}$$

We also define a six-dimensional vector $\boldsymbol{\zeta}$ by combining $\boldsymbol{A}$ and $\boldsymbol{L}$ in the fashion $\{A_1, A_2, A_3, L_1, L_2, L_3\}$. With these definitions, Equation 2.38 can be written as a six-dimensional eigenequation

$$\mathbf{N} \cdot \boldsymbol{\zeta} = p\boldsymbol{\zeta} \tag{2.49}$$

$$\text{where,} \quad \mathbf{N} = \begin{bmatrix} -(\boldsymbol{nn})^{-1}(\boldsymbol{nm}) & -(\boldsymbol{nn})^{-1} \\ -[(\boldsymbol{mn})(\boldsymbol{nn})^{-1}(\boldsymbol{nm}) - (\boldsymbol{mm})] & (\boldsymbol{mn})(\boldsymbol{nn})^{-1} \end{bmatrix}$$

which can then be solved for eigenvalues $p_\alpha, \alpha = 1, 2, \cdots, 6$ and the corresponding $\boldsymbol{A}_\alpha$ and $\boldsymbol{L}_\alpha$. Notice the difference from the sextic theory (in Step 2), where we solved the sixth-order equation for $\det(\{a_{ik}\}) = 0$ to get the p_α and $\boldsymbol{A}_\alpha$.

It can be shown that the following orthogonality relation holds between $\boldsymbol{A}_\alpha$ and $\boldsymbol{L}_\beta$ (where $\alpha, \beta = 1, 2, \cdots, 6$ are indexes over the six solutions of p),

$$\boldsymbol{A}_\alpha \cdot \boldsymbol{L}_\beta + \boldsymbol{A}_\beta \cdot \boldsymbol{L}_\alpha = \delta_{\alpha\beta} \tag{2.50}$$

The orthogonality relation is a pivotal result of the Stroh formalism since it facilitates in getting an explicit form for $D(\alpha)$.

The boundary conditions that the Burgers circuit has a discontinuity $\boldsymbol{b}$ and that there are no external force at the dislocation core (Step 4) become,

$$\sum_{\alpha=1}^{6} \mp D(\alpha)\boldsymbol{A}_\alpha = \boldsymbol{b} \tag{2.51}$$

$$\sum_{\alpha=1}^{6} \mp D(\alpha)\boldsymbol{L}_\alpha = \mathbf{0} \tag{2.52}$$

Multiplying Equation 2.51 by $\boldsymbol{L}_\beta$ and Equation 2.52 by $\boldsymbol{A}_\beta$, then summing and using the orthogonality relation (2.50), we readily determine that,

$$D(\alpha) = \mp \boldsymbol{L}_\alpha \cdot \boldsymbol{b} \tag{2.53}$$

Thus Stroh theory gives an explicit form for $D(\alpha)$. With $D(\alpha)$ known, the solution for the displacement and stresses can be inferred from Equations 2.46 as follows (Step 5),

$$\boldsymbol{u} = \frac{1}{2\pi i} \sum_{\alpha=1}^{6} \mp \boldsymbol{A}_\alpha [\boldsymbol{L}_\alpha \cdot \boldsymbol{b}] \ln \eta_\alpha \tag{2.54}$$

$$\sigma_{ij} = \frac{1}{2\pi i} \sum_{\alpha=1}^{6} \mp c_{ijkl} [m_l + p_\alpha n_l] A_k(\alpha) [\boldsymbol{L}_\alpha \cdot \boldsymbol{b}] \, \eta_\alpha^{-1} \tag{2.55}$$

2.7 Solute pair interaction energies

Interaction energy of solute pairs in a random alloy is an important quantity influencing strengthening in certain alloys which will be discussed in Chapter 5. We have already seen in Section 2.5.1 that mechanical interaction of a pair of solutes in insignificant, if any. The first few neighbour interactions which tends to be significant must, therefore, be calculated using molecular statics simulation (Section 2.1)

Interaction energy $U_{xy}^{int}(d)$ of a solute pair separated by distance d is the difference between the energy of the systems, where the solute pair is separated by distance d and where they have infinite(large) separation, embedded in an “average” medium.

$$U_{xy}^{int}(d) = E_{xy}(d) - E_{xy}(\infty) \tag{2.56}$$

where $E_{xy}(d)$ is the system energy where the solutes x and y are embedded in an average medium and are separated by distance d (Here all the system energies are of systems with same total number of atoms). The average medium is characterised by “average atoms”, which are lattice sites where the associated energetics is averaged over random occupancy of atomtypes conforming to the alloy compositon. Averaging can be performed explicitly over many random realizations, which is generally computationally expensive depending on the nature of the underlying interatomic interactions. Special quasi-random structures (SQS) can be used instead of random realizations to expedite convergence of the average [69]. For pair interatomic potentials, the averaging can be done analytically. Even for empirical potentials like the Embedded-atom method (EAM) with a many-body term, an “average atom” potential can be analytically formulated in a mean-field approach [54] as discussed in Section 2.1.3. When the interaction potentials are described via first-principles, Coherent Potential approximation[70] is used to describe the average medium. Therefore the interaction energy is computable for all kinds of energetics describing the interatomic interactions. Another computable energy quantity is the effective pair interactions, $V_{xy}^{eff}(d)$, which has also been used in Chapter 5. Effective pair interactions are defined as follows,

$$V_{xy}^{eff}(d) = E_{xx}(d) + E_{yy}(d) - 2E_{xy}(d) \tag{2.57}$$

The effective pair potentials come out as pair-interaction terms while expressing the configurational energy of a random alloy to lowest order in the generalised perturbation method framework and has been used to study phase stability in binary and high-entropy alloys[5, 71].

Since $E_{xx}(\infty)+E_{yy}(\infty)-2E_{xy}(\infty)=0$, one can readily deduce the following relation between effective pair interactions and interaction energies,

$$V_{xy}^{eff}(d)=U_{xx}^{int}(d)+U_{yy}^{int}(d)-2U_{xy}^{int}(d) \tag{2.58}$$

Note that the above relation holds true irrespective of the energetics describing the interatomic interactions.

In Chapter 5, we will need these pair interaction quantities for solute pairs across a stacking fault. Like shown in Equation 2.56, difference of system energies is taken between system with solutes at a specified separation and a system where they are far separated from each other. However the stacking fault must pass in between the solute pairs in both the systems and the distances of the two solutes from the stacking fault must be same in both the systems. The set up is schematically presented in Figure 2.6

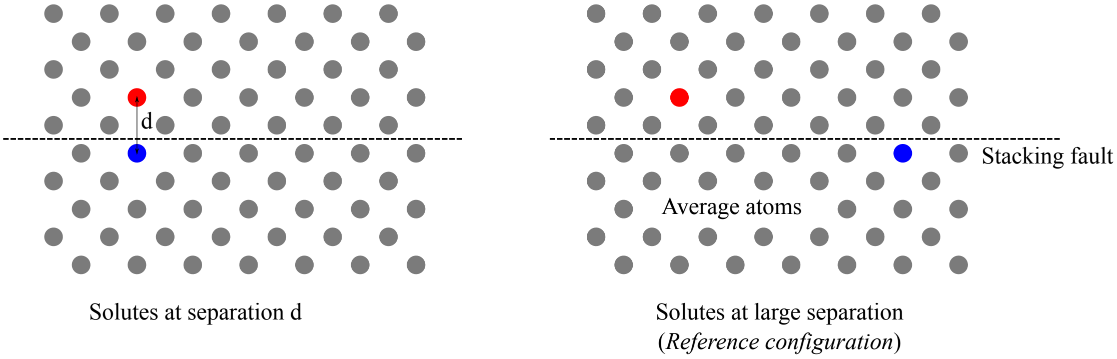

Figure 2.6 – Schematic of two the systems whose energy difference gives the interaction energy for the solute pairs indicated here with red and blue atoms.

2.8 Elementary probability theory

In this thesis, we are studying random alloys which are multicomponent alloys with constituent atoms randomly arranged on lattice sites. Some of the elementary concepts from probability theory needed to study these systems are presented in this section. We will focus on discrete random variables with finite set of outcomes which relevant for this thesis.

Random variables, events and probability

A random variable is a mapping from a set of possible outcomes, say Ω, to the set of real numbers $\mathbb{R}$. For example, when we toss a coin, we either get a head or a tail. “Getting a head” and “getting a tail” are the two possible outcomes and you can define a random variable say X which maps the outcomes to integers 1 and 0 respectively. So we say random variable X takes the value 1 when we drop a head and the value 0 for a tail.

An event is a subset of the set of possible outcomes. For example, if we roll a dice, there are six possible outcomes and rolling an even number is then an event. Here we can define a random variable X which takes the value of the number that has been rolled, i.e. from $1, 2, \ldots, 6$; then "X is even", "$X > 2$", etc. are all different events.

Probability is a measure assigned to every event which is a real number between 0 and 1. The sum of probabilities of all the possible outcomes is always 1. For a fair dice, for instance, the probability of rolling a number more than 3, $\mathbf{P}(X > 3)$, is $1/2$.

Joint probability

If E_1 and E_2 are two events, then their joint probability $\mathbf{P}(E_1, E_2)$, is the probability of event "E_1 *and* E_2".

Mutually exclusive events

If two events E_1 and E_2 are mutually exclusive, then their joint probability is zero. Mutually exclusive events are also called disjoint events.

If $E_1, E_2, \ldots, E_n$ are n disjoint events such that $\bigcup\limits_{i=1}^{n} E_i = \Omega$, where Ω is the set of all possible outcomes, then $\sum\limits_{i=1}^{n} \mathbf{P}(E_i) = 1$.

Independent events

If two events E_1 and E_2 are independent then their joint probability equals the product of their individual probabilities.

$$\mathbf{P}(E_1, E_2) = \mathbf{P}(E_1)\mathbf{P}(E_2) \tag{2.59}$$

A set of n events $\{E_i : i = 1, 2, \ldots, n\}$ are *mutually independent* iff,

$$\mathbf{P}(E_1, E_2, \ldots, E_n) = \prod_{i=1}^{n} \mathbf{P}(E_i) \tag{2.60}$$

Independent random variables

Let X and Y be two random variables each with a finite number of possible outcomes $x_1, x_2, \ldots, x_n$ and $y_1, y_2, \ldots, y_m$ respectively. The two random variables are said to be independent iff,

$$\mathbf{P}(X = x_i, Y = y_j) = \mathbf{P}(X = x_i)\mathbf{P}(Y = y_j) \quad \text{for all } x_i, y_j \tag{2.61}$$

Expectation or expected value

If X is a random variable with a finite number of possible outcomes $x_1, x_2, \ldots, x_n$ occuring with probabilities $p_1, p_2, \ldots, p_n$ respectively, then the expectation of X is defined as,

$$\langle X \rangle = \sum_{i=1}^{n} x_i p_i \tag{2.62}$$

The expectation of the product of two independent random variables is the product of their individual expectations, that is,

$$\langle XY \rangle = \langle X \rangle \langle Y \rangle \quad \textit{iff } X \text{ and } Y \text{ are independent} \tag{2.63}$$

Variance and Covariance

Variance of a random variable X is

$$\mathrm{Var}(X) = \langle X^2 \rangle - \langle X \rangle^2 \tag{2.64}$$

Covariance of random variables X and Y is

$$\mathrm{Cov}(X, Y) = \langle XY \rangle - \langle X \rangle \langle Y \rangle \tag{2.65}$$

Notice that $\mathrm{Cov}(X, X) = \mathrm{Var}(X)$

If X and Y are independent random variables, then $\mathrm{Cov}(X, Y) = 0$.

Variance of sum of two random variable is given by

$$\mathrm{Var}(X + Y) = \mathrm{Var}(X) + \mathrm{Var}(Y) + 2\mathrm{Cov}(X, Y) \tag{2.66}$$

Square root of variance is the standard deviation.

Conditional Probability

Conditional probability of an event E_1 given E_2, denoted as $\mathbf{P}(E_1|E_2)$, is basically the probability of event E_1 to occur when event E_2 has already occured. It is defined as,

$$\mathbf{P}(E_1|E_2) = \frac{\mathbf{P}(E_1, E_2)}{\mathbf{P}(E_2)} \tag{2.67}$$

One can easily deduce the Bayes' theorem from the above definition as

$$\mathbf{P}(E_1|E_2) = \frac{\mathbf{P}(E_2|E_1)\mathbf{P}(E_1)}{\mathbf{P}(E_2)} \tag{2.68}$$

If events E_1 and E_2 are independent then $\mathbf{P}(E_1|E_2) = \mathbf{P}(E_1)$.

If $\{B_i : i = 1, 2, \ldots, n\}$ is a set of n disjoint events such that $\bigcup_{i=1}^{n} B_i = \Omega$, where Ω is the set of all possible outcomes, then the probability of any event A can be expressed as follows,

$$\mathbf{P}(A) = \sum_{i=1}^{n} \mathbf{P}(A \cap B_i) = \sum_{i=1}^{n} \mathbf{P}(A|B_i)\mathbf{P}(B_i) \tag{2.69}$$

The above statement is the *law of total probability*.

If X is a random variable with a finite number of possible outcomes $x_1, x_2, \ldots, x_n$ and E is an event, then the *conditional expectation* of X given E is given as,

$$\langle X|E\rangle = \sum_{i=1}^{n} x_i \mathbf{P}(X = x_i|E) \tag{2.70}$$

Concurrent multiscale modeling Part I

Atomistic-to-continuum (a/c) coupling methods are a class of computational multiscale schemes that combine the accuracy of atomistic models with the efficiency of continuum elasticity. They are being utilized in materials science to study the fundamental mechanisms of material failure such as crack propagation and plasticity, which are governed by the interaction between crystal defects and long-range elastic fields.

The applicability of these methods to model defect behaviour (like dislocation nucleation from crack tip) relies on the decaying nonlinear behaviour with increasing distance from the defect core. Near the elastic singularity "interesting" nonlinear deformation and nucleation events take place which needs to be resolved with atomistics, while a continuum approximation with linear elasticity constitutive law can be employed to describe the far-field deformation.

Random alloys are multicomponent systems rife with compositional fluctuations, where every atom can be conceptualized as solute of a certain type embedded in an average medium with average elastic properties of the alloy. The defect interacts with these fluctuating solute environment either chemically (near its core) or through its elastic pressure field away (from the core). With increasing distance from the defect core, the defect interacts with solutes from a larger volume of the alloy and the sum of all these interactions has an average effect on the defect behaviour near its core. Thus the a/c methods are naturally applicable for studying defect behaviour in random alloys, where the far-field continuum is devoid of all compositional fluctuation and is described by the average elastic constants of the alloy.

Although the far-field compositional fluctuations can be neglected using a homogenized description, care must be taken in accounting for the fluctuations at the atomistic-to-continuum coupling interface. The coupling interface constitutes an overlap region where bidirectional information transfer takes place across the two domains; any mismatch in the underlying structure or elastic properties leads to coupling errors. While applying a/c coupling to random alloys, we are explicitly coupling an inhomogeneous atomistic domain to a homogeneous continuum, therefore such errors are inevitable *unless the coupling interface is carefully constructed.*

This Part of the thesis is concerned with the application of concurrent multiscale methods to random alloys and constitutes of one chapter (Chapter 3) which demonstrates the coupling errors and their magnitude in context of force-based coupling strategy. Two alternative methods of constructing the concurrent multiscale problem are proposed, studied and validated which mitigates the coupling errors by orders of magnitude. Although the methods are studied with a specific force-based coupling method, at least one of them can be readily extended to other concurrent multiscale methods. This is the only study in concurrent multiscale modeling literature, where a/c coupling has been applied to random alloys and the findings of this study will facilitate future application of multiscale methods to solid mechanics problems in random alloys involving interaction of crystal defects with long-range elastic fields.

3 Atomistic continuum coupling of random alloys

Disclaimer

This chapter is adapted from the following article, with permission from the coauthors and the publisher.
S. Nag, T. Junge, W. A. Curtin, "Atomistic-continuum coupling of random alloys", *Modelling and Simulation in Materials Science and Engineering* 27, 075004 (2019).

Random alloys have an inhomogeneous structure at the atomic scale, and this randomness determines many alloy properties. To understand and predict the mechanical behavior of random alloys, it is then necessary to study them at the atomistic scale. However, if the material is subject to small deformations over length scales much larger than the atomic scale, the material response becomes insensitive to the local randomness. The response is then governed by the average properties of the alloy, and a random alloy has well-defined macroscopic lattice constants and elastic constants. Small deformations are then well-described by elasticity, as if the alloy is homogeneous. Thus, it can be useful and feasible to use multiscale methods to study random alloys, with full atomic-scale randomness in regions containing atomistic defects and/or high deformations where the detailed atomistic response is essential, surrounded by continuum homogenized material over a much larger region to capture the surrounding elastic fields that influence the behavior in the atomistic domain. Problems of interest span a wide range of defect-defect interactions where the intimate atomic structure of different atomistic defects intersect, making linear elasticity descriptions highly inaccurate. Of particular interest are problems involving combinations of extended defects such as dislocations, cracks, and grain boundaries, which involve long-range strain fields and thus large sizes to handle accurately.

Multiscale atomistic/continuum (a/c) coupling methods for quasistatic zero-temperature mechanics problems are now very well-developed for elemental materials and ordered alloys, since both have well-defined and (usually) small unit cells [3, 8, 9]. Methods for finite-temperature, dynamic, and/or evolving systems are more complex, but have also been developed and continue to be refined [16, 21, 22, 72–76]. These methods have not yet been applied to random alloys, where there is no well-defined unit cell. Most importantly, the local compositional fluctuations in the random alloy create additional challenges in creating an interface between fully-atomistic and continuum descriptions, and these challenges must be identified and solved. In this chapter, we present two methods for force-based atomistic/continuum coupling of random alloys that resolve problems arising in the direct application of methods developed for elemental metals.

A general issue in developing a/c coupling for random alloys is the representation of the continuum domain. Random alloys have compositional fluctuations over all scales. However, if the system size is sufficiently large, consisting of many atoms, the response of the system under small loads converges to a well-defined elastic material with the symmetry of the underlying crystal. The zero-pressure average lattice constant of the random alloy also converges to a unique value. Given a set of interatomic potentials for the random alloy elemental constituents, the homogenized response of an effectively infinite domain can be computed numerically in advance. Convergence studies determine the size needed to obtain material properties with sufficiently high accuracy. Such a brute-force computational approach provides the relevant continuum-level alloy properties needed in a multiscale model. On the other hand, a/c coupling that uses the Cauchy-Born rule to derive the constitutive behavior of the continuum domain directly from the underlying atomistic response, as in the Quasicontinuum Method [13], cannot be feasibly done on random alloys. Furthermore, different specific atom-atom interactions in the random alloy are lost in the continuum representation but a/c coupling requires an intimate connection of the real atomistic domain to the continuum domain through a so-called “pad" of atoms overlapping the continuum domain. It is desirable to preserve those atom-specific atomic-scale interactions in the region where the coupling is performed.

An alternative approach to achieving the average alloy properties at the atomistic scale is via the creation of an “average atom” interatomic potential that embeds the random alloy average properties into a new single-atom potential [54, 55, 77]. Specifically, given a set of Embedded-Atom Method (EAM) potentials for the alloying elements X of interest, an “average atom” (A-atom) EAM potential for the average alloy atom A at alloy composition c_X can be created as described in Chapter 2 in Section 2.1.3. The lattice constant and elastic constants of the A-atom potential are generally close to those of the true infinite random alloy across various alloys. Results for the three alloys studied here are shown in Table 3.1. The A-atom method gives very good predictions for the lattice constants and good predictions for the elastic constants. The A-atom method also captures well the interactions of individual atom types with the average matrix, which can be important in the coupling domain of a multiscale model.

For multiscale modeling where we couple a region of true random atoms to some homogenized model, it is crucial that the homogenized model have the same lattice constant(s). Any small lattice constant differences translate directly into errors in strain, and thus errors in stress, that are not negligible. On the other hand, small errors in the elastic constants do not create significant error. Large converged direct simulations of random alloys are thus required to validate the A-atom approach to the necessary accuracy for the given alloy composition. Since the A-atom approach may have some error, it is advisable to adjust the composition of the A-atom alloy by small amounts Δc_X away from the true c_X to accurately match the lattice constants of the true random alloy. Such a correction is shown for the alloys studied here in Table 3.2, showing no significant change in the elastic constants. Thus, while the A-atom potential can be quite valuable in many aspects of modeling random alloys, care must be taken in applications for multiscale coupling. Here, we apply the A-atom potential in one forced-based coupling method (Method 2 in Section 3.3.2). As mentioned earlier, it should also find application in energy-based coupling schemes such as the Quasicontinuum Method.

Alloy		a (Å)	C_{11} (GPa)	C_{12} (GPa)	C_{44} (GPa)
FeNiCr	Random alloy	3.52166957	243.38	157.24	135.13
	Average alloy	3.52181862 (0.00423%)	246.61 (1.33%)	158.12 (0.56%)	138.53 (2.52%)
$Ni_{0.85}Al_{0.15}$	Random alloy	3.53478252	211.36	152.20	123.19
	Average alloy	3.53814763 (0.0951%)	224.21 (6.08%)	150.82 (-0.91%)	123.42 (0.19%)
$Al_{0.95}Mg_{0.05}$	Random alloy	4.05545782	107.49	58.90	30.46
	Average alloy	4.05639532 (0.0231%)	108.21 (0.67%)	57.83 (-1.82%)	30.92 (1.51%)

Table 3.1 – Lattice parameter and elastic constants of true random alloy and those of the corresponding A-atom potential, for the three random alloys studied in this paper. Errors in the A-atom quantities are indicated in parentheses.

Alloy	Δc_X	C_{11} (GPa)	C_{12} (GPa)	C_{44} (GPa)
FeNiCr	8.3295674E-3 (Fe)	247.11 (1.53%)	158.21 (0.62%)	138.86 (2.76%)
	-6.002575E-3 (Ni)			
	-2.326992E-3 (Cr)			
$Ni_{0.85}Al_{0.15}$	1.66733E-2 (Ni)	224.14 (6.05%)	150.90 (-0.85%)	124.0 (0.66%)
	-1.66733E-2 (Al)			
$Al_{0.95}Mg_{0.05}$	1.8525526E-3 (Al)	108.49 (0.93%)	57.98 (-1.56%)	31.13 (2.2%)
	-1.8525526E-3 (Mg)			

Table 3.2 – Perturbations Δc_X of the A-atom alloy away from the true alloy composition c_X so as to match the lattice constants of the random alloy upto 8 decimal places. The corresponding elastic constants of the A-atom potential are shown but differ negligibly from those at composition c_X; errors relative to the true random alloy are shown in parentheses.

In creating the homogeneous effective elastic material by whatever means, all of the fluctuations inherent in the underlying random material are eliminated. The effects of fluctuating properties in the domain that has been replaced by continuum material, on the fields in the atomistic domain are lost. The fields created by the fluctuations do decay with distance from the fluctuation, and so can safely be ignored beyond some distance from the atomistic region. Nonetheless, implicit in the a/c coupling is the notion that these fluctuations are not important for the phenomena of study in the atomistic domain. This can be studied theoretically and by convergence studies using the methods presented here, but requires further investigation that is beyond the scope of this thesis.

The remainder of this chapter focuses on the algorithmic aspects of a force-based atomistic/-continuum coupling method for random alloys. Section 3.1 demonstrates the non-negligible errors associated with the straightforward application of the force-based a/c method (refer Section 2.3) to a random alloy. Section 3.2 analyses the reasons behind the errors with a simple force-based 1D couple constructed with linear springs and proposes solutions, which are then used in Section 3.3 to introduce two complementary methods for a/c coupling of random alloys that mitigates the coupling errors in more complicated systems and coupling geometries and provides coupling with manageable errors. Section 3.4 summarizes our analysis and results.

3.1 Errors in application of standard a/c coupling to random alloys

The application of the standard a/c coupling (refer Section 2.3) to a random alloy leads to non-negligible errors, especially near the atomistic/continuum interface. The sharp transition from atomistic to continuum description occurs precisely at the transition between random and homogeneous materials. The pad atoms are tied to the computed deformation of the homogeneous continuum domain and so (i) do not have the exact average lattice constant or elastic constants, locally, of the infinite random alloy and (ii) cannot relax to adapt to the precise random arrangements of the nearby true atoms in the atomistic domain. The perfect crystalline lattice also does not correspond to the relaxed configuration of atoms in the random alloy. These issues give rise to spurious forces near the interface. Force-based methods are unsuitable for handling rapidly-varying forces acting at the interface [3], which can result in long-range spurious stresses in both atomistic and continuum domains. Spurious stresses can also arise at large deformations due to the replacement of the non-linear atomistic material by a linear elastic continuum.

To demonstrate the above points explicitly, we examine the spurious stress that arise in conventional a/c coupling within an infinite slab of crystalline material with a planar a/c interface longitudinally along its thickness. The test geometry is shown in Figure 3.1 and consists of a 3d cuboidal problem domain of dimensions $L_x = 50$ and $L_y = 20$ lattice units with periodic boundary conditions imposed in the x and y directions. In the coupled problem, the thickness of the atomistic and continuum domains are $L_z^A = 34$ and $L_z^C = 17$ lattice units respectively. We study the equicomposition FeNiCr alloy described by EAM potentials [78].

The continuum domain is solved by the Finite Element Method. The atoms in the atomistic domain and the pad atoms are initialized in the perfect crystalline lattice sites at the average lattice constant of the alloy. A finite element mesh is created by treating all atoms in the continuum domain as nodes because we are not seeking computational efficiency in this test case. The construction of the coupled problem, including the atoms and the FE mesh, is done using the CADD mesher of T. Junge [79]. We then use constant-strain elements and the pre-computed macroscopic average elastic constants of the true random alloy (reported in Table 3.1). The coupled problem is then relaxed to the equilibrium state with the surface at $z = L_z^A + L_z^C (= L_z)$ held at zero displacement $u_z(L_z) = 0$ and the surface at $z = 0$ held at a displacement corresponding to an imposed uniaxial strain ε_{zz}, $u_z(0) = -\varepsilon_{zz} L_z$, as indicated in Figure 3.1. Atomistic minimization is performed using the *fire* and/or *CG* minimizers of the open-source molecular dynamics code LAMMPS[48, 49]. The continuum equilibrium equations for every finite element are solved using the open-source parallel sparse direct solver MUMPS[60, 61]. Relaxation is performed in a staggered manner alternating between atomistic and continuum relaxations until a global force infinity norm tolerance of 10^{-8} is reached for the full coupled problem.

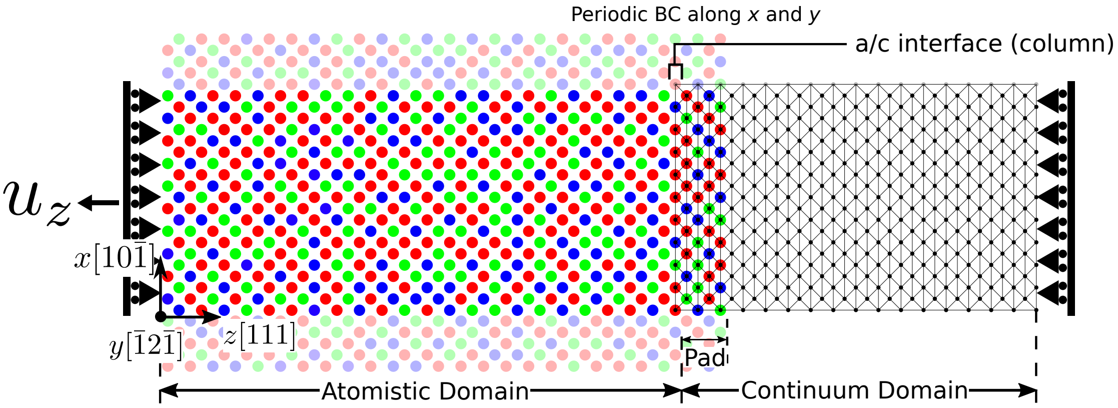

Figure 3.1 – **Schematic of an a/c couple under tensile elongation for an infinite slab of random alloy.** For all cases of a/c coupling examined for this study, this geometry has been used. Translucent atoms and nodes in the diagram are the periodic images of the boundary degrees of freedom in the $x-$ and $y-$ directions. The planar a/c interface perpendicular to the thickness of the slab ensures that any coupling-induced spurious stresses propagate through the specimen unattenuated. The thickness of the atomistic and continuum domains are 34 and 17 lattice units respectively, with the atomistic domain being larger so as to achieve converged values for the average lattice constant and elastic constants of the random alloy. The simulation box (with all the opaque atoms and nodes) is 50 lattice units in $x-$ direction and 20 lattice units in $y-$ direction. The thickness of the pad is determined by the cut-off radius of the interatomic potential which is typically one lattice unit in $z-$direction.

For reference, we perform a complementary study of a fully-random sample having exactly the same atomic configuration (atoms in the atomistic domain and pad atoms) as in the coupled system plus atoms in the continuum to create a sample of the same dimensions as the in the coupled problem. Under zero applied strain, all atoms in the fully-atomistic problem relax locally but no net stresses develop because the overall system has the correct macroscopic average lattice constant. Under an applied strain ε_{zz}, all atoms again relax locally and the average stress throughout the system is given by the average elastic constants and the applied strain through Hooke's Law.

To assess spurious effects due to the a/c coupling in the atomistic domain, we compute the atom-by-atom difference in virial stresses ($\Delta\sigma_i = \sigma_i^{AC} - \sigma_i^{ref}$) using the nominal average atomic volume of $a^3/4$ and not the local atomic volume. In the continuum domain, spurious stresses are the difference between the measured nodal stresses and the applied stress computed by Hooke's Law. In this planar problem, we then compute the average spurious stress over all N_k atoms or nodes in plane k parallel to the a/c interface as $\Delta\sigma^m(k) = \frac{1}{N_k}\sum_{i=1}^{N_k}\Delta\sigma_i$. We further compute the standard deviation of the spurious stresses over every plane k as $\Delta\sigma^{std}(k) = \sqrt{\frac{1}{N_k}\sum_{i=1}^{N_k}(\Delta\sigma_i - \Delta\sigma^m)^2}$.

Figure 3.2 presents the normal component $\Delta\sigma_{zz}$ of the spurious stress under zero applied strain for a number of different realizations of the random alloy. This stress component shows the largest error. In this effectively one-dimensional geometry, the coupling induces a constant long-range stress on the order of 100–200 MPa, with different spurious stresses in the atomistic and continuum domains. The standard deviation of the spurious stresses $\Delta\sigma_{zz}^{std}$ is large near the a/c interface but decreases slowly to 10–30 MPa far from the interface. Spurious stresses on the order of hundreds of MPa are unacceptable — they are large enough to cause dislocation motion or introduce additional stress intensity near a crack tip, for instance. In addition, the precise value of the far-field stresses depends sensitively on the specific alloy realization.

The random alloy has large local stress fluctuations naturally. The standard deviation in atomic virial stresses for a large fully-relaxed random alloy of FeNiCr is 2–4 GPa. While large, the net stresses over larger domains decrease steadily, with no net stress on large scales. Spurious stresses at the a/c interface introduced by coupling can approach the level of the intrinsic stress fluctuations of the alloy (standard deviation in spurious stresses reaching 1.5 GPa). And, while smaller in magnitude further from the interface, 100 MPa within 5 nm, the stresses remain non-negligible for practical purposes.

Under an applied strain, the spurious stresses in the coupled system are expected to remain on the same order of magnitude as at zero strain. The errors at zero strain are so overwhelming that errors under applied strain remains a secondary aspect. Also the spurious stresses again depend on the precise realization of the random system, and changes with increasing load might not be systematic.

The spurious stresses arise because there is an imbalance of forces at the a/c interface. The pad atoms are not initially at true equilibrium positions, but rather at perfect lattice positions. The pad domain is also described by the infinite-size alloy stiffness tensor. Meanwhile, the atoms in the atomistic domain near the coupling interface, experience local relaxations and local variations in effective stiffness. The force-based a/c coupling ensures continuity of displacements across the interface but does not consider continuity of tractions. Traction continuity indeed should not be imposed because the continuum interactions are local while the atomistic interactions are non-local. Imposing traction continuity, as done in energy-based coupling methods such as QC, leads to so-called ghost-force errors; these are normally avoided in force-based coupling. However, when high gradients of the deformation gradient, or high force gradients, exist at the interface, the force-based method gives rise to long-range stresses in effectively 1d problems [3]. Since an a/c coupling interface should never be positioned in a region with high gradients — the a/c coupling should occur where the gradients are small so that the continuum approximation is valid — this failure of the forced-based method is easily resolved by simply moving the interface to a region of lower gradients. However, in a/c coupling of the random alloy, the high gradients are induced by the coupling itself and are unavoidable, leading to the persistent and non-negligible errors shown in Figure 3.2.

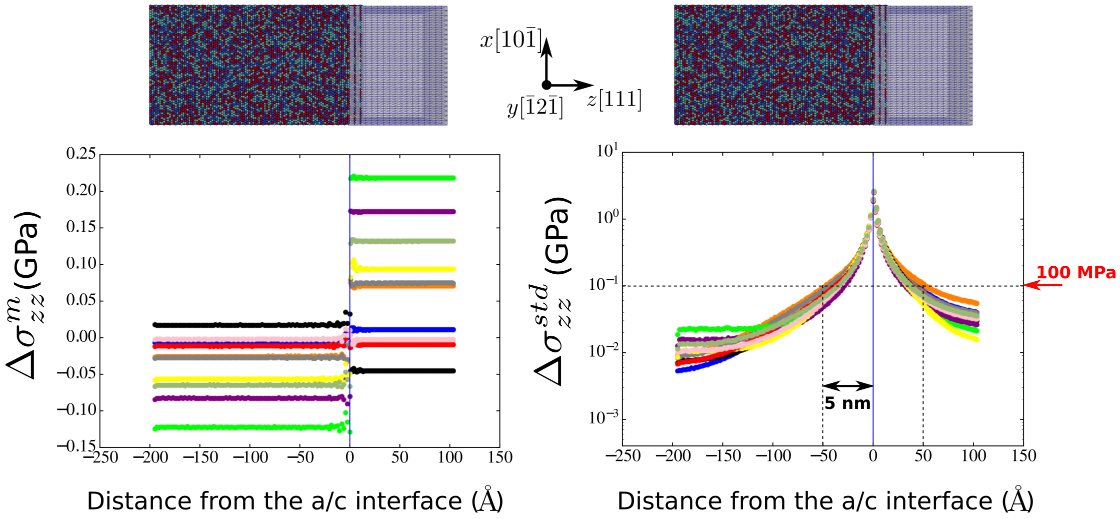

Figure 3.2 – **Standard a/c couple with no imposed deformation.** Coupling-induced spurious stresses along coupling direction $\Delta\sigma^{m}_{zz}$ and $\Delta\sigma^{std}_{zz}$ as a function of distance from the a/c interface. Results are for specimens of equicomposition FeNiCr held fixed at z-ends of the specimen (thus no imposed deformation). For each alloy, results for 10 different realizations are shown as indicated by the various colors.

3.2 Illustration of the problem with 1D array of linear springs and proposed solutions

A linear spring has two properties, its stiffness and its natural length. In this section, we will be studying a very simplified version of the a/c coupling of random alloys using linear springs connected in series. Randomizing the natural length and/or the stiffness of the springs will represent the random alloy (atomistics) with spatial fluctuations in lattice parameter and elastic constants. A complementary series of springs ("*average springs*") with average stiffness and natural length will represent the homogeneous continuum with average properties of the alloy. This simplified version captures the essence of the problem in standard a/c coupling of random alloys and will naturally lead us to the solutions which are very intuitive, yet not immediately obvious in the 3D coupling of random alloy with complicated interatomic interactions.

First we would study the situation where the system of springs have randomly different natural lengths, however all of them have the same stiffness. The average springs therefore will have the same stiffness and the average natural length of the ensemble of real springs. Figure 3.3 presents the random and the corresponding average emsembles of springs, each connected in series.

Random ensemble (*with varying natural lengths*)

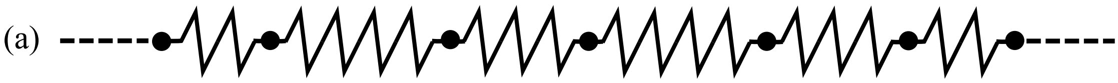

Average description (*with average natural length*)

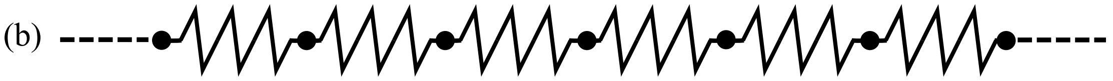

Figure 3.3 – A series of linear spring with same stiffness connected end-to-end, each of which has a different natural length. The average version of this ensemble is another series of linear springs ("average springs") with the same stiffness, where the natural length of every average spring is average of the natural lengths of real springs in the original series.

Now we construct a force-based couple with the random and average ensembles of springs, as depicted in Figure 3.4. The problem is evident in the fact that in absence of any external force, the force-based couple has nonzero force at the interface because the atomistic(real) spring in the pad has a different natural length than the average, yet by construction it is constrained — thus the random ensemble has an unbalanced force to start with of which the average ensemble is unaware of, leading to net spurious force at the interface of the force-based couple.

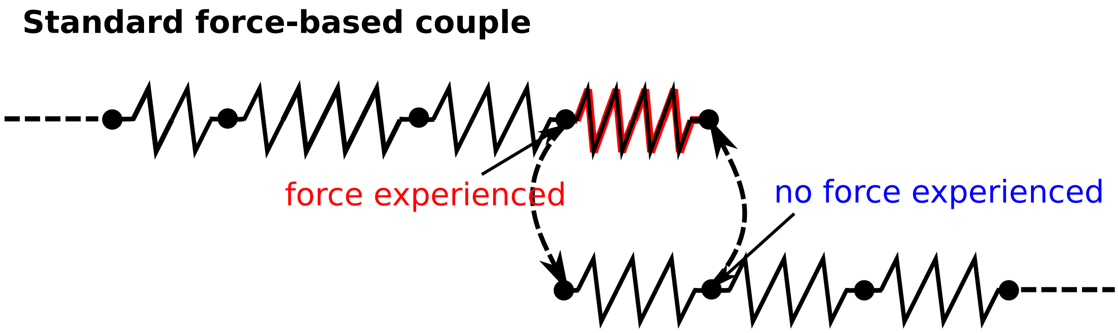

Figure 3.4 – A standard force-based couple constructed with the random and average ensemble of springs shown in Figure 3.3.

A manifestation of this problem is seen in Figure 3.2 for a 3D forced-based couple of equicomposition FeNiCr random alloy described by EAM interatomic potentials. Random spurious point forces act all over the a/c interface which gives rise to the fluctuation in spurious stresses on relaxation near the interface; and the magnitude of fluctuations diminishes with distance according to the Saint-Venant's principle. The spurious point forces at the interface does not cancel on average over the surface area of the a/c interface even though the alloy is random and gives rise to high long-range stresses. This can be attributed to the complex nonlinear EAM potential for the 3D problem and also the high (spurious) force gradients at the interface. Since a net spurious force acts on the non-rigid a/c interface, the resultant long-range stress is of opposite sign in the two domains of the a/c couple as evident from Figure 3.2.

The solution to the above problem is obvious, that is *to relax the real spring in the pad to its natural length before constructing the coupled problem* as depicted in Figure 3.5. This is essentially one of the solutions to the 3D random alloy coupled problem described as Method 1, we will see in the next section.

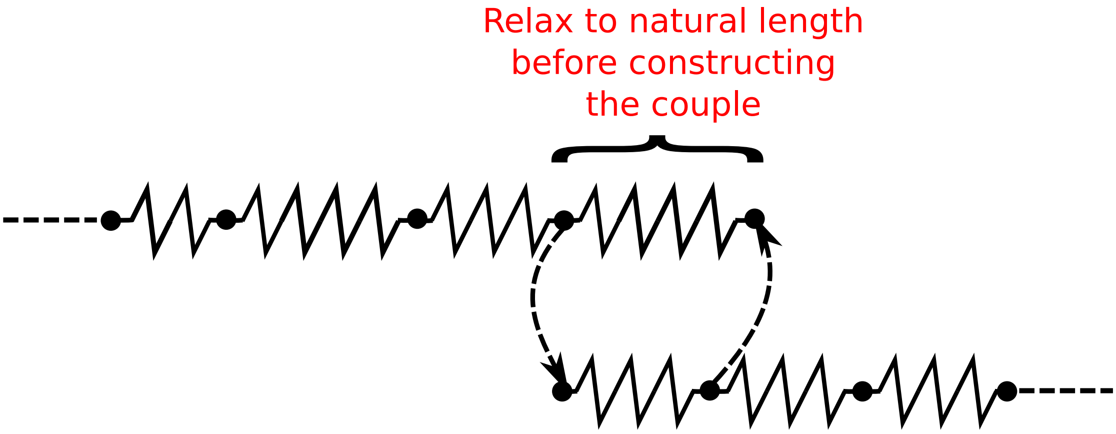

Figure 3.5 – Elimination of spurious force at the interface due to construction by relaxing the pad spring in the random ensemble to its natural length before constructing the coupled problem.

Having fixed the coupling error in absence of any external force, we will now focus our attention on problems that may arise on applying an external force. Errors that appear on application of external force must be related to spring stiffness. So we now consider a force-based couple for an ensemble of springs with varying stiffnesses, as depicted in Figure 3.6. The average ensemble will have springs with average stiffness of springs in the random ensemble.

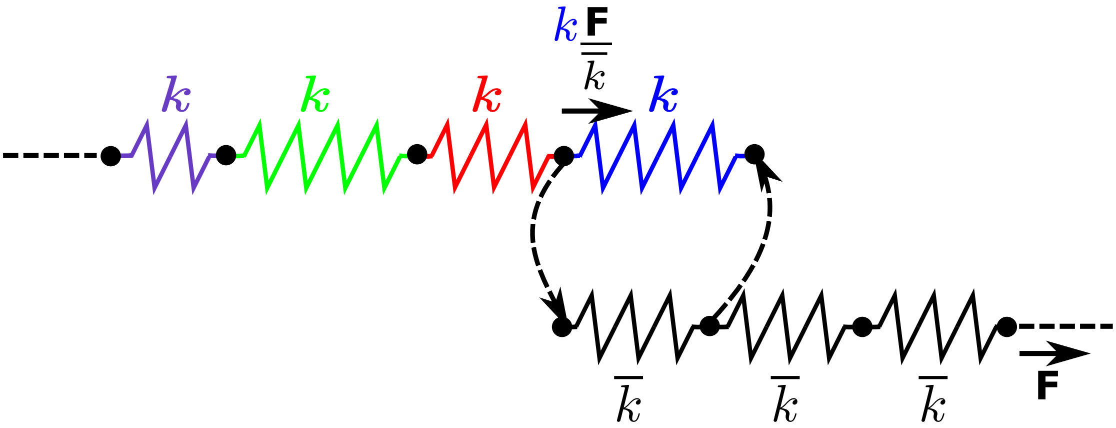

Figure 3.6 – Force-based couple with springs of varying stiffness and average springs with average stiffness $\bar{k}$.

When a force is applied to the coupled problem, every node should experience the same force. However, one can see in Figure 3.6 that it is not the case while coupling a random ensemble of springs to a homogenous one. With reference to Figure 3.6, when a force is applied to the ensemble of average springs, every spring in this ensemble gets stretched by $\mathbf{F}/\bar{k}$. As the pad spring in the random ensemble is constrained to stretch with the average ensemble, it gets stretched by $\mathbf{F}/\bar{k}$ as well. However it's stiffness is k and not $\bar{k}$. Therefore the force transmitted in the random ensemble is not $\mathbf{F}$, but $k\mathbf{F}/\bar{k}$. The imbalance of force in the two ensembles is equivalent to having a spurious nonzero force at the interface of the couple due to mismatch of local stiffness among the two ensembles in the pad region.

There are two solutions to the problem depicted in Figure 3.7 (a) one where we assign the stiffness of the pad spring in the random ensemble to the pad spring in the average ensemble and (b) the other where we replace the pad spring in the random ensemble with an average spring. In 3D coupling of random alloys with more realistic many-body potentials implementing the first solution is quite involved. However the second solution can be easily implemented with the help of "average atoms" discussed in Section 2.1.3. This is basically Method 2 for mitigating coupling errors which will be discussed in the next section.

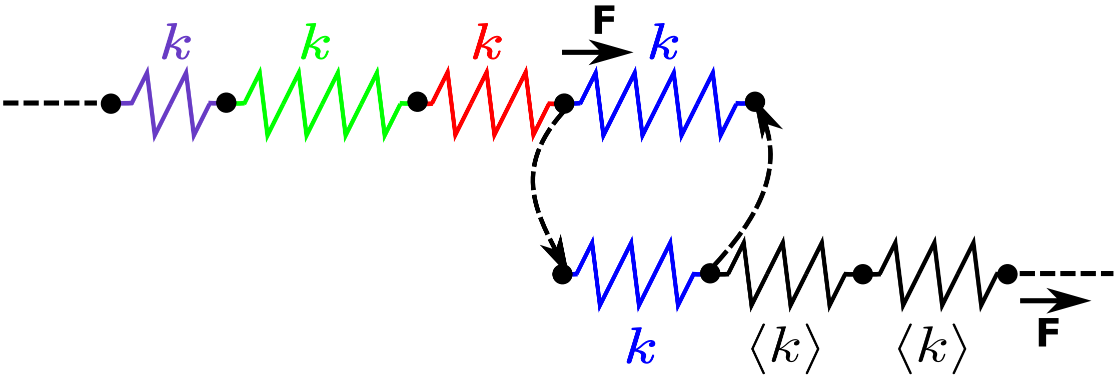

(a) Assigning the stiffness of the pad spring in the random ensemble to the pad spring in the average ensemble.

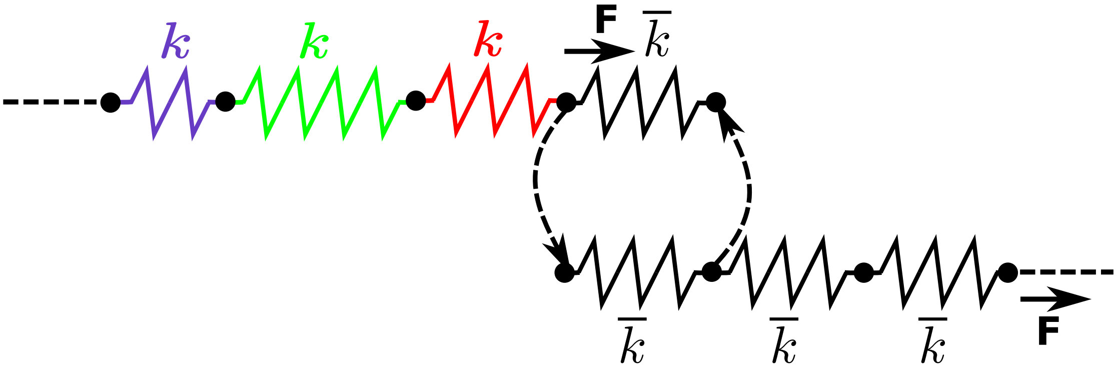

(b) Replacing the pad spring in the random ensemble with an average spring.

Figure 3.7 – The two solutions to resolve the errors due to coupling that manifest on application of external force.

In the next section, we will be taking concepts from this section and propose detailed algorithm for implementing the solutions to reduce coupling errors in 3D forced-based coupling of random alloys described with nonlinear many-body interatomic potentials.

3.3 Methods for accurate 3D a/c coupling of random alloys described by complex interatomic potentials

In this section we will propose two methods for construction of the a/c couple which will dramatically reduce the spurious stresses due to coupling (shown in Figure 3.2) to acceptable levels. The methods derive concepts from the solutions proposed in the previous section 3.2, for the simple case of 1D forced-based couple with a series of linear springs. The methods proposed in this section are also validated against three model random alloys, namely, equicomposition FeNiCr medium-entropy alloy, Al-5%Mg and Ni-15%Al alloys.

3.3.1 Method 1

To reduce the spurious stresses that arise in the standard a/c coupling method, we recall one source of the error: the pad atoms are initially assigned to perfect-lattice positions. This is analogous to the situation depicted in Figure 3.4 for an ensemble of linear springs with randomized natural lengths. The first method to reduce spurious stresses is thus simply to use the true equilibrium pad atom positions in the random alloy as the initial reference configuration in the a/c couple. The procedure is shown schematically in Figure 3.8.

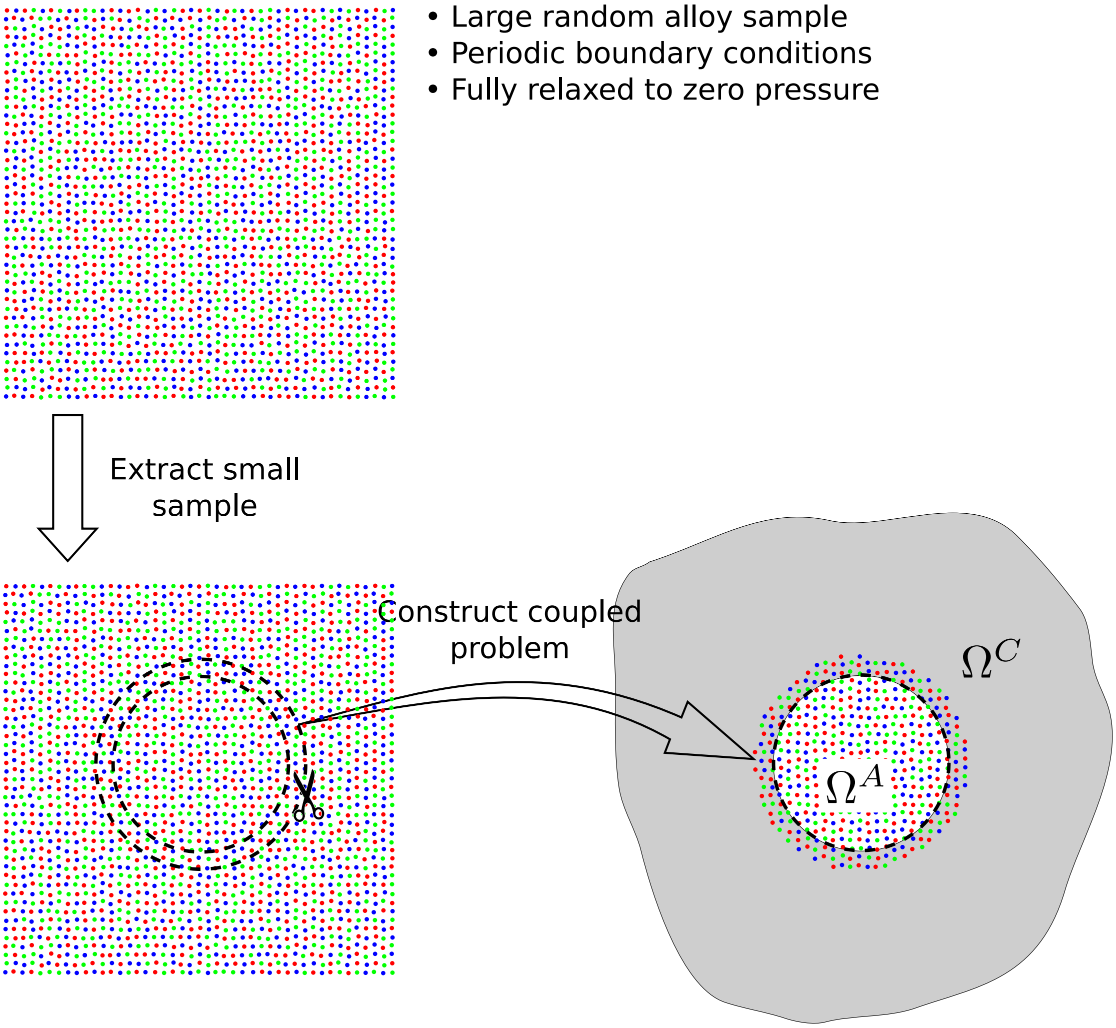
• Large random alloy sample
• Periodic boundary conditions
• Fully relaxed to zero pressure
Extract small sample
Construct coupled problem
Ω^C
Ω^A

Figure 3.8 – **A/C coupling for random alloys: Method 1** Ω^A and Ω^C are the atomistic and continuum domains respectively.

To create the atomistic domain and surrounding pad atom region, we start with a very large sample of random alloy relaxed to zero pressure under periodic boundary conditions. This “reference" sample is already needed to determine the average lattice and elastic constants. From this reference atomistic sample, in the fully relaxed state, we extract the desired atomistic plus pad atom domain to create the atomistic portion of the multiscale model. The atomistic domain thus inherits a structure that includes fluctuations from surrounding atoms in the large reference sample for that *one particular* atomistic realization. The results of the subsequent multiscale study will thus be influenced by those particular fluctuations, even though those atoms have been replaced by a continuum representation, with elastic constants of the random alloy (reported in Table 3.1). This points again to the general non-uniqueness of the multiscale solution due to fluctuations outside of the atomistic domain.

In Method 1, the initial reference atomic positions $\mathbf{r_A}$ are those of the *relaxed* sample, not the perfect lattice sites. The continuum domain is then constructed as usual, but with the initial interface nodes $\mathbf{r_C} = \mathbf{r_I}$ on the true initial interface atom positions, again not perfect lattice positions. It is also convenient, although not necessary, to use the true initial pad atom positions as nodes in the continuum, $\mathbf{r_C} = \mathbf{r_P}$, to avoid interpolation. The continuum domain, including the pad region, is still assigned the macroscopic elastic properties of the infinite true random alloy (the A-atom potential is not used).

By construction, this method creates zero spurious forces or displacements under zero load. The initial atomistic structure and pad are already in equilibrium from the start. Under an applied load, the elastic response of the pad is not exactly that of the true underlying random alloy and hence spurious stresses do arise. This is analogous to the situation depicted in Figure 3.6 for an ensemble of linear springs with randomized spring stiffnesses. We show next that the spurious stresses are small.

The spurious stresses under load using Method 1 are studied using the same geometry as in Figure 3.1. We study three different fcc random alloys, a dilute solid solution Al-5%Mg, a moderate-concentration solid solution Ni-15%Al, and again the medium-entropy alloy FeNiCr, all described by EAM potentials[78, 80, 81]. The continuum domain is meshed to atomistic resolution for accuracy (as in Section 3.1). A complementary fully atomistic problem is also constructed as a reference. This reference has exactly the same atomistic configuration as the multiscale model in the atomistic plus pad regions. The additional atoms in the continuum domain are taken from the original large “reference" sample from which the atomistic plus pad region is extracted. A uniaxial displacement corresponding to strain ε_{zz} is imposed on both the multiscale and atomistic reference systems as described in Section 3.1. Both systems are then relaxed to equilibrium (zero forces on all degrees of freedom) as described also in Section 3.1.

The spurious stresses in the atomistic domain caused by the a/c coupling are obtained again as the difference in atom-by-atom atomic virial stresses in the multiscale and reference systems ($\Delta\sigma_i = \sigma_i^{a/c} - \sigma_i^{ref}$). The planar average and standard deviation in each plane of atoms are then computed. In the continuum domain, spurious stresses are estimated as the difference between the nodal stresses computed from the stress states of the surrounding elements and the elastic prediction of the continuum stress, i.e. $\Delta\sigma_i = \sigma_i^{a/c} - \mathbf{C}\varepsilon$. Figure 3.9 shows $\Delta\sigma_{zz}^{m}$ and $\Delta\sigma_{zz}^{std}$ for a number of different realizations of each of the three random alloys under a uniaxial strain of $\varepsilon_{zz} = 0.1\%$. For all cases, the long-range spurious stresses are less than 5 MPa in both atomistic and continuum domains. Such an error is negligible for realistic problems involving cracks and dislocations in random alloys. The planar standard deviation $\Delta\sigma_{zz}^{std}$ is large very near the a/c interface but decreases below 5 MPa beyond a few atomic/nodal planes away from the a/c interface. Thus, the strain-induced deviations in local atomic environments lead to only small force errors that do not propagate significantly into the bulk of the multiscale specimen. Similar stress levels, or smaller, exist for smaller applied strains. Method 1 is thus deemed successful for accurate multiscale modeling of random alloys.

We note that at higher applied strains, approaching 1.0%, errors arise simply due to the linear elastic approximation (in the continuum) to the true non-linear response of the material. Even in a single-atom (non-alloy) material, deviations between the multiscale method and a full atomistic model arise at strain levels of 1.0%. These errors can be avoided/minimized by using a non-linear continuum. The easiest approach is to use the A-atom potential and the Cauchy-Born rule, following the guidelines of the Quasicontinuum Method but in a force-based setting. Alternatively, the size of the atomistic domain can simply be expanded so that the strains in the continuum domain are below 0.1%; this is not possible in the simple uniaxial geometry considered here.

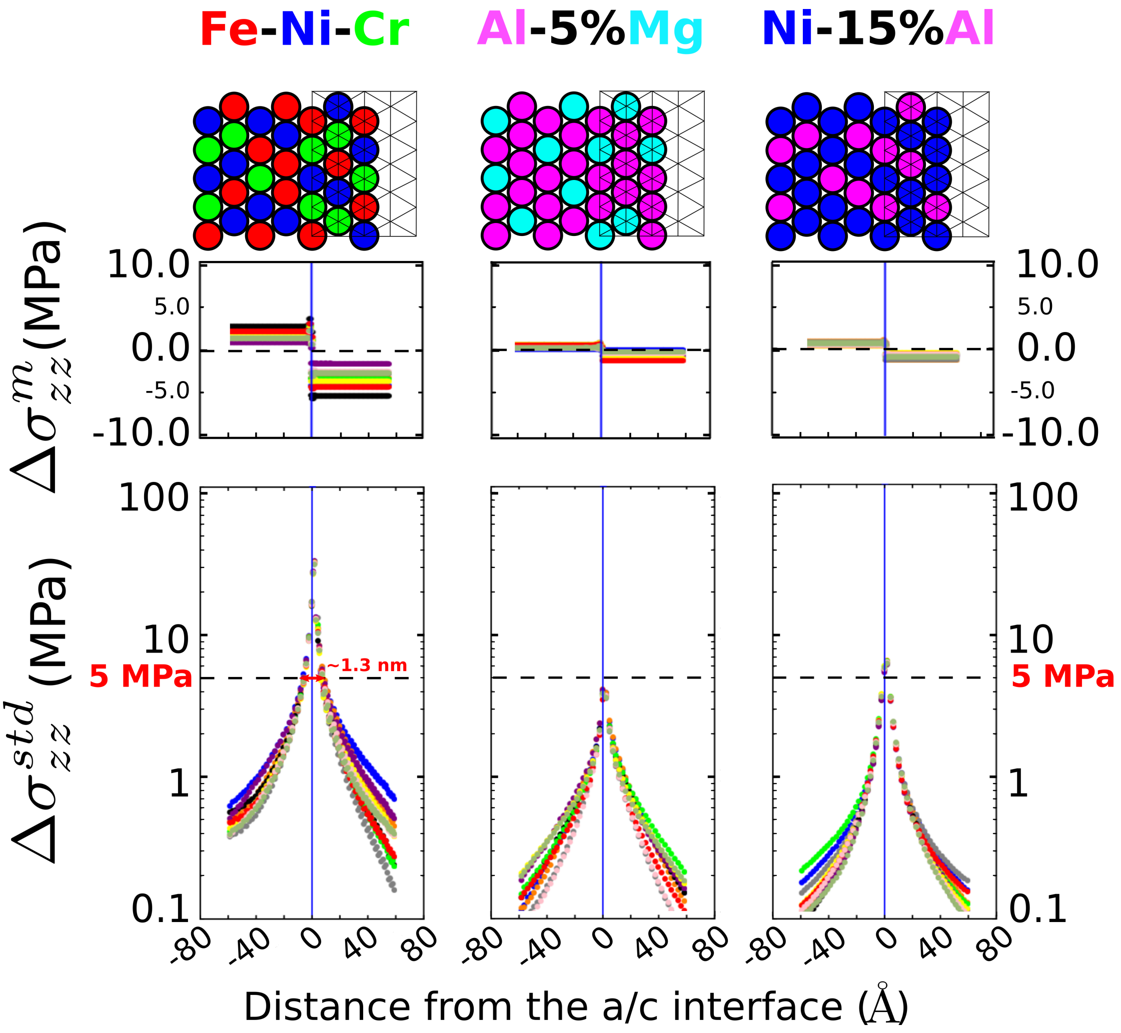

Figure 3.9 – **Method 1: results at $\varepsilon_{zz} = 0.1\%$** Coupling-induced spurious stresses for the normal component ($\Delta\sigma^{m}_{zz}$ and $\Delta\sigma^{std}_{zz}$) as a function of distance from the a/c interface, for test specimens of three types of random alloys stretched uniformly by 0.1% along coupling direction. For each alloy, results for 10 different realizations are shown as indicated by the various colors.

Note that Method 1 did not require assigning atomistic stiffness (of the pad atoms) to the continuum pad nodes, which was proposed in Figure 3.7a for the case of linear springs in Section 3.2. Such a correction will require calculation of the Hessian matrix for the pad atoms which is cumbersome and computationally expensive, and by doing so we will just gain marginally in accuracy since the errors without this correction are already negligible, ~ 5 MPa. This is an interesting and fortuitous aspect of this method.

It is also noteworthy that in Method 1 we have essentially moved the random/homogeneous transition away from the a/c interface, to the continuum domain.

3.3.2 Method 2

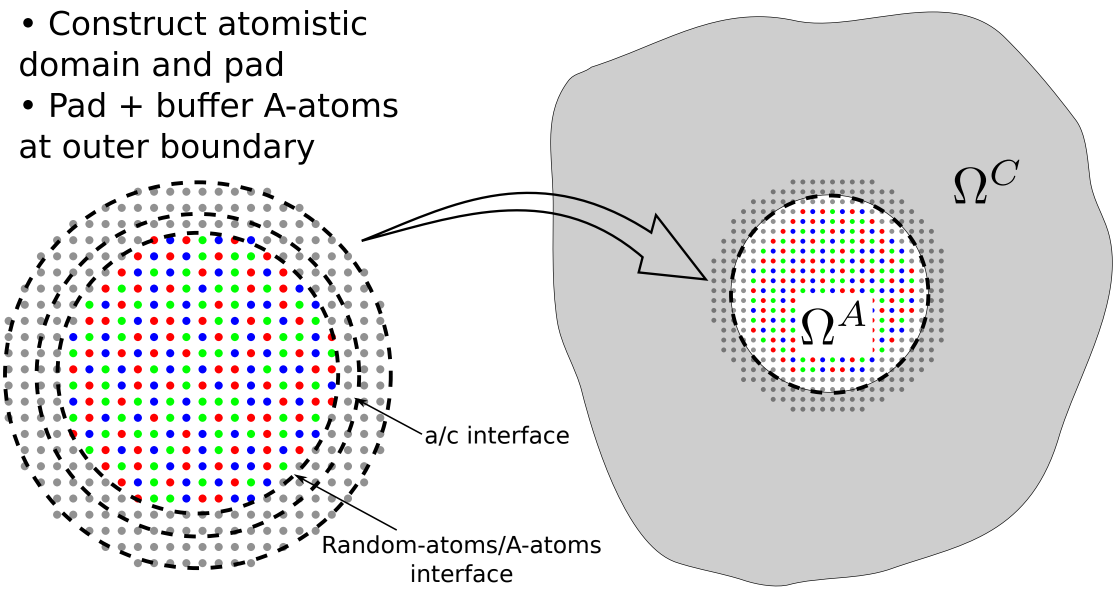
• Construct atomistic domain and pad
• Pad + buffer A-atoms at outer boundary
Ω^C
Ω^A
a/c interface
Random-atoms/A-atoms interface

Figure 3.10 – **A/C coupling in random alloys: Method 2** The random/homogeneous interface and the atomistic/continuum interface are separated by the introduction of a small buffer zone of A-atoms in the atomistic domain, with the pad atoms being A-atoms.

Since errors at the a/c interface arise due to having both the atom/continuum and random/homogeneous transition at the same physical location, another approach to minimizing errors is to separate these two transitions explicitly. Method 2 accomplishes this as schematically illustrated in Figure 3.10. Unlike Method 1, this method shifts the random/homogeneous transition towards the atomistic domain. In this method, the atomistic domain consists of the desired random alloy region surrounded by a few layers of A-atoms forming a thin buffer layer at the boundary of the atomistic domain; the pad is constructed with A-atoms. The A-atoms used in this method are corrected to match the true random alloy lattice constants (Table 3.2). All atoms including the pad atoms are initialized at the average crystalline lattice sites. The transition from random atoms to A-atoms thus occurs just before the a/c interface in the atomistic domain and is therefore handled fully atomistically. All these atoms in the atomistic domain can relax fully in response to the atomistic forces on each atom. The a/c interface is now identical to that of a single-element material, but using the A-atoms appropriate to the random alloy. Since the a/c interface is in the A-atom matrix we do not expect any spurious forces at the a/c interface. The continuum domain is handled in the usual manner, using the elastic constants of the random alloy (reported in Table 3.1). This method is inspired by the solution discussed for linear springs in Figure 3.7.

Method 2 does not require any initial reference sample from which the atomistic domain is sampled. The inner random alloy region in the atomistic domain can be changed to any other realization with no other changes to the overall multiscale implementation. This facilitates testing of different realizations of the atomistic domain. As in Method 1, the effects of fluctuations due to surrounding random atoms that arise in a fully atomistic simulation are lost due to the continuum approximation and the use of the A-atom buffer and pad atoms.

We quantify the magnitude and extent of any spurious stresses in Method 2 using the same displacement-controlled tensile tests as in Section 3.3.1 and with the same alloys. The only difference is in the construction of the multiscale sample as presented above. A complementary fully atomistic problem is also needed. In this case, the reference atomistic system is a bimaterial consisting of exactly the same random alloy region plus the A-atom buffer of the atomistic domain, plus A-atoms in the continuum domain. The spurious stresses in the atomistic domain are again computed as the difference in atomic virial stresses. In the continuum domain the spurious stresses are the differences of the nodal stresses of the coupled problem versus the virial stresses of the corresponding A-atoms at the same nodal sites. A planar average and standard deviation are again computed.

Figure 3.11 shows the spurious stresses for Method 2 under zero applied strain when using A-atoms at the a/c interface ($\mathbf{r_I}$) and just one additional layer of A-atoms in the atomistic domain. There is again negligible long-range stress $\Delta\sigma_{zz}^{m}$, typically 5 MPa or less, due to this coupling method. The standard deviation $\Delta\sigma_{zz}^{std}$ is larger at the interface, around 100 MPa, but decreases to below 10 MPa within just a few atomic/nodal planes and then below 5 MPa within ±20Å from the a/c interface. These errors could have small consquences for defects approaching the a/c interface, but remain fairly small. The errors arise because the random alloy distorts the A-atom matrix near the random/A-atom interface by 2-3%. The proximity of the a/c interface to this highly strained zone thus gives rise to spurious stresses since the continuum deformation is formulated with linear elasticity.

The spurious stresses can be reduced further by addition of just one more layer of A-atoms inside the atomistic domain (results not shown here). The difference in $\Delta\sigma_{zz}^{m}$ in the two domains then reduces further by ≈ 80%, 70% and 100% for FeNiCr, AlMg, NiAl respectively. The improved results come at the cost of additional atoms in the system, but this cost may be acceptable if deemed necessary for any given problem.

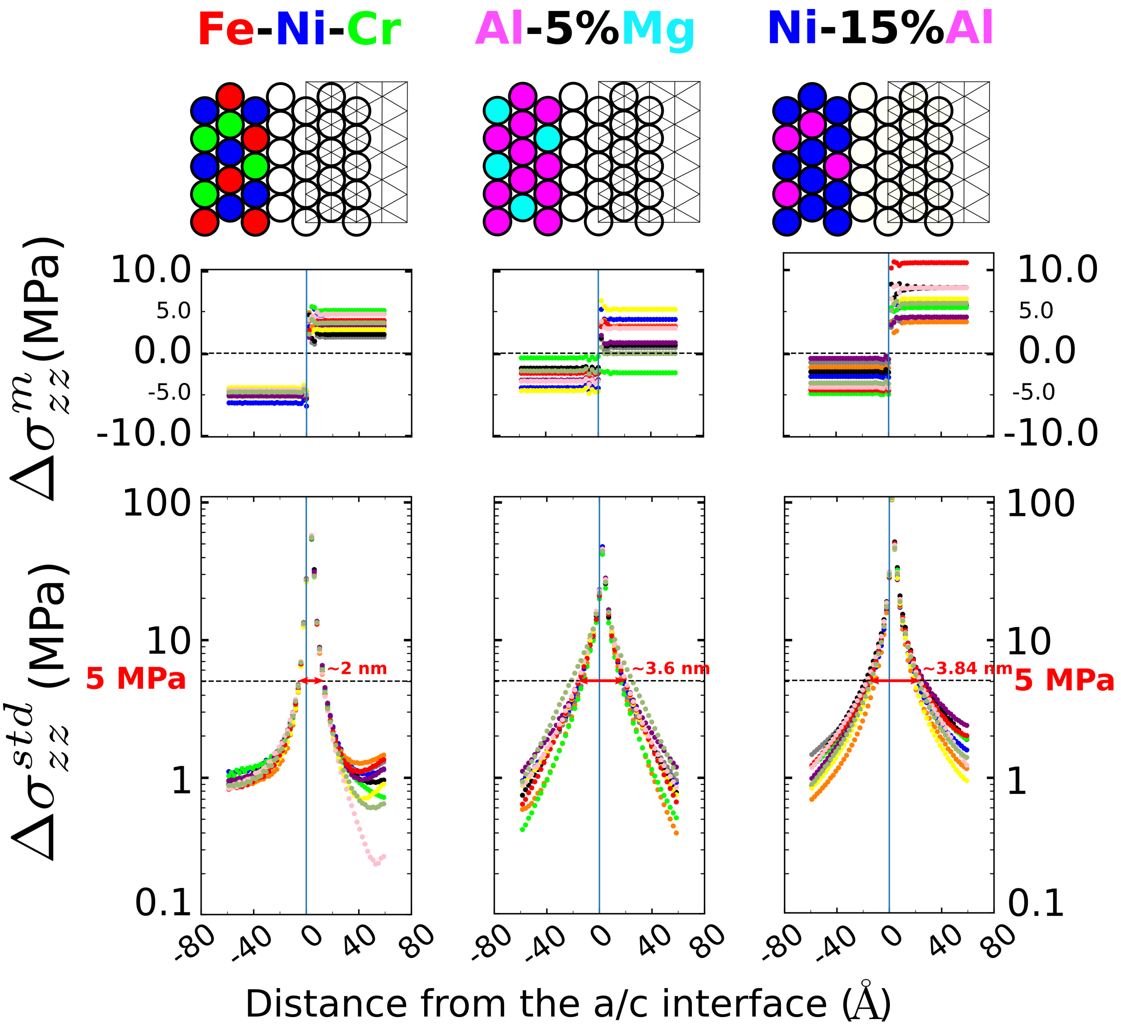

Figure 3.11 – **Method 2, no imposed deformation** Coupling-induced stress statistics of the normal component of spurious stress along coupling direction ($\Delta\sigma_{zz}^{m}$ and $\Delta\sigma_{zz}^{std}$) as a function of distance from the a/c interface, for test specimens of three random alloys with z-ends held fixed. For each alloy, results for 10 different realizations are shown as indicated by the various colors.

Under an applied uniaxial strain of $\varepsilon_{zz} = 0.1\%$, the spurious stress levels and trends are barely changed with respect to no loading, as shown in Figure 3.12. The adaptability of the A-atoms in the fully atomistic domain is evidently sufficient to prevent any deformation-induced errors. Comparing Figures 3.9 and 3.12, for Methods 1 and 2 under load respectively, Method 1 remains slightly better than Method 2. Nonetheless, we deem both methods to have acceptable errors.

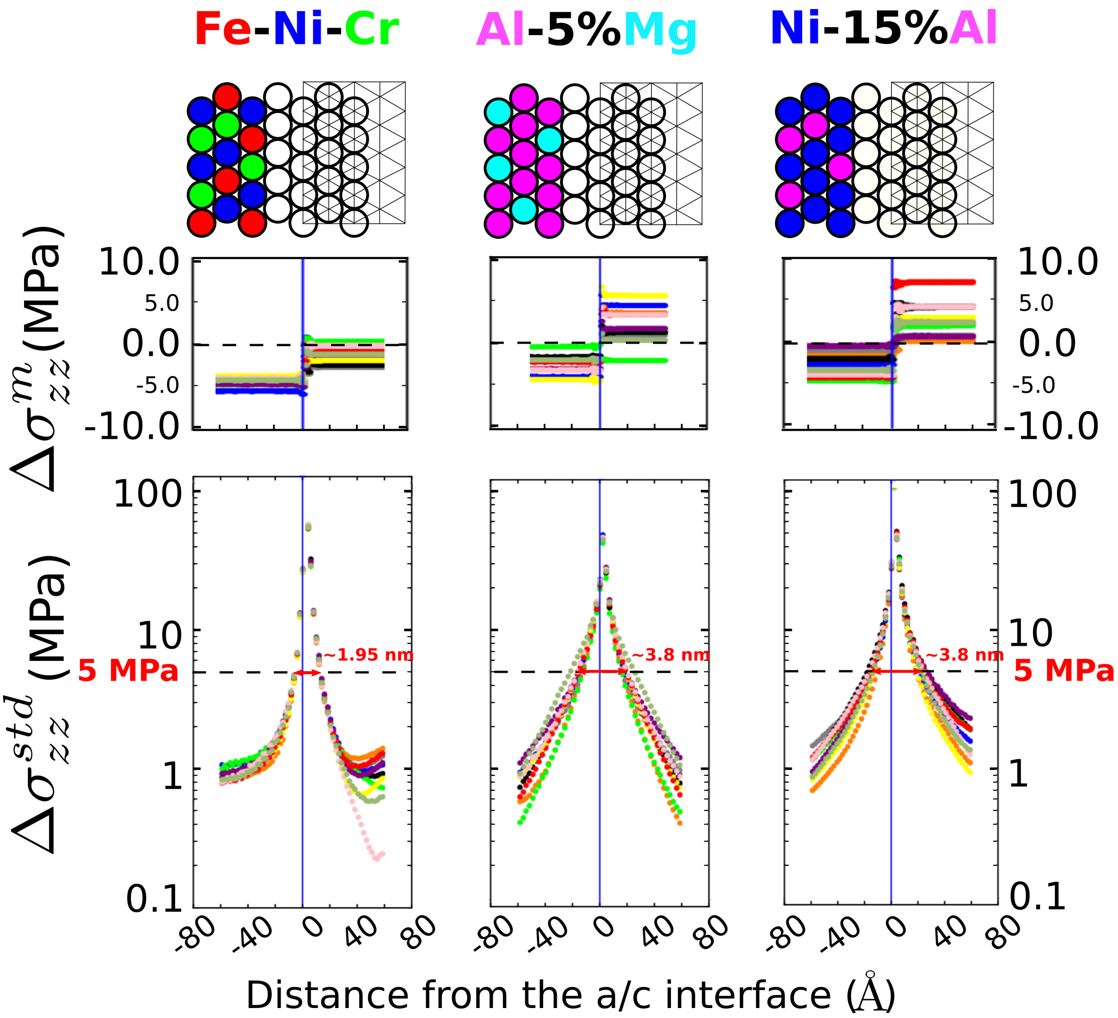

Figure 3.12 – **Method 2, results at $\varepsilon_{zz} = 0.1\%$** Coupling-induced stress statistics of the normal component of spurious stress along coupling direction ($\Delta\sigma_{zz}^{m}$ and $\Delta\sigma_{zz}^{std}$) as a function of distance from the a/c interface, for test specimens of three random alloys stretched uniformly by 0.1% along coupling direction. For each alloy, results for 10 different realizations are shown as indicated by the various colors.

It is evident from comparison of Figures 3.11 and 3.12 that the slightly different elastic constants of the tweaked A-atoms, compared to those of the random alloy, do not introduce considerable errors on deformation of the test specimens. This is rather obvious given the thin (two atomic layers thick) dimension of A-atom buffer in the atomistic domain.

Finally, we note that for Method 2 the dilute alloys have larger spurious stresses than the medium-entropy alloy and the $\Delta\sigma_{zz}^{std}$ also falls off more slowly for the dilute alloys. This can be attributed to the fact that the A-atoms for a dilute alloy mostly resemble the host atoms and the low-concentration (well-separated) solute atoms at the real-atom/A-atom interface heavily distort the homogenous A-atom region locally. This results in localised highly strained regions at the a/c interface and therefore causes large spurious forces. In the medium-entropy alloy, the A-atom potential is not biased towards any one constituent atom type, hence the A-atom region near the real-atom/A-atom interface is less distorted, resulting in small spurious forces at the a/c interface. In medium-entropy alloys, the local solute environments changes rapidly, therefore the fluctuation in spurious stresses dies down rapidly away from the a/c interface.

3.4 Discussion

Two methods for a/c coupling of random alloys have been proposed and validated here. The methods differ in the way in which fluctuations outside of the atomistic domain are incorporated. In Method 1, the initial atomic arrangement of atoms in atomistic domain and pad is specific to the reference sample from which they are extracted. However after relaxation the system loses memory of the large reference sample to some extent since a continuum with average stiffness of the alloy replaces the problem domain outside the atomistic region. In Method 2, an atomistic configuration, unrelaxed, is directly inserted into the atomistic domain, and all compositional fluctuations outside of this domain are explicitly discarded with A-atoms. The predictions of Methods 1 and 2 for the same inner atomistic realization of random atoms will therefore be slightly different.

Useful connections has been drawn between 1D force-based couple of linear springs and 3D a/c coupling of random alloys with nonlinear many-body interactions. The errors due to coupling can be easily rationalized with the simple force-based couple of linear springs and the solutions for this simple 1D problem captures the essence of the Methods proposed in Section 3.3 for the accurate 3D a/c coupling of random alloys with complex interatomic interactions.

In random alloys, any definitive study will require the use of multiple realizations of the atomistic domain. Analysis will then be required to extract the dominant composition-dependent effects (the average behavior) and the fluctuation effects due to the specific random realizations. We speculate that the average behavior will not be significantly different when using Methods 1 and 2 whereas the fluctuations might be larger for Method 1. As with all multiscale models, increasing the size of the atomistic domain will lead to more accurate results. In the case of random alloys, the larger sizes also accommodate more fluctuation effects surrounding the central domain where complex atomistic phenomena are taking place.

We do not specifically recommend either Method 1 or 2 preferentially. Method 1 has some overhead in the creation of the specific atomistic domain. However, multiple atomistic samples can be extracted from one very large periodic reference problem, so the overhead might be reduced at a given alloy composition. Method 2 is easy to use — different realizations are simply inserted into the inner atomistic domain at the initial perfect lattice positions, with the A-atom buffer, pad region, and FE domain unchanged. The computation of the A-atom potential is very easily done, and retains the EAM form so that implementation is trivial. Thus, if the lattice constants and elastic constants of the A-atom potential are assumed to be sufficiently accurate, there is no need to perform any large periodic reference samples; however, we recommend validation of the A-atom properties. More importantly, Method 2 is accomplished by straight-forward adaptation of the standard force-based a/c coupling; only the atomistic domain (including pad) are replaced by the random atoms and A-atoms, with the a/c interface inside the A-atom region. Method 2 is also directly amenable to extension to non-linear deformation in the continuum via application of the Cauchy-Born rule to the A-atom unit cell, as in the QC method. Method 2 is slightly more costly, however, due to the additional buffer of A-atoms. Since we have shown that just one layer of buffer atoms is needed for reliable coupling, this additional cost of Method 2 is moderate (a 3d atomistic domain of N^3 atoms becomes an atomistic domain of $(N+2)^3$ atoms, thus adding $\approx 6N^2$ atoms to the original N^3).

Regarding accuracy, we have shown that the methods create spurious stresses on the order of 5 MPa across several classes of random alloys. The 3D simulation cell we used in Section 3.3 with a single non-periodic direction normal to the a/c interface, is the worst-case geometry (of an infinite slab) where the long-range stresses propagate unattenuated across the thickness of the slab — since coupled problem is effective 1D (in the non-periodic direction) and 1D elastic Greens function has infinite range. In alloys, stresses of 5 MPa are rather smaller than the stresses required to move dislocations through the alloy. While the Peierls stresses for the pure elements (e.g. Al, Ni, Cu) are on the order of 1–20 MPa, the yield strengths of the solid solution alloys are significantly higher at moderate concentrations (Al-5%Mg strength of ~ 80 MPa, for instance, and ~ 300 MPa in FeNiCr). Thus, 5 MPa stress levels will not significantly affect dislocation motion. Dislocation interactions with grain boundaries typical involve stress levels of hundreds of MPa, so that again 5 MPa is negligible. Such stress levels acting on a crack in a standard K-test geometry will create negligible additional stress-intensity. There are many other cases, of course, but these examples suggest that the errors in the present coupling method are sufficiently small.

The present methodology applies to random alloys. Many alloys can exhibit short-range-order (SRO) due to specific atom-atom interactions and under suitable processing conditions of time and temperature [82–85]. Alloys susceptible to SRO can also exist in the random state, and be directly amenable to the methods here. However, even alloys with SRO can be studied with our a/c coupling methods. First, all alloys, with or without SRO, have macroscopic average lattice constants and elastic constants that can be computed using large-scale simulations ([86]). Thus, Method 1 is directly applicable to alloys with SRO using the computed macroscale properties in the continuum domain, and with the “pad" region conforming to the same SRO as the atomistic region (the two regions are generated together). Method 2 is not directly applicable because the average atom potential is derived for an explicit random alloy. Extension of the average atom method to alloys with SRO may be possible but this has not been studied. However, the differences in elastic and lattice constants between the SRO alloy and the random alloy may be small[87], enabling the use of an adjusted average atom potential to match the precise properties of the alloy with SRO. In such a case, the average atom pad and buffer domain will remain represented by the random alloy, introducing a small mismatch in local properties in this region. Thus, application of Method 2 would have some additional error. Overall, the multiscale modeling of alloys with SRO is beyond the scope of this thesis but merits further study as the investigations of atomistic behaviour in complex alloys becomes of increasing importance.

The present methods are for force-based a/c coupling. Similar concepts can be applied to energy-based a/c coupling such as the Quasicontinuum Method. In QC-like methods, we would not expect spurious long-range stresses. However, the QC method will generate ghost-forces, and hence spurious displacements, near the a/c interface. In random alloys, such spurious displacements may lead to spurious fields that extend further into the atomistic domain, in contrast to elemental materials where the errors are localized; this remains to be examined. The strength of QC — adaption of the atomistically-resolved domain as defects form and move through the structure [88] — becomes much more challenging in random alloys, especially for problems involving dislocations. In random alloys, the strengthening due to solutes comes from solute fluctuations in a domain extending well outside the dislocation core. Hence the sizes required for proper atomistic resolution of the dislocation cores may quickly become large and computationally expensive. In contrast, the force-based coupling here enables additional multiscale methods, in particular the Coupled Atomistic/Discrete Dislocation method (CADD), recently extended also to full 3d [17–19], where dislocations can exist in the continuum domain as discrete dislocations without atomistic resolution. The continuum dislocations must be informed about the appropriate effective Peierls stress due to solute strengthening, but this is mainly a calibration issue along with other calibrations of discrete-dislocation methods.

In summary, random alloys are an important class of structural materials where crucial behavior is controlled by the atomic scale structure and motion of defects through the lattice of random atoms. Thus, extending multiscale a/c coupling methods to random alloys is desirable. Here, we have presented and validated two force-based methods for a/c coupling of random alloys. We have further discussed the various subtle issues, mainly associated with fluctuations in local composition, that are unique to random alloys and that influence the formulation and application of multiscale models. The two methods here present no difficulties in implementation beyond those of existing standard methods, and so can be incorporated into existing multiscale codes with relative ease. These methods thus open avenues for accurate and efficient study of mechanics boundary value problems in random alloys for problems where it is essential to capture atomistic phenomena in some localized region of the sample.

Theory of Solute Strengthening Part II

Scientific and technological interest in both dilute solute-strengthened alloys (Al-Mg, Mg-Y, Ni-Al, and many others) and the high-entropy alloys (HEAs), which are essentially high-concentration solute-strengthened materials, has led to the development of a general theoretical model by Leyson et. al [31, 32] to predict solute strengthening in random alloys [31, 32]. This theory is based on the motion of edge dislocations, which typically control strength — as demostrated by the application of this framework to fcc screw dislocations [89] where the critical stress to move an edge dislocation at 0K was shown to be comparable, but slightly lower than the stress to move a screw dislocation. The full theory shows that the temperature- and strain-rate dependent flow strength stems from the intrinsic solute/dislocation interaction energies and the dislocation line tension [33, 90, 91]. The solute/dislocation interaction energies are challenging to determine in real alloys, especially HEAs, due to the need for computational study of the dislocation core via first principles methods [92]. Experiments cannot provide this information directly either.

To enable the use of experimental inputs and/or first-principles inputs, the full theory has been reduced to a simpler form by Varvenne et. al through the use of linear elasticity theory to compute the solute/dislocation interaction energies [4]. The elasticity model for solute strengthening then relies on fundamental material and solute quantities: elastic constants C_{ij}, dislocation Burgers vector $\mathbf{b}$, stable and unstable stacking fault energies γ_{ssf} and γ_{usf}, dislocation line tension Γ, and the solute misfit strain tensors $\varepsilon_{ij}^{\mathrm{misfit}}$ in the alloy. However the elasticity theory of solute strengthening has only been examined within isotropic elasticity.

This part of the thesis deals with extending the Leyson's theory and the reduced Varvenne's model for solute-strengthening by relaxing the underlying assumptions of the theory. There are three chapters in this part. The first chapter extends reduced Varvenne's isotropic model to predict solute-strengthening in elastically anisotropic fcc alloys. The second chapter in this part extends the Leyson's model for random alloys to include solute-solute interactions described by pair-wise interactions. Leyson's theory assumes that the yield strength of random alloys is controlled by solute-dislocation interactions. Solute-solute interactions exist and provide the energetic driving force for both short-range and long-range order but can then also affect yield strength even in the random alloy. Finally, the last chapter of this part formulates a new strengthening theory to predict yield strength of alloys with short-range order. In the limit of no short-range order, this new theory gives the same the predictions as the original theory for random alloys.

4 Solute-strengthening in elastically anisotropic fcc alloys

Disclaimer

This chapter is adapted from the following article, with permission from the coauthors and the publisher.
S. Nag, C. Varvenne, W. A. Curtin, "Solute-strengthening in elastically anisotropic fcc alloys", *Modelling and Simulation in Materials Science and Engineering* 28, 025007 (2020).

The theory of solute-strengthening in random alloys by Leyson et. al has been introduced in Section 1.2, along with simplification in Varvenne's reduced model through the use of linear elasticity theory to compute the solute-dislocation interaction energies. However, the reduced model has only been examined within isotropic elasticity. Yet the elemental fcc metals exhibit a range of anisotropies, as characterized by the Zener anisotropy $A = 2C_{44}/(C_{11} - C_{12})$ where C_{11}, C_{12}, and C_{44} are the three independent elastic constants in a cubic crystal, with $A \sim 1.22$ for Al, ~ 2.57 for Ni, ~ 3.21 for Cu, and ~ 2.85 for Au [93]. Dilute alloys based on Ni, Cu, and Au should thus be treated within anisotropic elasticity, and many fcc HEA families (e.g. Co-Cr-Fe-Mn-Ni-Al, Rh-Ir-Pt-Pd-Au-Ag-Ni-Cu) are at least moderately anisotropic. The aim of this chapter is therefore to provide general results for solute-strengthening in the anisotropic elastic reduced model for fcc random alloys.

The isotropic theory is useful in the sense that it has a simple analytic form of the dislocation pressure field needed to calculate the solute-dislocation interaction energies [4] and experimental measurements may only provide averaged isotropic elastic constants. Therefore, in the chapter results are presented in terms of the difference in predictions between anisotropic and isotropic models. We show that both elasticity assumptions lead to qualitatively identical results, which enables the use of the isotropic model with a correction factor to account for estimated or anticipated anisotropy. Our results also allow for an understanding of whether the isotropic estimate is an underestimate or an overestimate, and to what approximate degree. Overall, predictions using the full anisotropic theory and isotropic theory using the Voigt averaged isotropic moduli are in very good agreement (within a few %) over a wide range of anisotropy ratios, $0.5 < A < 4$.

The remainder of this chapter is organized as follows. Section 4.1 presents the reduced model for both anisotropic and isotropic elasticity assumptions. In Section 4.2, predictions of isotropic and anisotropic models over a wide range of parametric dislocation core structures are compared. Section 4.3 discusses how to apply the theory with limited experimental or first-principles properties. Section 4.4 summarizes the chapter.

4.1 Linear elasticity model

The key quantity in Leyson's model of solute-strengthening is the characteristic energy fluctuation per unit length of dislocation $\Delta\widetilde{E}_{\mathrm{p}}(w)$ (Section 1.2), which is defined as follows,

$$\Delta\widetilde{E}_{\mathrm{p}}(w) = \left[\sum_n c_n \sum_{ij} \left(U^n_{sd}(x_i - w, y_j) - U^n_{sd}(x_i, y_j)\right)^2\right]^{\frac{1}{2}}, \tag{4.1}$$

where w is the dislocation roughening amplitude in a random alloy, c_n is the concentration of the solute of type n and U^n_{sd} is the interaction energy between a solute of type n at in-plane position (x_i, y_j), and a straight dislocation aligned along z at the origin.

The theory then predicts (1) the zero-temperature yield stress τ_{y0}, (2) an associated zero-stress energy barrier ΔE_b, and (3) a temperature T and strain-rate $\dot{\epsilon}$ dependent flow stress, for a fcc random alloy using the following relations,

$$\Delta E_b = 1.22\left(\frac{w_c^2\Gamma\Delta\widetilde{E}_{\mathrm{p}}^2(w_c)}{b}\right)^{\frac{1}{3}} \tag{4.2a}$$

$$\tau_{y0} = \frac{\pi}{2}\frac{\Delta E_b}{b w_c \zeta_c} = 1.01\left(\frac{\Delta\widetilde{E}_{\mathrm{p}}^4(w_c)}{\Gamma b^5 w_c^5}\right)^{\frac{1}{3}} \tag{4.2b}$$

$$\tau_y(T,\dot{\epsilon}) = \tau_{y0}\left[1 - \left(\frac{k_{\mathrm{B}}T}{\Delta E_b}\ln\left(\frac{\dot{\epsilon}_0}{\dot{\epsilon}}\right)\right)^{\frac{2}{3}}\right] \tag{4.2c}$$

where w_c is the characteristic roughening amplitude of a dislocation in a random alloy. Γ and b are the dislocation line tension and the Burgers vector magnitude of an edge dislocation. $\dot{\epsilon}_0 \sim 10^4/s$ and k_{B} are a reference strain rate and Boltzmann's constant, respectively.

The solute-dislocation interaction energies $U^n_{sd}(x_i, y_j)$ can be computed using intensive first-principles methods [31–33, 94] for dilute alloys. Atomistic simulations using semi-empirical potentials can be employed, but are rarely quantitative for real materials and so such simulations are best used to test the theory and any approximations to it. It is thus valuable to gain broad insight through the introduction of reasonable approximations that enable great simplification of the theory.

4.1.1 Anisotropic elasticity for solute/dislocation interactions

In linear elasticity, the solute/dislocation interaction energy is

$$U^n_{sd}(x_i, y_j) = p(x_i, y_j)\Delta V_n, \tag{4.3}$$

where $p(x_i, y_j)$ is the pressure field created at position (x_i, y_j) by the dislocation centered at the origin. The above expression is specific to substitutional solutes in cubic materials; the general form involves the contraction of the stress tensor and the solute misfit strain tensor [38, 95–97] and is straightforward. Note that solute interactions with the stacking fault of the dissociated fcc dislocation are neglected here — see Varvenne et al. [33] for their inclusion and, when considering plastic flow at moderate temperatures, there is no solute diffusion to the stacking faults (and so no Suzuki effect). The pressure field of the dislocation depends on the dislocation core structure. The dislocation structure is characterized generally by the distribution of Burgers vector $\partial\mathbf{b}/\partial x$ along the glide plane; we discuss analytical descriptions of the core structure later. The pressure field generated by the dislocation structure is then a function of the Burgers vector distribution and the alloy elastic constants, and can be written in the form

$$p(x_i, y_j) = C_{44}\ f(x_i, y_j, \frac{C_{11}}{C_{44}}, A, \frac{\partial\mathbf{b}}{\partial x}), \tag{4.4}$$

where f is a dimensionless pressure field. f is obtained from the fundamental Stroh solution $\sigma^{\text{Stroh}}_{ij}$ for the components of the stress field (refer Section 2.6) created by an incremental Burgers vector $d\mathbf{b}(x')$ in an anisotropic material [98], followed by superposition of the fields due to all the increments of Burgers vector. Specifically, we can write

$$f(x_i, y_j) = \frac{1}{C_{44}}\int_{-\infty}^{\infty} \frac{\partial\sigma^{\text{Stroh}}_{kk}}{\partial\mathbf{b}}(x_i - x', y_j)\frac{\partial\mathbf{b}}{\partial x}(x')dx'. \tag{4.5}$$

Substituting the above approximation for $U(x_i, y_j)$ into all of the prior results leads to a decoupling of the solute misfit volume and the dislocation fields. The key energy quantity in Equation 4.1 becomes

$$\begin{aligned}\Delta\widetilde{E}_{\text{p}}(w) &= C_{44}\left(\sum_n c_n\Delta V_n^2\right)^{\frac{1}{2}}\left[\sum_{ij}\left(f(x_i - w, y_j) - f(x_i, y_j)\right)^2\right]^{\frac{1}{2}}, \\ &= C_{44}\left(\sum_n c_n\Delta V_n^2\right)^{\frac{1}{2}} g\left(w, \frac{C_{11}}{C_{44}}, A, \frac{\partial\mathbf{b}}{\partial x}\right).\end{aligned} \tag{4.6}$$

The minimization with respect to w to obtain w_c involves only the dislocation-core-structure-dependent quantity g via the solution of $dg/dw = g/2w$ (refer Section 1.2). The final quantities controlling the flow stress versus temperature and strain rate reduce to the forms

$$\Delta E_b = 1.22\left(w_c\ g\left(w_c\right)\right)^{\frac{2}{3}}\left(\frac{C_{44}^2\Gamma}{b}\right)^{\frac{1}{3}}\left(\sum_n c_n\Delta V_n^2\right)^{\frac{1}{3}}, \tag{4.7}$$

$$\tau_{y0} = 1.01\left(\frac{g^4\left(w_c\right)}{{w_c}^5}\right)^{\frac{1}{3}}\left(\frac{C_{44}^4}{\Gamma b^5}\right)^{\frac{1}{3}}\left(\sum_n c_n\Delta V_n^2\right)^{\frac{2}{3}}. \tag{4.8}$$

In a dilute alloy, for a given matrix the analysis is independent of the solute(s) added to create the alloy. In a concentrated alloy, the material properties (elastic constants, line tension, Burgers vector, stacking fault energy, and core structure) are those of a hypothetical average-alloy matrix. The solute misfit volume and concentration only enter through multiplication after all minimizations have been carried out. In the elasticity theory, we can thus address the key features of solute strengthening as a function of the elastic properties of the material, the line tension, and the dislocation structure as represented through $\partial\mathbf{b}/\partial x$. For non-dilute alloys or HEAs with more than one type of solute, the dislocation structure entering the theory are those for the concentrated alloy at the given composition.

4.1.2 Solute/dislocation interactions estimated with average isotropic elastic constants

The theory can be reduced further under the assumption of isotropy, in line with Ref. [4]. Introducing the average isotropic elastic constants μ_{avg} and ν_{avg}, the quantity g can be written as

$$g\left(w, \frac{C_{11}}{C_{44}}, A, \frac{\partial\mathbf{b}}{\partial x}\right) = \left(\frac{\mu_{\text{avg}}}{C_{44}}\right)\frac{1+\nu_{\text{avg}}}{1-\nu_{\text{avg}}}\ g^{\text{iso}}\left(w, \frac{\partial\mathbf{b}}{\partial x}\right). \tag{4.9}$$

In this form, the contribution to solute-dislocation interaction energy from dislocation structure (g^{iso}) and elasticity are fully decoupled. Note that the quantity g^{iso} is equal to the quantity $\frac{1}{3\pi}\left[\sum_{ij}\Delta f_{ij}^2(w)\right]^{\frac{1}{2}}$ in Ref. [4]. All predictions scale with μ_{avg} and ν_{avg}. Here, we examine the three standard averaging schemes of Voigt, Reuss, and Hill [99–101]. For all three, the bulk modulus is

$$K_{\text{avg}} = \frac{C_{11}+2C_{12}}{3}, \tag{4.10}$$

while the shear moduli are given by

$$\mu_{\text{avg}}^{\text{Voigt}} = \frac{C_{11}-C_{12}+3C_{44}}{5}, \tag{4.11}$$

$$\mu_{\text{avg}}^{\text{Reuss}} = \frac{5C_{44}\left(C_{11}-C_{12}\right)}{3C_{11}-3C_{12}+4C_{44}}, \tag{4.12}$$

$$\mu_{\text{avg}}^{\text{Hill}} = \frac{\mu_{\text{avg}}^{\text{Voigt}}+\mu_{\text{avg}}^{\text{Reuss}}}{2}. \tag{4.13}$$

The average Poisson's ratio ν_{avg} is then computed from μ_{avg} and K_{avg} as

$$\nu_{\mathrm{avg}} = \frac{3K_{\mathrm{avg}} - 2\mu_{\mathrm{avg}}}{2\left(3K_{\mathrm{avg}} + \mu_{\mathrm{avg}}\right)}. \tag{4.14}$$

The Voigt and Reuss results are polycrystalline upper and lower bounds, respectively. The intermediate Hill average was proposed because it tends to be closer to many experimental measurements of elastic constants in polycrystals than either of the bounds. Lastly, $\mu_{\mathrm{avg}}/C_{44}$ and ν_{avg} are dimensionless functions of only C_{11}/C_{44} and the anisotropy ratio A. Therefore, comparisons between isotropic and anisotropic elasticity depend only C_{11}/C_{44}, A, the slip density $\partial\mathbf{b}/\partial x$, and the chosen isotropic averaging scheme.

4.1.3 Dislocation core structure parameterization

The strengthening parameters depend on the dislocation structure as characterized by $\partial\mathbf{b}/\partial x$. In fcc systems, the relevant $a/2\langle 110\rangle$ dislocations dissociate into two Shockley partial dislocations, $\mathbf{b_{p,1}}$ and $\mathbf{b_{p,2}}$, of $a/6\langle 112\rangle$ type. Following Varvenne et. al [4], we parameterize the dislocation core structure in terms of two Gaussian functions of width σ separated by the Shockley partial separation d_p. The classical analytical Peierls-Nabarro model yields a Lorentzian distribution [102], and atomistic simulations of the shear displacement across the glide plane show a slow decay similar to the Lorentzian function. However, the atomistic simulations give the total shear displacement, not solely the "plastic" displacement associated with the distribution $\partial\mathbf{b}/\partial x$. The slow decay in atomistics is well-represented as arising from the elastic strain due to a *Gaussian* distribution of Burgers vector $\partial\mathbf{b}/\partial x$, as shown explicitly for atomistic models of Al, Cu, and Ni in Section A.1. The Burgers vector distribution is thus parameterized as

$$\frac{\partial\mathbf{b}}{\partial x}(x) = \frac{1}{\sqrt{2\pi\sigma^2}}\left(\mathbf{b}_{\mathbf{p},\mathbf{1}} e^{-\frac{(x+d_p/2)^2}{2\sigma^2}} + \mathbf{b}_{\mathbf{p},\mathbf{2}} e^{-\frac{(x-d_p/2)^2}{2\sigma^2}}\right). \tag{4.15}$$

When carrying out the minimization with respect to w, the solution can yield one or two local minima depending on the core structure [33]. Two local minima, $w_{c,1}$ and $w_{c,2}$, emerge when d_p is sufficiently larger than σ. In such situations, the Burgers vector distribution has two very distinct peaks, one for each partial, and the first minimum occurs at small w_c typically smaller than the partial separation d_p. Also, as evident from Figure 4.1, the "second" larger $w_{c,2}$ solution exists for all parameter values, with $w_{c,2}$ decreasing with decreasing d/b. The "first solution" $w_{c,1}$ exists for larger d_p/b but is subsumed by the "second solution" below $d_p/b \approx 6$. Unfortunately, the literature seems to suggest that it is the larger-w_c solution that emerges with increasing d_p/b whereas it is really the smaller w_c that emerges as a new solution. Later on we discuss results for both solutions when they arise.

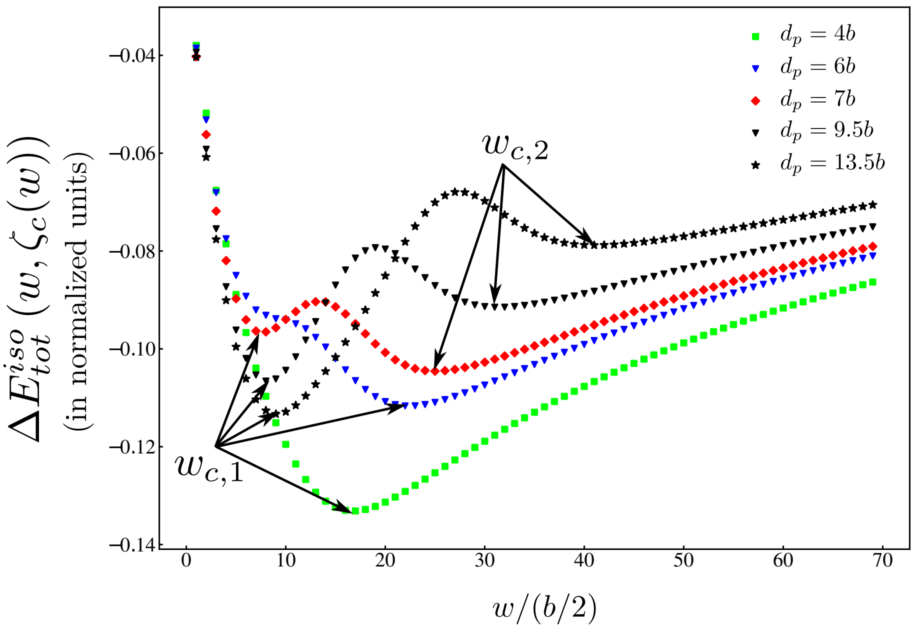

Figure 4.1 – Non-dimensional total energy of a wavy dislocation in a random alloy as a function of the amplitude, for various Shockley partial separation distances d_p at fixed partial peak width $\sigma/b = 1.5$ as computed assuming isotropic elasticity. For partial separations > $6b$, there are two minima at $w_{c,1}$ and $w_{c,2}$ while for small partial separations the first minimum is subsumed by the second minimum, resulting in a single minimum label as $w_{c,1}$.

4.2 Results

We now assess the accuracy of the easily-used isotropic model relative to the more-complex anisotropic model. Anisotropy enters in the theory through (i) the dislocation line tension, and (ii) the dislocation core structure quantity g. Both aspects are examined in the following.

4.2.1 Line tension

The line tension Γ enters the theory as $\Gamma^{1/3}$ in ΔE_b and as $\Gamma^{-1/3}$ in τ_{y0} (Equations 4.7 and 4.8), and hence results are weakly dependent on the precise value of Γ. However, the line tension scales with the elastic moduli, and so is in principle a function of the anisotropy. For fcc alloys, the line tension is best related to the shear modulus in the $< 111 >$ plane along the $< 110 >$ direction, $\mu_{111/110} = (C_{11} - C_{12} + C_{44})/3$ via the scaling relation $\Gamma = \alpha\mu_{111/110}b^2$. Values of $\alpha \sim 1/16 - 1/8$ have been used, with the larger value found in several atomistic studies of bowed-out dislocations [103]. In the presence of the crystal anisotropic elastic constants, $\mu_{111/110}$ must be appropriately estimated. Figures 4.2(a)-(c) thus displays the ratios $\mu_{\text{avg}}/\mu_{111/110}$ for the Voigt, Reuss and Hill averaging schemes, and for an important range of A and C_{11}/C_{44}. The ratio $(\mu_{\text{avg}}^{\text{Hill}}/\mu_{111/110})^{1/3}$ is nearly unity over a wide range of A and C_{11}/C_{44}, deviating by at most 5%. Thus, $\mu_{\text{avg}}^{\text{Hill}}$, which is close to the esperimental polycrystalline shear modulus, should be used in estimating the line tension. The Voigt averaged moduli should *not* be used for estimating the line tension [104].

Thus, to minimize the differences between isotropic and anisotropic results, the line tension must be calculated either directly from $\mu_{111/110}$, or from the isotropic polycrystal data.

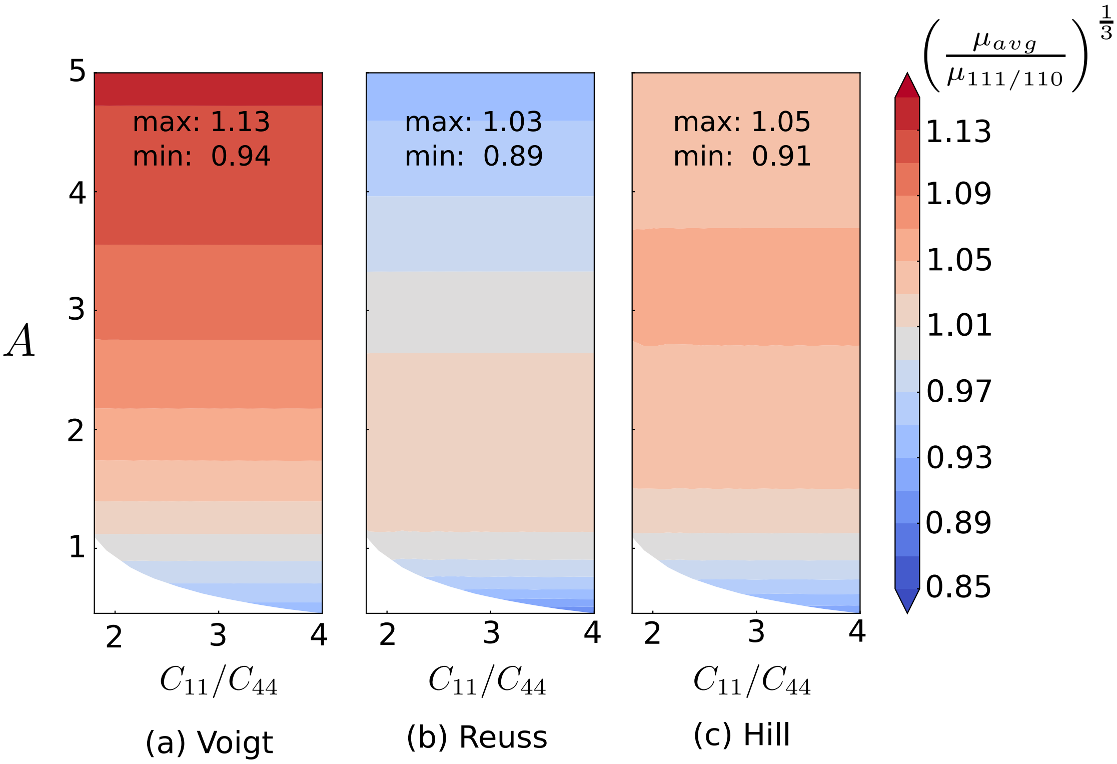

Figure 4.2 – Comparison of μ_{avg} with $\mu_{111/110}$ for the different isotropic averaging schemes as a function of C_{11}/C_{44} and A.

4.2.2 Error of the isotropic approximation

In no case does the isotropic approximation for g yield a different number of solutions for w_c than the anisotropic case. We can compute the relative error of the isotropic solution as

$$\frac{\Delta E_b^{\text{iso}} - \Delta E_b}{\Delta E_b} = \left[\left(\frac{\mu_{\text{avg}}}{C_{44}}\right)\frac{1+\nu_{\text{avg}}}{1-\nu_{\text{avg}}}\right]^{\frac{2}{3}} \left(\frac{w_c^{\text{iso}}}{w_c} \cdot \frac{g^{\text{iso}}\left(w_c^{\text{iso}}\right)}{g\left(w_c\right)}\right)^{\frac{2}{3}} - 1; \quad \text{and} \tag{4.16}$$

$$\frac{\tau_{y0}^{\text{iso}} - \tau_{y0}}{\tau_{y0}} = \left[\left(\frac{\mu_{\text{avg}}}{C_{44}}\right)\frac{1+\nu_{\text{avg}}}{1-\nu_{\text{avg}}}\right]^{\frac{4}{3}} \left(\frac{w_c}{w_c^{\text{iso}}}\right)^{\frac{5}{3}} \left(\frac{g^{\text{iso}}\left(w_c^{\text{iso}}\right)}{g\left(w_c\right)}\right)^{\frac{4}{3}} - 1. \tag{4.17}$$

The relative error is independent of (i) any absolute values of the elastic constants, (ii) the solute misfit volumes, (iii) dislocation line tension, (iv) total Burgers vector magnitude, and (v) any numerical prefactors. Thus, the results depend only on the ratios of anisotropic elastic constants, the isotropic averaging scheme (see equations 4.10–4.14) and the dislocation core structure. Note that the characteristic amplitude w_c^{iso} is independent of the isotropic averaging scheme.

These dependencies are fully described through the dimensionless elastic parameters $A = 2C_{44}/(C_{11}-C_{12})$, C_{11}/C_{44}, and core structure parameters d_p/b and σ/b. We study a wide range $0.5 < A < 5$, the full physical range of C_{11}/C_{44} for this range of A, and values $d_p/b = 3, 7, 11, 15$ and $\sigma/b = 1.0, 1.5, 2.0, 2.5$ that cover expected core structures (See Section A.1). We thus examine the range of possible errors defined in Equations 4.16 and 4.17 induced by the use of the isotropic approximation for these values.

4.2.3 Errors in energy barrier and zero-T strength

Overall, we find that the Voigt average provides the best agreement with the full anisotropic result. Indeed, Figure 4.3 presents the differences in energy barrier and strength versus A for the Voigt, Reuss, and Hill average, for a typical case ($C_{11}/C_{44} = 2.7$; $d_p/b = 7$; $\sigma/b = 1.5$). The error in the Hill result is typically twice that of the Voigt result, and of the opposite sign (negative rather than positive). Recall that the various isotropic models only differ via ratios of the dislocation pressure pre-factor $\mu_{\text{avg}}\left(1+\nu_{\text{avg}}\right)/\left(1-\nu_{\text{avg}}\right)$ (see Equation 4.9) and so results can be easily related analytically. We thus focus on the Voigt results below, which are generally the most accurate.

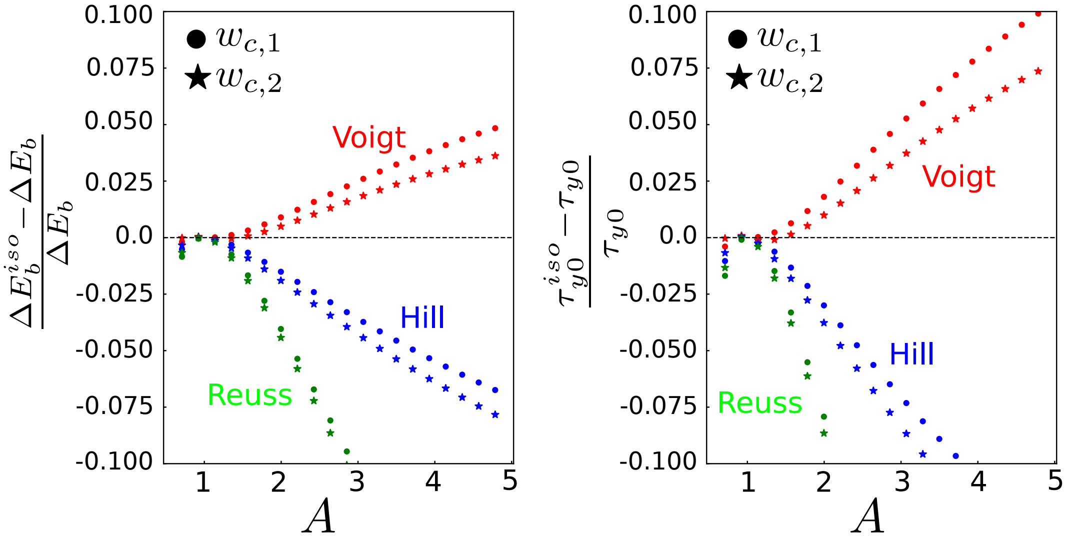

Figure 4.3 – Relative differences in ΔE_b and τ_{y0} estimated with average isotropic elastic constants versus those predicted with full stiffness tensor as a function of anisotropy ratio A (for $C_{11}/C_{44} = 2.7$ and dislocation core parameters being $d_p = 7b$ and $\sigma = 1.5b$). Results are reported for Voigt, Reuss and Hill isotropic averages. Filled circle markers: first minimum solution. Filled star markers: second minimum solution.

The differences in energy barrier and strength are very weakly dependent on C_{11}/C_{44}. Figure 4.4 presents the differences in energy barrier and strength versus A using the Voigt model for various values of C_{11}/C_{44}, again for a typical core structure ($d_p/b = 7$; $\sigma/b = 1.5$). The variations around the middle value of $C_{11}/C_{44} = 2.7$ are typically less than 1%. This is well below the accuracy of the elasticity theory itself and so can be neglected. All further results below thus correspond to $C_{11}/C_{44} = 2.7$.

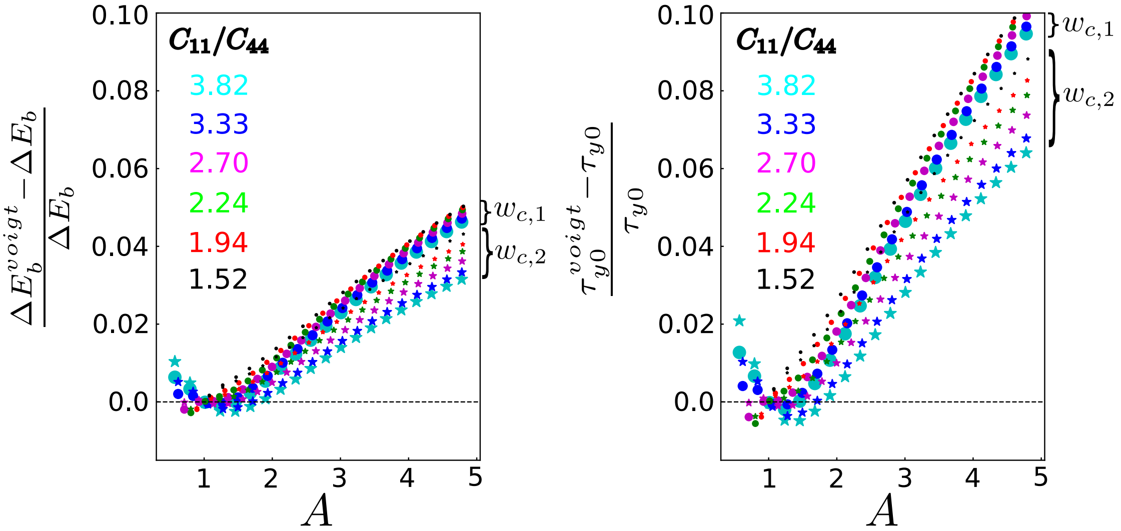

Figure 4.4 – Relative differences in ΔE_b and τ_{y0} as estimated with Voigt isotropic elastic constants versus full anisotropy as a function of C_{11}/C_{44} and anisotropy ratio (for dislocation core parameters $d_p = 7b$ and $\sigma = 1.5b$). Marker colors indicate different C_{11}/C_{44} values. Filled circles: first minimum solution; filled stars: second minimum solution.

Figure 4.5 shows the relative differences in w_c, ΔE_b and τ_{y0} between the Voigt isotropic model and the full anisotropic elasticity as a function of anisotropy A, for the first minimum $w_{c,1}$ for various dislocation core structure parameters ($d_p/b, \sigma/b$). Figure 4.6 shows the same quantities for the second minimum $w_{c,2}$. The differences in the value of w_c are zero for most cases, and differ by $\pm b/2$ in only a few cases. The difference is not systematic with σ/b, and may arise due to the discrete increments of $b/2$ used in determining the minimum energy and thus the appropriate discrete value for w_c. Specifically, a very small energy change due to the isotropic approximation can shift the discrete minimum by $b/2$; this has consequences for the energy barrier and strength. Overall, however, the amplitude of the dislocation waviness is generally well-preserved (within $b/2$) using the isotropic model.

The differences in energy barrier ΔE_b for both minima (Figures 4.5b, 4.6b) are typically positive and less than 5% over a wide range of parameters. Larger differences correlate with the changes in the w_c value by $b/2$. For the first solution ($w_{c,1}$), which controls the low-temperature behavior, the errors can be negative and reach $\approx 10\%$ but only for very high anisotropy, the narrowest core structures, and widest core separations. Overall, however, corrections to the energy barrier due to anisotropy are not significant except when the w_c is shifted by $b/2$, which occurs mainly for $\sigma/b = 1.0, 2.0$ and high levels of anisotropy.

The differences in zero-temperature strength τ_{y0} for both minima (Figures 4.5c, 4.6c) are typically positive and slightly larger than the energy barrier. For the second minimum ($w_{c,2}$) the errors are consistent across all core structures and generally remain below +5% for $A < 5$. For the first minimum ($w_{c,1}$), the error for core widths $\sigma/b = 1.0, 2.0$ and wide partial spacings $d_p/b = 15$ is over 10% error even at moderate anisotropy of $A = 2-3$. These errors correlate with the small shifts in $w_{c,1}$ by $b/2$ because the strength scales as $w_c^{-5/3}$ and $w_{c,1}$ is typically small ($\approx 5b$) so that shifts by $\pm b/2$ are not negligible. This suggests the use of a continuous w in the minimization rather than the use of a physical discrete set of w spaced by $b/2$; this would lead to continuous variation in behavior and more-precise agreement between the isotropic and anisotropic theories.

Overall, the errors when using the Voigt isotropic elastic constants are within 5% of the true anisotropic results, and typically overestimating. Deviations do increase with increasing A, but are almost always small for $A < 3$ and remain moderate for $A < 4$. We discuss the practical application of these results below.

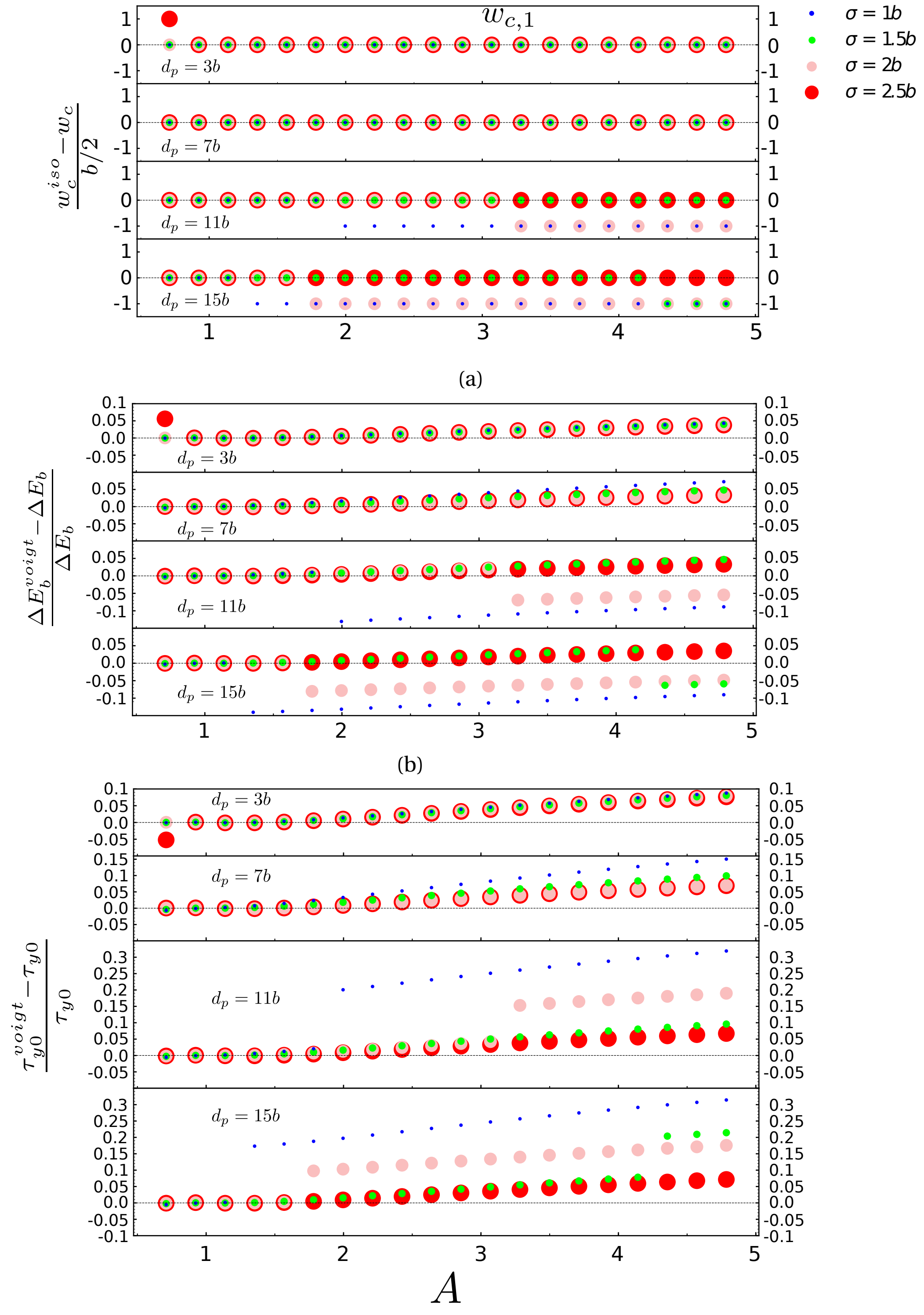

(a)

(b)

(c)

Figure 4.5 – Relative differences in (a) w_c, (b) ΔE_b and (c) τ_{y0} computed with the Voigt-averaged isotropic elastic constants versus full anisotropic results as a function of the anisotropy ratio A, for the first minimum solution.

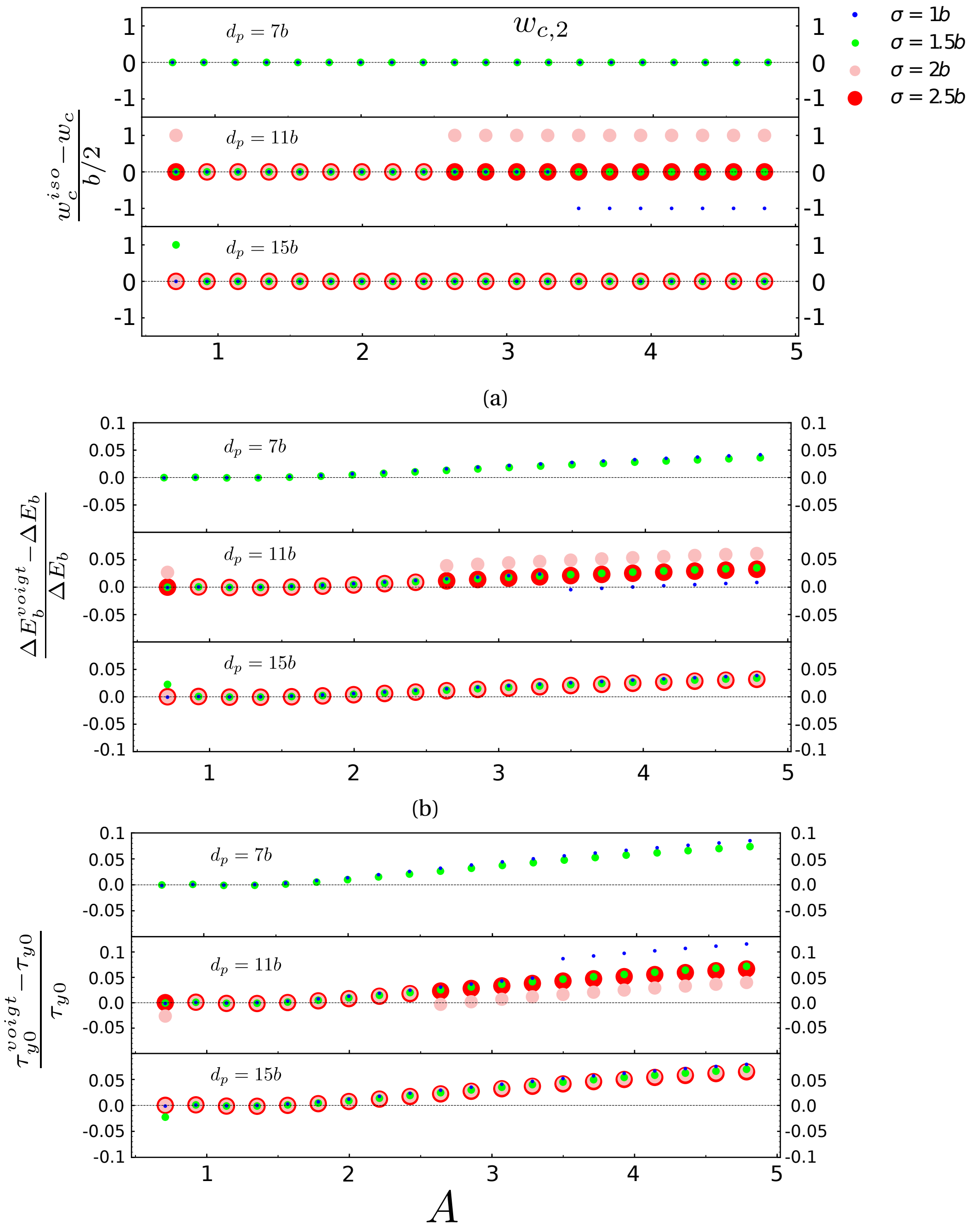

(a)

(b)

(c)

Figure 4.6 – Relative differences in (a) w_c, (b) ΔE_b and (c) τ_{y0} computed with the Voigt-averaged isotropic elastic constants versus full anisotropic results as a function of the anisotropy ratio A, for the second minimum solution. *Note that there is no second minimum solution for the wider partial spreads $\sigma/b = 2, 2.5$ when the partial separation is $7b$ since it is effectively one full dislocation undissociated.*

4.3 Practical application of the theory

We have seen that the difference between the Voigt isotropic model and the full anisotropic model are usually relatively small. The largest deviations arise when the isotropic model predicts a shift of $b/2$ in w_c relative to the full anisotropic model, which occurs almost exclusively for $\sigma/b = 1.0, 2.0$ and can thus be identified. Otherwise, we consider the errors of 5% to be well within the uncertainty of the elasticity model, relative to the full theory, and the full theory itself involves approximations. Thus, the isotropic theory can be used and then corrected to approach the anisotropic result based on available understanding. Experiments do not usually yield the Voigt moduli nor the core structure (especially σ), and application of the model also requires the line tension Γ. In this section, we therefore first present a parametric study of the predictions of the isotropic theory and then address how we envision the use of the anisotropic elasticity theory in combination with experimental or first-principles inputs.

4.3.1 Normalized results for w_c, ΔE_b and τ_{y0} using isotropic elasticity

We first present the isotropic results over the range of core structures. From Eqs. 4.7, 4.8 and 4.9, it is evident that the energy barrier and strength are functions of $w_c^{\text{iso}}(d_p/b, \sigma/b)$ and $g^{\text{iso}}(w_c, d_p/b, \sigma/b)$, with

$$\Delta E_b \propto \left(w_c^{\text{iso}} g^{\text{iso}}\right)^{2/3}, \tag{4.18}$$

$$\tau_{y0} \propto \left(g^{\text{iso}} / {w_c^{\text{iso}}}^{5/4}\right)^{4/3}. \tag{4.19}$$

Figures 4.7b and 4.7c show these normalized quantities over a wide range of $(d_p/b, \sigma/b)$ with the two solutions for w_c (where applicable). Figure 4.7a presents the $w_{c,1}$ and $w_{c,2}$, although these are not directly needed in practical application of the model.

Figure 4.7c shows that the strength quantity is quite sensitive to the partial core width σ, especially for small σ. The quantity σ, while correlated through the Peierls-Nabarro model to the unstable stacking fault energy and elastic constants of the alloy [102], is not well established. The atomistic simulations in A.1, and previous analyses in Ref. [4], indicate that a range $1.5 < \sigma/b < 2.5$ prevails across most materials. Subsequent applications of the model used the value $\sigma/b = 1.5$ across a wide range of materials with good success and we have seen above that the w_c for this value of σ/b agrees with that obtained in the full anisotropic model; this is further discussed below.

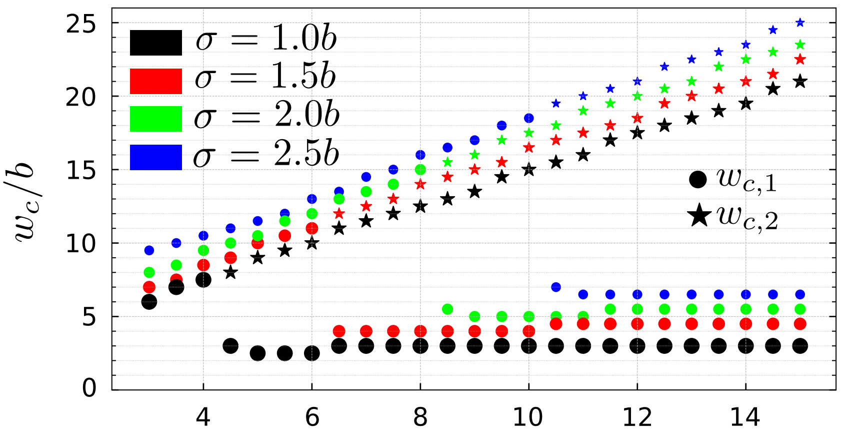

(a) Characteristic roughening amplitude w_c

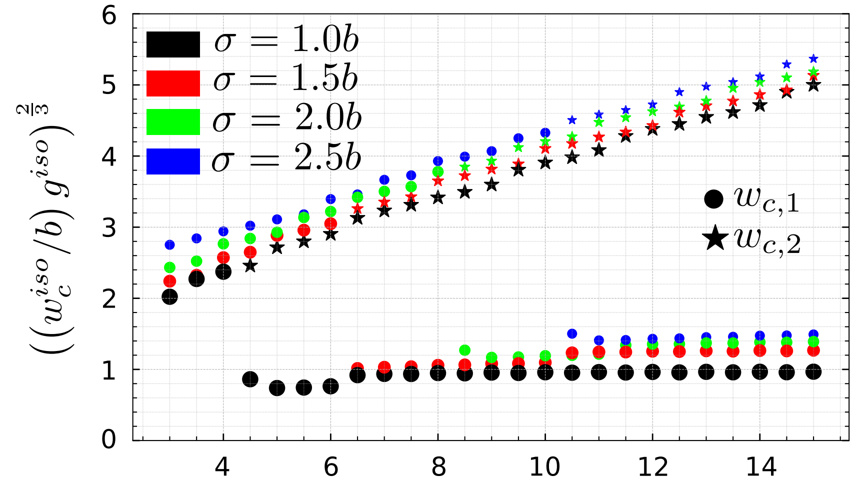

(b) zero-stress energy barrier ΔE_b

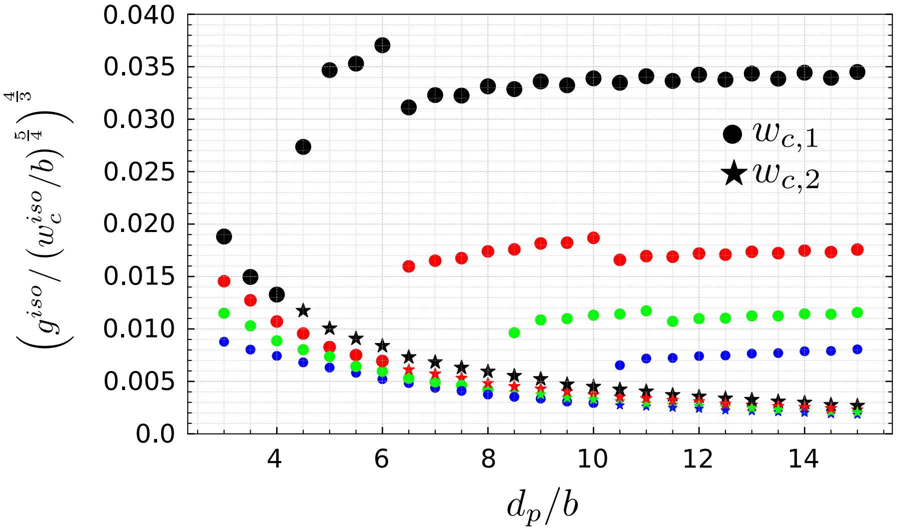

(c) T=0K yield stress τ_{y0}

Figure 4.7 – (a) Dislocation roughening amplitude w_c, (b) dimensionless ΔE_b, and (c) dimensionless τ_{y0} versus partial separation distance d_p/b, for different partial core spreading σ/b, as computed assuming isotropic elasticity.

4.3.2 Application using experimental or computational inputs

Here we provide a simple method for experimentalists and computational material scientists to investigate alloy strengthening in existing or new materials, reasonably accounting for elastic anisotropy. This is further illustrated on a specific HEA case.

In section 4.2 we have established that the dislocation line tension is well estimated as $\Gamma = \alpha\mu b^2$ using the Hill-average moduli. We have also compared the energy barrier for dislocation motion (ΔE_b) and the zero-temperature yield stress (τ_{y0}) using Voigt-averaged elastic constants versus full anisotropic stiffness tensor, and found a deviation of mostly 5% (occasionally ~ 10% for ΔE_b and ≥ 10% for τ_{y0}, but only for very high anisotropy). So, for a first estimation of the strengthening, we can avoid the cumbersome anisotropic formalism and instead make isotropic predictions $\Delta E_b^{\mathrm{Voigt}}$ and $\tau_{y0}^{\mathrm{Voigt}}$, using the Voigt-averaged elastic constants. The dimensionless coefficients of Equations 4.18 and 4.19 for ΔE_b and τ_{y0} are shown in Figure 4.7. Full results are then obtained by multiplying the dimensionless results by the appropriate prefactors using Voigt-averaged elastic constants

$$\Delta E_b \text{ prefactor:} \quad 1.22\left(\mu_{\mathrm{avg}}^{\mathrm{Voigt}}\frac{1+\nu_{\mathrm{avg}}^{\mathrm{Voigt}}}{1-\nu_{\mathrm{avg}}^{\mathrm{Voigt}}}\right)^{\frac{2}{3}}\left(\left(\sum_n c_n \Delta\bar{V}_n^2\right)\Gamma b\right)^{\frac{1}{3}}, \tag{4.20}$$

$$\tau_{y0} \text{ prefactor:} \quad 1.01\left(\mu_{\mathrm{avg}}^{\mathrm{Voigt}}\frac{1+\nu_{\mathrm{avg}}^{\mathrm{Voigt}}}{1-\nu_{\mathrm{avg}}^{\mathrm{Voigt}}}\right)^{\frac{4}{3}}\left(\frac{\left(\sum_n c_n \Delta\bar{V}_n^2\right)^2}{\Gamma b^{10}}\right)^{\frac{1}{3}}, \tag{4.21}$$

according to Equations 4.7 and 4.8. Finally, for a more-accurate prediction accounting for the elastic anisotropy, the above isotropic estimations for ΔE_b and τ_{y0} can be corrected by the additional factors shown in Figures 4.5 and 4.6.

The above procedure requires ingredients from either experiments or atomistic simulations: $\mu_{\mathrm{avg}}^{\mathrm{Voigt}}$ and $\nu_{\mathrm{avg}}^{\mathrm{Voigt}}$, the norm of the Burgers vector b, the solute misfit volumes ΔV_n, the line tension of the dislocation Γ and the Shockley partial separation (d) and partial spreading (σ). The Zener factor A is required for choosing the appropriate anisotropy correction factors. We detail in the following how to get all these quantities.

Elastic constants enable the determination of $\mu_{\mathrm{avg}}^{\mathrm{Voigt}}$, $\nu_{\mathrm{avg}}^{\mathrm{Voigt}}$, A, and $\Gamma \propto \mu_{111/110} \approx \mu_{\mathrm{avg}}^{\mathrm{Hill}}$. The C_{ij} can be obtained in several different ways, each with a different level of accuracy. The elastic constants can be computed using first-principles density-functional theory (DFT) calculations, which is reasonably accurate. They can also be estimated using the elemental values and a rule-of-mixtures law, $C_{ij}^{\mathrm{rom}} = \sum_n c_n C_{ij}^n$. The full stiffness tensor of an existing alloy sample can be measured using standard methods for single crystals and advanced techniques for polycrystals [105–107]. It is more conventional, however, to measure only the average elastic moduli of untextured polycrystals, which are typically close to the Hill approximation [101]. Γ can thus be computed using the experimental isotropic shear modulus. The Voigt-averaged values can then be estimated by using the anisotropy A of the rule-of-mixtures C_{ij}^{rom} and the measured isotropic elastic constants with equations 4.10–4.14 as

$$\mu_{\text{avg}}^{\text{Voigt}} \approx \mu_{\text{avg}}^{\text{expt}} \frac{(2A+3)(3A+2)}{3A^2+19A+3}, \tag{4.22}$$

$$\nu_{\text{avg}}^{\text{Voigt}} \approx \frac{\mu_{\text{avg}}^{\text{expt}}\left(1+\nu_{\text{avg}}^{\text{expt}}\right)-\mu_{\text{avg}}^{\text{Voigt}}\left(1-2\nu_{\text{avg}}^{\text{expt}}\right)}{2\mu_{\text{avg}}^{\text{expt}}\left(1+\nu_{\text{avg}}^{\text{expt}}\right)+\mu_{\text{avg}}^{\text{Voigt}}\left(1-2\nu_{\text{avg}}^{\text{expt}}\right)}. \tag{4.23}$$

The lattice constant can be computed using first-principles methods or atomistic simulations with suitable interatomic potentials, or measured by diffraction. The solute misfit volumes can be computed with some additional effort [37, 54]. The misfit volumes can be determined in principle from experiments on alloys at different compositions followed by interpolation, but this requires fabrication of the alloys [108]. Lattice constants and misfit volumes can also be estimated using Vegard's law, which has been shown to be fairly accurate over a range of alloys [4, 37, 109, 110].

The dislocation core parameters d_p/b and σ/b are more challenging to assess. Fortunately, most results are insensitive to d_p/b for $d_p/b \geq 7$. The partial separation d_p/b can be estimated from knowledge of the stable stacking fault energy γ_{ssf} and analytic and/or Peierls-Nabarro models. It can also be measured, on average, via TEM [111, 112]. The partial core spreading σ/b is the least accessible quantity, yet the results are rather sensitive to this value. The uncertainty in σ/b likely dominates the overall uncertainty of the elasticity model, whether isotropic or anisotropic. Successful past applications have used a single value of $\sigma/b = 1.5$ with the Leyson et. al model, which is on the low end of physical values seen in several fcc atomistic core structures (Section A.1). This value may partially compensate for (i) additional "chemical" contributions in the core that are not included in the elasticity model and (ii) a larger σ/b combined with a larger numerical prefactor (see Ref. [109] and discussion below). For example, for Al-X binary alloys, the full DFT-computed X-solute interactions energies were computed [32] but the final results could be well represented by the Leyson et. al elasticity model with $\sigma/b = 1.5$.

As an illustrative example, here we compute the strength of the CoCrFeMnNi Cantor alloy using available experimental and computational inputs. The uniaxial tensile yield strength has been measured experimentally as 125 MPa at T=293K and strain rate 10^{-3}s^{-1} [113], after extrapolating the Hall-Petch grain-size effect to infinite grain size. Our prediction here is a refinement of the prediction of Varvenne et. al of 125 MPa based on isotropic elasticity [4] with the experimental polycrystal elastic constants, which was in very good agreement with the experimental value.

The single crystal elastic constants of the Cantor alloy have recently been measured by Teramoto et. al to be $C_{11} = 195.9\,\text{GPa}$, $C_{12} = 117.7\,\text{GPa}$, and $C_{44} = 129.3\,\text{GPa}$ [114]. The experimentally measured partial dislocation spacing of the edge dislocations d_p is $\sim 5-8\,\text{nm}$ [111]. The lattice constant obtained from X-ray diffraction is 3.6 Å [115] and therefore the Burgers vector b is 2.5456 Å; so $d_p/b \gg 7$. The average misfit volumes $\Delta\bar{V}_n$ were estimated in Ref. [4], based on experimental lattice constant data on Ni-Co, Ni-Cr, and Ni-Fe binaries and a range of Mn-containing HEAs and the application of Vegard's law, leading to the values (−0.864, −0.684, 0.286, 0.466, 0.796 Å^3) for (Ni, Co, Fe, Cr and Mn), respectively.

With the above inputs, we predict the yield strength using the isotropic theory with Voigt elastic constants and the additional corrections accounting for anisotropy obtained from Figures 4.5 and 4.6. The anisotropy is characterized by $A = 3.3$ and $C_{11}/C_{44} = 1.52$. The Voigt-averaged elastic constants are then computed to be $\mu_{\text{avg}}^{\text{Voigt}} = 93.22$ GPa and $\nu_{\text{avg}}^{\text{Voigt}} = 0.233$ (from Equations 4.11, 4.14). The line tension is computed as $\Gamma = (1/8)\mu_{111/110}b^2 = 0.3497$ eV/Å. The prefactors for computing ΔE_b and τ_{y0} using the Voigt moduli can be then computed from Equations 4.20 and 4.21 as 0.847 eV and 5.314 GPa, respectively. The additional correction factors for anisotropy obtained from Figures 4.5b and 4.5c are 0.976 for ΔE_b and 0.95 for τ_{y0} (first minimum $w_{c,1}$ relevant here).

The remaining quantities needed in the theory that are not directly connected with the anisotropy are the misfit quantity$\sum_n c_n \Delta\bar{V}_n^2 = 0.43\,\text{Å}^6$, d_p/b already established to be $\gg 6$, and σ/b. We use the value $\sigma/b = 1.5$ to be consistent with Varvenne et. al. With these values, we obtain the dimensionless quantities for τ_{y0} (0.01758) and ΔE_b (1.277) from Figure 4.7.

Multiplying all of the components discussed above yields $\tau_{y0} = 88.75$ MPa and $\Delta E_b = 1.056$ eV. The uniaxial tensile yield strength at temperature and strain rate $\sigma_y = 3.06\tau_y$ is then computed from Equation 4.2c as 128.7 MPa, where the Taylor factor 3.06 for untextured fcc polycrystals is used. This prediction is in very good agreement with the experimental value of 125 MPa. The additional anisotropy factors do not lead to any significant change in the prediction in this particular case. This level of agreement is well within the uncertainty of the model and is not expected to be achieved for all alloys.

In the absence of the single-crystal elastic moduli, we would estimate the strength using the reported isotropic polycrystalline moduli $\mu = 80-81$ GPa and $\nu = 0.25-0.265$ [115–117] as follows. The Voigt-average elastic moduli require A. This is estimated using the rule-of-mixtures C_{ij}^{rom} obtained from the elemental moduli. For the Cantor alloy, where not all elements crystallize in fcc at low temperature, we use the first-principles DFT values for these elements in the fcc structure [118]. The resulting C_{ij}^{rom} yields the estimate $A = 2.35$, somewhat lower than the experimental value but still indicating a non-negligible level of anisotropy. The Voigt-averaged elastic constants are then computed to be $\mu_{\text{avg}}^{\text{Voigt}} = 87.061$ GPa, ~ 6.5% lower than the single-crystal value, and $\nu_{\text{avg}}^{\text{Voigt}} = 0.248$ using Equations 4.22 and 4.23 respectively. The line tension uses the experimental shear modulus, $\Gamma = (1/8)\mu b^2 = 0.406$ eV/Å. The anisotropic correction factors for ΔE_b and τ_{y0} are 0.98 and 0.97 respectively (See Figure 4.5). The remaining inputs to the theory are unchanged. Using the components computed above yields the new predictions of $\tau_{y0} = 82.15$ MPa and $\Delta E_b = 1.089$ eV with a tensile yield strength at temperature and strain rate of 121.82 MPa. The difference with the more-complete prediction is small, and within the uncertainty of the theory.

The example above is intended mainly to show how the anisotropic results can be applied in practice, depending on the availability of experimental data. The objective is not to show that the anisotropic model gives better agreement with experiment in this particular case. In general, the anisotropic model gives higher strengths than the isotropic model because the Voigt-averaged elastic constants that best-capture the anisotropy are always larger than the isotropic elastic constants.

4.4 Discussion and Summary

The illustration in the previous section shows how experimental measurements provide some guidance on the relevant material properties needed in the theory. As noted, in the absence of experiments, many of these quantities can be estimated or computed using first-principles [37]. Thus, there are different avenues for evaluating the parameters needed in the model. Alloy design and discovery will follow the route of computation. The use of experimental inputs on materials that have been fabricated and tested can further validate the theory or help identify if other factors (solute-solute interactions; chemical short-range order; microstructure) are important in determining strength.

There are uncertainties associated with each material quantity, and the errors associated with these uncertainties can accumulate. The elasticity theory itself is an approximation to a more-complete theory, and even the full theory is not perfect. Nonetheless, the theory provides general guidance for understanding what material variables determine the strength, and their relative importance. This allows for the rationalization of experimental trends across families of alloys and provides a framework for searching higher-performance alloys.

The underlying theory of this complex process of a dislocation moving through a random alloy continues to evolve. In application to edge dislocations in bcc alloys, a new general stochastic analysis of the wavy dislocation configuration has been presented [109]. This analysis involves a more-detailed statistical analysis of the wavy dislocation structure via stochastic modeling of the structure segment-by-segment and including the full statistical distribution of possible segment energy changes due to the solute fluctuations. This analysis leads to additional numerical coefficients $\kappa = 0.56$ and $\beta = 0.833$ multiplying the line energy and potential energy terms appearing in Equation 4.2a, respectively, and a change in the energy barrier by a factor $\sqrt{2}/(\sqrt{2} - 0.25) = 1.214$. The same analysis applies to fcc alloys, and the net effects are a factor of $\sqrt{\kappa/\beta} = 0.82$ multiplying the line tension and the factor of 1.214 for the energy barrier, which then also enters the zero-temperature strength. These effects change the numerical coefficients in Equations 4.2a and 4.2b from (1.22, 1.01) to (1.39, 1.31), respectively. Thus, the successful use of $\sigma/b = 1.5$, which is smaller than values seen in simulations (see Section A.1), together with the original Leyson model may reflect some cancellation of effects. For instance, using $\sigma/b = 2.0$ and the corresponding dimensionless coefficient for τ_{y0} of ~ 0.012 (see Figure 4.7c) with the revised prefactor of 1.31 gives a net factor of ~ 0.016 which is nearly equal to that obtained using the present Leyson model with $\sigma/b = 1.5$ (dimensionless coefficient ~ 0.017) and with the Leyson coefficient 1.01, giving a net factor ~ 0.017. However, for overall consistency with the previous literature and successful quantitative application of the Leyson model, we advocate continued use of the original Leyson model coefficients. We also note that these coefficients do not enter into any *difference* between isotropic and anisotropic theories, and so do not affect the primary analyses of this chapter.

The theory has been extended to include the effects of solute-solute interactions, while remaining in the random alloy limit [7]. Currently, a new strengthening theory is in development which accounts for the presence of short-range order (SRO), however the present elastic theory using solute-dislocation interactions is an integral part of it (Chapter 6). The anisotropic elasticity theory presented here will remain valuable because the solute-solute interactions and SRO contributions can be incorporated and integrated along with the elasticity contributions to solute/dislocation interactions. Thus, the theory will continue to improve by incorporating increasing, but realistic, complexity.

In summary, we have shown that the predictions of a fully anisotropic elastic model for solute strengthening can be obtained using an isotropic elasticity model with the Voigt-averaged elastic constants for the dislocation field and the Hill-averaged elastic constants for the line tension. Additional small correction factors to match the anisotropic result precisely are also provided. The effects of anisotropy are not negligible — the use of the standard Hill estimate for the isotropic moduli in equations 4.16 and 4.17 leads to rather lower strength predictions for high anisotropy ($A = 3-4$). Since many HEAs to date have anisotropy in the range of $A = 2-4$, these corrections are valuable for making refined predictions. We have provided some guidelines on obtaining the data needed to make predictions. Results then follow using the coefficients presented graphically here, which we hope assists with application of the theory. The elastic theory provides an approximate but firm and analytical foundation for understanding trends in solute strengthening. Since the composition space in multi-component random alloys is immense, and experimental searching through that entire space is not feasible, the present theory provides a framework for rapid probing of the entire space in the search for attractive compositions for desired performance.

5 Effect of Solute-Solute Interactions on strengthening of random alloys

Disclaimer

This chapter is adapted from the following article, with permission from the coauthor and the publisher.

S. Nag, W. A. Curtin, “Effect of solute-solute interactions on strengthening of random alloys from dilute to high entropy alloys”, *Acta Materialia* 200, 659–673 (2020).

The yield strength of random metal alloys, i.e. alloys with random occupation of the crystalline lattice sites by the elemental constituent atoms all considered as solutes, is primarily understood as controlled by solute-dislocation interactions. The Leyson’s theory for the yield strength of random alloys composed of any number of components at any concentration has provided good predictions across a range of alloys, both dilute [31, 32, 38, 119] and HEAs [4, 33, 37, 109, 110, 120, 121]. While random, such alloys still possess the underlying solute-solute interactions, and these interactions can influence mechanical properties of the random alloy. In this chapter, the Leyson’s model, as introduced in Chapter 1: Section 1.2, has been extended to incorporate the effects of solute-solute interactions into the prediction of yield strength in random alloys.

In a random alloy, there is no statistical preference for the occurrence of particular solute-solute pairs at any distance, independent of whether there are solute-solute interactions. The passage of a dislocation along a crystalline glide plane shifts the relative positions of atoms above the glide plane with respect to the atoms below the glide plane (see Figure 5.1). On average, the glide creates no change to the number of solute-solute pairs at any distance. Therefore, there is no average effect of solute-solute interactions on the yield strength. Locally over finite slip areas, however, the actual number of solute-solute pairs of all types will change upon slip. Thus, there are scale-dependent *fluctuations* in the solute-solute interaction energies as the dislocation moves through the random alloy. At the same time, the individual solutes - independent of the surrounding solutes - interact with the dislocation. On average these interactions also sum to zero but have local fluctuations (deviations from the average). The dislocation thus experiences energy fluctuations due to both the individual solutes and the solute-solute interactions. These total fluctuations can attract or repel the dislocation. The dislocation thus adopts a wavy configuration so as to minimize its total energy, lowering the energy by moving into regions where solute fluctuations are favorable and avoiding regions where the fluctuations are unfavorable. With the dislocation residing in the low-energy environments, a combination of applied stress and temperature is required to move the dislocation segments, via thermal activation, over the nearby high energy regions. This determines the strain-rate and temperature-dependent flow stress.

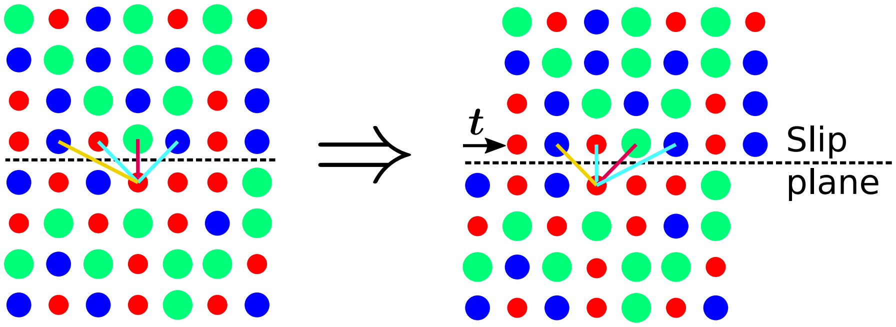

Figure 5.1 – Schematic illustration of pair changes across the slip plane due to slip by a lattice vector $\boldsymbol{t}$. Selected atom pairs are indicated by colored lines in both figures. Considering distances only in the two planes just above and below the slip plane for simplicity, upon slip 1st NN pairs become 2nd NN pairs (e.g. red-green), 2nd NN pairs can become 1st NN pairs (e.g. red-red) or 3rd NN pairs (e.g. red-blue), and 3rd NN pairs can become become 2nd NN pairs (e.g. red-blue) or 4th NN pairs (not shown). These changes combine with solute-solute interactions to create the fluctuations in energy upon slip that lead to strengthening.

Here, we derive and validate an analytical expression for the fluctuations in energy change due to solute-solute interactions as a dislocation glides in a random alloy (e.g. Figure 5.1). Specific results are provided for both fcc and bcc crystal structures. The general result is incorporated into the theory of strengthening in random alloys, originally proposed by Leyson et. al. The quantitative effects of solute-solute interactions on yield strength due to edge dislocations are then assessed in bcc MoNbTaW, bcc NbTaV and fcc Ni-Al. The strengthening due to solute-solute interactions is negligible in the bcc alloys and significant in Ni-Al at low (2–10%) Al concentrations due to the very strong Al-Al first-neighbor repulsion. The Ni-Al results vary widely depending on the source of the input material properties. Connections are made to simulations on Ni-Al alloys in published literature.

Since solute-solute interaction energies in concentrated and high-entropy alloys are not always available and can be cumbersome to calculate via atomistic simulation, we also suggest a strategy to estimated apriori what level of solute-solute interactions would be necessary to have a notable impact on strengthening. If the required level of interactions is sufficient to likely cause phase-separation, then one can conclude with no further calculation that the real effects of solute-solute interactions in a single-phase alloy are not important for strengthening.

The remainder of this chapter is organized as follows. Section 5.1 revisits the solute-strengthening theory to incorporate solute-solute interactions. Section 5.2 presents the derivation of the variance in energy change upon slip in a random alloy due to solute-solute interactions. Section 5.3 validates the analytical expression for the variance via numerical studies on model alloys. Section 5.4 quantitatively assesses the role of solute-solute interactions in solute-strengthening in the bcc and fcc alloys. Section 5.5 summarizes our results and their implications.

5.1 Solute-strengthening theory accounting for solute-solute interactions

The theory for strengthening in a random alloy first envisions a wavy edge dislocation having a wavelength 4ζ and amplitude w. The typical solute-related energy fluctuations over length ζ are taken equal to the standard deviation $\sigma_{\Delta E_p}$ of the total solute-related energy fluctuations. We extract out the explicit dependence on dislocation segment length ζ by writing $\sigma_{\Delta E_p} = \left(\zeta\rho_L\right)^{\frac{1}{2}}\Delta\widetilde{E}_{\mathrm{p}}(w)$ where ρ_L is the density of lattice sites along the dislocation line direction. ρ_L equals $1/(\sqrt{3}b)$ for fcc alloys and $1/(2\sqrt{2}b)$ for bcc alloys. The quantity $\Delta\widetilde{E}_{\mathrm{p}}(w)$ is the standard deviation of the energy change, per periodic length along the dislocation line, when the dislocation glides a distance w. There is also an elastic energy cost per wavy unit equal to $\Gamma\frac{w^2}{2\zeta}$ where Γ is the dislocation line tension. The total energy of a long dislocation of length L having the wavy structure characterized by ζ and w is then

$$\Delta E_{\mathrm{tot}}(\zeta, w) = \left[\Gamma\frac{w^2}{2\zeta} - \left(\zeta\rho_L\right)^{\frac{1}{2}}\Delta\widetilde{E}_{\mathrm{p}}(w)\right]\left(\frac{L}{2\zeta}\right) \tag{5.1}$$

A characteristic wavelength and amplitude (ζ_c, w_c) emerge by minimizing the total energy of the long dislocation with respect to both ζ and w. The length ζ_c is obtained directly as

$$\zeta_c = \left(\frac{4\Gamma^2 w^4}{\rho_L\Delta\widetilde{E}_{\mathrm{p}}^2(w)}\right)^{\frac{1}{3}} \tag{5.2}$$

The amplitude w_c then follows from a second minimization $\frac{\partial\Delta E_{\mathrm{tot}}(\zeta_c(w),w)}{\partial w} = 0$ that reduces to the solution of

$$\frac{\partial\Delta\widetilde{E}_{\mathrm{p}}(w)}{\partial w} = \frac{\Delta\widetilde{E}_{\mathrm{p}}(w)}{2w} \tag{5.3}$$

The total reduction in energy per length ζ_c, $\Delta E_c = \Delta E_{\mathrm{tot}}(\zeta_c, w_c)\frac{2\zeta_c}{L}$, then sets an energy scale for pinning of the dislocation. The length scale w_c along the glide plane sets the glide distance between local favorable and unfavorable solute environments. The dislocation must be thermally-activated, assisted by a resolved shear stress τ, out of the local minimum energy of the favorable environments across the barriers created by the adjacent unfavorable environments. The outcome of the analysis is a zero-temperature yield stress τ_{y0}, an associated zero-stress energy barrier ΔE_b, and a stress-dependent activation barrier $\Delta E(\tau)$ given by

$$\Delta E_b = 1.467\left(\rho_L w_c^2 \Gamma \Delta\widetilde{E}_\mathrm{p}^2(w_c)\right)^{\frac{1}{3}} \tag{5.4a}$$

$$\tau_{y0} = \frac{\pi}{2}\frac{\Delta E_b}{b w_c \zeta_c} = 1.45\left(\frac{\rho_L^2 \Delta\widetilde{E}_\mathrm{p}^4(w_c)}{\Gamma b^3 w_c^5}\right)^{\frac{1}{3}} \tag{5.4b}$$

$$\Delta E(\tau) = \Delta E_b\left(1 - \frac{\tau}{\tau_{y0}}\right)^{\frac{3}{2}} \tag{5.4c}$$

In combination with an Arrhenius law for the thermal activation, these lead to a temperature T and strain-rate $\dot{\epsilon}$ dependent flow stress given by

$$\tau_y(T,\dot{\epsilon}) = \tau_{y0}\left[1 - \left(\frac{k_\mathrm{B}T}{\Delta E_b}\ln\left(\frac{\dot{\epsilon}_0}{\dot{\epsilon}}\right)\right)^{\frac{2}{3}}\right] \tag{5.5}$$

where $\dot{\epsilon}_0 \sim 10^4/s$ and k_B are a reference strain rate and Boltzmann's constant, respectively. With increasing temperature, the expression for strengthening is modified to account for multiscale waviness as discussed in [36] but these details are not important for this paper.

The energy fluctuations due to the random solute environment enter only through $\sigma_{\Delta E_p}$ and $\Delta\widetilde{E}_\mathrm{p}(w)$. Here, we assume that the fluctuations due to solute-dislocation interactions and solute-solute interactions are independent. That is, the direct interaction of a single solute with the dislocation does not depend on the identity of any surrounding solutes. Then, the fluctuations due to shifting of relative solute positions as the dislocation glides are independent of the single-solute positions. The variance (square of the standard deviation) of the total energy change upon glide of a dislocation is then the sum of the variances of the two independent contributions,

$$\sigma^2_{\Delta E_p} = \sigma^2_{\Delta E_{sd}} + \sigma^2_{\Delta E_{ss}} \tag{5.6}$$

The standard deviation due to solute-dislocation interactions $\sigma_{\Delta U_\mathrm{s-d}}$ has been considered previously in [4, 31, 32, 119, 120] and is

$$\sigma_{\Delta E_{sd}} = \left(\zeta\rho_L\right)^{\frac{1}{2}}\sqrt{\sum_{\substack{i,j\\n}} c_n\left(U^n_{sd}(x_i - w, y_j) - U^n_{sd}(x_i, y_j)\right)^2} = \left(\zeta\rho_L\right)^{\frac{1}{2}}\Delta\widetilde{E}_{\mathrm{p},sd}(w) \tag{5.7}$$

where $U^n_{sd}(x_i, y_j)$ is the solute-dislocation interaction energy of a solute of type n at the projected in-plane position (x_i, y_j) with respect to the dislocation line at the origin with line direction z. With the assumption of linear elasticity and a Burgers vector distribution characterized by full (for bcc) or partial (for fcc) dislocation core spreading σ and, for fcc, a partial separation distance d_p, $\Delta\widetilde{E}_{\mathrm{p},sd}(w)$ can be decoupled into a composition-plus-misfit-volume term, an elastic prefactor, and a dislocation core structure coefficient term as

$$\Delta\widetilde{E}_{\mathrm{p},sd}(w) = g\left(w, d_p, \sigma\right)\mu^V \frac{1+\nu^V}{1-\nu^V}\sqrt{\sum_n c_n \Delta V_n^2} \tag{5.8}$$

where c_n and ΔV_n are the concentration and misfit volume of solute x in the alloy, μ^V and ν^V are the Voigt averaged shear modulus and Poisson ratio of the alloy, and $g\left(w, d_p, \sigma\right)$ is a numerical coefficient that depends on the glide distance w, the dislocation core structure parameters (σ and d_p); in principle, g also depends on the Zener elastic anisotropy parameter A, but the dependence is weak when the Voigt-averaged elastic constants are used [120].

The w_c obtained from the solution of Equation 5.3 using only solute-dislocation interaction energies (refer Figure 4.7a), leads to a dimensionless computed numerical coefficient $g\left(w_c, d_p, \sigma\right)$. Figure 5.2 presents $g\left(w_c\right)$ for different fcc dislocation core structures $\left(\sigma, d_p\right)$ (extracted from Figures 4.7b and 4.7c). In addition, for sufficiently large partial separation distances d_p the minimization process gives rise to two solutions $w_{c,1}$ and $w_{c,2}$, and hence two solutions for g, as shown in Figure 5.2. One solution has a high zero-T strength and low zero-stress barrier, and controls the strength at lower temperatures. The second solution has a lower strength and higher barrier and controls the strength at higher temperatures. The two solutions will emerge as relevant in our later study of fcc Ni-Al. Related results for edge dislocations in bcc alloys can be derived from results in [109].

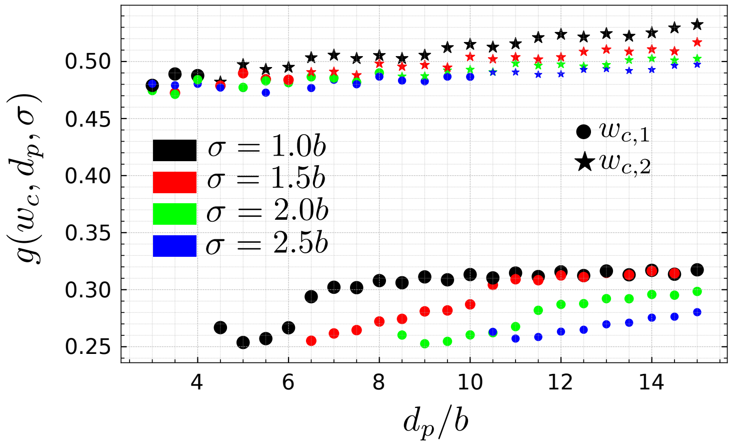

Figure 5.2 – Dimensionless solute-dislocation energy fluctuation quantity $g(w_c, d_p, \sigma)$ for fcc alloys as a function of the partial dislocatoin separation d_p/b, for different dislocation core structures characterized by partial core spreading σ/b.

The variance $\sigma^2_{\Delta E_{ss}}$ in energy changes due to fluctuations in solute-solute pairs scales with the number of atoms N on the glide plane over which glide has occurred. Here we are interested in the normalized variance $\widetilde{\sigma}^2_{\Delta E_{ss}} = \sigma^2_{\Delta E_{ss}}/N$ where N is the number of atoms swept during glide of a dislocation segment of length ζ by distance w. We neglect the fact that atoms near the dislocation core experience fractional slip (e.g. less than one partial Burgers vector for the

Shockley partials in fcc crystals and less than one Burgers vector for the full dislocations in bcc crystals). N then depends only on the crystal structure and slip plane. As shown in Figure 5.3, there are three relevant cases in bcc and fcc crystals. For a compact full dislocation typical in bcc, $N = \rho_L \rho_G \zeta w$ where ρ_L is the density of atomic sites along the line direction and ρ_G is the density of projected atomic sites in the glide direction. ρ_G equals $2/b$ for fcc alloys and $3/b$ for bcc alloys. For dissociated dislocations typical in fcc, there are two cases. When the glide distance is $w < d_p$, the leading partial shifts material from the unslipped perfect crystal to a partially-slipped structure while the trailing partial shifts the previous partially-slipped region back to perfect crystal, so $N = 2\rho_L \rho_G \zeta w$. When the glide distance is $w > d_p$, new stacking fault is formed, the previous partially slipped region reverts back to perfect crystal, and a new fully-slipped region is formed. The number of partially-slipped atoms on the glide plane is then $N_p = 2\rho_L \rho_G d_p \zeta$ with normalized standard deviation denoted as $\tilde{\sigma}_{\Delta E_{ss},p}$ and the number of atoms in the fully-slipped region is $N_f = \rho_L \rho_G (w - d_p)\zeta$ with normalized standard deviation denoted as $\tilde{\sigma}_{\Delta E_{ss},f}$.

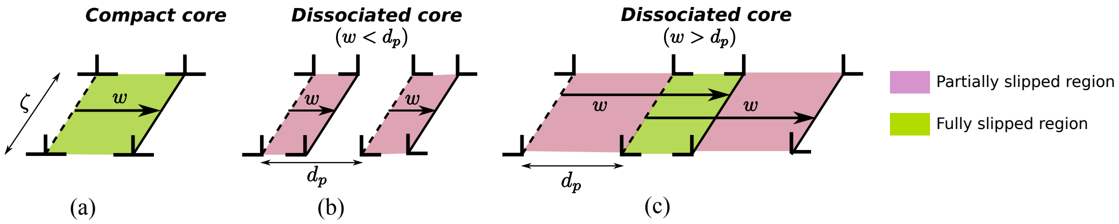

Figure 5.3 – Schematic of areas swept during dislocation glide by a distance w. (a) bcc crystal (no dissociation); (b) fcc crystal (dissociated core) with $w < d_p$; (c) fcc crystal (dissociated core) with $w > d_p$.

The variance due to all solute-solute interaction when a dislocation segment of length ζ glides by w is thus

$$\sigma_{\Delta E_{ss}} = \begin{cases} \sqrt{\zeta w \rho_L \rho_G \tilde{\sigma}^2_{\Delta E_{ss},f}} & \text{Compact core} \\ \sqrt{2\zeta w \rho_L \rho_G \tilde{\sigma}^2_{\Delta E_{ss},p}} & \text{Dissociated core, } w < d_p \\ \sqrt{\zeta w \rho_L \rho_G \tilde{\sigma}^2_{\Delta E_{ss},f} + \zeta d_p \rho_L \rho_G (2\tilde{\sigma}^2_{\Delta E_{ss},p} - \tilde{\sigma}^2_{\Delta E_{ss},f})} & \text{Dissociated core, } w > d_p \end{cases} \tag{5.9}$$

The normalized variances will be derived in the next Section. Factoring out the common term $(\zeta \rho_L)^{\frac{1}{2}}$ and adding the contribution from solute-dislocation interactions, the key energetic quantity $\Delta \tilde{E}_{\mathrm{p}}(w)$ in the theory can be written as

$$\Delta \tilde{E}_{\mathrm{p}}(w) = \begin{cases} \sqrt{\Delta \tilde{E}^2_{\mathrm{p},sd}(w) + w \rho_G \tilde{\sigma}^2_{\Delta E_{ss},f}} & \text{Compact core} \\ \sqrt{\Delta \tilde{E}^2_{\mathrm{p},sd}(w) + 2 w \rho_G \tilde{\sigma}^2_{\Delta E_{ss},p}} & \text{Dissociated core, } w < d_p \\ \sqrt{\Delta \tilde{E}^2_{\mathrm{p},sd}(w) + w \rho_G \tilde{\sigma}^2_{\Delta E_{ss},f} + d_p \rho_G (2\tilde{\sigma}^2_{\Delta E_{ss},p} - \tilde{\sigma}^2_{\Delta E_{ss},f})} & \text{Dissociated core, } w > d_p \end{cases} \tag{5.10}$$

where $\Delta\widetilde{E}_{\mathrm{p},sd}(w)$ is the solute-dislocation fluctuation contribution that appears in the original theory and the second terms on the right-hand side of Equation 5.10 can be similarly denoted as $\Delta\widetilde{E}_{\mathrm{p},ss}(w)$. Recalling Equation 5.3, the minimization to obtain w_c can be shown to be unchanged by the introduction of solute-solute interactions for the compact core and the dissociated $w < d_p$ core,

$$\frac{\partial\Delta\widetilde{E}_{\mathrm{p}}(w)}{\partial w} = \frac{\Delta\widetilde{E}_{\mathrm{p}}(w)}{2w} \Leftrightarrow \frac{\partial\Delta\widetilde{E}_{\mathrm{p},sd}(w)}{\partial w} = \frac{\Delta\widetilde{E}_{\mathrm{p},sd}(w)}{2w} \tag{5.11}$$

For the dissociated core with $w > d_p$, the minimization may not be greatly affected if the additional term $d_p\rho_G(2\widetilde{\sigma}^2_{\Delta E_{ss},p} - \widetilde{\sigma}^2_{\Delta E_{ss},f})$ is small; this must be verified in any specific case. This analysis demonstrates that the introduction of solute-solute interactions does not change w_c relative to the value in the absence of solute-solute interactions for two important cases (dissociated core with $w < d_p$ common in fcc alloys and compact core common in bcc alloys).

The fact that w_c can be independent of solute-solute interactions enables a very rapid parametric assessment of their importance to strengthening. First, the analytic elasticity theory using only solute-dislocation interactions can be applied using Equation 5.8 to compute $\Delta\widetilde{E}_{\mathrm{p},sd}(w_c)$ and the w_c can be obtained from the core structure. Then, a magnitude of solute-solute interactions (i.e. the magnitude of $\widetilde{\sigma}_{\Delta E_{ss}}$ in Equation 5.10) can be *assumed* and $\Delta\widetilde{E}_{\mathrm{p},ss}(w_c)$ computed. Solute-solute interactions are only important (e.g. > 10% increase in strength) if $\Delta\widetilde{E}_{\mathrm{p},ss}(w_c) > 0.45\Delta\widetilde{E}_{\mathrm{p},sd}(w_c)$. If the magnitude of the *assumed* solute-solute interactions to achieve this level is unrealistic (e.g. so high that the alloy would likely phase separate or form LRO at the fabrication temperatures), then the *true* smaller solute-solute interactions can be neglected and do not need to be determined.

Estimates for solute-solute interaction energies can also be made using the heat of mixing of binary alloys as computed (e.g. Ref. [122]) or determined from CALPHAD or other standard tools. The heats of mixing of binary pairs in a multicomponent alloy has been used to judge whether a proposed alloy composition is amenable to fabrication as single-phase material [122]. Here, such estimates can be used to estimate the effects of solute-solute interactions on strengthening.

Since there are many equations and symbols in this paper, we provide a *"List of Symbols"* for reference.

List of Symbols

a, b	Cubic lattice constant, Burgers vector
d_p, σ	Partial separation and partial core spreading
ρ_L, ρ_G	Lattice site densities along the dislocation line and glide directions
μ^V, ν^V	Voigt averaged shear modulus and Poisson's ratio respectively
Γ	Dislocation line tension
c_x	Concentration of type x in the alloy
ΔV_x	Misfit volume of solute of type x
$w, w_{c,1}, w_{c,2}$	Dislocation roughening amplitude and its two characteristic values
ζ, ζ_c	$\frac{1}{8}$ Lateral dislocation roughing scale and its characteristic value
$\sigma_{\Delta E_p}$, $\sigma_{\Delta E_{sd}}$, $\sigma_{\Delta E_{ss}}$	Standard deviation of dislocation energy due to total solute fluctuations, the solute-dislocation contribution, and the solute-solute contribution interactions
$\widetilde{\sigma}_{\Delta E_{ss}}$	$\sigma_{\Delta E_{ss}}$ divided by $\left(\zeta w \rho_L \rho_G\right)^{\frac{1}{2}}$
$\widetilde{\sigma}_{\Delta E_{ss},p}$, $\widetilde{\sigma}_{\Delta E_{ss},f}$	$\widetilde{\sigma}_{\Delta E_{ss}}$ corresponding to slip by partial and lattice vector respectively
$\Delta\widetilde{E}_{\mathrm{p}}, \Delta\widetilde{E}_{\mathrm{p,s-d}}$	$\sigma_{\Delta E_p}$ and $\sigma_{\Delta E_{sd}}$ divided by $\left(\zeta \rho_L\right)^{\frac{1}{2}}$
ΔE_{tot}	Total energy change for wavy dislocation relative to a straight configuration in a random alloy
V_{xy}^{eff}	Effective interaction potential of $x-y$ solute pair
d	Normalized pair distances in a lattice
N_d	Number of lattice sites at distance d (Sec. 5.3)
s_{ix}	Occupation variable for site i and type x
$\Theta_{dd'}$	Structure factor for lattice site pair distances (d, d')
ΔE_b	Energy barrier for dislocation glide
$\Delta E(\tau)$	Stress-dependent activation barrier
τ_{y0}, τ_y	Zero- and finite-temperature yield stress
g	Numerical coefficient in $\Delta\widetilde{E}_{\mathrm{p,s-d}}$
$U_{sd}^x(\mathrm{x}_i, \mathrm{y}_j)$	Interaction energy of type-x solute at position $(\mathrm{x}_i, \mathrm{y}_j)$ relative to a dislocation at the origin
$\boldsymbol{t}$	Slip vector
U_{xy}	Bond energy of $x-y$ solute pair
U_{AA}	Bond energy of alloy average-atom A
U_{xA}	Bond energy of solute x - average atom A pair
U_{xy}^{int}	Interaction energy of $x-y$ solute pair

Finally, before proceeding with the detailed analysis of the normalized variance $\widetilde{\sigma}^2_{\Delta E_{ss}} = \sigma^2_{\Delta E_{ss}}/N$, we note that the sum of the variances in Equation 5.6 is a reasonable approximation for two reasons. First, favorable solute fluctuations should typically have more solutes on one side of the glide plane and fewer on the other, decreasing the number of solute pairs across the glide plane in any low-energy pinned region of the dislocation. However, solute-dislocation interactions are not localized to the atomic sites just above and below the glide plane [31, 32, 119] and solute/stacking fault interactions are equivalent on both sides of the glide plane, so the approximation is reasonable. Second, there could be a correlation between local solute misfit volume and local environment, and the local environment involves solute-solute pairs. However, computational studies of variations in local solute misfit volumes indicates that variations are small relative to the misfit volumes themselves. First principles studies of the changes in misfit volume for close solute pairs relative to isolated solutes also show small effects (e.g. for Al in Ni, the misfit volume of Al is 1.62Å^3 and that for each of two strongly-repelling near-neighbor Al atoms is 1.82Å^3[67]). Therefore, neglecting correlated fluctuations between single solutes and solute pairs appears to be a good assumption.

5.2 Analytical expression for normalized variance $\widetilde{\sigma}^2_{\Delta E_{ss}}$ for multicomponent alloys

We now compute the normalized variance $\widetilde{\sigma}^2_{\Delta E_{ss}}$ in energy changes due to fluctuations in solute-solute pairs as one half of a crystal slips by some slip vector **t** over the other half across a specified slip plane. The analysis is basically topological (Figure 5.1). Atoms are assigned to each perfect lattice site. For two solutes m and n, we seek the fluctuation in the number of $m-n$ pair *changes* across the slip plane at any pair separation distance due to slip. Actual local deviations from the perfect lattice positions, which occur in the real material when relaxed to equilibrium, are neglected because they do not change the number of $m-n$ pairs.

We describe the interaction between atoms m and n at lattice sites i and j at a separation distance $\|\boldsymbol{r}_{ij}\|$ by a pair potential $U_{mn}(\|\boldsymbol{r}_{ij}\|)$. We will subsequently translate our results into other forms involving the pair interaction energies $U^{int}_{mn}(\|\boldsymbol{r}_{ij}\|)$ and effective pair potentials $V^{eff}_{mn}(\|\boldsymbol{r}_{ij}\|)$ defined later. For a given realization of the random alloy (i.e. specific occupation of each lattice site by one particular solute of the alloy), the total energy of the initial (unslipped) crystal is

$$E^i = \frac{1}{2}\sum_{\substack{i,j\\ i\neq j}}\sum_{m,n} s_{im}s_{jn}U_{mn}(\|\boldsymbol{r}_{ij}\|) \tag{5.12}$$

Here, s_{im} is an indicator variable which equals 1 if site i is occupied by solute m and equals 0 otherwise. After slip of the upper half of the crystal relative to the lower half of the crystal by a vector $\boldsymbol{t}$ parallel to the slip plane, the total energy of the system is

$$E^f = \frac{1}{2} \sum_{\substack{i,j \\ i\neq j \\ i,j>0}} \sum_{m,n} s_{im} s_{jn} U_{mn}(\|\boldsymbol{r}_{ij}\|) + \frac{1}{2} \sum_{\substack{i,j \\ i\neq j \\ i,j<0}} \sum_{m,n} s_{im} s_{jn} U_{mn}(\|\boldsymbol{r}_{ij}\|) + \sum_{\substack{i,j \\ i<0,j>0}} \sum_{m,n} s_{im} s_{jn} U_{mn}(\|\boldsymbol{r}_{ij} + \boldsymbol{t}\|) \tag{5.13}$$

The energy change is the difference between the final and initial energies. Energy changes due to all pairs $i-j$ exclusively below $(i, j < 0)$ or above $(i, j > 0)$ the slip plane are zero, leaving only changes due to pairs $(i < 0, j > 0)$ across the slip plane. The energy change ΔE_{ss} upon slip due to solute-solute interactions is then

$$\Delta E_{ss} = \sum_{\substack{i,j \\ i<0,j>0}} \sum_{m,n} s_{im} s_{jn} \Big(U_{mn}(\|\boldsymbol{r}_{ij} + \boldsymbol{t}\|) - U_{mn}(\|\boldsymbol{r}_{ij}\|) \Big) \tag{5.14}$$

The average energy change is obtained by averaging over all possible random (uncorrelated) occupations of each site. Thus, with $\langle\cdot\rangle$ denoting averaging, $\langle s_{im} s_{jn}\rangle = c_m c_n$ where c_m and c_n are the concentrations of m and n atoms, respectively, we obtain

$$\langle \Delta E_{ss}\rangle = \sum_{m,n} c_m c_n \Big(\sum_{\substack{i,j \\ i<0,j>0}} U_{mn}(\|\boldsymbol{r}_{ij} + \boldsymbol{t}\|) - \sum_{\substack{i,j \\ i<0,j>0}} U_{mn}(\|\boldsymbol{r}_{ij}\|) \Big). \tag{5.15}$$

If $\boldsymbol{t}$ is a lattice vector, the two sums are equal and $\langle \Delta E_{ss}\rangle = 0$, i.e. there is no change in average energy upon slip, as expected. For slip by a partial Burgers vector, there will be a change in average energy equal to the energy of the stacking fault of the alloy.

The effect of solute-solute interactions thus only arises through the fluctuations, as represented by the variance $\langle \Delta E_{ss}^2\rangle - \langle \Delta E_{ss}\rangle^2$. With lattice sites labeled by i, k taken to be below the slip plane and sites labeled j, l to be above the slip plane, the quantity ΔE_{ss}^2 is

$$\Delta E_{ss}^2 = \sum_{i,j} \sum_{m,n} s_{im} s_{jn} \Big(U_{mn}(\|\boldsymbol{r}_{ij} + \boldsymbol{t}\|) - U_{mn}(\|\boldsymbol{r}_{ij}\|) \Big) \sum_{k,l} \sum_{p,q} s_{kp} s_{lq} \Big(U_{pq}(\|\boldsymbol{r}_{kl} + \boldsymbol{t}\|) - U_{pq}(\|\boldsymbol{r}_{kl}\|) \Big) \tag{5.16}$$

Taking the average, we use the facts that (i) $\langle s_{im} s_{jn} s_{kp} s_{lq}\rangle = \langle s_{im} s_{kp}\rangle \langle s_{jn} s_{lq}\rangle$ and (ii) $\langle s_{im} s_{kp}\rangle = \delta_{ik}\delta_{mp} c_m + (1-\delta_{ik}) c_m c_p$ (and similarly $\langle s_{jn} s_{lq}\rangle = \delta_{jl}\delta_{nq} c_n + (1-\delta_{jl}) c_n c_q$). Then, we obtain

$$\begin{aligned}
\langle \Delta E_{ss}^2 \rangle = &\sum_{i,j} \sum_{m,n} c_m c_n \Big(U_{mn}(\|\boldsymbol{r}_{ij} + \boldsymbol{t}\|) - U_{mn}(\|\boldsymbol{r}_{ij}\|) \Big)^2 \\
&+ \sum_{i} \sum_{m} c_m \sum_{\substack{j,l \\ j \neq l}} \sum_{n,q} c_n c_q \Big(U_{mn}(\|\boldsymbol{r}_{ij} + \boldsymbol{t}\|) - U_{mn}(\|\boldsymbol{r}_{ij}\|) \Big) \Big(U_{mq}(\|\boldsymbol{r}_{il} + \boldsymbol{t}\|) - U_{mq}(\|\boldsymbol{r}_{il}\|) \Big) \\
&+ \sum_{\substack{i,k \\ i \neq k}} \sum_{m,p} c_m c_p \sum_{j} \sum_{n} c_y \Big(U_{mn}(\|\boldsymbol{r}_{ij} + \boldsymbol{t}\|) - U_{mn}(\|\boldsymbol{r}_{ij}\|) \Big) \Big(U_{pn}(\|\boldsymbol{r}_{kj} + \boldsymbol{t}\|) - U_{pn}(\|\boldsymbol{r}_{kj}\|) \Big) \\
&+ \sum_{\substack{i,k \\ i \neq k}} \sum_{m,p} c_m c_p \sum_{\substack{j,l \\ j \neq l}} \sum_{n,q} c_n c_q \Big(U_{mn}(\|\boldsymbol{r}_{ij} + \boldsymbol{t}\|) - U_{mn}(\|\boldsymbol{r}_{ij}\|) \Big) \Big(U_{pq}(\|\boldsymbol{r}_{kl} + \boldsymbol{t}\|) - U_{pq}(\|\boldsymbol{r}_{kl}\|) \Big)
\end{aligned} \tag{5.17}$$

Making use of the fact that $\langle s_{im} s_{jn} \rangle = c_m c_n$ (and similarly $\langle s_{kp} s_{lq} \rangle = c_p c_q$), one can show by similar manipulations that

$$\langle \Delta E_{ss} \rangle^2 = \sum_{i,k} \sum_{j,l} \sum_{m,n,p,q} c_m c_n c_p c_q \Big(U_{mn}(\|\boldsymbol{r}_{ij} + \boldsymbol{t}\|) - U_{mn}(\|\boldsymbol{r}_{ij}\|) \Big) \Big(U_{pq}(\|\boldsymbol{r}_{kl} + \boldsymbol{t}\|) - U_{pq}(\|\boldsymbol{r}_{kl}\|) \Big) \tag{5.18}$$

The variance $\sigma^2_{\Delta E_{ss}}$ is therefore

$$\begin{aligned}
\sigma^2_{\Delta E_{ss}} = &\sum_{m,n} c_m c_n \sum_{\substack{i,j \\ i<0, j>0}} \Big(U_{mn}(\|\boldsymbol{r}_{ij} + \boldsymbol{t}\|) - U_{mn}(\|\boldsymbol{r}_{ij}\|) \Big)^2 \\
&+ \sum_{m,n,q} c_m c_n c_q \sum_{\substack{i \\ i<0}} \sum_{\substack{j,l \\ j,l>0 \\ j \neq l}} \Big(U_{mn}(\|\boldsymbol{r}_{ij} + \boldsymbol{t}\|) - U_{mn}(\|\boldsymbol{r}_{ij}\|) \Big) \Big(U_{mq}(\|\boldsymbol{r}_{il} + \boldsymbol{t}\|) - U_{mq}(\|\boldsymbol{r}_{il}\|) \Big) \\
&+ \sum_{m,n,p} c_m c_n c_p \sum_{\substack{i,k \\ i,k<0 \\ i \neq k}} \sum_{\substack{j \\ j>0}} \Big(U_{mn}(\|\boldsymbol{r}_{ij} + \boldsymbol{t}\|) - U_{mn}(\|\boldsymbol{r}_{ij}\|) \Big) \Big(U_{pn}(\|\boldsymbol{r}_{kj} + \boldsymbol{t}\|) - U_{pn}(\|\boldsymbol{r}_{kj}\|) \Big) \\
&- \sum_{m,n,p,q} c_m c_n c_p c_q \sum_{\substack{i,k \\ i,k<0}} \sum_{\substack{j,l \\ j,l>0 \\ j=l \text{ if } i \neq k}} \Big(U_{mn}(\|\boldsymbol{r}_{ij} + \boldsymbol{t}\|) - U_{mn}(\|\boldsymbol{r}_{ij}\|) \Big) \Big(U_{pq}(\|\boldsymbol{r}_{kl} + \boldsymbol{t}\|) - U_{pq}(\|\boldsymbol{r}_{kl}\|) \Big)
\end{aligned} \tag{5.19}$$

The variance $\sigma^2_{\Delta E_{ss}}$ is a fourth-order polynomial in concentrations. For fcc and bcc, the second and third terms in Equation 5.19 are equal. For the usual situation in which interactions decay sufficiently fast with distance, $\sigma^2_{\Delta E_{ss}}$ scales with the number of atomic sites N on the slip plane such that the normalized quantity $\widetilde{\sigma}^2_{\Delta E_{ss}}$ is independent of N, as used in the previous Section.

In real materials, atoms do not interact via pair potentials but rather by many-body interactions. Such multibody interactions are often represented by either interaction energies U_{mn}^{int} or effective pair potentials V_{mn}^{eff} [123] that can be derived from total system energies computed using first-principles methods or multibody interatomic potentials. A.2 elucidates more on these effective interaction quantities and how they relate to each other. In systems with atoms interacting via pair potentials, the effective pair potentials are related to the pair potentials by the relation

$$V_{mn}^{eff}(\|\boldsymbol{r}_{ij}\|) = U_{mm}(\|\boldsymbol{r}_{ij}\|) + U_{nn}(\|\boldsymbol{r}_{ij}\|) - 2U_{mn}(\|\boldsymbol{r}_{ij}\|) \tag{5.20}$$

Note that the effective pair potentials are non-zero only for non-equal pairs of atoms. Interaction energies involve the energies of m and n atoms at separation $\|\boldsymbol{r}_{ij}\|$ when embedded in a surrounding average representation of the alloy. This is equivalent to a statistical average over all possible random arrangements of all the atoms in the system except atom x at site i and atom y at site j. Relating to pair potentials, an average atom A can be introduced such that the $A-A$ interaction is $U_{AA}(\|\boldsymbol{r}_{ij}\|) = \sum_{m,n} c_m c_n U_{mn}(\|\boldsymbol{r}_{ij}\|)$ (refer Section 2.1.3). The interaction of an m atom and an A atom is then described as $U_{mA}(\|\boldsymbol{r}_{ij}\|) = \sum_n c_n U_{mn}(\|\boldsymbol{r}_{ij}\|)$. The interaction energy between atoms x and y can then be defined as

$$U_{mn}^{int}(\|\boldsymbol{r}_{ij}\|) = U_{mn}(\|\boldsymbol{r}_{ij}\|) - U_{mA}(\|\boldsymbol{r}_{ij}\|) - U_{nA}(\|\boldsymbol{r}_{ij}\|) + U_{AA}(\|\boldsymbol{r}_{ij}\|) \tag{5.21}$$

Derivations of Equations 5.20 and 5.21 are shown in A.2. It is easy to then show the sum rule $\sum_m c_m U_{mn}^{int}(\|\boldsymbol{r}_{ij}\|) = 0$ for all atomtypes n, which is useful below. Finally, the effective pair interaction and the interaction energy can be related without reference to any pair potential as

$$V_{mn}^{eff}(\|\boldsymbol{r}_{ij}\|) = U_{mm}^{int}(\|\boldsymbol{r}_{ij}\|) + U_{nn}^{int}(\|\boldsymbol{r}_{ij}\|) - 2U_{mn}^{int}(\|\boldsymbol{r}_{ij}\|) \tag{5.22}$$

With the above definitions, we can replace U_{xy} in Eq. 5.19 by $U_{mn}^{int} + U_{mA} + U_{nA} - U_{AA}$ (derived from Equation 5.21) and use the sum rule above to obtain the remarkably simple result

$$\sigma_{\Delta E_{ss}}^2 = \sum_{m,n} c_m c_n \sum_{\substack{i,j \\ i<0,j>0}} \left(U_{mn}^{int}(\|\boldsymbol{r}_{ij} + \boldsymbol{t}\|) - U_{mn}^{int}(\|\boldsymbol{r}_{ij}\|) \right)^2 + \mathscr{E}_{int} \tag{5.23}$$

where

$$\mathscr{E}_{int} = 2 \sum_{\substack{i \\ i<0}} \sum_{m} c_m (1 - c_m) \left(\sum_{\substack{j \\ j>0}} \left(U_{mA}(\|\boldsymbol{r}_{ij} + \boldsymbol{t}\|) - U_{mA}(\|\boldsymbol{r}_{ij}\|) \right) \right)^2 \tag{5.24}$$

is an extra term that is non-zero only for non-lattice slip vectors $\boldsymbol{t}$ (e.g. partial dislocations in fcc) but it is negligible (numerically validated in the next section). We will use this result in Section 5.4 where the interaction energies are obtained from full multi-body interactions.

Since the sums involve only pair distances and crystal structure, the normalized variance can further be written in a convenient form based only on normalized pair distances (d, d') in the crystal lattice as

$$\widetilde{\sigma}^2_{\Delta E_{ss}} = \sum_{m,n} c_m c_n \sum_{d,d'} U^{int}_{mn}(d) U^{int}_{mn}(d')\, \Theta_{dd'} + \mathscr{E}_{int} \tag{5.25}$$

where $U^{int}_{mn}(d)$ is the pair interaction at physical distance da with a the lattice constant. The numerical factor $\Theta_{dd'}$[1] depends only on the crystal structure and the slip system; values for full slip ($a/6[111]$) along a (110) plane in a bcc crystal and for full ($a/2[1\bar{1}0]$) and partial ($a/6[1\bar{2}1]$) slip along a (111) plane in an fcc crystal are shown in Table 5.1. Similarly, in terms of effective pair potentials, the normalized variance can be expressed as

$$\begin{aligned}\widetilde{\sigma}^2_{\Delta E_{ss}} = &\frac{1}{4} \sum_{m,n} c_m c_n \sum_{d,d'} V^{eff}_{mn}(d) V^{eff}_{mn}(d')\, \Theta_{dd'} \\ &- \frac{1}{2} \sum_{m,n,q} c_m c_n c_q \sum_{d,d'} V^{eff}_{mn}(d) V^{eff}_{mq}(d')\, \Theta_{dd'} \\ &+ \frac{1}{4} \sum_{m,n,p,q} c_m c_n c_p c_q \sum_{d,d'} V^{eff}_{mn}(d) V^{eff}_{pq}(d')\, \Theta_{dd'} + \mathscr{E}_{int}\end{aligned} \tag{5.26}$$

where we must note that $V^{eff}_{mm} = 0$ for all types m.

For a binary alloy, say $X_c Y_{1-c}$, Equation 5.26 simplifies to,

$$\widetilde{\sigma}^2_{\Delta E_{ss}} = c^2 (1-c)^2 \sum_{d,d'} V^{eff}_{XY}(d) V^{eff}_{XY}(d')\, \Theta_{dd'} \tag{5.27}$$

---

[1] Each diagonal element of $\Theta_{dd'}$, i.e. Θ_{dd}, is the sum of the number of d-distance pairs created and destroyed across the slip plane upon slip by $\boldsymbol{t}$ for each lattice site below the slip plane. Each off-diagonal element of $\Theta_{dd'}$ is the negative of the sum of the number of d-distance pairs that changed to d'-distance pairs and vice-versa upon slip by $\boldsymbol{t}$ for each lattice site below the slip plane.

d' d	0.866	1.0	1.414	1.658	1.732	2.0	2.179	2.236
0.866	4	-2	-2	0	0	0	0	0
1.0		4	0	-2	0	0	0	0
1.414			12	-8	0	0	-2	0
1.658				28	-4	-4	0	-8
1.732					8	0	-4	0
2.0			SYMMETRIC			8	0	0
2.179							36	-12
2.236								40

(a) $\Theta_{dd'}$ for $a/6[111]$ slip along (110) plane in bcc.

d' d	0.707	1.0	1.225	1.414	1.581	1.732	1.871	2.0	2.121	2.236
0.707	4	-2	-2	0	0	0	0	0	0	0
1.0		6	-2	0	-2	0	0	0	0	0
1.225			18	-4	-6	-2	-2	0	0	0
1.414				12	-4	0	-4	0	0	0
1.581					30	0	-6	-4	-6	-2
1.732						12	-8	0	0	0
1.871			SYMMETRIC				56	0	-16	-8
2.0								12	-4	0
2.121									66	-14
2.236										48

(b) $\Theta_{dd'}$ for $a/2[1\bar{1}0]$ slip along (111) plane in fcc.

d' d	0.707	1.0	1.155	1.225	1.354	1.414	1.581	1.683	1.732
0.707	2	-2	0	0	0	0	0	0	0
1.0		6	0	-4	0	0	0	0	0
1.155			2	-2	0	0	0	0	0
1.225				14	-4	0	-4	0	0
1.354					12	-4	-4	0	0
1.414			SYMMETRIC			6	0	-2	0
1.581							24	-4	-4
1.683								12	0
1.732									9

(c) $\Theta_{dd'}$ for $a/6[1\bar{2}1]$ slip along (111) plane in fcc.

Table 5.1 – Structure factors $\Theta_{dd'}$ in Equations 5.25 and 5.26 for various fcc and bcc slip systems in terms of pair distances (d, d'). The extended form of the third subtable for partial slip in fcc is provided in Ref. [7].

5.3 Validation of $\widetilde{\sigma}_{\Delta E_{ss}}$

To validate the results in the last section, we use model Lennard-Jones(LJ) pair potentials. We define 15 different pair interactions among 5 different types of atoms with the general form

$$U_{mn}(r) = 4\alpha_{mn}\epsilon\left[\left(\frac{\beta_{mn}\sigma}{r}\right)^{12} - \left(\frac{\beta_{mn}\sigma}{r}\right)^{6}\right] \tag{5.28}$$

where ϵ and σ are reference LJ energy and length quantities and α_{mn} and β_{mn} are dimensionless scaling parameters for each specific solute pair considered. Figure 5.4 shows the pair potentials U_{mn} versus radial distance r for the 15 different pairs among the five atom types denoted by A, B, C, D, and E; the respective α_{mn} and β_{mn} are tabulated alongside. These potentials have no physical significance — they are randomly chosen only to represent a complex multicomponent model system with a broad range of solute-solute interaction energies relative to the reference energy. The potential is also taken to be zero at distances beyond 10th neighbors in an fcc lattice and 8th neighbors in a bcc lattice. The pair potentials, crystal structure, and associated normalized pair distances d are the only quantities needed to compute $\widetilde{\sigma}^2_{\Delta U_{s-s}}$ using the results in the previous section (Equations 5.25, 5.26 and 5.24).

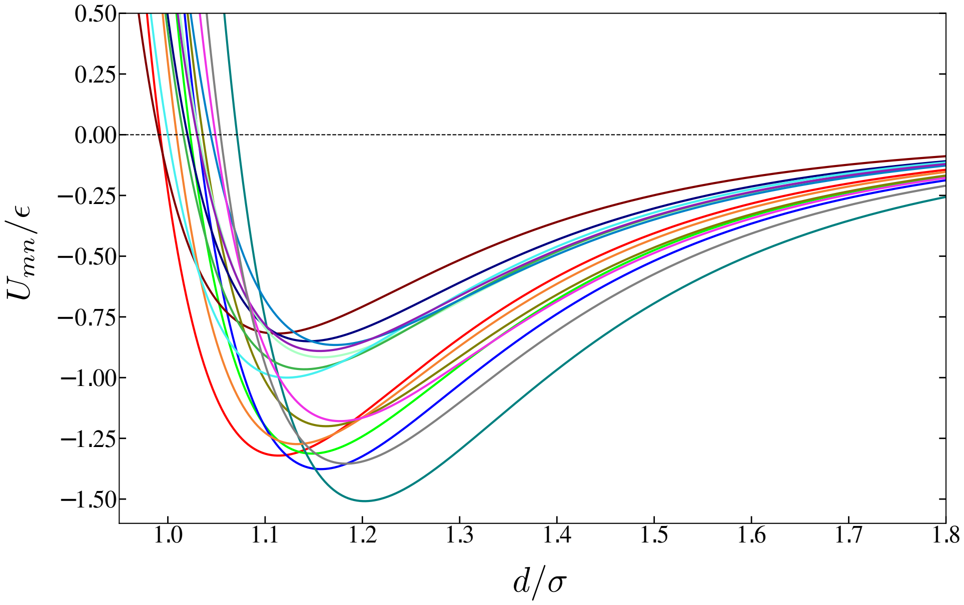

Atom pairs mn	α_{mn}	β_{mn}
AA	1.321	0.9922
BA	1.3128	1.023
BB	1.3768	1.0309
CA	0.8185	0.9906
CB	1.2	1.0359
CC	1.5086	1.0712
DA	0.8503	1.0201
DB	0.9164	1.0318
DC	1.2737	1.0090
DD	0.9657	1.016
EA	1.0	1.0
EB	0.8656	1.0442
EC	0.8904	1.03
ED	1.1792	1.0489
EE	1.3542	1.0541

Figure 5.4 – Lennard-Jones pair potentials U_{mn} versus radial distance r for all pairs among the 5 different atomtypes A, B, C, D, E. Every pair is tabulated alongside labelled by color, with the respective scaling parameters α_{mn} and β_{mn}.

The lattice constant for any given alloy composition is obtained by minimizing the total average energy of the alloy with respect to volume without allowing local relaxation of atoms away from the perfect lattice sites. This can be done analytically for both fcc and bcc lattices, leading to

$$a = \sigma \sqrt[6]{\frac{6\sum_{m,n} c_m c_n \alpha_{mn} \beta_{mn}^{12} \sum_d N_d / d^{12}}{\sum_{m,n} c_m c_n \alpha_{mn} \beta_{mn}^{6} \sum_d N_d / d^{6}}} \tag{5.29}$$

where d are the normalized pair distances and N_d the number of pairs in the lattice at normalized distance d, as shown in Table 5.2 for both fcc and bcc lattices.

d	0.866	1.0	1.414	1.658	1.732	2.0	2.179	2.236
N_d	8	6	12	24	8	6	24	24

(a) bcc

d	0.707	1.0	1.225	1.414	1.581	1.732	1.871	2.0	2.121	2.236
N_d	12	6	24	12	24	8	48	6	36	24

(b) fcc

Table 5.2 – Normalized neighbor distance and number of sites at that distance for bcc and fcc crystals.

Direct numerical simulations of the fluctuations in energy change due to slip in explicit random alloys are obtained as follows. We create a cuboidal simulation cell of lattice sites for the desired crystal structure conforming to the lattice parameter computed using Equation 5.29 for the respective alloy composition, with the z direction normal to the eventual slip plane. We randomly populate the atomic sites with A, B, C, D, and E atoms consistent with the alloy composition using the *random.choice* routine of *NumPy*[124]. Specifically, the probability that any site is occupied by an m atom is equal to the concentration c_m of the alloy. We impose periodic boundary conditions in the x and y directions to avoid boundary effects. We compute the total system energy for this initial random configuration of the alloy. We then displace the atoms in the upper half of the sample ($z > 0$) by the desired slip vector ($\mathbf{t}$) and compute the total energy of the sample. The difference between final and initial energies is ΔE_{ss} for the specific sample. For each alloy composition, this procedure is performed for a minimum of 1000 different realizations and the normalized standard deviation $\tilde{\sigma}_{\Delta E_{ss}}/\epsilon$ is computed with the ΔE_{ss} values associated with the realizations. We perform the above exercise on 10621 different alloy compositions consisting of binary, ternary, quaternary and quinary alloys, exhaustively covering the composition space of A-B-C-D-E alloys.

For fcc, the crystallographic orientation of the simulation cell is $x[\bar{1}01]$, $y[1\bar{2}1]$ and $z[111]$ with slip along the central (111) plane. The cell lengths are $L_x = 300a_f/\sqrt{2}$ and $L_y = 300a_f\sqrt{6}/2$ and $L_z = 2r_{cut}$ where r_{cut} is the cut-off radius of the pair potentials and a_f is the lattice parameter for fcc. Slip is induced by displacing the upper half of the simulation cell (i) by $a_f/\sqrt{2}$ along x direction for a full Burgers vector and (ii) by $a_f/\sqrt{6}$ along y direction for a Shockley partial Burgers vector. For bcc, the crystallographic orientation of the simulation cell is $x[111]$, $y[\bar{1}2\bar{1}]$ and $z[\bar{1}01]$ with slip along the central $[\bar{1}01]$ plane. The cell lengths are $L_x = 20a_b\sqrt{3}/2$, $L_y = 20a_b\sqrt{6}$ $(> 4r_{cut})$ and again $L_z = 2r_{cut}$ (Here a_b is the lattice parameter for bcc). Slip is induced by displacing the upper half of the simulation cell by $a_b\sqrt{3}/2$ along the x direction, which is a full Burgers vector.

Figure 5.5 compares the analytical prediction versus the simulation results for $\widetilde{\sigma}_{\Delta E_{ss}}/\epsilon$, for full slip in bcc, full slip in fcc, and partial slip in fcc, for all alloy compositions studied. In all cases, excellent agreement is obtained, validating the analytical prediction for $\widetilde{\sigma}_{\Delta E_{ss}}$. The spread of simulation results around the analytical predictions is expected because we use a finite number of simulations, leading to fluctuations around the exact $\widetilde{\sigma}_{\Delta E_{ss}}$ value that is derived in the theory. The fluctuations are thus larger for full slip in fcc (1000 realizations) as compared to bcc (5000 realizations).

The numerical simulations further enable us to determine the contribution of the term $\mathscr{E}_{int}$ in Equations 5.25 and 5.26 for partial slip in fcc. The *maximum* fractional errors (absolute value) across all the fcc random alloys studied here are 3.1%, 0.15% and 0.037% for binary, ternary and quaternary alloys, respectively. As a result, we advocate neglect of the additional term $\mathscr{E}_{int}$, which then enables the use of only interaction energies or effective pair potentials for assessing solute-solute effects due to partial slip.

With the results of Section 5.2 fully validated, we can now apply the theory and assess the practical consequences of solute-solute interactions on the yield strength of various alloys.

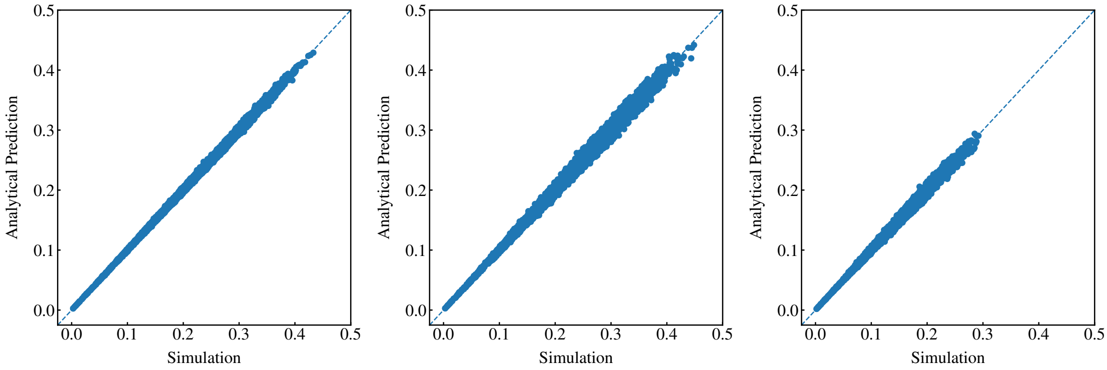

(a) $\frac{a}{2}[111](\bar{1}01)$, bcc (b) $\frac{a}{2}[\bar{1}01](111)$, fcc (c) $\frac{a}{6}[1\bar{2}1](111)$, fcc

Figure 5.5 – Validation of analytical prediction for $\widetilde{\sigma}_{\Delta E_{ss}}$ derived in Setion 5.2 against simulations. Data corresponding to 10621 different alloy composition with the five atomtypes consisting of binary, ternary, quaternary and quinary alloys, is shown. The dashed line corresponds to exact agreement; deviations arise only due to statistical variations in the simulations due to a finite number of samples studied.

5.4 Strengthening in high entropy and dilute binary alloys due to solute-solute interactions

5.4.1 MoNbTaW and NbTaV bcc high- and medium- entropy alloys

Strengthening due to solute-dislocation interactions has been predicted recently in MoNbTaW based on control of the yield stress by edge dislocations[109]. The predictions are in good quantitative agreement with experiments over a range of temperatures. However, Körmann et al. recently calculated effective pair potentials versus distance for all pair combinations in the MoNbTaW using a first-principles method [5]. These interactions are shown in Figure 5.6, where it is seen that the near-neighbor effective pair interaction (positive indicating a preference for unlike pair binding) exceeds 100 meV for Mo-Ta and exceeds 60 meV for Mo-Nb and W-Ta. The B2 phase is found to be stable for this HEA[5] which means stronger binding energies for unlike pairs compared to like pairs — justifying the mostly positive near-nearbour effective pair interactions in Figure 5.6. These effective pair potentials are comparable to individual solute-dislocation interaction energies in the dislocation core [109] and hence the solute-solute interaction energies could possibly affect the yield strength. Applying the theory here to calculate $\widetilde{\sigma}_{\Delta E_{ss}}$ based on the Körmann et al. results, we find that solute-solute interactions make a very small contribution to the strengthening. Specifically, Table 5.3 shows the solute-dislocation interaction energy parameter $\Delta\widetilde{E}_{\mathrm{p},sd}(w_c)$, w_c, and the solute-solute interaction contribution $\sqrt{w_c \rho_G}\widetilde{\sigma}_{\Delta E_{ss},f}$ computed via Equation 5.10, and finally the resulting total energy parameter $\Delta\widetilde{E}_{\mathrm{p}}(w_c)$ accounting for both solute-solute and solute-dislocation interactions. The solute-solute interaction energies then increase the strength by only 2%.

Maresca et al. also studied several model bcc HEAs in the Mo-Nb-Ta-V-W family as described by EAM potentials [125–127]. They compared theory using only solute-dislocation interaction energies to direct molecular statics simulations at T=0K and found generally good agreement, suggesting that solute-solute contributions are again small. Here, we consider the ternary alloy NbTaV as an example. The interaction energies $U^{int}_{mn}(d)$ for this system were computed using the same interatomic EAM potentials[128]. The values are typically smaller than those in MoNbTaW obtained from first-principles, and so even smaller effects on strengthening can be anticipated. The predictions of the total energy parameter without and with the solute-solute interactions, and the resulting difference in strength, are also shown in Table 5.3. The strengthening due to solute-solute interactions in the model NbTaV alloy is negligible, ~ 0.5%.

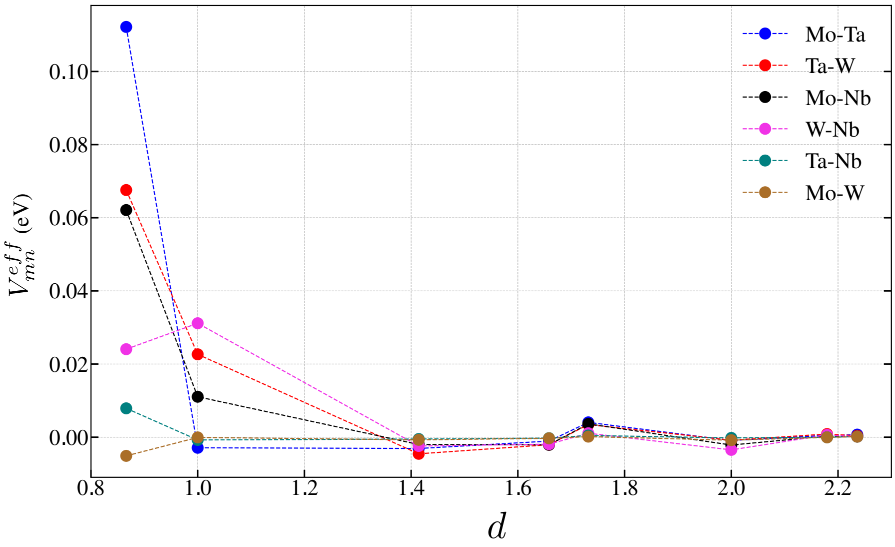

Figure 5.6 – The effective pair potentials V_{mn}^{eff} as a function of normalized nearest-neighbour pair separation d, for bcc MoNbTaW calculated via first principles[5].

Alloys	$w_c/(b/3)$	$\Delta\widetilde{E}_{\mathrm{p},sd}(w_c)$ (eV)	$\sqrt{w_c \rho_G}\widetilde{\sigma}_{\Delta E_{ss},f}$ (eV)	$\Delta\widetilde{E}_{\mathrm{p}}(w_c)$ (eV)	τ_{y0}/τ_{y0}^{sd}
MoNbTaW (DFT inputs [5])	13	0.766	0.1323	0.7773	1.0197
NbTaV (EAM inputs [125–127])	13	0.7343	0.06	0.7368	1.0045

Table 5.3 – Role of solute-solute interactions in solute solution hardening of bcc MoNbTaW and NbTaV high-entropy alloys, with inputs from either DFT or interatomic potentials. For each alloy, the characteristic amplitude w_c, solute-dislocation interaction energy parameter $\Delta\widetilde{E}_{\mathrm{p},sd}(w_c)$, solute-solute interaction energy parameter computed from the solute interactions and w_c, and the total energy parameter $\Delta\widetilde{E}_{\mathrm{p}}(w_c)$ are shown. The strengthening with solute-solute interactions is compared to the strengthening with only solute-dislocation interactions, and the increases in strength are negligible.

The above applications demonstrate that solute-solute interactions have little effect on strengthening in the bcc refractory HEAs when the effective pair interactions are ~ 100meV or smaller. This result stems in part because the T=0K strength due to solute-dislocation interactions is very high in these alloys. With increasing pair interaction energies, alloys are generally susceptible to decomposition into intermetallic phases. Körmann et al. show that the computed near-neighbor interactions in MoNbTaW are sufficient to drive B2 ordering at a temperature of ~ 1300K and that inclusion of the longer-range interactions decreases this transition temperature to ~ 750K. Thus, the random MoNbTaW alloy has interaction energies in a range where order can be created at fairly high temperatures and yet these solute-solute interactions make negligible contributions to the yield strength. We can tentatively conclude that for those bcc alloys able to be fabricated as single-phase random alloys, the solute-solute interaction energies will be sufficiently small that their effects on yield strength can be neglected.

5.4.2 Dilute Ni-Al fcc solid solution alloys

In Ni alloys with Al solutes, it is well-established that Al-Al pairs have a strong repulsion at first neighbour distance (0.243 eV as computed by first-principles[67]). This repulsion plays a key role in the formation of ordered NiAl precipitates that are the basis of Ni superalloys. While the ordered precipitates in NiAl superalloys consume most of the Al, the Ni-rich matrix can retain ~ 12% Al in solution. Thus, it is of interest to examine the strengthening of Ni by Al in the composition range 0–12% Al. Although the large near-neighbor Al-Al repulsion might easily drive SRO in the real material, here we assess whether the large repulsion has an effect on the yield strength of the random solid solution.

We study Ni-Al random alloys using inputs from DFT calculations[67] and two available EAM potentials (Mishin 2004 [129] denoted as M04; Pun-Mishin 2009 [81] denoted as PM09). Figure 5.7 shows the computed Al-Al interaction energies for the first three neighbor distances, the Al and Ni misfit volumes, and the alloy elastic constants, as a function of Al concentration for the two EAM potentials using the accurate average alloy approximation (see Section 2.1.3). The elastic constants are nearly composition-independent and there is excellent agreement among the two potentials and experiments [130]. The Al-Al interactions in bulk and across the stacking fault differ by less than 3.7% across all compositions; the figure shows the average of the two cases. Figure 5.7 also shows the Al and Ni misfit volumes obtained from experimental lattice-parameter data [6] on Ni-Al alloys. The Al misfit volume for the M04 potential agrees well with experiments while that for the PM09 potential deviates significantly, and varies dramatically with Al concentration, being very low at low Al content. Experimental solute pair interaction energies are not obtainable so we compare with the DFT interaction energy of 0.243 eV (computed using 2 first-neighbor Al atoms in a fully-periodic 108-atom cell with 106 Ni atoms). The value for PM09 agrees reasonably well with the DFT value but the value for M04 is nearly twice as large. While not shown here, the stable stacking fault energy for the M04 potential is strongly composition-dependent, decreasing from 134 $\mathrm{mJ/m^2}$ in pure Ni to 45 $\mathrm{mJ/m^2}$ at 12% Al. For the PM09 potential, the variation is smaller, from 134 $\mathrm{mJ/m^2}$ in pure Ni to 87.5 $\mathrm{mJ/m^2}$ at 12%Al. Overall, neither of the two EAM potentials can be considered quantitative for real Ni-Al; the various trends they exhibit with Al concentration will greatly influence the overall strength predictions and also the relative contributions of the solute-dislocation and solute-solute interactions.

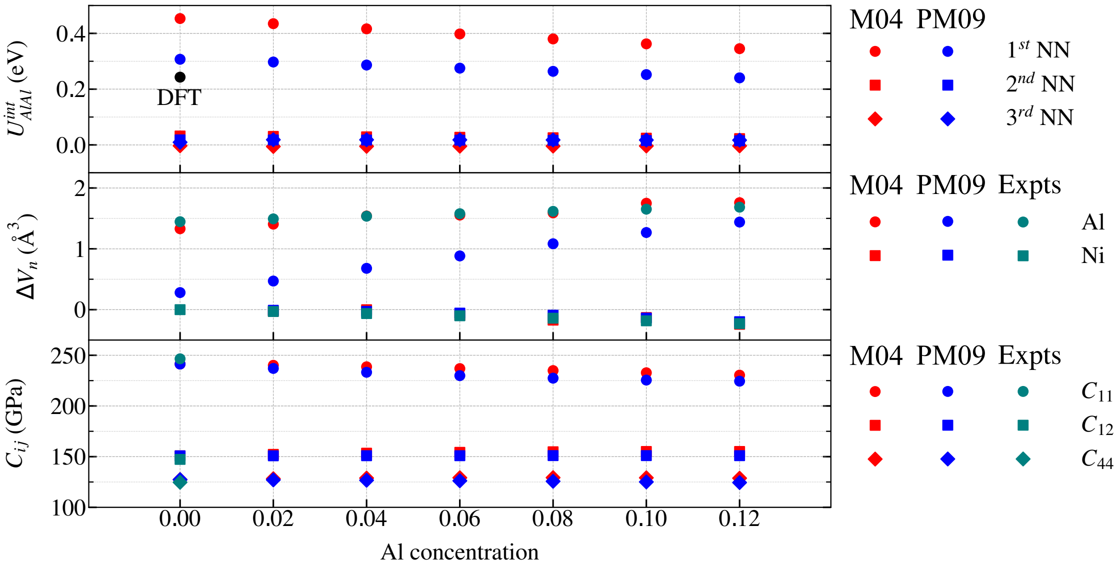

Figure 5.7 – Alloy-specific inputs for strength prediction versus Al concentration: Al-Al interaction energies U^{int}_{AlAl}, solute(n) misfit volume ΔV_n and elastic constants C_{ij}. The Al-Al interaction energies are shown for the first three near-neighbour(NN) distances across the slip plane, only the first NN interaction is significant. Misfit volumes are computed from experimental data[6] on lattice parameter versus composition.

The interaction energies, misfit volumes and the elastic constants constitute the major necessary inputs for strengthening due to solute-dislocation interaction energies using the elasticity theory as per Equation 5.8 and solute-solute interaction energies using Equation 5.10. However, the partial core separation d_p and the partial core spreading σ determine the dislocation roughening amplitude w_c and eventually the structural coefficient $g(w_c, d_p, \sigma, A)$ in Equation 5.8. Here we use $d_p = 9b$ and $\sigma = 2b$ that are close to those obtained from the potentials for pure Ni. For this d_p, there are two solutions $w_{c,1} = 5b$ and $w_{c,2} = 16b$, as mentioned earlier and first identified in [119]. The corresponding structural coefficients are $g(w_{c,1}, d_p, \sigma, A) \sim 0.25$ and $g(w_{c,2}, d_p, \sigma, A) \sim 0.47$. The Zener anisotropy ratio $A = 2.5 - 3.33$ leads to minimal corrections [120].

A few details merit comment. First, the strong composition dependence of the stacking fault energy of the M04 potential implies that the partial separation d_p is composition dependent. For simplicity, this is neglected here. Second, since $w_{c,2} > d_p$ the solution for $w_{c,2}$ should account for solute-solute interactions. However, in this system where only first-neighbor interactions are important, $\Theta_{dd'}$ for full slip is twice that for partial slip, and so the additional term $2\tilde{\sigma}^2_{\Delta E_{ss},p} - \tilde{\sigma}^2_{\Delta E_{ss},f}$ in Eq. 5.10 is negligible. Third, predictions based on the DFT-computed Al-Al interaction energy are made using the experimental misfit volumes and elastic constants.

With the above information, we can now assess the energy fluctuation quantity $\Delta\widetilde{E}_{\mathrm{p}}(w_c)$ that determines all subsequent alloy strengthening properties. To reveal the role of solute-solute interactions, we show in Figure 5.8a the (i) the fluctuation quantity $\Delta\widetilde{E}_{\mathrm{p}}(w_c)$ accounting for both solute-solute and solute-dislocation interactions and (ii) the contribution $\Delta\widetilde{E}_{\mathrm{p},sd}(w_c)$ due to solute-dislocation interactions only, as a function of Al concentration. For the DFT interaction energies, the role of solute-solute interactions increases steadily with increasing concentration for both w_c solutions— with the total energy fluctuation increasing by ~ 15% at 2%Al and by ~ 50% at 12%Al relative to $\Delta\widetilde{E}_{\mathrm{p},sd}(w_c)$ due to the addition of solute-solute interactions. For the potentials, the solute-solute contributions are much larger. The M04 potential, which has a reasonable misfit volume but very large interaction energy, predicts more than 40% increase even at 2% Al and ~ 100% increase at 12% Al. The PM09 potential, which has a reasonable solute-solute interaction energy but a much smaller Al misfit at low Al concentrations, predicts a ~ 130% increase at 2% Al and ~ 90% increase 12% Al. The solute-solute effects are significant across all cases at 12%Al, with the interatomic potentials showing very large effects that, however, are likely due to the inaccuracies of the potentials.

Figure 5.8b shows the fractional increase in zero-temperature flow stress above that due to solute-dislocation interactions only. The effects of solute-solute interactions on the flow stress are larger than on the energy parameter because $\tau_{y0} \sim \Delta\widetilde{E}_{\mathrm{p}}^{4/3}(w_c)$. These results highlight the significant differences between potentials and DFT, especially for the PM09 potential at low Al concentrations because of the very small misfit volume of Al for that potential. At the realistic residual Al concentration of 12% in Ni-Al superalloys, the strength of an assumed random Ni-Al matrix is predicted, using DFT/experimental inputs, to be 70% higher than the strength considering solute-dislocation interactions alone.

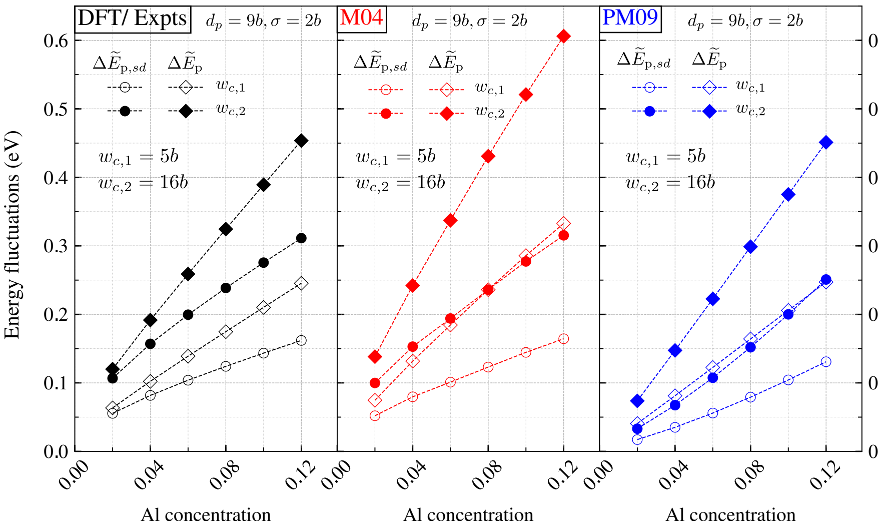

(a) The energy fluctuation quantities, $\Delta\widetilde{E}_{\mathrm{p}}(w_c)$ and $\Delta\widetilde{E}_{\mathrm{p},sd}(w_c)$, key to the solute-strengthening theory, the former with solute-solute interactions and the latter without (accounts only for solute-dislocation interactions).

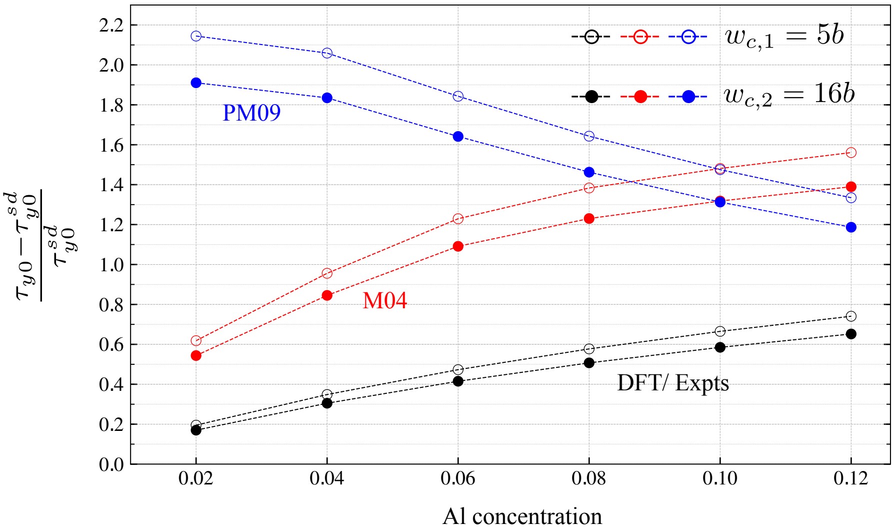

(b) Relative contribution of the solute-solute interactions to yield stress at T=0K. Note that $\tau_{y0}/\tau_{y0}^{sd} = \left[\Delta\widetilde{E}_{\mathrm{p}}(w_c)/\Delta\widetilde{E}_{\mathrm{p},sd}(w_c)\right]^{4/3}$.

Figure 5.8 – (a) Total energy fluctuations entering the solute-strengthening theory and the contribution of solute-dislocation interactions only, for DFT and EAM potential inputs and for both solutions of w_c; (b) Predicted fractional increase in T=0K yield stress due to the inclusion of solute-solute interactions, for DFT and EAM potential inputs, for both solutions of w_c.

We now make some comparisons of our predictions against simulation results of Antillon et.al[131], who used the M04 potential. Antillon et al. performed molecular dynamics studies at T=1K and also reported that molecular statics (energy minimization) results showed strengths estimated to be 1.4 times larger. Our experience with MD of dislocation motion in random alloys suggests that there are dynamic instabilities that can trigger unabated dislocation motion at stresses well below the values that are predicted and obtained using molecular statics methods. The release of energy upon the initial motion of segments pinned at lower-than-average barriers can then start a dynamic process that might not be possible under conditions more typical of experiments (much lower stresses, much longer time scales). In Ni-Al, we predict, however, two solutions — one with high stress and low barrier and another with a low stress and high barrier. We postulate that the dislocation motion observed in dynamic MD simulations can be halted by the large barriers of the second solution, which are harder to overcome by dynamic effects, while the quasistatic (energy minimization simulations) may be controlled more by the first solution. We will thus compare the simulations of Antillon et al. to predictions of both the first and second solutions. In their numerical interpretation of their simulations, Antillon et al. did not consider the existence of this second solution, but rather considered the multi-scale roughening model of Zaiser [132] and Leyson et al. [36].

Antillon et al. reported values for ζ_c and w_c derived from the correlation function along the dislocation line at a stress just below the measured flow stress. Figure 5.9a shows our predicted $\zeta_{c,1}$ and $\zeta_{c,2}$ corresponding to solutions of $w_{c,1}$ and $w_{c,2}$, respectively, versus Al concentration along with the values from Antillon et al. There is reasonable agreement between $\zeta_{c,2}$ and the critical value of Antillon et al. just below flow. This suggests that our postulate that the Antillon simulations are controlled by the second solution is reasonable. The roughening amplitude w_c reported by Antillon et.al for Ni-10%Al is 10–12.5b, midway between our predictions for $w_{c,1}$ and $w_{c,2}$. We do note that $w_{c,2}$ would be larger at higher concentrations if the concentration-dependence of d_p was considered.

Figure 5.9b shows our predictions of the critical resolved shear stress τ_{y0} and the simulations of Antillon et al. as a function of Al concentration. We present both solutions corresponding to $w_{c,1}$ and $w_{c,2}$, and also the dynamic and (estimated) quasistatic results from Antillon et al. The estimated quasistatic simulations are in reasonable agreement with the first solution, corresponding to the smaller barriers that are predicted to control low-T strength under more realistic experimental conditions and in non-dynamic (energy-minimizing) simulations. The dynamic simulations align more closely with, but overestimate, the second solution that corresponds to the large barriers. The critical stresses in the simulations were taken after dislocation motion of $\sim 42b$. This is larger than the value for overcoming individual barriers, $\gg w_{c,2}/2 (= 8b)$. Thus, the simulation values are expected to be higher than the theory because a finite length dislocation line will encounter ever-stronger pinning environments with increasing glide distance, as demonstrated in [4]. The longest finite-length simulations in Antillon et al., however, are generally $\gg \zeta_c$ so that this effect is less prominent than found in Varvenne et al. Overall, the level of agreement between the present theory and simulations is not quantitative, but the simulations have challenges and the theoretical predictions have no fitting parameters at all. The ability of the parameter-free theory to bracket the simulations is encouraging.

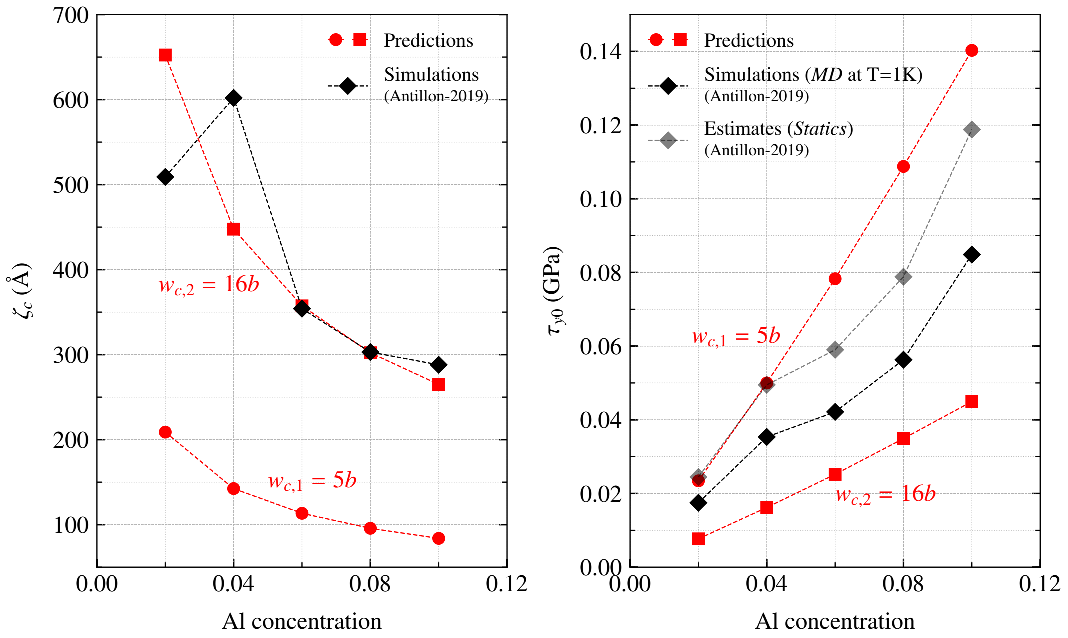

Figure 5.9 – Validation of theory against simulations: characteristic wavelength of dislocation waviness and the yield stress. M04 interatomic potential is used for both predictions and simulations.

Quasistatic simulations of dislocation motion at T=0K using the PM09 potential were presented briefly by Proville et al.[133]. Those simulations used a dislocation line length of 69Å, which is somewhat smaller than the lengths ζ_c predicted for all Al concentrations studied. The present theory is not directly applicable at such short lengths. Varvenne et al. showed that a modified analysis could be applied for dislocation lengths at ζ_c, but that result is not directly extendable to other lengths. We therefore cannot make reliable predictions associated with the simulations of Proville et al.

5.5 Summary

We have presented the theoretical framework for the incorporation of specific solute-solute interactions into a previous theory for solute strengthening in random alloys. The previous theory considered only the solute-dislocation interaction energies. We derived and validated an exact general expression for the energy fluctuations due to solute-solute interactions during dislocation glide. Specific results were provided for fcc and bcc crystal structures, and the analysis validated on over 10,000 model fcc and bcc alloy compositions described by Lennard-Jones pair potentials. We also demonstrated that, in a number of situations, the characteristic amplitude w_c of the wavy dislocation is unchanged upon the introduction of solute-solute interactions, making their inclusion into the existing theory far easier. The key results of the original theory within the analytic elasticity limit are shown here in Figure 5.2 to enable easy application of the theory by researchers in the field.

The new theory has been applied to several alloys. Most importantly, it has been applied to the bcc MoNbTaW high-entropy alloy for which effective solute-solute pair interactions were recently reported. We show that the solute-solute interactions make a negligible contribution to the strengthening even though the effective pair energies can be as high as 100meV. A similar conclusion was reached in analysis of a model NbTaV alloy described by EAM potentials. The theory was also applied to dilute fcc Ni-Al alloys, where the Al-Al interactions are very strong and the solute-dislocation strengthening much lower than in other alloys. For this material, solute-solute interactions can play an important role in strengthening, with a 60% increase in strength at 10% Al when using DFT-computed interaction energy. We also show that existing Ni-Al interatomic potentials have widely differing properties and hence yield very different results for the effects of solute-solute strengthening (typically much higher than that predicted with DFT/experimental inputs). We then made some connection to atomistic simulations reported in the literature, with some insights revealed.

The current theory with solute-solute interactions can be challenging to implement due to the difficult of determining the the solute-solute interactions. The recent DFT studies show that estimated interactions can be obtained with extensive computations, and this is likely the only path for obtaining realistic values. However, it remains possible to execute parametric studies to determine what levels of solute-solute interactions would be needed to significantly increase the strength and then determine empirically whether such interactions are reasonable if the alloy is to be a single-phase random alloy. This latter strategy is strongly recommended as a first step before embarking on expensive first-principles calculations.

Strong solute-solute interactions can lead to the development of short-range order (SRO). The present theory applies only to random alloys with no SRO, and so is relevant to alloys processed at sufficiently high temperatures and quenched to low temperatures such that SRO is minimized. The inclusion of SRO into the theory can be made by using the current general framework and introducing the appropriate solute-solute correlation functions (e.g. Warren-Cowley short-range order parameters), but specific analytic results remain challenging. We will report on a theory for SRO in the near future.

With the present inclusion of solute-solute interactions, we believe the theory for strengthening in random alloys is essentially complete. As with all theories, there are approximations and those approximations must be assessed carefully. However, the theory has no adjustable parameters. The challenge in applying the theory is in obtaining the necessary material parameters. The reduced elasticity theory simplifies the problem for solute-dislocation interactions, such that the required inputs are the elastic constants, lattice constant, misfit volumes of the solutes, and the dislocation core structure in the alloy. The first three can be computed using first-principles methods [37, 121] but the core structure remains very challenging. Fortunately, studies indicate that the dependence on the core structure may be small in some important cases (fcc with low SFE; bcc edge dislocations), but this remains a source of uncertainty. As discussed above, determining the solute-solute interactions requires computationally intensive first-principles methods which should be reserved for alloys where the solute-dislocation interactions are weak and/or where solute-solute interactions can be anticipated to be large, e.g. by considering the heats of formation of binary sub-alloys. This remains an area for future research.

Based on all the findings here, we advocate for the application of the previous solute-dislocation theory only as a means of theoretically-guided search for promising new alloys. Deviations between theory and experiment in any such new alloys would then motivate a more-detailed study of the role of solute-solute interactions and, ultimately, the role of possible short-range-order.

6 Solute-strengthening in alloys with short-range order

The thesis principally focuses on random alloys, since they are an important limiting case. In the solute-strengthening part of the thesis, heretofore a theory has been developed for random alloys which addresses the energy contributions responsible for pinning dislocation segments in favourable solute environments, thus strengthening the alloy. These contributions are from solute-dislocation interactions and solute-solute interactions across the slip plane. However, solute-solute interactions can thermodynamically drive chemical ordering in the form of short-range order (SRO) and long-range order (LRO). They can also drive phase separation or precipitation. Generally due to slow kinetics in complex alloys the alloy at room temperature is out of equilibrium and retains negligible or no SRO from the processing conditions in which it was heat-treated. However in service the equilibrium ordering may develop eventually or in case some solute pairs interacts strongly some residual SRO may be present. A considerable research in recent years has been devoted to identify SRO in medium- and high-entropy alloys and to study their effect on alloy strength [41–43, 47, 84, 85, 134–136]. SRO has been studied extensively for binary alloys during the 1950s and 1960s, when experimental methods were devised to measure SRO [39, 40] and analytical prediction of strengthening due to SRO was attempted [44–46]. Recently there have been a couple of studies improving on experimental characterization of SRO in binary alloys [137, 138] and they suggested the influence of SRO on strength and stacking fault energy [139–141].

In light of the prevailing interest on this topic of chemical ordering in both dilute and complex alloys, this final chapter of the "solute-strengthening" part of the thesis is devoted to a general theory for solute-strengthening which will account for SRO, and will revert back to the theory presented in Chapter 5 in the limit of random alloys (no SRO). Comparisons are made with already existing theories [45, 47] which either incomplete or partially incorrect in handling the energy fluctuations due to different solute interactions. The new theory presented here will still encompass two solute interactions, one with the dislocation and the other with other solutes across the slip plane. However unlike random alloys, here the solute-solute interactions causes an "*average strengthening*" effect in alloys with SRO, which was first addressed qualitatively by Fisher [44]. In alloys with SRO, certain solute pairs either prefer to stay as neighbours or they avoid close proximity. The slip associated with dislocation glide can bring unfavourable pairs together or drift apart favourable solute pairs *on average* — this is associated with an energy cost that needs to be paid by externally applied stress to sustain unabated glide of dislocation line, thereby strengthening the alloy. The local strengthening due to glide of characteristic dislocation segments of length ζ_c in a fluctuating solute environment also gets modified in the presence of SRO.

To predict the role of SRO on alloy strength, first we need to characterize SRO mathematically. Section 6.1 characterizes SRO with correlation functions and relates pair correlation functions to the well-known Warren-Cowley parameter [39, 142, 143]. Section 6.2 discusses some useful properties of the pair correlation functions. The new strengthening theory depends on higher-order correlation functions involving more than two sites. Higher-order correlation functions are not obtained experimentally and are not easily available. Therefore Section 6.3 introduces a superposition approximation for higher-order correlation functions which approximates the latter in terms of only pair correlation functions. The section also discusses the implications of the superposition approximation. Section 6.4 presents the new theory, elaborating in detail the average strengthening observed in alloys with SRO. Section 6.5 derives expression for the variance in energy change due to the glide of dislocation segments of length ζ by distance w, which is the pivotal energy quantity controlling local strengthening in alloys. Section 6.6 summarizes the chapter.

6.1 Characterizing short-range order

Short-range order(SRO) is said to exist when the occupancy of an atomic site i by an atom type n is conditional on the atom types occupying the surrounding atomic sites. In this section, we are going to formulate SRO mathematically. Readers must refer Section 2.8 for notations and basic concepts in probability which will be relevant here.

Let s_i^n be the site occupation variable which is 1 when site i is occupied by atom type n and 0 otherwise. Therefore occupancy of site i by atom type n is given by $s_i^n = 1$. **P** being the probability operator, the probability of distinct sites $i, j, \ldots$ to be occupied by types $n, m, \ldots$ respectively is given by $\mathbf{P}(s_i^n = 1, s_j^m = 1, \ldots)$. In an alloy with SRO, we define the joint probabilities for site occupancy as follows using correlation functions $\lambda_{nm\ldots}^{ij\ldots}$,

$$\begin{aligned}
\mathbf{P}(s_i^n = 1) &= c_n \quad \forall i, \;\; c_n \text{ is the concentration of type } n \\
\mathbf{P}(s_i^n = 1, s_j^m = 1) &= \lambda_{nm}^{ij}\, c_n c_m \quad \forall i, j \;\; \text{s.t. } i \neq j, \\
\mathbf{P}(s_i^n = 1, s_j^m = 1, s_k^p = 1) &= \lambda_{nmp}^{ijk}\, c_n c_m c_p \quad \forall i, j, k \;\; \text{s.t. } i \neq j \neq k, \\
\mathbf{P}(s_i^n = 1, s_j^m = 1, s_k^p = 1, s_l^t = 1) &= \lambda_{nmpt}^{ijkl}\, c_n c_m c_p c_t \quad \forall i, j, k, l \;\; \text{s.t. } i \neq j \neq k \neq l, \\
&\vdots
\end{aligned} \tag{6.1}$$

where $\lambda^{ij}_{nm}, \lambda^{ijk}_{nmp}, \lambda^{ijkl}_{nmpt}, \ldots$ are the pair, 3-site, 4-site, … correlation functions. In this chapter we will require upto 4-site correlation functions. *Henceforward, different site indices will mean different physical sites unless in summations or mentioned otherwise.* In random alloys where all the lattice site occupancies are mutually independent, every correlation function in Equations 6.1 equals 1.

The pair correlation function λ^{ij}_{nm} is invariant to whether site i is occupied by n and j by m or vice-versa since it depends only the distance between the two sites. Mathematically, $\lambda^{ij}_{nm} = \lambda^{ij}_{mn}$. Other properties of the pair correlation functions are discussed in Section 6.2.

In the literature, the 2-site correlations for alloys with SRO are characterized by the Warren-Cowley parameters α^{ij}_{nm} [39], which are given by

$$\alpha^{ij}_{nm} = 1 - \frac{\mathbf{P}(s^n_i = 1 \big| s^m_j = 1)}{c_n} \tag{6.2}$$

where $\mathbf{P}(s^n_i = 1 \big| s^m_j = 1)$ is the conditional probability of site i being occupied by type n when site j is already occupied by type m. Using the definition of conditional probability (Equation 2.67) and Equation 6.1, Equation 6.2 can be simplified as

$$\alpha^{ij}_{nm} = 1 - \frac{\mathbf{P}(s^n_i = 1, s^m_j = 1)}{c_n c_m} = 1 - \lambda^{ij}_{nm} \tag{6.3}$$

Using λ is convenient since we do not have to carry a one in all our upcoming derivations. However we will be expressing our results as a sum of random alloy term plus a term accounting for SRO contribution — the latter will have $1 - \lambda$ which is the well-known Warren-Cowley parameter.

6.2 Properties of pair correlation functions

From a material science point of view, the pair correlation functions are not arbitrary but related to the underlying energetics of the alloy. If a certain solute pair has lower energy than the rest of the pairs, then we can say that solute pair forms a strong bond and the corresponding solutes attract. Then the pair correlation λ for that pair is more than one. Likewise, the pair correlation function for a pair of solutes which repels is less than one. Quantitative relation between energetics of the system and the pair correlation functions is elusive, but a qualitative understanding like the one stated above is more tangible.

The pair correlation functions satisfies certain inequalities. These can be deduced with the help of conditional probabilities of the sort $\mathbf{P}(s^n_i = 1 \big| s^m_j = 1)$, which implies the probability of finding type n at site i given that site j is occupied by type m. Using Equations 2.67 and 6.1, we can write the following expressions with conditional probabilities

$$\mathbf{P}(s_i^n = 1 | s_j^m = 1) = \lambda_{nm}^{ij}\, c_n$$
$$\mathbf{P}(s_i^m = 1 | s_j^n = 1) = \lambda_{mn}^{ij}\, c_m$$

Since $\lambda_{nm}^{ij} = \lambda_{mn}^{ij}$ and probability is non-negative and ≤ 1, one can easily deduce from the above two equations that

$$0 \leq \lambda_{nm}^{ij} \leq \min\left(\frac{1}{c_n}, \frac{1}{c_m}\right) \tag{6.4}$$

Also all the pair correlation functions are not independent. Since the sum of probabilities of all possible outcomes equals 1, we can write

$$\sum_n \mathbf{P}(s_i^n = 1 | s_j^m = 1) = 1 \quad \forall m$$

In terms of pair correlation functions the above expression can be rewritten as,

$$\sum_n \lambda_{nm}^{ij}\, c_n = 1 \quad \forall m \tag{6.5}$$

which shows that the pair correlation functions are not independent. The pair correlation functions for solutes of the same type can be expressed in terms of the pair correlation functions of solutes of unlike types as follows,

$$\lambda_{mm}^{ij} = \frac{1}{c_m}\left(1 - \sum_{\substack{n \\ n \neq m}} \lambda_{nm}^{ij} c_n\right) \quad \forall m \tag{6.6}$$

Based on Equation 6.6 and the symmetry $\lambda_{nm}^{ij} = \lambda_{mn}^{ij}$, one can deduce that for an alloy with M components, there are only $\frac{M(M-1)}{2}$ independent pair correlation functions for every pair of sites (i, j). Therefore, for instance, there is only one independent pair correlation function for binary (M=2) alloy and three independent pair correlation functions for ternary (M=3) alloy and so on.

In terms of the Warren-Cowley parameters α_{nm}^{ij}, Equation 6.6 can be rewritten as,

$$\begin{aligned}\lambda_{mm}^{ij} &= \frac{1}{c_m}\left(1 - \sum_{\substack{n \\ n\neq m}} (1-\alpha_{nm}^{ij})c_n\right) \\ &= \frac{1}{c_m}\left(1-(1-c_m) + \sum_{\substack{n \\ n\neq m}} \alpha_{nm}^{ij}c_n\right) = 1 + \frac{1}{c_m}\sum_{\substack{n \\ n\neq m}} \alpha_{nm}^{ij}c_n\end{aligned}$$

$$\text{Therefore,} \quad \alpha_{mm}^{ij} = -\frac{1}{c_m}\sum_{\substack{n \\ n\neq m}} \alpha_{nm}^{ij}c_n \quad \forall m \tag{6.7}$$

6.3 Superposition approximation for higher-order correlation functions

With the superposition approximation, the higher-order correlation functions (3-site, 4-site, ...) assumes the following form

$$\begin{aligned}\lambda_{pqr}^{ijk} &= \lambda_{pq}^{ij}\lambda_{pr}^{ik}\lambda_{qr}^{jk} \\ \lambda_{pqrt}^{ijkl} &= \lambda_{pq}^{ij}\lambda_{pr}^{ik}\lambda_{qr}^{jk}\lambda_{qt}^{jl}\lambda_{rt}^{kl}\lambda_{pt}^{il} \\ &\vdots\end{aligned} \tag{6.8}$$

There is no general quantification of the goodness of this approximation. However in binary Ni-Zr system, the approximation has been reported to work well in the limit when the pair correlation functions are small [144]. In this section we will prove however that only in the limit of small pair correlation functions does the approximation conforms to a valid probability space.

The sum of probabilities of site i being occupied by the different atom types must always be 1. Therefore for sites i, j, k, the following is always true

$$\begin{aligned}&\sum_p \mathbf{P}(s_i^p = 1 | s_j^q = 1, s_k^r = 1) = 1 \\ \Longrightarrow &\sum_p \frac{\lambda_{pqr}^{ijk}}{\lambda_{qr}^{jk}} c_p = 1 \quad \text{(Using Equations 2.67 and 6.1)}\end{aligned} \tag{6.9}$$

For the superposition approximation to be a valid probability description, Equation 6.9 must hold true under the approximation for λ^{ijk}_{pqr} (Equation 6.8). Therefore,

$$\begin{aligned}
\sum_p \frac{\lambda^{ijk}_{pqr}}{\lambda^{jk}_{qr}} c_p &= \sum_p \lambda^{ij}_{pq}\lambda^{ik}_{pr} c_p \\
&= \sum_p (1-\alpha^{ij}_{pq})(1-\alpha^{ik}_{pr}) c_p \\
&= \sum_p c_p - \sum_p \alpha^{ij}_{pq} c_p - \sum_p \alpha^{ik}_{pr} c_p + \sum_p \alpha^{ij}_{pq}\alpha^{ik}_{pr} c_p \\
&= 1 - \sum_p \alpha^{ij}_{pq} c_p - \sum_p \alpha^{ik}_{pr} c_p + \sum_p \alpha^{ij}_{pq}\alpha^{ik}_{pr} c_p
\end{aligned}$$

The first order summation terms simplify to zero using Equation 6.7,

$$\sum_p \alpha^{ij}_{pq} c_p = \alpha^{ij}_{qq} c_q + \sum_{\substack{p \\ p\neq q}} \alpha^{ij}_{pq} c_p = \alpha^{ij}_{qq} c_q - \alpha^{ij}_{qq} c_q = 0$$

Therefore, we have

$$\sum_p \frac{\lambda^{ijk}_{pqr}}{\lambda^{jk}_{qr}} c_p = 1 + \sum_p \alpha^{ij}_{pq}\alpha^{ik}_{pr} c_p$$

So the summation over probabilities differs from 1 to the second-order in α, meaning if Warren-Cowley parameters $|\alpha| \ll 1$ then the sum rule in Equation 6.9 holds to a good approximation. This is a necessary condition for the superposition approximation for 3-site correlation functions to conform to a valid probability space. One can reach a similar conclusion for all higher-order correlation functions where the first order terms are zero and the sum rule differ from unity in the higher order terms of the Warren-Cowley parameters.

6.4 Solute-strengthening theory: accounting for short-range order (SRO)

Dislocations in an alloy attain a wavy configuration since segments of it stray about the mean dislocation position to get pinned by favourable solute environments which reduces the system energy. So two possible sources of strengthening can be envisaged, namely (1) *the average strengthening*, where there is an energy cost to the system when the average dislocation line glides in the alloy; in such situation an externally applied stress is needed to reimburse this penalty and sustain the glide (2) *the local strengthening* due to the stress needed to unpin the locally pinned dislocation segments over some barrier.

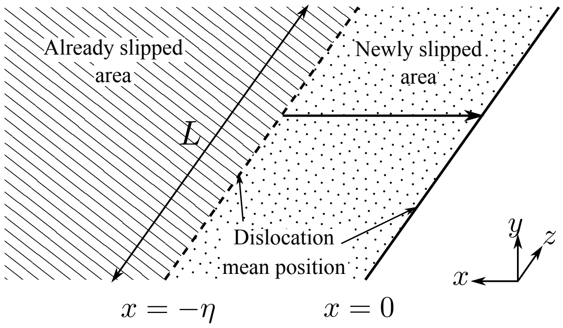
Already slipped area
Newly slipped area
L
Dislocation mean position
y
z
x
$x = -\eta$
$x = 0$

(a) Glide of dislocation mean position

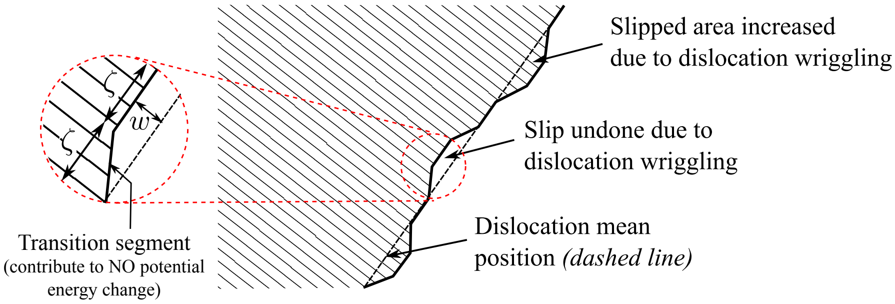
Slipped area increased due to dislocation wriggling
Slip undone due to dislocation wriggling
Dislocation mean position *(dashed line)*
ζ
ζ
w
Transition segment (contribute to NO potential energy change)

(b) Undulation of a straight dislocation due to solute fluctuations

Figure 6.1 – Schematic representation of “average” and “local” strengthening in alloys in subfigures (a) and (b) respectively. Average strengthening is related to the stress required to pay for any energy penalty associated with dislocation motion in an alloy. Subfigure (a) shows the glide of average dislocation line from $x = -\eta$ to $x = 0$ — if an energy cost per unit area is associated with the newly created slipped area, then there will be an associated average strengthening. Local strengthening or strengthening due to fluctuations, on the other hand, is related to the stress required to unpin dislocation segments locally from favourable solute environments to resume and sustain unabated glide. Subfigure (b) shows dislocation segments of length ζ in an undulated dislocation line which are pinned by favourable solute environments w distance away from the dislocation mean position.

6.4.1 Average strengthening in alloys with SRO

Average strengthening refers to the externally applied stress needed to compensate for the energy cost associated with the glide of average dislocation line as schematically depicted in Figure 6.1a. Let γ be the average energy cost per unit area of the slipped surface. To sustain dislocation glide, this energy cost must be balanced by the work done per unit slipped area by an externally applied critical resolved shear stress τ_A on the glide plane in the glide direction, which is $\tau_A b$, where b is the Burgers vector. Therefore, $\tau_A = \gamma / b$.

The total potential energy change ΔE_p of the system due to dislocation glide has two contributions (1) one due to interaction of solute n at site i with the dislocation at the origin, say $U^n_{sd}(x_i, y_i)$ and (2) other due to pair interaction of solute p at site k below the slip plane with solute q at site l above the slip plane; we call this energy to be $U_{pq}(\|\boldsymbol{r}_{kl}\|)$, where $\boldsymbol{r}_{kl}$ is the vector joining sites k and l. Therefore, the total potential energy change due to glide of a straight dislocation of length L by distance η (as depicted in Figure 6.1a) can be expressed as,

$$\begin{aligned}\Delta E_p(L,\eta) &= \sum_i \sum_n s_i^n \underbrace{\left(U_{sd}^n(x_i,y_i) - U_{sd}^n(x_i+\eta,y_i)\right)}_{\Delta U_{sd,i}^n(\eta)} + \sum_{\substack{k,l\\ y_k<0\\ y_l>0}} \sum_{p,q} s_k^p s_l^q \underbrace{\left(U_{pq}(\|\boldsymbol{r}_{kl}+\boldsymbol{t}\|) - U_{pq}(\|\boldsymbol{r}_{kl}\|)\right)}_{\Delta U_{ss,kl}^{pq}} \\ &= \sum_i \sum_n s_i^n \Delta U_{sd,i}^n(\eta) + \sum_{\substack{k,l\\ y_k<0\\ y_l>0}} \sum_{p,q} s_k^p s_l^q \Delta U_{ss,kl}^{pq} = \Delta E_{sd} + \Delta E_{ss}\end{aligned} \tag{6.10}$$

where $\boldsymbol{t}$ is the slip vector and (x_i, y_i, z_i) are the coordinates of site i according to the Cartesian coordinate system specified in Figure 6.1a.

The energy penalty γ due to dislocation glide is defined earlier as the average energy cost per unit area of the slipped surface; thereby γ can be expressed as $\gamma = \langle \Delta E_p \rangle / (\eta L)$ by definition, where $\langle \cdot \rangle$ is the expectation operator and ηL is the area slipped when a dislocation of length L glides a distance η (Figure 6.1a). With ρ_L the density of atomic sites along the dislocation line direction and ρ_G the density of projected atomic sites in the glide direction (like in Chapter 5), the area ηL can be expressed as $\mathbf{N}_a/(\rho_L \rho_G)$, where $\mathbf{N}_a$ is the number of atomic sites in the area ηL. Therefore the energy cost γ can be rewritten as $\gamma = (\langle \Delta E_p \rangle / \mathbf{N}_a)\rho_L \rho_G$. Using linearity of the expectation operator, we have $\langle \Delta E_p \rangle = \langle \Delta E_{sd} \rangle + \langle \Delta E_{ss} \rangle$ following Equation 6.10.

In Equation 6.10, we have seen that the expression for energy change due to solute-dislocation interactions $\Delta E_{sd} = \sum_i \sum_n s_i^n \Delta U_{sd,i}^n(\eta)$ has no product of occupation variables s_i^n. Therefore, the average energy change due to solute-dislocation interactions $\langle \Delta E_{sd} \rangle$ will not have any dependence of correlation functions and will have nothing to do with SRO. Therefore, $\langle \Delta E_{sd} \rangle = 0$, just like in the case of random alloys [32]. *This implies that there is no contribution to average strengthening from solute-dislocation interactions.*

So the average strengthening in alloys with SRO is solely due to solute-solute interactions. In an alloy with SRO, slip associated with dislocation glide disrupts the chemical ordering of solutes across the slip plane, bringing together unfavourable solute pairs and separating the favourable ones. This results in a positive γ. Here we are going to derive the expression for the critical resolved shear stress τ_A required to balance γ, in terms of effective pair interactions of solute pairs (Section 2.7 and Equations 5.20 and 5.22), the Warren-Cowley SRO parameter and the alloy composition.

To derive an expression for τ_A in average strengthening, we need to derive an expression for the average energy change due to solute-solute interactions $\langle \Delta E_{ss} \rangle$, since we know that $\tau_A b = (\langle \Delta E_{ss} \rangle / \mathbf{N}_a)\rho_L \rho_G$ from our earlier discussion (Note that since $\langle \Delta E_{sd} \rangle = 0$, $\langle \Delta E_p \rangle = \langle \Delta E_{ss} \rangle$).

Recalling Equation 6.10, the energy change during dislocation glide, due to solute-solute interactions across the slip plane is given by

$$\Delta E_{ss} = \sum_{\substack{k,l \\ y_k<0 \\ y_l>0}} \sum_{p,q} s_k^p s_l^q \Big(U_{pq}(\|\boldsymbol{r}_{kl} + \boldsymbol{t}\|) - U_{pq}(\|\boldsymbol{r}_{kl}\|) \Big) \tag{6.11}$$

Using $\langle s_k^p s_l^q \rangle = \lambda_{pq}^{kl} c_p c_q$ (Equation 6.1), the expected energy change upon slip turns out to be,

$$\langle \Delta E_{ss} \rangle = \sum_{p,q} c_p c_q \sum_{\substack{k,l \\ y_k<0 \\ y_l>0}} \lambda_{pq}^{kl} \Big(U_{pq}(\|\boldsymbol{r}_{kl} + \boldsymbol{t}\|) - U_{pq}(\|\boldsymbol{r}_{kl}\|) \Big) \tag{6.12}$$

Let $n_{dd'}$ be the number of pairs across the slip plane (per lattice site on the slip plane), which were at pair separation d' before slip and are at pair separation d after slip ($d \neq d'$). Let M_d be the number of pairs across the slip plane (per lattice site on the slip plane), which were at pair separation d before slip and are at pair separation $\neq d$ after slip.

In terms of pair distances across the slip plane Equation 6.12 can be rewritten as,

$$\langle \Delta E_{ss} \rangle / \mathbf{N}_a = \sum_{p,q} c_p c_q \sum_{d} U_{pq}(d) \left(\sum_{\substack{d' \\ d' \neq d}} \lambda_{pq}(d') n_{dd'} - \lambda_{pq}(d) M_d \right) \tag{6.13}$$

For slip by a lattice vector (or full slip), $\langle \Delta E_{ss} \rangle = 0$ for random alloys (recall Equation 5.15). For slip by a non-lattice vector, M_d is zero for the pair distances d which do not exist in the pristine crystal structure before slip. Table 6.1 tabulates the $n_{dd'}$ values for pair distance (d, d') upto 10 nearest-neighbors for full slip in fcc and bcc.

Equation 6.13 can be rewritten in terms of Warren-Cowley parameters as,

$$\langle \Delta E_{ss} \rangle / \mathbf{N}_a = \sum_{d} \sum_{p,q} c_p c_q U_{pq}(d) \left(N_d - M_d \right) - \sum_{d} \sum_{p,q} c_p c_q U_{pq}(d) \left(\sum_{\substack{d' \\ d' \neq d}} \alpha_{pq}(d') n_{dd'} - \alpha_{pq}(d) M_d \right) \tag{6.14}$$

where N_d is the number of pairs across the slip plane (per lattice site on the slip plane), which were at pair separation $\neq d$ before slip and are at pair separation d after slip, therefore implying

$$N_d = \sum_{\substack{d' \\ d' \neq d}} n_{dd'} \tag{6.15}$$

The first term in Equation 6.14 is same as the average energy change for a random alloy and the second term is the additional energy change on average due to SRO. Since we already know $\langle \Delta E_{ss} \rangle = 0$ for slip by a lattice vector in random alloys (Equation 5.15), the first term in

Equation 6.14 will always be zero for slip by a lattice vector with $N_d = M_d$. Therefore, in the case of slip by lattice vector, Equation 6.14 can be rewritten as

$$\langle \Delta E_{ss} \rangle / \mathbf{N}_a = -\sum_d \sum_{p,q} c_p c_q U_{pq}(d) \left(\sum_{\substack{d' \\ d' \neq d}} \alpha_{pq}(d') n_{dd'} - \alpha_{pq}(d) M_d \right) \tag{6.16}$$

Equation 6.16 is expressed in terms of bond energies which is not very useful, since alloys described with semi-empirical potentials or first principles entail many-body interatomic interactions. However effective pair potentials V_{pq}^{eff} is well-defined for any system irrespective of the total potential energy formulation for the system (Section 2.7). Therefore, we are going to simplify Equation 6.16 to express $\langle \Delta E_{ss} \rangle / \mathbf{N}_a$ in terms of effective pair potentials, as follows

$$\begin{aligned}
\langle \Delta E_{ss} \rangle / \mathbf{N}_a &= -\sum_d \sum_{p,q} c_p c_q U_{pq}(d) \left(\sum_{\substack{d' \\ d' \neq d}} \alpha_{pq}(d') n_{dd'} - \alpha_{pq}(d) M_d \right) \\
&= -\sum_d \sum_p c_p^2 U_{pp}(d) \left(\sum_{\substack{d' \\ d' \neq d}} \alpha_{pp}(d') n_{dd'} - \alpha_{pp}(d) M_d \right) \\
&\quad -\sum_d \sum_{\substack{p,q \\ p \neq q}} c_p c_q U_{pq}(d) \left(\sum_{\substack{d' \\ d' \neq d}} \alpha_{pq}(d') n_{dd'} - \alpha_{pq}(d) M_d \right)
\end{aligned}$$

Using the sum rule $\alpha_{pp} = -\frac{1}{c_p} \sum_{\substack{q \\ q \neq p}} \alpha_{pq} c_q \quad \forall p$ (Equation 6.7)

$$\begin{aligned}
&= \sum_d \sum_{\substack{p,q \\ p \neq q}} c_p c_q U_{pp}(d) \left(\sum_{\substack{d' \\ d' \neq d}} \alpha_{pq}(d') n_{dd'} - \alpha_{pq}(d) M_d \right) \\
&\quad -\sum_d \sum_{\substack{p,q \\ p \neq q}} c_p c_q U_{pq}(d) \left(\sum_{\substack{d' \\ d' \neq d}} \alpha_{pq}(d') n_{dd'} - \alpha_{pq}(d) M_d \right) \\
&= \frac{1}{2} \sum_d \sum_{\substack{p,q \\ p \neq q}} c_p c_q \big(U_{pp}(d) + U_{qq}(d) - 2U_{pq}(d) \big) \left(\sum_{\substack{d' \\ d' \neq d}} \alpha_{pq}(d') n_{dd'} - \alpha_{pq}(d) M_d \right)
\end{aligned}$$

Using the relation $V_{pq}^{eff} = U_{pp} + U_{qq} - 2U_{pq}$ (Equation 5.20)

$$= \frac{1}{2} \sum_d \sum_{\substack{p,q \\ p \neq q}} c_p c_q V_{pq}^{eff}(d) \left(\sum_{\substack{d' \\ d' \neq d}} \alpha_{pq}(d') n_{dd'} - \alpha_{pq}(d) M_d \right) \tag{6.17}$$

Recall from Equation 5.22, that $V_{pq}^{eff} = U_{pp}^{int} + U_{qq}^{int} - 2U_{pq}^{int}$, where U_{pq}^{int} is the interaction energy between solutes p and q. On reversing the steps of the derivation in Equation 6.17 and replacing the bond energies U by the interaction energies U^{int}, one can derive $\langle \Delta E_{ss} \rangle / \mathbf{N}_a$ in terms of interaction energies as,

$$\langle \Delta E_{ss} \rangle / \mathbf{N}_a = -\sum_{d} \sum_{p,q} c_p c_q U_{pq}^{int}(d) \left(\sum_{\substack{d' \\ d' \neq d}} \alpha_{pq}(d') n_{dd'} - \alpha_{pq}(d) M_d \right) \tag{6.18}$$

The critical shear stress for average strengthening τ_A is given by

$$\tau_A = (\langle \Delta E_{ss} \rangle / \mathbf{N}_a) \frac{\rho_L \rho_G}{b} \tag{6.19}$$

Full Burgers vector magnitude b is $a/\sqrt{2}$ for fcc and $a\sqrt{3}/2$ for bcc, where a is the cubic lattice constant. ρ_L is $1/(\sqrt{3}b)$ for fcc and $1/(2\sqrt{2}b)$ for bcc. ρ_G is $2/b$ for fcc and $3/b$ for bcc. Using the above inputs,

$$\frac{\rho_L \rho_G}{b} = \begin{cases} \frac{4\sqrt{2}}{\sqrt{3}} \frac{1}{a^3} & \text{for fcc} \\ \frac{2\sqrt{2}}{\sqrt{3}} \frac{1}{a^3} & \text{for bcc} \end{cases} \tag{6.20}$$

Combining Equations 6.17/6.18, 6.19 and 6.20, the critical shear stress τ_A for fcc and bcc alloys is given by

In terms of effective pair potentials

$$\tau_A = \begin{cases} \frac{2\sqrt{2}}{\sqrt{3}} \frac{1}{a^3} \sum_d \sum_{\substack{p,q \\ p \neq q}} c_p c_q V_{pq}^{eff}(d) \left(\sum_{\substack{d' \\ d' \neq d}} \alpha_{pq}(d') n_{dd'} - \alpha_{pq}(d) M_d \right) & \text{for fcc} \\ \frac{\sqrt{2}}{\sqrt{3}} \frac{1}{a^3} \sum_d \sum_{\substack{p,q \\ p \neq q}} c_p c_q V_{pq}^{eff}(d) \left(\sum_{\substack{d' \\ d' \neq d}} \alpha_{pq}(d') n_{dd'} - \alpha_{pq}(d) M_d \right) & \text{for bcc} \end{cases}$$

In terms of interaction energies

$$\tau_A = \begin{cases} -\frac{4\sqrt{2}}{\sqrt{3}} \frac{1}{a^3} \sum_d \sum_{p,q} c_p c_q U_{pq}^{int}(d) \left(\sum_{\substack{d' \\ d' \neq d}} \alpha_{pq}(d') n_{dd'} - \alpha_{pq}(d) M_d \right) & \text{for fcc} \\ -\frac{2\sqrt{2}}{\sqrt{3}} \frac{1}{a^3} \sum_d \sum_{p,q} c_p c_q U_{pq}^{int}(d) \left(\sum_{\substack{d' \\ d' \neq d}} \alpha_{pq}(d') n_{dd'} - \alpha_{pq}(d) M_d \right) & \text{for bcc} \end{cases} \tag{6.21}$$

Equation 6.21 is an important result of this chapter, since average strengthening is unique to alloys with SRO and the above equation helps to calculate it for fcc and bcc alloys, with the knowledge of the effective pair interactions (or interaction energies) and Warren-Cowley SRO parameters.

In the special case, where the atoms in the alloy interact only with their first neighbours and the Warren-Cowley SRO parameters are also non-zero only for the first neighbours, the following expression for τ_A can be deduced for fcc and bcc alloys from Equation 6.21 using $n_{dd'}$ values from Table 6.1 and the sum rule in Equation 6.15 for M_d (recall $N_d = M_d$ for full slip),

In terms of effective pair potentials

$$\tau_A = \begin{cases} -\frac{4\sqrt{2}}{\sqrt{3}}\frac{1}{a^3}\sum_{\substack{p,q \\ p\neq q}} c_p c_q \alpha_{pq}(d_1) V_{pq}^{eff}(d_1) & \text{for fcc} \\ -\frac{2\sqrt{2}}{\sqrt{3}}\frac{1}{a^3}\sum_{\substack{p,q \\ p\neq q}} c_p c_q \alpha_{pq}(d_1) V_{pq}^{eff}(d_1) & \text{for bcc} \end{cases}$$

In terms of interaction energies

$$\tau_A = \begin{cases} \frac{8\sqrt{2}}{\sqrt{3}}\frac{1}{a^3}\sum_{p,q} c_p c_q \alpha_{pq}(d_1) U_{pq}^{int}(d_1) & \text{for fcc} \\ \frac{4\sqrt{2}}{\sqrt{3}}\frac{1}{a^3}\sum_{p,q} c_p c_q \alpha_{pq}(d_1) U_{pq}^{int}(d_1) & \text{for bcc} \end{cases} \tag{6.22}$$

where d_1 denotes 1^{st} nearest neighbour distance. Flinn [45] arrived at the above result for fcc binary alloys in terms of effective pair potentials and recently Antillon et. al [47] also arrived at the same above result for fcc multicomponent alloys but they expressed τ_A in terms of interaction energies. Mohri et. al [46] derived an expression for τ_A for binary fcc alloys considering solute pair interactions and correlations up to second nearest neighbour, which matches Equation 6.21 of this chapter, when evaluated for two nearest neighbour distances using Table 6.1.

		Pair distances after slip									
	d/a d'/a	0.707	1.0	1.225	1.414	1.581	1.732	1.871	2.0	2.121	2.236
Pair distances before slip	0.707	-	1	1	0	0	0	0	0	0	0
	1.0	1	-	1	0	1	0	0	0	0	0
	1.225	1	1	-	2	3	1	1	0	0	0
	1.414	0	0	2	-	2	0	2	0	0	0
	1.581	0	1	3	2	-	0	3	2	3	1
	1.732	0	0	1	0	0	-	4	0	0	0
	1.871	0	0	1	2	3	4	-	0	8	4
	2.0	0	0	0	0	2	0	0	-	2	0
	2.121	0	0	0	0	3	0	8	2	-	7
	2.236	0	0	0	0	1	0	4	0	7	-

(a) $a/2[1\bar{1}0]$ slip along (111) plane in fcc.

		Pair distances after slip									
	d/a d'/a	0.866	1.0	1.414	1.658	1.732	2.0	2.179	2.236	2.449	2.598
Pair distances before slip	0.866	-	1	1	0	0	0	0	0	0	0
	1.0	1	-	0	1	0	0	0	0	0	0
	1.414	1	0	-	4	0	0	1	0	0	0
	1.658	0	1	4	-	2	2	0	4	1	0
	1.732	0	0	0	2	-	0	2	0	0	0
	2.0	0	0	0	2	0	-	0	0	0	2
	2.179	0	0	1	0	2	0	-	6	6	0
	2.236	0	0	0	4	0	0	6	-	0	6
	2.449	0	0	0	1	0	0	6	0	-	6
	2.598	0	0	0	0	0	2	0	6	6	-

(b) $a/2[111]$ slip along (110) plane in bcc.

Table 6.1 – The structure factors $n_{dd'}$ for every pair of normalized pair distances (d, d') for full slip in fcc and bcc.

In this section a very general expression for the average strengthening (τ_A) in fcc and bcc alloys is provided in terms of effective pair interactions (and interaction energies), the Warren-Cowley SRO parameters, alloy composition and lattice constant in Equation 6.21. τ_A be calculated for fcc and bcc alloys with solute pair interactions extending upto 10 nearest neighbours with the help of Table 6.1; which is more than sufficient given the short-ranged chemical interactions among different atoms in metal alloys. τ_A expression for the special case of first-neighbour interactions and correlations are also provided and compared to previously studies in the literature.

It is difficult to decide just based on Equation 6.21 alone whether τ_A is positive or negative given a set of Warren-Cowley SRO parameters α_{pq}. However, the physics of the problem requires τ_A to be positive, since a slip will always disrupt chemical ordering thus increasing the system's potential energy. Therefore, τ_A can *only* be negative if the SRO parameters are improperly chosen; for example, for a strong $p-q$ bond (implying preferential pairing of p and q), if the corresponding $\alpha_{pq} > 0$, then that's improperly chosen. If the SRO parameters are consistent with the underlying solute pair interactions in the system, then τ_A will always be positive, which will in turn mean strengthening for alloys with SRO. This is easier to illustrate for the special case when we assume the solute pair interactions and correlations are restricted to first neighbour, that is, Equation 6.22. Notice that τ_A is positive if the products $\alpha_{pq}(d_1)V_{pq}^{eff}(d_1)$ are negative and the products $\alpha_{pq}(d_1)U_{pq}^{int}(d_1)$ are positive[1]. This implies the effective pair interactions needs to be positive and the interaction energies negative for a negative SRO parameter $\alpha_{pq}(d_1)$. Negative $\alpha_{pq}(d_1)$ implies attractive solute pairs, which is consistent with corresponding positive V_{pq}^{eff} ($p-q$ is favoured energetically than $p-p$ and $q-q$) and a negative U_{pq}^{int} (system energy reduces on bringing the solutes p and q at first neighbour distance from infinite separation). Therefore, we see that the consistency between SRO parameter and the interactions of solute pairs is pivotal for having the correct sign for τ_A, which is always positive.

So far, we have focused on slip by lattice vector, while discussing average strengthening. For slip by non-lattice vector (for example, partial slip by $\frac{a}{6} < 112 >$ in fcc), the first term in Equation 6.14 is the stable stacking fault energy (γ_{ssf}) in random alloy and the second term is the change in γ_{ssf} due to SRO. Difference in γ_{ssf} due to SRO, changes the average spacing between partials d_p, however it does not influence average strengthening. It might influence local strengthening due to fluctuating solute environment, which we will be discussing next; however we have seen for random alloys in Figure 4.7 that changing d_p does not influence strengthening when $d_p > 7b$. Therefore, it is speculated that the change in stacking fault energy due to SRO will not have a notable impact on alloy yield strength. However, recent studies, corroborating the change in γ_{ssf} due to SRO, have implicated its impact on strengthening [41, 82, 141]. The influence of γ_{ssf} on strengthening, if at all significant, cannot be addressed by the current theoretical framework.

The following subsection will discuss the local strengthening in alloys with SRO, which is the stress required to unpin dislocation segments from favourable solute environments. Also, it will be demonstrated that at finite temperatures, unlike average strengthening, the local strengthening is thermally-activated involving an energy barrier.

---

[1] It is not a necessary condition though since there can be some cancellation among different terms in case of a multicomponent alloy. However for a binary alloy $A-B$, the product $\alpha_{AB}(d_1)V_{AB}^{eff}(d_1)$ definitely has to be negative to have positive τ_A.

6.4.2 Local strengthening in alloys with SRO

Having discussed "average strengthening", we will now focus our attention on "local strengthening" or strengthening due to fluctuations. A dislocation in an alloy undulates in response to surrounding solute environment — dislocation segments will glide towards regions of favourable solute fluctuations to minimize total system energy. However this undulation of the dislocation line with respect to its straight configuration at average dislocation position, does not contribute to the energy penalty γ since equal area will be swept on either side of the dislocation mean position resulting in no nett increase in the slipped area (illustrated schematically in Figure 6.1b). However there is a nett decrease in potential energy of the system since dislocation segments glide towards favourable solute fluctuations.

We assume an undulated configuration of a dislocation of length L as depicted in Figure 6.1b where alternating segments of length ζ glide $+w$ and $-w$ respectively with respect to the mean dislocation position and they are connected by transition segments. Since the dislocation segments glide towards favourable solute fluctuations, it will decrease potential energy and therefore average decrease in potential energy of a straight segment of length ζ gliding by distance w is typically the negative of the standard deviation of $\Delta E_p(\zeta, w)$ (Refer Equation 6.10; note that the relevant length scale here is ζ and w). Also note that the standard deviation $\sigma_{\Delta E_p}$ is an even function of w. As a result the nett decrease in system energy due to undulation of a straight dislocation is given by $-\sigma_{\Delta E_p}(\zeta, w)\frac{L}{2\zeta}$. We have already seen in Equation 6.10 that $\Delta E_p = \Delta E_{sd} + \Delta E_{ss}$. So $\sigma_{\Delta E_p}(\zeta, w)$ can be derived as follows,

$$\begin{aligned}
\Delta E_p &= \Delta E_{sd} + \Delta E_{ss} \\
\sigma^2_{\Delta E_p} &= \langle \Delta E_p^2 \rangle - \langle \Delta E_p \rangle^2 \\
&= \langle \Delta E_{sd}^2 + \Delta E_{ss}^2 + 2\Delta E_{sd}\Delta E_{ss} \rangle - \langle \Delta E_{sd} \rangle^2 - \langle \Delta E_{ss} \rangle^2 - 2\langle \Delta E_{sd} \rangle \langle \Delta E_{ss} \rangle \\
&= \Big(\langle \Delta E_{sd}^2 \rangle - \langle \Delta E_{sd} \rangle^2 \Big) + \Big(\langle \Delta E_{ss}^2 \rangle - \langle \Delta E_{ss} \rangle^2 \Big) + 2\Big(\langle \Delta E_{sd}\Delta E_{ss} \rangle - \langle \Delta E_{sd} \rangle \langle \Delta E_{ss} \rangle \Big) \\
\sigma^2_{\Delta E_p} &= \sigma^2_{\Delta E_{sd}} + \sigma^2_{\Delta E_{ss}} + 2\mathrm{cov}(\Delta E_{sd}, \Delta E_{ss}) \quad \text{(Recall Equation 2.66)} \qquad (6.23)
\end{aligned}$$

where cov is the covariance operator. Sections 6.5.1, 6.5.2 and 6.5.3 derives expressions for $\sigma^2_{\Delta E_{ss}}$, $\sigma^2_{\Delta E_{sd}}$ and $\mathrm{cov}(\Delta E_{sd}, \Delta E_{ss})$ respectively in terms of solute-solute pair interactions across the slip plane, solute-dislocation interaction energies, SRO parameters and the alloy composition.

Figure 6.2 schematically shows the different regions in space corresponding to energy change due to solute-dislocation and solute-solute interactions when a positive edge dislocation (along z-axis) glides a distance w. From the figure it is evident that energy change due to solute-dislocation interactions are mainly around the dislocation at both positions, before and after glide. The change in solute-dislocation interaction energy due to dislocation glide by w can be viewed as the interaction energy of solutes interacting with a dislocation dipole with separation w and this field dies down fast at $\sim 1/r^2$, r being the distance from the dipole. So the variance in energy change due to solute-dislocation interactions $\sigma^2_{\Delta E_{sd}}$ will scale with the dislocation line length ζ. The slipped area ζw created by dislocation glide will correspond to energy change due to solute-solute interactions which are short-ranged and only extend across a few planes above and below the glide plane. Therefore the variance in energy change due to solute-solute interactions $\sigma^2_{\Delta E_{ss}}$ will depend on the slipped area ζw. Evident from Figure 6.2, there is an overlap region near the dislocation core where atomic sites contribute to both energy changes significantly, viz. due to solute-solute and solute-dislocation interactions. The covariance of the two energy change contributions, ΔE_{sd} and ΔE_{ss}, will therefore scale with the dislocation line length ζ (just like $\sigma^2_{\Delta E_{sd}}$). However the covariance is expected to be smaller than the variance $\sigma^2_{\Delta E_{sd}}$ due to the small size of the overlap region of these two contributions.

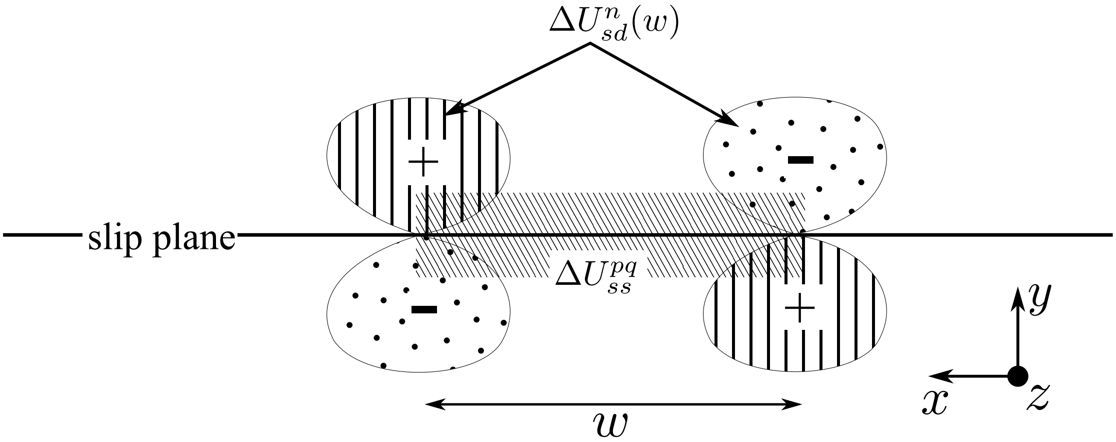

Figure 6.2 – Schematic illustration of spatial distribution of energy changes due to solute-dislocation and solute-solute interactions when a positive edge dislocation (along z-axis) glides a distance w. The solute-dislocation interactions extends upto infinity but decreases with distance from the core — the bounded regime of solute-dislocation interaction is just for illustration.

The undulation will cost some elastic energy which is attributed to the increase in length of the transition segments. So the theory hypothesizes that the straight gliding segments contribute only to change in potential energy and the transition segment joining the gliding segments contribute only to elastic energy cost. This average energy cost per transition segment can be approximated as $\Gamma\left(\frac{w^2}{2\zeta}\right)$ [32], where Γ is the dislocation line tension.

Thus the total energy change of the system due to undulation of the dislocation with respect to its straight configuration at the mean position, can be expressed as

$$\Delta E_{\text{tot}}(\zeta, w) = \left[\Gamma\left(\frac{w^2}{2\zeta}\right) - \sigma_{\Delta E_p}(\zeta, w)\right]\left(\frac{L}{2\zeta}\right) \tag{6.24}$$

In Sections 6.5.2 and 6.5.3, we will show that the ζ-dependence can be explicitly extracted out from each of $\sigma^2_{\Delta E_{sd}}$ and $\text{cov}(\Delta E_{sd}, \Delta E_{ss})$. However in Section 6.5.1 we will see that the variance in energy change due to solute-solute interactions $\sigma^2_{\Delta E_{ss}}$ is quadratic function of the slipped area (ζw) with no constant term. In the limit of random alloys the $(\zeta, w)^2$ term vanishes. Here as an approximation, we will ignore the $(\zeta, w)^2$ term which helps us to retain the same structure of solute-strengthening theory for random alloys, with energy fluctuation quantities modified to account for SRO. Given the above approximation, the variance $\sigma_{\Delta E_p}(\zeta, w)$ can be expressed as $\sigma_{\Delta E_p}(\zeta, w) = \left(\rho_L \zeta\right)^{1/2} \Delta\widetilde{E}_{\mathrm{p}}(w)$ like in the original theory (Recall Section 1.2), where ρ_L is the density of atomic sites along the dislocation line and $\Delta\widetilde{E}_{\mathrm{p}}$ is the principle energy fluctuation quantity for the theory which depends only on the roughening amplitude w and not on ζ.

Now, there will be a critical (ζ_c, w_c) which will minimize the total energy change ΔE_{tot}, and this is the typical undulated configuration the dislocation will attain so as to minimize total energy. ζ_c has a closed-form expression as a function of w_c which is given as follows,

$$\zeta_c = \left(\frac{4\Gamma^2 w_c^4}{\rho_L \Delta\widetilde{E}^2_{\mathrm{p}}(w_c)} \right)^{\frac{1}{3}} \tag{6.25}$$

w_c does not have a closed-form expression and has to be obtained numerically as solution to the following equation,

$$\frac{\partial \Delta\widetilde{E}_{\mathrm{p}}(w)}{\partial w} = \frac{\Delta\widetilde{E}_{\mathrm{p}}(w)}{2w} \tag{6.26}$$

A stress τ_y^F will be required to unpin any dislocation segment of length ζ_c from the favourable solute environment, which will in turn involve overcoming an energy barrier ΔE_b due to unfavourable solute fluctuations. This energy barrier is $\sqrt{2}$ times the standard deviation $\sigma_{\Delta E_p}(\zeta_c, w_c)$ plus the gain in elastic energy $\Gamma\left(\frac{w_c^2}{2\zeta_c}\right)$ and can thus be expressed as

$$\Delta E_b = \sqrt{2}\sigma_{\Delta E_p}(\zeta_c, w_c) - \Gamma\left(\frac{w_c^2}{2\zeta_c}\right) = 1.467\left(\rho_L w_c^2 \Gamma \Delta\widetilde{E}^2_{\mathrm{p}}(w_c)\right)^{\frac{1}{3}} \tag{6.27}$$

The energy landscape $E(x)$ for a dislocation segment of length ζ_c pinned at favourable solute fluctuation can be approximated by a cosine $\frac{\Delta E_b}{2}\left(1 - \cos\left(\frac{\pi x}{w_c}\right)\right)$[32] plus an energy penalty term $\gamma\zeta_c x$ (from average strengthening). Note that while formulating $E(x)$ we are describing the potential energy surface for a gliding dislocation, be it originally at $-w_c$ or $+w_c$ (Figure 6.1b) — so there will always be an energy penalty of $\gamma\zeta_c x$ for creating additional slipped area of $\zeta_c x$ by glide. An applied resolved shear stress τ_{y0} needed to glide the dislocation at 0K temperature would be such that the modified energy landscape $E(x, \tau_{y0})$ will no longer have a minimum or a maximum in $[0, w_c]$ but will have an inflection point at $x = w_c/2$. Formally, it would be as follows,

$$\begin{aligned}
E(x) &= \frac{\Delta E_b}{2}\left(1-\cos\left(\frac{\pi x}{w_c}\right)\right)+\gamma\zeta_c x\\
E(x,\tau) &= \frac{\Delta E_b}{2}\left(1-\cos\left(\frac{\pi x}{w_c}\right)\right)+\gamma\zeta_c x-\tau b\zeta_c x\\
\left.\frac{\partial E(x,\tau)}{\partial x}\right|_{(\hat{x},\tau_{y0})} &= \frac{\pi}{2}\frac{\Delta E_b}{w_c}\sin\left(\frac{\pi\hat{x}}{w_c}\right)+\gamma\zeta_c-\tau_{y0}b\zeta_c=0 \implies \tau_{y0}=\frac{\pi}{2}\frac{\Delta E_b}{b\zeta_c w_c}\sin\left(\frac{\pi\hat{x}}{w_c}\right)+\gamma/b\\
\left.\frac{\partial^2 E(x,\tau)}{\partial x^2}\right|_{(\hat{x},\tau_{y0})} &= \frac{\pi^2}{2}\frac{\Delta E_b}{w_c^2}\cos\left(\frac{\pi\hat{x}}{w_c}\right)=0 \implies \cos\left(\frac{\pi\hat{x}}{w_c}\right)=0 \quad \text{(Inflection at } x=\hat{x}=w_c/2)\\
\therefore \tau_{y0} &= \frac{\pi}{2}\frac{\Delta E_b}{b\zeta_c w_c}+\gamma/b=\tau_{y0}^F+\tau_A
\end{aligned} \tag{6.28}$$

So the net yield strength at zero-temperature τ_{y0}, has two components, (1) τ_{y0}^F, the local strengthening due to pinning of dislocation segments in a fluctuation solute environment and (2) τ_A, the average strengthening, which is discussing at length in Section 6.4.1.

For $\tau < \tau_{y0}$, $\partial E(x,\tau)/\partial x = 0$ in Equation 6.28 has two solutions, one for energy minimum $E_{\min}$ and other for energy maximum $E_{\max}$ and the difference of the two is the stress-dependent energy barrier $\Delta E(\tau)$. Leyson et.al [32] showed that $\Delta E(\tau)$ can be approximated (within 6%) by

$$\Delta E(\tau) \approx \Delta E_b\left(1-\frac{\tau-\tau_A}{\tau_{y0}^F}\right)^{\frac{3}{2}} \tag{6.29}$$

For a quasistatic loading, the rate of unpinning of dislocation segments ν from local minima by activation over the stress-dependent barrier height $\Delta E(\tau)$ can be approximated using transition state theory as $\nu = \nu_0 \exp(-\Delta E(\tau)/k_B T)$, where ν_0 is the attempt frequency, T is the temperature and k_B is Boltzmann's constant. The microscopic dislocation escape rate ν can be related to the macroscopic strain rate by the well-established Kocks model, that is $\dot{\varepsilon} = \dot{\varepsilon}_0 \exp(-\Delta E(\tau)/k_B T)$, where $\dot{\varepsilon}$ and $\dot{\varepsilon}_0$ are proportional to ν and ν_0 respectively with proportionality constant $\rho b d$ (ρ is the dislocation density per unit area and d is the flight distance over which the dislocation moves after each escape). This relation, along with Equation 6.29, can be inverted to obtain the yield stress ($\tau = \tau_y(T,\dot{\varepsilon})$) at temperature T and applied strain rate $\dot{\varepsilon}$ as follows,

$$\tau_y(T,\dot{\varepsilon}) = \tau_{y0}^F\left[1-\left(\frac{k_B T}{\Delta E_b}\ln\left(\frac{\dot{\varepsilon}_0}{\dot{\varepsilon}}\right)\right)^{\frac{2}{3}}\right]+\tau_A \tag{6.30}$$

where $\dot{\varepsilon}_0 \sim 10^4/s$ and k_B are a reference strain rate and Boltzmann's constant respectively. The first term in Equation 6.30 is the temperature-dependent contribution to yield stress τ_y^F due to local strengthening. It is noteworthy that the second term corresponding to average strengthening is temperature-independent, implying that *the average strengthening in alloys with SRO is not thermally activated.* Also note that for random alloys, i.e. for $\gamma = 0$, Equation 6.30 reverts back to that derived for random alloys in Ref. [32].

In the following section, we will be deriving the variance in energy change when a dislocation of length ζ glides a distance w, that is, $\sigma^2_{\Delta E_p}$. This will be done in three subsections, each deriving expressions for the three contributions to $\sigma^2_{\Delta E_p}$, namely $\sigma^2_{\Delta E_{ss}}$, $\sigma^2_{\Delta E_{sd}}$ and $\mathrm{cov}(\Delta E_{sd}, \Delta E_{ss})$ (Equation 6.23).

6.5 Variance in energy change due to dislocation glide $\sigma^2_{\Delta E_p}$

6.5.1 Contribution due to solute-solute interactions $\sigma^2_{\Delta E_{ss}}$

The variance of ΔE_{ss} is given by $\sigma^2_{\Delta E_{ss}} = \langle \Delta E^2_{ss} \rangle - \langle \Delta E_{ss} \rangle^2$. With lattice sites indexed by i, k for sites below the slip plane with atomtypes u, p respectively and sites above the slip plane indexed by j, l with atomtypes v, q respectively, the quantity ΔE^2_{ss} is given by,

$$\Delta E^2_{ss} = \sum_{k,l} \sum_{p,q} s^p_k s^q_l \underbrace{\left(U_{pq}(\|\boldsymbol{r}_{kl} + \boldsymbol{t}\|) - U_{pq}(\|\boldsymbol{r}_{kl}\|) \right)}_{\Delta U^{pq}_{ss,kl}} \sum_{i,j} \sum_{u,v} s^u_i s^v_j \underbrace{\left(U_{uv}(\left\|\boldsymbol{r}_{ij} + \boldsymbol{t}\right\|) - U_{uv}(\left\|\boldsymbol{r}_{ij}\right\|) \right)}_{\Delta U^{uv}_{ss,ij}} \tag{6.31}$$

Taking expectation on either sides,

$$\langle \Delta E^2_{ss} \rangle = \sum_{i,j,k,l} \sum_{p,q,u,v} \langle s^u_i s^v_j s^p_k s^q_l \rangle \Delta U^{pq}_{ss,kl} \Delta U^{uv}_{ss,ij} \tag{6.32}$$

Using the probability definitions in Equation 6.1 and the mutual exclusivity of occupancy of any site by different atom types, the expectation $\langle s^u_i s^v_j s^p_k s^q_l \rangle$ can be derived as follows (i, j, k, l need not be distinct),

$$\begin{aligned}
\langle s^u_i s^v_j s^p_k s^q_l \rangle &= \delta_{ik}\delta_{up}\delta_{jl}\delta_{vq} \langle \left(s^p_k\right)^2 \left(s^q_l\right)^2 \rangle \\
&+ \delta_{ik}\delta_{up}(1-\delta_{jl}) \langle \left(s^p_k\right)^2 s^v_j s^q_l \rangle \\
&+ (1-\delta_{ik})\delta_{jl}\delta_{vq} \langle s^u_i s^p_k \left(s^q_l\right)^2 \rangle \\
&+ (1-\delta_{ik})(1-\delta_{jl}) \langle s^u_i s^v_j s^p_k s^q_l \rangle \\
&= \delta_{ik}\delta_{up}\delta_{jl}\delta_{vq} \lambda^{kl}_{pq} c_p c_q \\
&+ \delta_{ik}\delta_{up}(1-\delta_{jl}) \lambda^{kjl}_{pvq} c_p c_v c_q \\
&+ (1-\delta_{ik})\delta_{jl}\delta_{vq} \lambda^{ikl}_{upq} c_u c_p c_q \\
&+ (1-\delta_{ik})(1-\delta_{jl}) \lambda^{ijkl}_{uvpq} c_u c_v c_p c_q
\end{aligned} \tag{6.33}$$

Therefore, $\langle \Delta E_{ss}^2 \rangle$ can be simplified as,

$$\begin{aligned}\langle \Delta E_{ss}^2 \rangle &= \sum_{p,q} c_p c_q \sum_{k,l} \lambda_{pq}^{kl} \left(\Delta U_{ss,kl}^{pq}\right)^2 \\ &+ \sum_{p,v,q} c_p c_v c_q \sum_{\substack{k,j,l \\ j\neq l}} \lambda_{pvq}^{kjl} \Delta U_{ss,kl}^{pq} \Delta U_{ss,kj}^{pv} \\ &+ \sum_{u,p,q} c_u c_p c_q \sum_{\substack{i,k,l \\ i\neq k}} \lambda_{upq}^{ikl} \Delta U_{ss,kl}^{pq} \Delta U_{ss,il}^{uq} \\ &+ \sum_{u,v,p,q} c_u c_v c_p c_q \sum_{\substack{i,j,k,l \\ i\neq k \\ j\neq l}} \lambda_{uvpq}^{ijkl} \Delta U_{ss,kl}^{pq} \Delta U_{ss,ij}^{uv}\end{aligned} \tag{6.34}$$

Making use of the fact that $\langle s_k^p s_l^q \rangle = \lambda_{pq}^{kl} c_p c_q$ (and similarly $\langle s_i^u s_j^v \rangle = \lambda_{uv}^{ij} c_u c_v$), one can show by similar manipulations that

$$\langle \Delta E_{ss} \rangle^2 = \sum_{p,q} c_p c_q \sum_{k,l} \lambda_{pq}^{kl} \Delta U_{ss,kl}^{pq} \sum_{u,v} c_u c_v \sum_{i,j} \lambda_{uv}^{ij} \Delta U_{ss,ij}^{uv} \tag{6.35}$$

which is square of Equation 6.12

Therefore,

$$\begin{aligned}\sigma_{\Delta E_{ss}}^2 &= \langle \Delta E_{ss}^2 \rangle - \langle \Delta E_{ss} \rangle^2 \\ &= \sum_{p,q} c_p c_q \sum_{k,l} \lambda_{pq}^{kl} \left(\Delta U_{ss,kl}^{pq}\right)^2 \\ &+ \sum_{p,v,q} c_p c_v c_q \sum_{\substack{k,j,l \\ j\neq l}} \lambda_{pvq}^{kjl} \Delta U_{ss,kl}^{pq} \Delta U_{ss,kj}^{pv} \\ &+ \sum_{u,p,q} c_u c_p c_q \sum_{\substack{i,k,l \\ i\neq k}} \lambda_{upq}^{ikl} \Delta U_{ss,kl}^{pq} \Delta U_{ss,il}^{uq} \\ &+ \sum_{u,v,p,q} c_u c_v c_p c_q \sum_{\substack{i,j,k,l \\ i\neq k \\ j\neq l}} \lambda_{uvpq}^{ijkl} \Delta U_{ss,kl}^{pq} \Delta U_{ss,ij}^{uv} \\ &- \sum_{p,q} c_p c_q \sum_{k,l} \lambda_{pq}^{kl} \Delta U_{ss,kl}^{pq} \sum_{u,v} c_u c_v \sum_{i,j} \lambda_{uv}^{ij} \Delta U_{ss,ij}^{uv}\end{aligned} \tag{6.36}$$

It is straightforward to verify that with all correlation functions equal to 1 like in the case of random alloys, Equation 6.36 above reverts back to Equation 5.19 for random alloys; let's call that variance $\sigma_{\Delta E_{ss},\mathrm{R}}^2$. Like Equation 5.19, for fcc and bcc crystal structures, the second and third terms in Equation 6.36 are equal.

As mentioned earlier, the higher-order correlation functions are generally unavailable. Here we have made further approximations to express the variance $\sigma^2_{\Delta E_{ss}}$ in Equation 6.36 in terms of Warren-Cowley SRO parameters only, which can be calculated with atomistic simulations using Monte-Carlo algorithm [41, 43] and can also be obtained experimentally for binary alloys [39, 40, 42].

Using superposition approximation for the higher-order correlation functions, we can rewrite Equation 6.36 for bcc and fcc in terms of pair correlation functions only,

$$\begin{aligned}
\sigma^2_{\Delta E_{ss}} &= \sum_{p,q} c_p c_q \sum_{k,l} \lambda^{kl}_{pq} \left(\Delta U^{pq}_{ss,kl}\right)^2 \\
&\quad + 2 \sum_{p,v,q} c_p c_v c_q \sum_{\substack{k,j,l \\ j \neq l}} \lambda^{kl}_{pq} \lambda^{jl}_{vq} \lambda^{kj}_{pv} \Delta U^{pq}_{ss,kl} \Delta U^{pv}_{ss,kj} \\
&\quad + \sum_{u,v,p,q} c_u c_v c_p c_q \sum_{\substack{i,j,k,l \\ i \neq k \\ j \neq l}} \lambda^{kl}_{pq} \lambda^{jl}_{vq} \lambda^{kj}_{pv} \lambda^{ij}_{uv} \lambda^{ik}_{up} \lambda^{il}_{uq} \Delta U^{pq}_{ss,kl} \Delta U^{uv}_{ss,ij} \\
&\quad - \sum_{p,q} c_p c_q \sum_{k,l} \lambda^{kl}_{pq} \Delta U^{pq}_{ss,kl} \sum_{u,v} c_u c_v \sum_{i,j} \lambda^{ij}_{uv} \Delta U^{uv}_{ss,ij}
\end{aligned} \tag{6.37}$$

Expressing the pair correlation functions in Equation 6.37 in terms of the Warren-Cowley parameters and then taking only the first order terms in αs, we can again approximate the variance $\sigma^2_{\Delta E_{ss}}$ as

$$\begin{aligned}
\sigma^2_{\Delta E_{ss}} - \sigma^2_{\Delta E_{ss},\mathrm{R}} &= - \sum_{p,q} c_p c_q \sum_{k,l} \alpha^{kl}_{pq} \left(\Delta U^{pq}_{ss,kl}\right)^2 \\
&\quad - 2 \sum_{p,v,q} c_p c_v c_q \sum_{\substack{k,j,l \\ j \neq l}} \left(\alpha^{kl}_{pq} + \alpha^{jl}_{vq} + \alpha^{kj}_{pv}\right) \Delta U^{pq}_{ss,kl} \Delta U^{pv}_{ss,kj} \\
&\quad - \sum_{u,v,p,q} c_u c_v c_p c_q \sum_{\substack{i,j,k,l \\ i \neq k \\ j \neq l}} \left(\alpha^{kl}_{pq} + \alpha^{jl}_{vq} + \alpha^{kj}_{pv} + \alpha^{ij}_{uv} + \alpha^{ik}_{up} + \alpha^{il}_{uq}\right) \Delta U^{pq}_{ss,kl} \Delta U^{uv}_{ss,ij} \\
&\quad + 2 \sum_{p,q} c_p c_q \sum_{k,l} \alpha^{kl}_{pq} \Delta U^{pq}_{ss,kl} \sum_{u,v} c_u c_v \sum_{i,j} \Delta U^{uv}_{ss,ij}
\end{aligned} \tag{6.38}$$

where $\sigma^2_{\Delta E_{ss},\mathrm{R}}$ is variance in energy change due to solute-solute interactions in random alloys (Section 5.2 in Chapter 5). The above expression thus gives the contribution to the variance $\sigma^2_{\Delta E_{ss}}$ due to SRO in terms of solute pair interactions, Warren-Cowley SRO parameter and the alloy composition.

6.5.2 Contribution due to solute-dislocation interactions $\sigma^2_{\Delta E_{sd}}$

Let $U^n_{sd}(x_i, y_i)$ be the interaction of dislocation line along z-axis with solute atom of type n at site i with coordinates (x_i, y_i) with respect to the dislocation position at the origin.

The change in potential energy due to solute-dislocation interactions when a dislocation glides distance w is given by (Recall Equation 6.10),

$$\Delta E_{sd} = \sum_i \sum_n s_i^n \underbrace{\left(U_{sd}^n(x_i, y_i) - U_{sd}^n(x_i + w, y_i)\right)}_{\Delta U_{sd,i}^n(w)} \tag{6.39}$$

Since $\Delta U_{sd,i}^n(w)$ only depends on the x and y coordinates, we can break $\sum_i$ into $\sum_i \sum_k$ where index i runs over atomic sites projected on the z-plane and index k runs over the sites along the z-axis (hence, parallel to the dislocation line) for the respective i^{th} column. So in this section, the atomic sites are indexed by a tuple (ik). Therefore Equation 6.39 can also be expressed as,

$$\Delta E_{sd} = \sum_{i,n} \left(\sum_{k=1}^{\mathbf{N}_l} s_{(ik)}^n \right) \Delta U_{sd,i}^n(w) \tag{6.40}$$

Since $\langle s_{ik}^n \rangle = c_n$ (refer Equation 6.1),

$$\langle \Delta E_{sd} \rangle = \mathbf{N}_l \sum_n c_n \underbrace{\sum_i \Delta U_{sd,i}^n(w)}_{=0} = 0 \tag{6.41}$$

where $\langle \cdot \rangle$ is the expectation operator and $\mathbf{N}_l$ is the number of atomic sites along the dislocation line. *The expectation $\langle \Delta E_{sd} \rangle$ equals zero like in the case of random alloys.*

Variance in ΔE_{sd}, $\sigma_{\Delta E_{sd}}^2 = \langle \Delta E_{sd}^2 \rangle - \langle \Delta E_{sd} \rangle^2 = \langle \Delta E_{sd}^2 \rangle$

$$\begin{aligned} \Delta E_{sd}^2 &= \left(\sum_{i,n} \left(\sum_k s_{(ik)}^n \right) \Delta U_{sd,i}^n(w) \right)^2 \\ &= \sum_{i,j,n,n'} \left(\sum_{k,l} s_{(ik)}^n s_{(jl)}^{n'} \right) \Delta U_{sd,i}^n(w) \Delta U_{sd,j}^{n'}(w) \end{aligned} \tag{6.42}$$

Using the definition in Equation 6.1 and the fact that $s_{(ik)}^n = 1$ and $s_{(ik)}^{n'} = 1$ are *mutually exclusive* for $n \neq n'$, the expectation $\langle s_{(ik)}^n s_{(jl)}^{n'} \rangle$ can be derived as,

$$\begin{aligned} \langle s_{(ik)}^n s_{(jl)}^{n'} \rangle &= \delta_{ij} \delta_{kl} \delta_{nn'} \langle \left(s_{(ik)}^n \right)^2 \rangle + \left(1 - \delta_{ij} \delta_{kl} \right) \langle s_{(ik)}^n s_{(jl)}^{n'} \rangle \\ &= \delta_{ij} \delta_{kl} \delta_{nn'} c_n + \left(1 - \delta_{ij} \delta_{kl} \right) \lambda_{nn'}^{(ik)(jl)} c_n c_{n'} \end{aligned} \tag{6.43}$$

Therefore,

$$\begin{aligned}
\sigma^2_{\Delta E_{sd}} &= \langle \Delta E^2_{sd} \rangle \\
&= \sum_{i,j,n,n'} \left(\sum_{k,l} \langle s^n_{(ik)} s^{n'}_{(jl)} \rangle \right) \Delta U^n_{sd,i}(w) \Delta U^{n'}_{sd,j}(w) \\
&= \left(\sum_{k,l} \delta_{kl} \right) \sum_{i,j,n,n'} \delta_{ij} \delta_{nn'} c_n \Delta U^n_{sd,i}(w) \Delta U^{n'}_{sd,j}(w) \\
&+ \sum_{n,n'} c_n c_{n'} \sum_{i,j} \Delta U^n_{sd,i}(w) \Delta U^{n'}_{sd,j}(w) \sum_{k,l} (1 - \delta_{ij}\delta_{kl})\, \lambda^{(ik)(jl)}_{nn'} \\
&= \mathbf{N}_l \sum_n c_n \sum_i \left(\Delta U^n_{sd,i}(w) \right)^2 + \\
&+ \sum_i \sum_n c_n \Delta U^n_{sd,i}(w) \sum_{n'} c_{n'} \Delta U^{n'}_{sd,i}(w) \sum_{\substack{k,l \\ k \neq l}} \lambda^{(ik)(il)}_{nn'} \\
&+ \sum_{\substack{i,j \\ i \neq j}} \sum_n c_n \Delta U^n_{sd,i}(w) \sum_{n'} c_{n'} \Delta U^{n'}_{sd,j}(w) \sum_{k,l} \lambda^{(ik)(jl)}_{nn'} \qquad (6.44)
\end{aligned}$$

$\sum_n c_n \Delta U^n_{sd,i}(w) = 0$ since $\sum_n c_n U^n_{sd}(x_i, y_i) = 0$ for any site i, irrespective of any short-range order; although individual solute interaction energies with the dislocation U^n_{sd} may not be the same for random alloys and alloys with SRO. Therefore in case of random alloys, where λ is always unity, we have $\sigma^2_{\Delta E_{sd}} = \mathbf{N}_l \sum_n c_n \sum_i \left(\Delta U^n_{sd,i}(w) \right)^2$.

Despite correlations, in absence of long-range order (LRO), there will be a distance d_{cut} beyond which $\lambda_{nn'} = 1$ for all solute pairs (n, n').

Now let us revisit the second and the third terms in Equation 6.44. The second term can be simplified as follows,

$$\begin{aligned}
2^{nd} \text{ term} &= \sum_i \sum_n c_n \Delta U^n_{sd,i}(w) \sum_{n'} c_{n'} \Delta U^{n'}_{sd,i}(w) \sum_{\substack{k,l \\ k \neq l}} \lambda^{(ik)(il)}_{nn'} \\
&= \mathbf{N}_l \sum_i \sum_n c_n \Delta U^n_{sd,i}(w) \sum_{n'} c_{n'} \Delta U^{n'}_{sd,i}(w) \sum_{\substack{l=-l_{max} \\ l \neq 0}}^{l_{max}} \lambda_{nn'}(d_l) \\
&+ \mathbf{N}_l \left(\sum_{\substack{l \\ |l| > l_{max}}} 1 \right) \sum_i \underbrace{\sum_n c_n \Delta U^n_{sd,i}(w)}_{=0} \underbrace{\sum_{n'} c_{n'} \Delta U^{n'}_{sd,i}(w)}_{=0} \\
&= \mathbf{N}_l \sum_i \sum_n c_n \Delta U^n_{sd,i}(w) \sum_{n'} c_{n'} \Delta U^{n'}_{sd,i}(w) \sum_{\substack{l=-l_{max} \\ l \neq 0}}^{l_{max}} \lambda_{nn'}(d_l) \qquad (6.45)
\end{aligned}$$

where d_l is the distance of a site l relative to a site k along the z-axis and note that position of site k (or $l = 0$) does not matter and we can express the 2nd term in term of d_l since the pair correlation function $\lambda_{nn'}$ depends on intersite distances and not on the position of the sites. l_{max} is the furthest site from any site k along the dislocation line such that their separation is $\leq d_{cut}$. Also we assume $l_{max} \ll \mathbf{N}_l$ and we ignore error due to finite $\mathbf{N}_l$.

The second term can be rewritten in terms of Warren-Coley parameters as follows,

$$\begin{aligned}
2^{nd}\ \text{term} &= 2l_{max}\mathbf{N}_l \sum_{i,j} \underbrace{\sum_{n} c_n \Delta U^{n}_{sd,i}(w)}_{=0} \underbrace{\sum_{n'} c_{n'} \Delta U^{n'}_{sd,i}(w)}_{=0} \\
&\quad - \mathbf{N}_l \sum_{i} \sum_{n} c_n \Delta U^{n}_{sd,i}(w) \sum_{n'} c_{n'} \Delta U^{n'}_{sd,i}(w) \sum_{\substack{l=-l_{max} \\ l\neq 0}}^{l_{max}} \alpha_{nn'}(d_l) \\
&= -\mathbf{N}_l \sum_{i} \sum_{n} c_n \Delta U^{n}_{sd,i}(w) \sum_{n'} c_{n'} \Delta U^{n'}_{sd,i}(w) \sum_{\substack{l=-l_{max} \\ l\neq 0}}^{l_{max}} \alpha_{nn'}(d_l) \qquad (6.46)
\end{aligned}$$

Similarly the third term can be simplified as,

$$\begin{aligned}
3^{rd}\ \text{term} &= \sum_{\substack{i,j \\ i\neq j}} \sum_{n} c_n \Delta U^{n}_{sd,i}(w) \sum_{n'} c_{n'} \Delta U^{n'}_{sd,j}(w) \sum_{k,l} \lambda^{(ik)(jl)}_{nn'} \\
&= \mathbf{N}_l \sum_{i} \sum_{\substack{j \\ 0<\|\boldsymbol{r}_{(i0)}-\boldsymbol{r}_{(j0)}\|\leq d_{cut}}} \sum_{n} c_n \Delta U^{n}_{sd,i}(w) \sum_{n'} c_{n'} \Delta U^{n'}_{sd,j}(w) \sum_{l=-l^{j}_{max}}^{l^{j}_{max}} \lambda_{nn'}(d_l) \\
&= \mathbf{N}_l \sum_{i} \sum_{\substack{j \\ 0<\|\boldsymbol{r}_{(i0)}-\boldsymbol{r}_{(j0)}\|\leq d_{cut}}} (2l^{j}_{max}+1) \underbrace{\sum_{n} c_n \Delta U^{n}_{sd,i}(w)}_{=0} \underbrace{\sum_{n'} c_{n'} \Delta U^{n'}_{sd,j}(w)}_{=0} \\
&\quad - \mathbf{N}_l \sum_{i} \sum_{\substack{j \\ 0<\|\boldsymbol{r}_{(i0)}-\boldsymbol{r}_{(j0)}\|\leq d_{cut}}} \sum_{n} c_n \Delta U^{n}_{sd,i}(w) \sum_{n'} c_{n'} \Delta U^{n'}_{sd,j}(w) \sum_{l=-l^{j}_{max}}^{l^{j}_{max}} \alpha_{nn'}(d_l) \\
&= -\mathbf{N}_l \sum_{i} \sum_{\substack{j \\ 0<\|\boldsymbol{r}_{(i0)}-\boldsymbol{r}_{(j0)}\|\leq d_{cut}}} \sum_{n} c_n \Delta U^{n}_{sd,i}(w) \sum_{n'} c_{n'} \Delta U^{n'}_{sd,j}(w) \sum_{l=-l^{j}_{max}}^{l^{j}_{max}} \alpha_{nn'}(d_l) \qquad (6.47)
\end{aligned}$$

Figure 6.3 schematically explains the supremum indices l_{max} and l^{j}_{max} used in Equations 6.46 and 6.47.

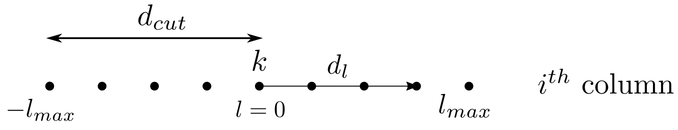

(a) 2nd term

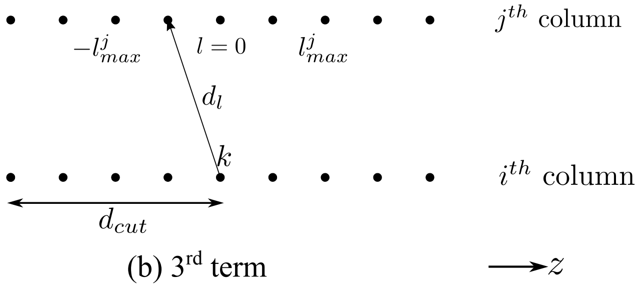

(b) 3rd term

Figure 6.3 – Schematic of the distances and indexes used in (a) Equation 6.46 and (b) Equation 6.47, which basically simplifies the 2^{nd} and 3^{rd} terms in Equation 6.44 respectively.

Using Equations 6.44, 6.45, 6.46 and 6.47, $\sigma^2_{\Delta E_{sd}}/\mathbf{N}_l$ can be expressed as,

$$\begin{aligned}
\sigma^2_{\Delta E_{sd}}/\mathbf{N}_l = &\sum_n c_n \sum_i \left(\Delta U^n_{sd,i}(w)\right)^2 \\
&+ \sum_n c_n \sum_i \Delta U^n_{sd,i}(w) \left(\sum_{n'} c_{n'} \Delta U^{n'}_{sd,i}(w) \sum_{\substack{l=-l_{max} \\ l\neq 0}}^{l_{max}} \lambda_{nn'}(d_l) \right) \\
&+ \sum_n c_n \sum_i \Delta U^n_{sd,i}(w) \left(\sum_{n'} c_{n'} \sum_{\substack{j \\ 0<\|\boldsymbol{r}_{(i0)}-\boldsymbol{r}_{(j0)}\|\leq d_{cut}}} \Delta U^{n'}_{sd,j}(w) \sum_{l=-l^j_{max}}^{l^j_{max}} \lambda_{nn'}(d_l) \right) \\
= &\sum_n c_n \sum_i \left(\Delta U^n_{sd,i}(w)\right)^2 \\
&- \sum_n c_n \sum_i \Delta U^n_{sd,i}(w) \left(\sum_{n'} c_{n'} \Delta U^{n'}_{sd,i}(w) \sum_{\substack{l=-l_{max} \\ l\neq 0}}^{l_{max}} \alpha_{nn'}(d_l) \right) \\
&- \sum_n c_n \sum_i \Delta U^n_{sd,i}(w) \left(\sum_{n'} c_{n'} \sum_{\substack{j \\ 0<\|\boldsymbol{r}_{(i0)}-\boldsymbol{r}_{(j0)}\|\leq d_{cut}}} \Delta U^{n'}_{sd,j}(w) \sum_{l=-l^j_{max}}^{l^j_{max}} \alpha_{nn'}(d_l) \right) \qquad (6.48)
\end{aligned}$$

Note that the expression for the first term in Equation 6.48 is same as the expression for $\sigma^2_{\Delta E_{sd}}/\mathbf{N}_l$ in case of random alloys; however the first term won't evaluate to same value for random alloys and alloys with SRO since the solute-dislocation interaction energies U^n_{sd} might differ for alloys with and without SRO.

Finally, since the number of atomic sites along the dislocation line of length ζ is given by $\mathbf{N}_l =$

$\rho_L \zeta$, the variance $\sigma^2_{\Delta E_{sd}}$ for a dislocation segment of length ζ is given by $\sigma^2_{\Delta E_{sd}} = \left(\sigma^2_{\Delta E_{sd}} / \mathbf{N}_l\right) \rho_L \zeta$, where $\left(\sigma^2_{\Delta E_{sd}} / \mathbf{N}_l\right)$ calculated with Equation 6.48 depends solely on solute-dislocation interaction energies, Warren-Cowley SRO parameters and the alloy composition.

6.5.3 Correlation between the energy changes due to solute-solute (ΔE_{ss}) and solute-dislocation (ΔE_{sd}) interactions

In this section we are going to derive the covariance of the energy changes ΔE_{ss} and ΔE_{sd}, which is given by

$$\operatorname{cov}(\Delta E_{ss}, \Delta E_{sd}) = \langle \Delta E_{ss} \Delta E_{sd} \rangle - \langle \Delta E_{ss} \rangle \underbrace{\langle \Delta E_{sd} \rangle}_{=0} = \langle \Delta E_{ss} \Delta E_{sd} \rangle \tag{6.49}$$

Expressions for ΔE_{ss} and ΔE_{sd} were mentioned earlier in Equations 6.10, 6.11 and 6.39. Using those expressions, the product of the two energy changes can be expressed as follows,

$$\begin{aligned}
\Delta E_{ss} \Delta E_{sd} &= \sum_{\substack{k,l \\ y_k<0 \\ y_l>0}} \sum_{p,q} s_k^p s_l^q \underbrace{\left(U_{pq}(\|\boldsymbol{r}_{kl} + \boldsymbol{t}\|) - U_{pq}(\|\boldsymbol{r}_{kl}\|)\right)}_{\Delta U^{pq}_{ss,kl}} \sum_i \sum_n s_i^n \underbrace{\left(U^n_{sd}(x_i, y_i) - U^n_{sd}(x_i + w, y_i)\right)}_{\Delta U^n_{sd,i}(w)} \\
&= \sum_{\substack{k,l \\ y_k<0 \\ y_l>0}} \sum_{p,q} s_k^p s_l^q \Delta U^{pq}_{ss,kl} \sum_i \sum_n s_i^n \Delta U^n_{sd,i}(w) \\
&= \sum_{\substack{k,l \\ y_k<0 \\ y_l>0}} \sum_{p,q} s_k^p s_l^q \Delta U^{pq}_{ss,kl} \Bigg(\sum_{\substack{i \\ y_i<0}} \sum_n s_i^n \Delta U^n_{sd,i}(w) + \sum_{\substack{i' \\ y_{i'}>0}} \sum_{n'} s_{i'}^{n'} \Delta U^{n'}_{sd,i'}(w) \Bigg) \\
&= \sum_{\substack{i \\ y_i<0}} \sum_{\substack{k,l \\ y_k<0 \\ y_l>0}} \sum_n \sum_{p,q} s_i^n s_k^p s_l^q \Delta U^{pq}_{ss,kl} \Delta U^n_{sd,i}(w) \\
&+ \sum_{\substack{i \\ y_i>0}} \sum_{\substack{k,l \\ y_{k'}<0 \\ y_l>0}} \sum_n \sum_{p,q} s_i^n s_k^p s_l^q \Delta U^{pq}_{ss,kl} \Delta U^n_{sd,i}(w)
\end{aligned} \tag{6.50}$$

Taking expectation of either sides of Equation 6.50, we have

$$\begin{aligned}
\langle \Delta E_{ss} \Delta E_{sd} \rangle &= \sum_{\substack{i \\ y_i<0}} \sum_{\substack{k,l \\ y_k<0 \\ y_l>0}} \sum_n \sum_{p,q} \langle s_i^n s_k^p s_l^q \rangle \Delta U^{pq}_{ss,kl} \Delta U^n_{sd,i}(w) \\
&+ \sum_{\substack{i \\ y_i>0}} \sum_{\substack{k,l \\ y_k<0 \\ y_l>0}} \sum_n \sum_{p,q} \langle s_i^n s_k^p s_l^q \rangle \Delta U^{pq}_{ss,kl} \Delta U^n_{sd,i}(w)
\end{aligned} \tag{6.51}$$

We will simplify the two term in the above equation separately and then add them. Before that, we need to first simplify $\langle s_i^n s_k^p s_l^q \rangle$. If $y_i < 0, y_k < 0, y_l > 0$, then

$$\begin{aligned}\langle s_i^n s_k^p s_l^q \rangle &= \delta_{ik}\delta_{np}\langle \left(s_k^p\right)^2 s_l^q \rangle + (1-\delta_{ik})\langle s_i^n s_k^p s_l^q \rangle \\ &= \delta_{ik}\delta_{np}\lambda_{pq}^{kl} c_p c_q + (1-\delta_{ik})\lambda_{npq}^{ikl} c_n c_p c_q \end{aligned} \tag{6.52}$$

Similarly, if $y_i > 0, y_k < 0, y_l > 0$, then

$$\begin{aligned}\langle s_i^n s_k^p s_l^q \rangle &= \delta_{il}\delta_{nq}\langle s_k^p \left(s_l^q\right)^2 \rangle + (1-\delta_{il})\langle s_i^n s_k^p s_l^q \rangle \\ &= \delta_{il}\delta_{nq}\lambda_{pq}^{kl} c_p c_q + (1-\delta_{il})\lambda_{npq}^{ikl} c_n c_p c_q \end{aligned} \tag{6.53}$$

Using the above result for $\langle s_i^n s_k^p s_l^q \rangle$, the first term of Equation 6.51 simplying as follows,

$$\begin{aligned}1^{st}\text{ term of Eqn. 6.51} &= \sum_{\substack{i\\ y_i<0}} \sum_{\substack{k,l\\ y_k<0\\ y_l>0}} \sum_n \sum_{p,q} \left(\delta_{ik}\delta_{np}\lambda_{pq}^{kl} c_p c_q + (1-\delta_{ik})\lambda_{npq}^{ikl} c_n c_p c_q\right)\Delta U_{ss,kl}^{pq}\Delta U_{sd,i}^{n}(w) \\ &= \sum_{\substack{k,l\\ y_k<0\\ y_l>0}} \sum_{p,q} \lambda_{pq}^{kl} c_p c_q \Delta U_{ss,kl}^{pq}\Delta U_{sd,k}^{p}(w) \\ &+ \sum_{\substack{k,l\\ y_k<0\\ y_l>0}} \sum_{\substack{i\\ y_i<0\\ i\neq k}} \sum_n \sum_{p,q} \lambda_{npq}^{ikl} c_n c_p c_q \Delta U_{ss,kl}^{pq}\Delta U_{sd,i}^{n}(w) \end{aligned} \tag{6.54}$$

Similarly, the second term of Equation 6.51 simplifies as

$$\begin{aligned}2^{nd}\text{ term of Eqn. 6.51} &= \sum_{\substack{i\\ y_i>0}} \sum_{\substack{k,l\\ y_k<0\\ y_l>0}} \sum_n \sum_{p,q} \left(\delta_{il}\delta_{nq}\lambda_{pq}^{kl} c_p c_q + (1-\delta_{il})\lambda_{npq}^{ikl} c_n c_p c_q\right)\Delta U_{ss,kl}^{pq}\Delta U_{sd,i}^{n}(w) \\ &= \sum_{\substack{k,l\\ y_k<0\\ y_l>0}} \sum_{p,q} \lambda_{pq}^{kl} c_p c_q \Delta U_{ss,kl}^{pq}\Delta U_{sd,l}^{q}(w) \\ &+ \sum_{\substack{k,l\\ y_k<0\\ y_l>0}} \sum_{\substack{i\\ y_i>0\\ i\neq l}} \sum_n \sum_{p,q} \lambda_{npq}^{ikl} c_n c_p c_q \Delta U_{ss,kl}^{pq}\Delta U_{sd,i}^{n}(w) \end{aligned} \tag{6.55}$$

Combining the two terms the covariance of ΔE_{ss} and ΔE_{sd} can be expressed as,

$$
\begin{aligned}
\mathrm{cov}\left(\Delta E_{ss}, \Delta E_{sd}\right) &= \langle \Delta E_{ss} \Delta E_{sd} \rangle \\
&= \sum_{\substack{k,l\\ y_k<0\\ y_l>0}} \sum_{p,q} \lambda^{kl}_{pq} c_p c_q \Delta U^{pq}_{ss,kl} \left(\Delta U^{p}_{sd,k}(w) + \Delta U^{q}_{sd,l}(w) \right) \\
&+ \sum_{\substack{k,l\\ y_k<0\\ y_l>0}} \sum_{p,q} \sum_{\substack{i\\ i\neq k\neq l}} \sum_{n} \lambda^{ikl}_{npq} c_n c_p c_q \Delta U^{pq}_{ss,kl} \Delta U^{n}_{sd,i}(w) \\
&= \sum_{\substack{k,l\\ y_k<0\\ y_l>0}} \sum_{p,q} c_p c_q \Delta U^{pq}_{ss,kl} \left(\Delta U^{p}_{sd,k}(w) + \Delta U^{q}_{sd,l}(w) \right) \\
&- \sum_{\substack{k,l\\ y_k<0\\ y_l>0}} \sum_{p,q} \alpha^{kl}_{pq} c_p c_q \Delta U^{pq}_{ss,kl} \left(\Delta U^{p}_{sd,k}(w) + \Delta U^{q}_{sd,l}(w) \right) \\
&+ \sum_{\substack{k,l\\ y_k<0\\ y_l>0}} \sum_{p,q} \sum_{\substack{i\\ i\neq k\neq l}} c_p c_q \Delta U^{pq}_{ss,kl} \underbrace{\sum_{n} c_n \Delta U^{n}_{sd,i}(w)}_{=0} \\
&- \sum_{\substack{k,l\\ y_k<0\\ y_l>0}} \sum_{p,q} \sum_{\substack{i\\ i\neq k\neq l}} \sum_{n} \alpha^{ikl}_{npq} c_n c_p c_q \Delta U^{pq}_{ss,kl} \Delta U^{n}_{sd,i}(w) \qquad (6.56)
\end{aligned}
$$

Notice that for random alloys, when $\lambda = 1$ (or $\alpha = 0$), the first term is not zero — So the covariance between ΔE_{ss} and ΔE_{sd} is not zero for random alloys, but is expected to be small (Recall Figure 6.2).

In Equation 6.56, change in energy due to solute-solute interactions and the energy change due to solute-dislocation interactions are multiplied in every term of the equation. The former scales with area of the slip plane swept by the dislocation when it glides and the latter scales with dislocation line length — so their product will scale with dislocation line length. So the covariance $\mathrm{cov}\left(\Delta E_{ss}, \Delta E_{sd}\right)$ scales with the number of sites along the dislocation line $\mathbf{N}_l$. This is also a consequence of the short-ranged solute-solute interactions across the slip plane (again recall Figure 6.2). Since for a dislocation segment of length ζ, $\mathbf{N}_l = \rho_L \zeta$ as discussed earlier, the covariance $\mathrm{cov}\left(\Delta E_{ss}, \Delta E_{sd}\right)$ corresponding to the glide of a dislocation segment of length ζ is given by $\mathrm{cov}\left(\Delta E_{ss}, \Delta E_{sd}\right) = \left(\mathrm{cov}\left(\Delta E_{ss}, \Delta E_{sd}\right)/\mathbf{N}_l\right) \rho_L \zeta$, where $\mathrm{cov}\left(\Delta E_{ss}, \Delta E_{sd}\right)/\mathbf{N}_l$ depends solely on solute pair interactions, solute-dislocation interaction energies, pair correlation functions and the alloy composition.

Using superposition approximation for 3-site correlation function λ_{npq}, Equation 6.56 can be rewritten as

$$\begin{aligned}\mathrm{cov}\left(\Delta E_{ss}, \Delta E_{sd}\right) = &\sum_{\substack{k,l\\ y_k<0\\ y_l>0}} \sum_{p,q} \lambda^{kl}_{pq} c_p c_q \Delta U^{pq}_{ss,kl} \left(\Delta U^{p}_{sd,k}(w) + \Delta U^{q}_{sd,l}(w)\right) \\ &+ \sum_{\substack{k,l\\ y_k<0\\ y_l>0}} \sum_{p,q} \sum_{\substack{i\\ i\neq k\neq l}} \sum_{n} \lambda^{ik}_{np} \lambda^{il}_{nq} \lambda^{kl}_{pq} c_n c_p c_q \Delta U^{pq}_{ss,kl} \Delta U^{n}_{sd,i}(w)\end{aligned} \tag{6.57}$$

Expanding the pair correlation functions in terms of Warren-Cowley SRO parameters (that is, $\lambda^{kl}_{pq} = 1 - \alpha^{kl}_{pq}$) and retaining only the first-order terms in the latter, we can rewrite Equation 6.57 as,

$$\begin{aligned}\mathrm{cov}\left(\Delta E_{ss}, \Delta E_{sd}\right) = &\sum_{\substack{k,l\\ y_k<0\\ y_l>0}} \sum_{p,q} c_p c_q \Delta U^{pq}_{ss,kl} \left(\Delta U^{p}_{sd,k}(w) + \Delta U^{q}_{sd,l}(w)\right) \\ &- \sum_{\substack{k,l\\ y_k<0\\ y_l>0}} \sum_{p,q} \alpha^{kl}_{pq} c_p c_q \Delta U^{pq}_{ss,kl} \left(\Delta U^{p}_{sd,k}(w) + \Delta U^{q}_{sd,l}(w)\right) \\ &+ \sum_{\substack{k,l\\ y_k<0\\ y_l>0}} \sum_{p,q} \sum_{\substack{i\\ i\neq k\neq l}} c_p c_q \Delta U^{pq}_{ss,kl} \underbrace{\sum_{n} c_n \Delta U^{n}_{sd,i}(w)}_{=0} \\ &- \sum_{\substack{k,l\\ y_k<0\\ y_l>0}} \sum_{p,q} \sum_{\substack{i\\ i\neq k\neq l}} \alpha^{kl}_{pq} c_p c_q \Delta U^{pq}_{ss,kl} \underbrace{\sum_{n} c_n \Delta U^{n}_{sd,i}(w)}_{=0} \\ &- \sum_{\substack{k,l\\ y_k<0\\ y_l>0}} \sum_{p,n} \sum_{\substack{i\\ i\neq k\neq l}} \alpha^{ik}_{np} c_n c_p \left(\sum_{q} c_q \Delta U^{pq}_{ss,kl}\right) \Delta U^{n}_{sd,i}(w) \\ &- \sum_{\substack{k,l\\ y_k<0\\ y_l>0}} \sum_{q,n} \sum_{\substack{i\\ i\neq k\neq l}} \alpha^{il}_{nq} c_n c_q \left(\sum_{p} c_p \Delta U^{pq}_{ss,kl}\right) \Delta U^{n}_{sd,i}(w)\end{aligned}$$

Notice the last two terms are equal (interchange dummy indices p and q).

Therefore, $\mathrm{cov}\left(\Delta E_{ss}, \Delta E_{sd}\right)$ can be expressed in terms of the solute pair interactions, solute-dislocation interaction energies, Warren-Cowley SRO parameter and the alloy composition as follows,

$$
\begin{aligned}
\operatorname{cov}(\Delta E_{ss}, \Delta E_{sd}) = & \sum_{\substack{k,l \\ y_k<0 \\ y_l>0}} \sum_{p,q} c_p c_q \Delta U^{pq}_{ss,kl} \Big(\Delta U^{p}_{sd,k}(w) + \Delta U^{q}_{sd,l}(w) \Big) \\
& - \sum_{\substack{k,l \\ y_k<0 \\ y_l>0}} \sum_{p,q} \alpha^{kl}_{pq} c_p c_q \Delta U^{pq}_{ss,kl} \Big(\Delta U^{p}_{sd,k}(w) + \Delta U^{q}_{sd,l}(w) \Big) \\
& -2 \sum_{\substack{k,l \\ y_k<0 \\ y_l>0}} \sum_{p,n} \sum_{\substack{i \\ i\neq k\neq l}} \alpha^{ik}_{np} c_n c_p \left(\sum_{q} c_q \Delta U^{pq}_{ss,kl} \right) \Delta U^{n}_{sd,i}(w)
\end{aligned}
\tag{6.58}
$$

It has been discussed that the covariance involves the sites near the dislocation position in both the initial and final configurations during dislocation glide (Recall Figure 6.2). At those sites the assumption of uniform slip vector $\boldsymbol{t}$ is not valid and therefore the error due to this assumption scales with $\mathbf{N}_l$ just like the covariance we derived in Equation 6.56. *To calculate the covariance, one should therefore consider the correct slip distribution around the dislocation line instead of the constant slip vector* $\boldsymbol{t}$.

6.6 Discussion and Summary

This chapter presents a theoretical framework for solute-strengthening in alloys with SRO. Short-range order has been characterized with n-site correlation functions and the relation of the pair correlation functions with the well-known Warren-Cowley SRO parameters has been established. The theory requires 2-site(pair), 3-site and 4-site correlation functions; however the higher-order correlation functions are inaccessible experimentally and are generally unavailable. So a superposition approximation has been introduced which approximates the higher-order correlation functions as product of certain pair correlation functions. The validity of using this approximation for small pair correlations has been ascertained.

Using the mathematical framework of SRO, the new theory of solute-strengthening is formulated. Like in random alloys, the fluctuation in energy change due to gliding dislocation segments has two contributions, one due to solute-dislocation interactions and the other due to solute-solute interactions across the slip plane. Unlike random alloys, the energy change due to solute-solute interactions is not zero on average and therefore when a dislocation glides in an alloy with SRO it leaves behind a high-energy slip plane (like a fault plane). This is caused by the slip associated with dislocation glide, when energetically favourable solute pairs are separated and unfavourable solute pairs are brought closer, thus rising the energy *on average* due to solute-solute interactions across the slip plane. An externally applied stress must pay for this energy penalty, thus introducing an additional strengthening component for alloys with SRO, which we call "*average strengthening*". The average strengthening has received significant attention in the literature, however they were limited in their analysis. In this chapter, expressions are derived for predicting the average strengthening, which takes as inputs the effective pair interactions of solutes across the slip plane, the Warren-Cowley SRO parameters and the alloy composition. Agreement of the derived expressions in this study with those proposed in previous studies on average strengthening has been established for some special cases. This is the most important result of this chapter and is deemed to be the significant additional strengthening factor due to SRO. It is also shown that the average strengthening is not thermally-activated.

Like in random alloys, the thermally-activated strengthening component due to glide of locally pinned dislocation segments over energy barriers presented by the fluctuating solute environment, is also present in the case of alloys with SRO. In Chapter 5, we have seen that local strengthening is controlled by the variances in energy change due to solute-dislocation and solute-solute interactions. In the case of SRO, these variances get modified and in this chapter we have derived expressions for these variances in terms of correlation functions, solute-dislocation interaction energies, solute-solute bond energies and the alloy composition. The variance in energy change due to solute-solute interactions depends on 3-site and 4-site correlation functions in addition to pair correlation functions. Using the superposition approximation for higher-order correlation functions, approximate expression for the above variance is derived which depends only on pair correlations. Finally, the two contributions to energy change (solute-solute and solute-dislocation) are correlated, and the net fluctuation in energy change controlling local strengthening must also consider the covariance of the two contributions. The covariance is non-zero even for random alloys, however we neglected it in Chapter 5 since only very few sites near the dislocation core contribute to this term. In the general theory proposed in this chapter, we have considered the covariance and derived its expression, thus giving a complete theoretical framework to the problem of solute-strengthening in alloys.

The current theory is complete in its analysis of average strengthening and the latter can be predicted for any multicomponent fcc or bcc alloy with the knowledge of the effective pair interactions among different solute pairs and the Warren-Cowley SRO parameters. However the two aforesaid inputs are not easily obtained by experiments. The effective pair interactions and Warren-Cowley SRO parameters can be calculating with DFT calculations and Monte-Carlo simulations, but these are expensive calculations. Determination of average strengthening for different dilute and complex concentrated alloys is the primary future goal of this ongoing project. The modification to the local strengthening due to SRO might be significant for some alloys, however certain challenges needs to addressed before we can study this contribution for different alloys. First of all the expressions derived for variance in energy change controlling local strengthening are in terms of solute pair bond energies. Realistic metallic alloys modeled with empirical interatomic potentials like EAM or with first principles, entail many-body interactions among its constituents. Solute pair interaction quantities like the interaction energies or effective pair potentials can be uniquely defined for any system with the help of an average atom concept (Recall Chapter 5). So, the expressions for variances and covariances in Section 6.5 of this chapter must be reformulated in terms of interaction energy and effective pair interaction in order to study local strengthening under SRO for realistic alloys. Secondly, approximations like the superposition approximation for higher-order correlation functions or the ignoring the second-order terms in the variance for solute-solute interactions are all premised on the assumption that the Warren-Cowley SRO parameters are small. It remains to be examined how small the SRO parameters need to be for these approximations to be valid, while still having a notable SRO effect on solute-strengthening.

The theory presented in this chapter, despite lacking full maturity, lays the groundwork for further modification and improvement with the aim to have a complete and adequate theoretical framework for predicting yield strength of alloys with any compositional complexity. This will assist the metallurgical and materials community in more efficient alloy design.

7 Summary

Alloying enhances strength and other desirable mechanical properties of metals. A new class of complex concentrated alloys with 5 or more constituents, called high(medium)-entropy alloys (HEAs/MEAs), shows promising strength and fracture toughness. Under common alloy processing conditions, HEAs often form single-phase random alloys, with no correlation in the occupancy of lattice sites by the constituent atom types. Random alloys are an important limiting case of no chemical ordering and the current thesis primarily addresses two problems pertaining to random alloys, namely, (1) concurrent multiscale modeling and (2) solute-strengthening.

Random alloys are rife with compositional fluctuations, which in turn result in fluctuation in local atomic configurations and elastic stiffnesses. For accurate functioning of a force-based atomistic/continuum (a/c) couple, it is important that the underlying material description in both the atomistic and the continuum domains are the same near the a/c interface. A/c coupling of random alloys violate this criterion since the atomistics is inherently inhomogeneous and the continuum is described with the average elastic constants of the alloy. The resulting errors due to coupling are of the order of 100 MPa in long-range spurious stresses and spurious stress fluctuations near the interface. Two methods of constructing the coupled problem for random alloys have been proposed in the thesis which mitigate errors arising in the standard method. In one method, the desired atomistic domain and its nearby surroundings are fully relaxed to an equilibrium structure and then inserted into the coupled problem as the reference configuration. This reduces the effects of the random-to-homogeneous transition near the a/c interface, and guarantees no spurious stress at zero load. In the second method, the random-to-homogeneous transition is spatially separated from the atomistic-continuum transition by introducing a small buffer zone of well-defined '*average atoms*'. The random-to-homogeneous transition is then accomplished fully atomistically while the atomistic to continuum transition is accomplished in a homogeneous material. The two methods are validated through comparisons of the stresses in the coupled method versus the true atomistic system for three different solid solution alloys (Al-5%Mg, Ni-15%Al, and medium-entropy FeNiCr) as described by EAM interatomic potentials. Spurious stresses for both methods and across all three materials are negligible (≈ 5 MPa) relative to stresses arising in realistic mechanical problems of interest. These new methods thus enable the accurate study of mechanics boundary value problems in random alloys for problems where it is essential to capture atomistic phenomena in some localized region of the random alloy.

Solute strengthening in random alloys is mediated through the impediment to dislocation motion caused by random compositional fluctuations. Dislocation segments get pinned at favourable solute fluctuations and externally applied shear stress coupled with thermal activation is needed to unpin the dislocation and resume motion. Both the local minima and maxima in the energy landscape traversed by the segments are dictated by the solute-dislocation interactions and the solute-solute interactions across the slip plane. A recent theory predicts the strengthening as a function of the solute-dislocation interaction energies and composition. First-principles calculations of solute-dislocation interaction energies are computationally expensive, therefore an elasticity model for the interaction has been formulated which reduces the solute-dislocation interaction energy to the product of the dislocation pressure field and the solute misfit volume. In the thesis, the elasticity model is formulated and evaluated for cubic anisotropy in fcc metals, and compared to a previous isotropic model. The prediction using the isotropic model with Voigt-averaged elastic constants is shown to represent the full anisotropic results within a few percent, and so is the recommended approach for studying anisotropic alloys. Application of the elasticity model using accessible experimentally-measured properties and/or first-principles-computed properties is then discussed so as to guide use of the model for estimating strengths of existing and newly proposed alloys. On the other hand, the contribution of the solute-solute interactions, described by pairwise interactions, has been modeled in terms of the standard deviation in total solute-solute interaction energies as a dislocation segment glides through the material, which changes specific solute-solute pairs across the glide plane at every pair distance. An analytic expression is derived for the above standard deviation and validated against numerical simulations on a wide range of model random alloys consisting of 2–5 elements interacting via Lennard-Jones pair potentials. The theory is applied to the bcc MoNbTaW high entropy alloy, using solute-solute interactions computed via first-principles, and a model NbTaV alloy, described by EAM potentials, where the strength increases negligibly by 2% and 0.45%, respectively. Application to random dilute fcc Ni(Al), where the first-neighbor Al-Al interaction is very strongly repulsive, shows significant strengthening of 60–100% at 10% Al, depending on the origin of the inputs. Some connections to literature atomistic simulations on Ni(Al) are also presented. Overall, the strengthening theory presented in this thesis provides a quantitative framework for assessing the relative roles of solute-dislocation and solute-solute interactions on strengthening in random alloys.

Finally, the thesis also addresses the role of chemical ordering in the form of short-range order in influencing strength of alloys. Alloys having strongly disproportionate solute-solute interactions can lead to the development of short-range order (SRO) or long-range order (LRO), for example the exceptionally strong Al-Al repulsion in Ni(Al) alloys. Average strengthening observed only in alloys with SRO, had received considerable attention in the past. Since

SRO promotes the existence of higher-than-random favourable solute pairs and lower-than-random unfavourable pairs, the slip associated with dislocation glide disrupts this order on average, thus leaving behind a high-energy slipped area over the region traversed by the dislocation line. This average energy cost is balanced by the work done by externally applied stress to sustain unabated dislocation glide. Expression for the average strengthening effect have been derived in the thesis in terms of solute pair interaction energies, the well-known Warren-Cowley SRO parameter and the alloy composition. The strengthening theory accounting for SRO is still in progress and some challenges need to be addressed before the theory can be applied to predict the yield strength of non-random alloys. However, the preliminary development of the theory presented in the thesis is the first step towards having an all-encompassing theory of solute-strengthening for dilute and complex concentrated alloys.

8 Outlook

The thesis has explored some new areas of research in multicomponent alloys which were either uncharted or came into limelight recently. In this chapter we are going to discuss the future possibilities of application and extension of the concepts introduced in the thesis.

The thesis proposed two methods of constructing a multiscale problem for random alloys for accurate atomistic-to-continuum coupling under force-based setting and validated the methods with an effectively one-dimensional coupling geometry for proof of concept. Now the methods need to be implemented to solve solid mechanics problems in random alloys of a multiscale nature. An ideal problem would be to study the nucleation of dislocations from a crack tip leading to crack tip blunting. A classic problem of this sort is to determine whether cleavage will be favoured over dislocation emission, which is an important determinant of material performance. A related problem of more multiscale nature would be to address the same question but when there are already preexisting dislocations surrounding the crack tip. These problems are studied for elemental solid in the context of fatigue failure [11, 145, 146] and it would be interesting to see how compositional fluctuations surrounding the crack tip influence dislocation emission and crack tip blunting. Coupled atomistic-dislocation dynamics (CADD) method is often used to study these problems since evolution of dislocation network and calculation of the long-range elastic field of a collection of dislocations are robustly handled under linear elasticity assumption by dislocation dynamics (DD) method. The crack front presents a plane strain problem and normally the coupling interface is therefore constructed parallel to the crack front. In such a situation, if the emanating and preexisting dislocations are also parallel to the crack front, the dislocations can cross domains without ever actually crossing the atomistic-continuum (a/c) interface through the pad region. Studying this problem in the context of random alloys is straightforward using both the proposed methods of constructing the coupled problem. Dislocation in the atomistic domain glides toward the continuum domain upto some critical distance from the coupling interface and then it is hopped onto the continuum domain keeping the resulting elastic fields consistent; the dislocation can then glide in the continuum domain with some phenomenological mobility law. If the dislocation happens to exist simultaneously in both the domain as a "*hybrid*" dislocation [17–19], then such a situation is complicated. For elemental solid, an atomistic template is chosen specific to the dislocation line orientation at the couple interface and that template is used to patch the dislocation across the two domains. Choosing such a template for a random alloy in Method 1 is unwieldy since the template needs to be specific to the local compositional fluctuation. However in Method 2 using average atoms such a template can be easily devised since coupling interface is in the average atoms region. However mobility of the dislocation in the explicit random alloy and in the average atoms might be different which might lead to certain artifacts, which remains to be examined.

The two methods for constructing a multiscale problem are proposed in this thesis in the context of force-based coupling. However there exists the energy-based methods which is an active field of research (refer to the brief review in Section 1.1). Method 2 of this thesis with average atoms, can be readily extended to any multiscale method designed for elemental solids, since the coupling interface is in the monoatomic average atoms. In the Quasi-continuum (QC) method for example, Method 2 is directly amenable to extension to nonlinear deformation in the continuum via application of the Cauchy-Born rule to the average atom unit cell. One advantage of the energy-based methods is the automatic adaptability of the multiscale problem — regions of high deformation are tracked down and finely resolved on-the-fly. There are robust non-local QC cluster-based methods [16, 20] which do not explicitly differentiate between atoms and continuum degrees of freedom and make a seamless transition from full atomistics to the coarse-grained atomistic description — these methods are designed for automatic adaptability and do not suffer from ghost-force issues (refer to the brief review in Section 1.1). However, automatic adaptability itself can be tricky in random alloys since it has been established by the solute-strengthening theory [32] that solute fluctuations beyond the dislocation core contribute significantly to the yield stress of the alloy. Therefore retaining all the necessary fluctuations in an automatic adaptability scheme for random alloy would basically mean doing full atomistics, when the dislocation network gets, even moderately, dense — for instance, the dislocation network beneath an indenter. However there is a way to circumvent this problem and use Method 2 in an automatic adaptability scheme with the non-local QC methods. The non-local QC methods [16, 20] define the total energy functional for the multiscale problem by summing over the energies of selected *sampling atoms* multiplied by some weights (refer to Section 1.1 for more details on the methods). The weight associated with any sampling atom is related to the number of real atoms the former is replacing as a part of the homogenization protocol. In a simulation with dislocations, regions near the dislocation core resolved to full atomistics must have all explicit real atomtypes of the random alloy, while the sampling atoms in the coarse-grained regions must be average atoms (as proposed in Method 2 in Chapter 3). The missing compositional fluctuations in the coarse-grained region can be incorporated in the total energy functional of the multiscale problem, as energy of interaction of the misfit volume ΔV of a solute at any lattice site with the pressure p at that site — which is $p\Delta V$ under linear elasticity assumption. The pressure p is obtained from the degrees of freedom of the multiscale problem using interpolation functions. In this way, we can perform coarse-graining with average atoms, yet retaining the compositional fluctuations in the coarse-grained regions. The advantage of such an automatic adaptation scheme in an energy-based setting over force-based CADD is that the mobility of all the dislocations in the problem domain will be controlled by atomistics and not a phenomenological mobility law. This idea connects concepts from atomistic-continuum coupling and solute-strengthening theory. The proposed idea remains to be implemented and examined for accuracy and must be validated with multiscale problems like indentation.

In Chapter 4, the solute strengthening theory under linear elasticity assumption has been discussed in the context of anisotropic elasticity. An important outcome of the analysis is that the isotropic theory of Varvenne et. al with Voigt-averaged elastic constants agrees well with the anisotropic theory over a range of anisotropy ratios and dislocation core structure. The Chapter also reports the normalized results for the isotropic theory. However the analysis is specific to edge dislocations in fcc alloys. It would be interesting to study other dislocation orientations in fcc alloys. The 60° dislocation in fcc is particularly noteworthy. When the dislocation line is at 60° to the full Burgers vector, the leading Shockey partial is purely edge of magnitude $b/\sqrt{3}$ while the trailing Shockley partial is mixed with a larger screw component of magnitude $b/2$ and a smaller edge component of magnitude $b/(2\sqrt{3})$. Since only edge dislocations interacts with dilatational solutes for the isotropic model, it would be interesting to study the solute-strengthening for the asymmetric Burgers vector distribution of the 60° dislocation in fcc.

The theory of solute-strengthening has been extended to include solute-solute interactions. Only three test cases were studied as a part of this thesis, out of which two were high- and medium- entropy alloys. There are a lot of other high-entropy alloy families where solute-solute interactions can play a dominant role. For example, Ref. [147] used isotropic reduced model of the strengthening theory to study strengthening in Au-Cu-Ni-Pd-Pt family of HEAs and the predictions do not match experiments. It might be possible that solute pair interaction energies have a notable contribution to strengthening in these alloys. Another example is the NiCoCr system, where a strong Cr-Cr repulsion has been reported both experimentally and via first-principles calculations [41, 42].

Finally the thesis has made the first attempt in developing a general theory of solute-strengthening accounting for short-range order (SRO). Expressions predicting average strengthening, unique to SRO, has been derived in terms of effective pair potentials and Warren-Cowley SRO parameter. Both of the inputs mentioned above are unavailable experimentally, so the future plan is to calculate them via first principles and Monte-Carlo simulation for different multicomponent alloys and then use these inputs for predicting average strengthening. The new theory is also incomplete since the energy fluctuation quantities needed to predict local strengthening due to dislocation pinning in favourable solute environments are expressed in terms bond energies, which are irrelevant for alloys described by semi-empirical potentials or by first principles. So it is vital to express the energy fluctuation quantities in terms of interaction energies, which is an area for future study.

A Appendix

A.1 Slip density in fcc elements

In elements having an fcc crystal structure of lattice parameter a, the prevailing $a/2 < 110 >$ dislocations gliding on the {111} planes dissociate into two mixed $a/6 < 112 >$-type Shockley partial dislocations $\mathbf{b}_{\mathbf{p},1}$ and $\mathbf{b}_{\mathbf{p},2}$. The partials are separated by an intrinsic stable stacking fault of energy γ_{ssf}. The separation distance is determined by a balance between the repulsive elastic force between the partials and the attractive configurational force due to the stacking fault.

The cores of the Shockley partials are not delta-functions; the Burgers vector is spread along the glide plane over some range of atoms. The most widely-used model for describing the Burgers vector density of dislocation cores is the Peierls-Nabarro (P-N) model [102]. Under certain simplifications of the generalized stacking fault energy curve, the P-N model predicts a Lorentzian form of Burgers vector density as $\frac{\mathbf{b}}{\pi}\frac{\zeta}{x^2+\zeta^2}$ where ζ characterizes the width. Analysis shows that $\zeta \sim 1/\gamma_{\mathrm{usf}}$ where γ_{usf} is the unstable stacking fault energy. However, the computed values of ζ for partial cores are typically about 1/2 those observed in simulations of atomistic dislocation cores [148]. Here, we show that a Gaussian function provides a better description of the plastic displacements associated with the atomistic dislocation core structure.

The Burgers vector distribution is the plastic slip distribution along the glide plane. The plastic slip is not the same as the total shear strain, due to the additional elastic shearing. In the centers of the partial cores of the dislocation, the elastic shearing is indeed small and the use of elasticity questionable. Away from the centers of the partial cores, the shear distribution is composed of both plastic and elastic contributions, and the elastic contributions stem from the elastic fields of the plastic slip distribution along the entire slip plane.

We have examined the slip distribution of fully-relaxed atomistic edge dislocation cores for Al, Ni, and Cu as predicted by widely-used interatomic potentials [149, 150]. Specifically, the core structure is created in the standard manner. In an initial cylindrical sample of fcc crystal of radius $100b$ with orientation x= (Burgers vector and glide direction {110}), y = (normal to the slip plane {111}), z = (dislocation line direction {112}), we impose the anisotropic displacement field corresponding to a Volterra edge dislocation lying along the z axis of the cylinder with the cut-plane for slip lying along the (x-y) slip plane in the region ($x < 0$, $y = 0$). The displacements of a thin annular region of atoms on the outer boundary of the cylinder are held fixed at the Volterra solution and all interior atoms are then relaxed to their equilibrium positions to create the dissociated dislocation. The displacement $\mathbf{u}(x)$ of every atom away from its initial fcc position is then measured. We focus on the atoms in the planes just above and just below the slip plane, and denote their positions by the coordinate x_i along the glide plane direction. The difference in shear displacements across the slip plane is computed by finite differences in the discrete system as

$$\left.\frac{D\Delta\mathbf{u}}{Dx}\right|_{(x_i+x_{i+1})/2} = \frac{\Delta\mathbf{u}(x_{i+1}) - \Delta\mathbf{u}(x_i)}{b/2}. \tag{A.1}$$

Figure A.1 shows the computed $D\Delta u_x/Dx$ and $D\Delta u_z/Dx$ from the atomistic calculations for the edge and screw components respectively of a edge full dislocation in Al, Ni and Cu.

We are interested only in the plastic displacements, which are the discrete atomistic counterparts of the slip density $\partial\mathbf{b}/\partial x$. We consider the measured shear strains $D\Delta u_x/(b/\sqrt{1.5}) > 0.01$ (corresponding to $D\Delta u_x/Dx > 0.016$) to be dominated by the plastic displacements. We thus fit the measured $D\Delta\mathbf{u}/Dx$ in this region to a sum of two Gaussians (Equation 4.15) as

$$\frac{D\Delta\mathbf{u}}{Dx} \approx \frac{1}{\sqrt{2\pi\sigma^2}}\left(\mathbf{b}_{\mathbf{p},\mathbf{1}}\mathrm{e}^{-\frac{(x+d/2-x_c)^2}{2\sigma^2}} + \mathbf{b}_{\mathbf{p},\mathbf{2}}\mathrm{e}^{-\frac{(x-d/2-x_c)^2}{2\sigma^2}}\right). \tag{A.2}$$

d/b is taken as the distance between the peaks in $D\Delta u_x/Dx$ and the average or center position x_c of the full dislocation is taken as the middle of the peaks. σ/b is then the only fitting parameter, computed by a least-squares method, considering both components $\frac{\partial b_x}{\partial x}$ and $\frac{\partial b_z}{\partial x}$. Figure A.1 shows the best-fit results using dislocations symbols $\perp$ and the fitted value of σ/b is shown in each figure. The fits are generally good, with root-mean-square error below ~ 0.01. We note that fits to other types of functions, viz. logistic, Lorentzian, Gaussian-Lorentzian mixture, are not significantly better or worse in this region.

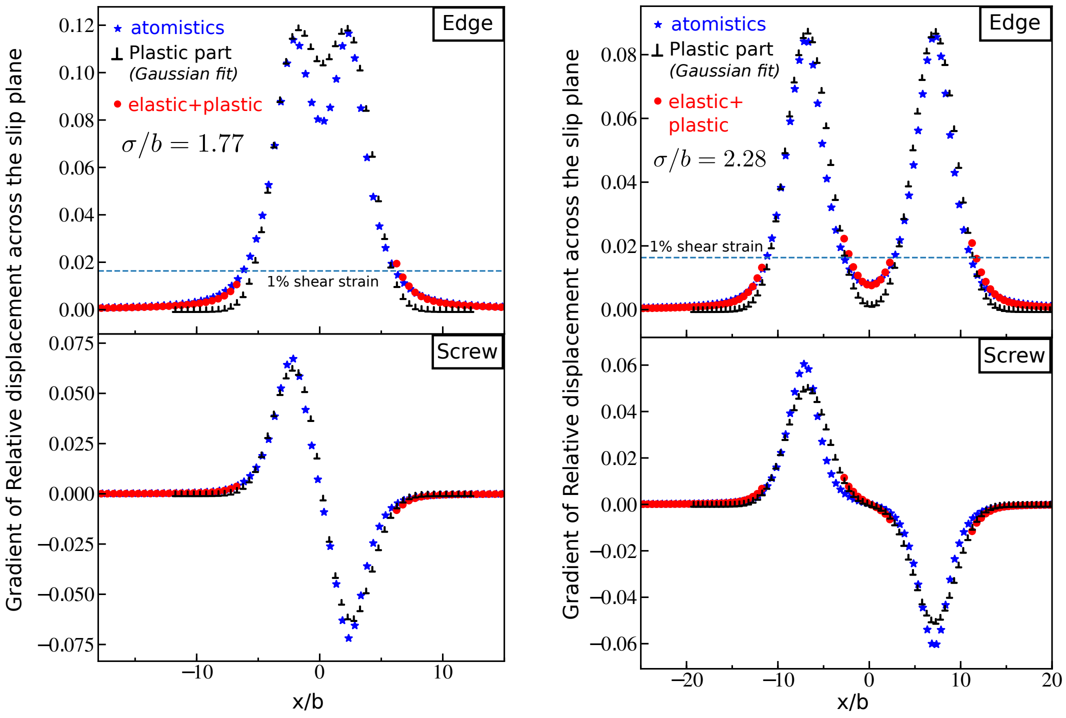

(a) Al

(b) Cu

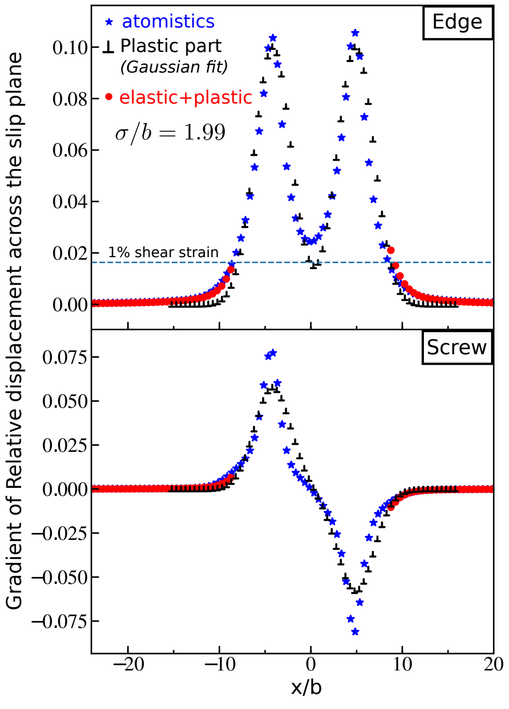

(c) Ni

Figure A.1 – Analysis of the dislocation core: atomistics, Gaussian fit and relative displacement gradient due to the fitted Gaussian core. The blue stars ★ are the $D\Delta\mathbf{u}/Dx$ computed from atomistic displacements near the dislocation core, the dislocations ⊥ are from bimodal Gaussian fit to the atomistic $D\Delta\mathbf{u}/Dx$ (explained in the text) and the red filled circles ● are the $D\Delta\mathbf{u}^{\mathbf{tot}}/Dx$ computed from the anisotropic displacement field due to the dislocations ⊥ (also explained in the text).

In the small shear strain region < 1%, Figure A.1 shows that the best-fit Gaussian plastic slip is significantly smaller than the total atomistic slip. This discrepancy may have tended to movitate the use of the Lorentzian function of the original PN model. However, in this regime, the total shear strains are dominated by the elastic shear strains caused by the Gaussian distribution of plastic slip. To demonstrate this, we compute the total anisotropic displacements $\mathbf{u}^{\mathrm{tot}}(x)$ at every atomic site generated by the best-fit bimodal Gaussian Burgers vector distribution using the Stroh formalism and the superposition principle to obtain the elastic contribution, similar to Equation 4.5. The quantity $D\Delta\mathbf{u}^{\mathrm{tot}}/Dx$ is then computed from $\mathbf{u}^{\mathrm{tot}}$ using finite differences as above. Figure A.1 shows the total slip distribution (elastic plus plastic) in the region outside the cores, and the results closely match the full atomistic results. The two-Gaussian model thus captures both the underlying plastic slip distribution and the surrounding elastic shearing for dissociated fcc dislocations.

Atomistically-computed dislocation core structures require either DFT or atomistic interatomic potentials. DFT can be performed on elemental metals but alloy studies automatically include the response of the atoms to the random environment, preventing extraction of the underlying structure of the average alloy. In this case, computation of GPFE curves together with a double-Gaussian modeling of the dislocation core structure could be useful. Atomistic potentials are available for a number of elements, and some alloy systems, but with the usual caveats about accuracy relative to the real materials. For alloys, the average-atom potential [54] can be created and used to examine the average core structure, but again relies on accuracy of the underlying potentials for the elemental constituents and their interactions. Typical values of σ are thus valuable. In Figure A.1, we find values $1.75 < \sigma/b < 2.25$ for Al, Cu, and Ni. This range is consistent with the range $1.5 < \sigma/b < 2.5$ obtained by Varvenne et. al [4] for Fe-Ni-Cr alloys. They then showed that $\sigma/b = 1.5$ provided good predictions for strength across a range of alloys, and this value was then used in subsequent work. While the solute strengthening does depend on σ/b, we thus remain consistent with previous work in suggesting the use of $1.5b$ in all fcc materials unless there is compelling evidence that a significantly different value should apply (see Section 4.4).

A.2 Interaction energies, Effective Pair Interactions and Bond energies

Interaction energy of a solute pair separated by distance d, $U^{int}_{xy}(d)$, is the difference in system energy between the systems, where the solute pair is separated by distance d and where they have infinite(large) separation, embedded in an “average” medium.

$$U^{int}_{xy}(d) = E_{xy}(d) - E_{xy}(\infty) \tag{A.3}$$

where $E_{xy}(d)$ is the system energy where the solutes x and y are embedded in an average medium and are separated by distance d (Here all the system energies are of systems with same total number of atoms). The average medium is characterised by “average atoms”, which are lattice sites where the associated energetics in averaged over random occupancy of atomtypes conforming to the alloy compositon. Averaging can be performed explicitly over many random realizations, which is generally computation expensive depending on the nature of the underlying interatomic interactions. Special quasi-random structures (SQS) can be used instead of random realizations to expedite convergence of the average [69]. For pair interatomic potentials, the averaging can be done analytically. Even for empirical potentials like the Embedded-atom method (EAM) with a many-body term, an “average atom” potential can be analytically formulated in a mean-field approach [54]. When the interaction potentials are described via first-principles, Coherent Potential approximation[70] is used to describe the average medium. Therefore the interaction energy is computable for all kinds of energetics describing the interatomic interactions. Another computable energy quantity is the effective pair interactions, $V_{xy}^{eff}(d)$, which is defined as follows,

$$V_{xy}^{eff}(d) = E_{xx}(d) + E_{yy}(d) - 2E_{xy}(d) \tag{A.4}$$

The effective pair potentials come out as pair-interaction terms while expressing the configurational energy of a random alloy to lowest order in the generalised perturbation method framework and has been used to study phase stability in binary and high-entropy alloys[5, 71].

Since $E_{xx}(\infty) + E_{yy}(\infty) - 2E_{xy}(\infty) = 0$, one can readily deduce the following relation between effective pair interactions and interaction energies,

$$V_{xy}^{eff}(d) = U_{xx}^{int}(d) + U_{yy}^{int}(d) - 2U_{xy}^{int}(d) \tag{A.5}$$

Note that the above relation holds true irrespective of the energetics describing the interatomic interactions.

In the remainder of this Appendix section, we will be expressing the interaction energies and effective pair potentials in terms of bond energies in a system where the energetics is decribed by pair interatomic potentials — basically we will be deriving Equations 5.20 and 5.21 which we will be using in Section 5.2 to express the energy fluctuation quantity $\sigma^2_{\Delta U_{\text{s-s}}}$ in terms of (i) interaction energies and (ii) effective pair potentials.

In a system described with pair potentials, let the bond energy between two solutes x and y at separation d be $U_{xy}(d)$, between a solute x and average atom A be $U_{xA}(d)$ and between two average atoms be $U_{AA}(d)$. To study $U_{xy}^{int}(d)$ and $V_{xy}^{eff}(d)$, we will first express the system energy for any arrangement of atoms of types x, y and A on a lattice.

Let s_i be the site occupation variable for site i, such that,

$$s_i = \begin{cases} 1 & \text{if } x \text{ occupies site } i \\ 0 & \text{if } A \text{ occupies site } i \\ -1 & \text{if } y \text{ occupies site } i \end{cases}$$

We now define three polynomials with s_i,

$$P_{ix} = \frac{1}{2}s_i(1+s_i), \quad P_{iy} = -\frac{1}{2}s_i(1-s_i), \quad P_{iA} = 1 - s_i^2$$

One can easily recognise that polynomial P_{ix} equals 1 for site i occupied by x and 0 otherwise and similar inferences can be drawn for P_{iy} and P_{iA}.

Energy of a given configuration $\{s_i\}$ on N atomic sites is given by,

$$\begin{aligned} E(\{s_i\}) = \frac{1}{2}\sum_{\substack{i,j \\ i\neq j}} \Big(& P_{ix}P_{jx}U_{xx}(\|\boldsymbol{r}_{ij}\|) + P_{iy}P_{jy}U_{yy}(\|\boldsymbol{r}_{ij}\|) + P_{iA}P_{jA}U_{AA}(\|\boldsymbol{r}_{ij}\|) \\ & (P_{ix}P_{jy}+P_{iy}P_{jx})U_{xy}(\|\boldsymbol{r}_{ij}\|)+(P_{ix}P_{jA}+P_{iA}P_{jx})U_{xA}(\|\boldsymbol{r}_{ij}\|)+(P_{iy}P_{jA}+P_{iA}P_{jy})U_{yA}(\|\boldsymbol{r}_{ij}\|)\Big) \end{aligned} \tag{A.6}$$

where $\boldsymbol{r}_{ij}$ is the vector from site i to site j. Let us denote $U_{xy}^{ij} = U_{xy}(\|\boldsymbol{r}_{ij}\|)$ for brevity. Therefore,

$$\begin{aligned} E(\{s_i\}) = \frac{1}{2}\sum_{\substack{i,j \\ i\neq j}} \Bigg(& \frac{1}{4}s_is_j(1+s_i)(1+s_j)U_{xx}^{ij} + \frac{1}{4}s_is_j(1-s_i)(1-s_j)U_{yy}^{ij} + (1-s_i^2)(1-s_j^2)U_{AA}^{ij} \\ & -\frac{1}{4}s_is_j\Big((1+s_i)(1-s_j)+(1-s_i)(1+s_j)\Big)U_{xy}^{ij} + \frac{1}{2}\Big(s_i(1+s_i)(1-s_j^2)+s_j(1-s_i^2)(1+s_j)\Big)U_{xA}^{ij} \\ & -\frac{1}{2}\Big(s_i(1-s_i)(1-s_j^2)+s_j(1-s_i^2)(1-s_j)\Big)U_{yA}^{ij}\Bigg) \end{aligned} \tag{A.7}$$

Equation A.7 can be simplified as,

$$\begin{aligned} E(\{s_i\}) = \frac{1}{2}\sum_{\substack{i,j \\ i\neq j}} \Bigg(& s_i^2s_j^2\left(\frac{1}{2}U_{xy}^{ij} + U_{AA}^{ij} - U_{xA}^{ij} - U_{yA}^{ij} + \frac{1}{4}U_{xx}^{ij} + \frac{1}{4}U_{yy}^{ij}\right) \\ & + s_i^2s_j\left(\frac{1}{4}U_{xx}^{ij} - \frac{1}{4}U_{yy}^{ij} - \frac{1}{2}U_{xA}^{ij} + \frac{1}{2}U_{yA}^{ij}\right) + s_is_j^2\left(\frac{1}{4}U_{xx}^{ij} - \frac{1}{4}U_{yy}^{ij} - \frac{1}{2}U_{xA}^{ij} + \frac{1}{2}U_{yA}^{ij}\right) \\ & + s_is_j\left(\frac{1}{4}U_{xx}^{ij} + \frac{1}{4}U_{yy}^{ij} - \frac{1}{2}U_{xy}^{ij}\right) + s_i^2\left(\frac{1}{2}U_{xA}^{ij} + \frac{1}{2}U_{yA}^{ij} - U_{AA}^{ij}\right) + s_j^2\left(\frac{1}{2}U_{xA}^{ij} + \frac{1}{2}U_{yA}^{ij} - U_{AA}^{ij}\right) \\ & + \frac{1}{2}s_i\left(U_{xA}^{ij} - U_{yA}^{ij}\right) + \frac{1}{2}s_j\left(U_{xA}^{ij} - U_{yA}^{ij}\right) + U_{AA}^{ij}\Bigg) \end{aligned} \tag{A.8}$$

Using Equation A.8 above for the energy of any configuration $\{s_i\}$, we will now derive the system energies for specific configurations, namely $E_{xy}(d)$, $E_{xx}(d)$ and $E_{yy}(d)$ defined in Equations A.3 and A.4.

If the configuration has one x atom and one y atom at separation d and the rest A atoms, then the system energy $E_{xy}(d)$ is given by,

$$
\begin{aligned}
E_{xy}(d) &= \left(\frac{1}{2}U_{xy}(d) + U_{AA}(d) - U_{xA}(d) - U_{YA}(d) + \frac{1}{4}U_{xx}(d) + \frac{1}{4}U_{yy}(d)\right) \\
&\quad - \left(\frac{1}{4}U_{xx}(d) + \frac{1}{4}U_{yy}(d) - \frac{1}{2}U_{xy}(d)\right) + \underbrace{N \sum_{\substack{j \\ j\neq i_0}} \left(\frac{1}{2}U^{i_0 j}_{xA} + \frac{1}{2}U^{i_0 j}_{yA} - U^{i_0 j}_{AA}\right)}_{S} + \underbrace{\frac{N}{2} \sum_{\substack{j \\ j\neq i_0}} U^{i_0 j}_{AA}}_{E_0} \\
&= U_{xy}(d) - U_{xA}(d) - U_{yA}(d) + U_{AA}(d) + S + E_0
\end{aligned}
\tag{A.9}
$$

Similarly, the system energy $E_{xx}(d)$ and $E_{yy}(d)$ are given by,

$$
\begin{aligned}
E_{xx}(d) &= \left(\frac{1}{2}U^{ij}_{xy} + U^{ij}_{AA} - U^{ij}_{xA} - U^{ij}_{yA} + \frac{1}{4}U^{ij}_{xx} + \frac{1}{4}U^{ij}_{yy}\right) \\
&\quad + \left(\frac{1}{2}U^{ij}_{xx} - \frac{1}{2}U^{ij}_{yy} - U^{ij}_{xA} + U^{ij}_{yA}\right) + \left(\frac{1}{4}U^{ij}_{xx} + \frac{1}{4}U^{ij}_{yy} - \frac{1}{2}U^{ij}_{xy}\right) \\
&\quad + \underbrace{N \sum_{\substack{j \\ j\neq i_0}} \left(\frac{1}{2}U^{i_0 j}_{xA} + \frac{1}{2}U^{i_0 j}_{yA} - U^{i_0 j}_{AA}\right)}_{S} + \underbrace{\frac{N}{2} \sum_{\substack{j \\ j\neq i_0}} \left(U^{i_0 j}_{xA} - U^{i_0 j}_{yA}\right)}_{S'} + \underbrace{\frac{N}{2} \sum_{\substack{j \\ j\neq i_0}} U^{i_0 j}_{AA}}_{E_0} \\
&= U_{xx}(d) - 2U_{xA}(d) + U_{AA}(d) + S + S' + E_0
\end{aligned}
\tag{A.10}
$$

$$
\begin{aligned}
E_{yy}(d) &= \left(\frac{1}{2}U^{ij}_{xy} + U^{ij}_{AA} - U^{ij}_{xA} - U^{ij}_{yA} + \frac{1}{4}U^{ij}_{xx} + \frac{1}{4}U^{ij}_{yy}\right) \\
&\quad - \left(\frac{1}{2}U^{ij}_{xx} - \frac{1}{2}U^{ij}_{yy} - U^{ij}_{xA} + U^{ij}_{yA}\right) + \left(\frac{1}{4}U^{ij}_{xx} + \frac{1}{4}U^{ij}_{yy} - \frac{1}{2}U^{ij}_{xy}\right) \\
&\quad + \underbrace{N \sum_{\substack{j \\ j\neq i_0}} \left(\frac{1}{2}U^{i_0 j}_{xA} + \frac{1}{2}U^{i_0 j}_{yA} - U^{i_0 j}_{AA}\right)}_{S} - \underbrace{\frac{N}{2} \sum_{\substack{j \\ j\neq i_0}} \left(U^{i_0 j}_{xA} - U^{i_0 j}_{yA}\right)}_{S'} + \underbrace{\frac{N}{2} \sum_{\substack{j \\ j\neq i_0}} U^{i_0 j}_{AA}}_{E_0} \\
&= U_{yy}(d) - 2U_{yA}(d) + U_{AA}(d) + S - S' + E_0
\end{aligned}
\tag{A.11}
$$

Assuming $U_{xy}(\infty) = U_{xA}(\infty) = U_{AA}(\infty) = 0$,

$$
U^{int}_{xy}(d) = E_{xy}(d) - E_{xy}(\infty) = U_{xy}(d) - U_{xA}(d) - U_{yA}(d) + U_{AA}(d). \tag{A.12}
$$

$$\begin{aligned}
V_{xy}^{eff}(d) &= E_{xy}(d) - \frac{1}{2}(E_{xx}(d) + E_{yy}(d)) \\
&= U_{xx}(d) - 2U_{xA}(d) + U_{AA}(d) + S + S' + E_0 \\
&+ U_{yy}(d) - 2U_{yA}(d) + U_{AA}(d) + S - S' + E_0 \\
&- 2U_{xy}(d) + 2U_{xA}(d) + 2U_{yA}(d) - 2U_{AA}(d) - 2S - 2E_0 \\
&= U_{xx}(d) + U_{yy}(d) - 2U_{xy}(d)
\end{aligned} \tag{A.13}$$

Note that Equations A.12 and A.13 are same as Equations 5.21 and 5.20 in the main text.

Also, one can easily verify from Equations A.12 and A.13, the relation (Equation A.5) between interaction energies and effective pair potentials.

Bibliography

[1] Easo P George, Dierk Raabe, and Robert O Ritchie. High-entropy alloys. *Nature Reviews Materials*, 4(8):515–534, 2019.

[2] Ronald E Miller and Ellad B Tadmor. Hybrid continuum mechanics and atomistic methods for simulating materials deformation and failure. *MRS bulletin*, 32(11):920–926, 2007.

[3] W A Curtin and Ronald E Miller. Atomistic/continuum coupling in computational materials science. *Modelling and Simulation in Materials Science and Engineering*, 11(3):R33–R68, apr 2003.

[4] Céline Varvenne, Aitor Luque, and William A Curtin. Theory of strengthening in fcc high entropy alloys. *Acta Materialia*, 118:164–176, 2016.

[5] Fritz Körmann, Andrei V. Ruban, and Marcel H.F. Sluiter. Long-ranged interactions in bcc NbMoTaW high-entropy alloys. *Materials Research Letters*, 5(1):35–40, 2017.

[6] Tao Wang, Jingzhi Zhu, Longqing Chen, Zi-Kui Liu, and Rebecca A Mackay. Modeling of lattice parameter in the ni-al system. *Metallurgical and Materials Transactions A*, 35(8):2313–2321, 2004.

[7] S Nag and WA Curtin. Effect of solute-solute interactions on strengthening of random alloys from dilute to high entropy alloys. *Acta Materialia*, 2020.

[8] Ronald E Miller and E B Tadmor. A unified framework and performance benchmark of fourteen multiscale atomistic/continuum coupling methods. *Modelling and Simulation in Materials Science and Engineering*, 17(5):053001, may 2009.

[9] Mitchell Luskin and Christoph Ortner. Atomistic-to-continuum coupling. *Acta Numerica*, 22:397–508, 2013.

[10] E Weinan, Bjorn Engquist, Xiantao Li, Weiqing Ren, and Eric Vanden-Eijnden. Heterogeneous multiscale methods: a review. *Communications in computational physics*, 2(3):367–450, 2007.

[11] AK Nair, DH Warner, RG Hennig, and WA Curtin. Coupling quantum and continuum scales to predict crack tip dislocation nucleation. *Scripta Materialia*, 63(12):1212–1215, 2010.

[12] AK Nair, DH Warner, and RG Hennig. Coupled quantum–continuum analysis of crack tip processes in aluminum. *Journal of the Mechanics and Physics of Solids*, 59(12):2476–2487, 2011.

[13] VB Shenoy, Ronald Miller, EB Tadmor, David Rodney, Rob Phillips, and Michael Ortiz. An adaptive finite element approach to atomic-scale mechanics—the quasicontinuum method. *Journal of the Mechanics and Physics of Solids*, 47(3):611–642, 1999.

[14] S Kohlhoff, P Gumbsch, and HF Fischmeister. Crack propagation in bcc crystals studied with a combined finite-element and atomistic model. *Philosophical Magazine A*, 64(4):851–878, 1991.

[15] J Knap and M Ortiz. An analysis of the quasicontinuum method. *Journal of the Mechanics and Physics of Solids*, 49(9):1899–1923, 2001.

[16] JS Amelang, GN Venturini, and DM Kochmann. Summation rules for a fully nonlocal energy-based quasicontinuum method. *Journal of the Mechanics and Physics of Solids*, 82:378–413, 2015.

[17] G Anciaux, T Junge, M Hodapp, J Cho, J-F Molinari, and WA Curtin. The coupled atomistic/discrete-dislocation method in 3d part i: Concept and algorithms. *Journal of the Mechanics and Physics of Solids*, 118:152–171, 2018.

[18] M Hodapp, G Anciaux, J-F Molinari, and WA Curtin. Coupled atomistic/discrete dislocation method in 3d part ii: Validation of the method. *Journal of the Mechanics and Physics of Solids*, 119:1–19, 2018.

[19] Jaehyun Cho, Jean-Francois Molinari, William A Curtin, and Guillaume Anciaux. The coupled atomistic/discrete-dislocation method in 3d. part iii: dynamics of hybrid dislocations. *Journal of the Mechanics and Physics of Solids*, 118:1–14, 2018.

[20] Bernhard Eidel and Alexander Stukowski. A variational formulation of the quasicontinuum method based on energy sampling in clusters. *Journal of the Mechanics and Physics of Solids*, 57(1):87–108, 2009.

[21] Dennis M Kochmann and Gabriela N Venturini. A meshless quasicontinuum method based on local maximum-entropy interpolation. *Modelling and simulation in materials science and engineering*, 22(3):034007, 2014.

[22] Laurent M Dupuy, Ellad B Tadmor, Ronald E Miller, and Rob Phillips. Finite-temperature quasicontinuum: Molecular dynamics without all the atoms. *Physical Review Letters*, 95(6):060202, 2005.

[23] Robert E Rudd and Jeremy Q Broughton. Coarse-grained molecular dynamics: Nonlinear finite elements and finite temperature. *Physical Review B*, 72(14):144104, 2005.

[24] J Friedel. Les dislocations. *Gauthier-VillarsParis*, page 205, 1956.

[25] Robert L Fleischer. Solution hardening. *Acta metallurgica*, 9(11):996–1000, 1961.

[26] Robert L Fleischer. Substitutional solution hardening. *Acta metallurgica*, 11(3):203–209, 1963.

[27] N. F. Mott and F. R. N. Nabarro. Report of a conference on strength of solids. *The Physical Society, London*, pages 1–19, 1948.

[28] Rea Labusch. A statistical theory of solid solution hardening. *physica status solidi (b)*, 41(2):659–669, 1970.

[29] R Labusch. Statistische theorien der mischkristallhärtung. *Acta metallurgica*, 20(7):917–927, 1972.

[30] GPM Leyson and WA Curtin. Friedel vs. labusch: the strong/weak pinning transition in solute strengthened metals. *Philosophical Magazine*, 93(19):2428–2444, 2013.

[31] Gerard Paul M Leyson, William A Curtin, Louis G Hector, and Christopher F Woodward. Quantitative prediction of solute strengthening in aluminium alloys. *Nature materials*, 9(9):750–755, 2010.

[32] Gerard Paul M Leyson, LG Hector Jr, and William A Curtin. Solute strengthening from first principles and application to aluminum alloys. *Acta Materialia*, 60(9):3873–3884, 2012.

[33] Céline Varvenne, Gerard Paul M Leyson, Maryam Ghazisaeidi, and William A Curtin. Solute strengthening in random alloys. *Acta Materialia*, 124:660–683, 2017.

[34] Ali Argon. *Strengthening mechanisms in crystal plasticity*, volume 4. Oxford University Press on Demand, 2008.

[35] R Labusch. Cooperative effects in alloy hardening. *Czechoslovak Journal of Physics B*, 38(5):474–481, 1988.

[36] GPM Leyson and WA Curtin. Solute strengthening at high temperatures. *Modelling and Simulation in Materials Science and Engineering*, 24(6):065005, 2016.

[37] Binglun Yin and William A Curtin. First-principles-based prediction of yield strength in the RhIrPdPtNiCu high-entropy alloy. *npj Computational Materials*, 5(1):1–7, 2019.

[38] A Tehranchi, B Yin, and WA Curtin. Solute strengthening of basal slip in mg alloys. *Acta Materialia*, 151:56–66, 2018.

[39] N Norman and BE Warren. X-ray measurement of short range order in Ag-Au. *Journal of Applied Physics*, 22(4):483–486, 1951.

[40] P Cenedese, F Bley, and S Lefebvre. Diffuse scattering in disordered ternary alloys: neutron measurements of local order in a stainless steel $Fe_{0.56}Cr_{0.21}Ni_{0.23}$. *Acta Crystallographica Section A: Foundations of Crystallography*, 40(3):228–240, 1984.

[41] Jun Ding, Qin Yu, Mark Asta, and Robert O Ritchie. Tunable stacking fault energies by tailoring local chemical order in CrCoNi medium-entropy alloys. *Proceedings of the National Academy of Sciences*, 115(36):8919–8924, 2018.

[42] FX Zhang, Shijun Zhao, Ke Jin, H Xue, G Velisa, H Bei, R Huang, JYP Ko, DC Pagan, JC Neuefeind, et al. Local structure and short-range order in a NiCoCr solid solution alloy. *Physical review letters*, 118(20):205501, 2017.

[43] Qing-Jie Li, Howard Sheng, and Evan Ma. Strengthening in multi-principal element alloys with local-chemical-order roughened dislocation pathways. *Nature communications*, 10(1):1–11, 2019.

[44] JC Fisher. On the strength of solid solution alloys. *Acta metallurgica*, 2(1):9–10, 1954.

[45] PA Flinn. Solute hardening of close-packed solid solutions. *Acta metallurgica*, 6(10):631–635, 1958.

[46] T Mohri, D De Fontaine, and JM Sanchez. Short range order hardening with second neighbor interactions in fcc solid solutions. *Metallurgical Transactions A*, 17(2):189–194, 1986.

[47] E Antillon, C Woodward, SI Rao, B Akdim, and TA Parthasarathy. Chemical short range order strengthening in a model fcc high entropy alloy. *Acta Materialia*, 2020.

[48] Steve Plimpton. Fast parallel algorithms for short-range molecular dynamics. *Journal of computational physics*, 117(1):1–19, 1995.

[49] Steve Plimpton. Sandia LAMMPS Molecular Dynamics Simulator http://lammps.sandia.gov.

[50] Murray S. Daw and M. I. Baskes. Semiempirical, quantum mechanical calculation of hydrogen embrittlement in metals. *Phys. Rev. Lett.*, 50:1285–1288, Apr 1983.

[51] Murray S. Daw and M. I. Baskes. Embedded-atom method: Derivation and application to impurities, surfaces, and other defects in metals. *Phys. Rev. B*, 29:6443–6453, Jun 1984.

[52] M. W. Finnis and J. E. Sinclair. A simple empirical n-body potential for transition metals. *Philosophical Magazine A*, 50(1):45–55, 1984.

[53] Graeme Ackland, Adrian Sutton, and Vasek Vitek. Twenty five years of finnis–sinclair potentials. *Philosophical Magazine*, 89(34-36):3111–3116, 2009.

[54] Céline Varvenne, Aitor Luque, Wolfram G. Nöhring, and William A. Curtin. Average-atom interatomic potential for random alloys. *Phys. Rev. B*, 93:104201, Mar 2016.

[55] Richard W. Smith and Gary S. Was. Application of molecular dynamics to the study of hydrogen embrittlement in ni-cr-fe alloys. *Phys. Rev. B*, 40:10322–10336, Nov 1989.

[56] Gilbert Strang. *Computational science and engineering*. 2007.

[57] Y C Fung and Pin Tong. *Classical and Computational Solid Mechanics*. WORLD SCIENTIFIC, 2001.

[58] Anders Logg and Garth N. Wells. Dolfin: Automated finite element computing. *ACM Transactions on Mathematical Software*, 37(2), 2010.

[59] Anders Logg, Garth N. Wells, and Johan Hake. *DOLFIN: a C++/Python Finite Element Library*, chapter 10. Springer, 2012.

[60] Patrick R. Amestoy, Iain S. Duff, Jean-Yves L'Excellent, and Jacko Koster. A fully asynchronous multifrontal solver using distributed dynamic scheduling. *SIAM Journal on Matrix Analysis and Applications*, 23(1):15–41, 2001.

[61] Patrick R. Amestoy, Abdou Guermouche, Jean-Yves L'Excellent, and Stéphane Pralet. Hybrid scheduling for the parallel solution of linear systems. *Parallel Computing*, 32(2):136 – 156, 2006. Parallel Matrix Algorithms and Applications (PMAA'04).

[62] W A Curtin and Ronald E Miller. Atomistic/continuum coupling in computational materials science. *Modelling and Simulation in Materials Science and Engineering*, 11(3):R33–R68, apr 2003.

[63] LE Shilkrot, Ronald E Miller, and William A Curtin. Multiscale plasticity modeling: coupled atomistics and discrete dislocation mechanics. *Journal of the Mechanics and Physics of Solids*, 52(4):755–787, 2004.

[64] Max Hodapp, G Anciaux, and WA Curtin. Lattice green function methods for atomistic/-continuum coupling: Theory and data-sparse implementation. *Computer Methods in Applied Mechanics and Engineering*, 348:1039–1075, 2019.

[65] JD Eshelby. Distortion of a crystal by point imperfections. *Journal of Applied Physics*, 25(2):255–261, 1954.

[66] JD Eshelby. The elastic interaction of point defects. *Acta metallurgica*, 3(5):487–490, 1955.

[67] Received via private communication from B. Yin (binglun.yin@epfl.ch).

[68] J. P. Hirth, J. Lothe. *Theory of dislocations (Second Edition)*. 1982.

[69] S.-H. Wei, L. G. Ferreira, James E. Bernard, and Alex Zunger. Electronic properties of random alloys: Special quasirandom structures. *Phys. Rev. B*, 42:9622–9649, Nov 1990.

[70] Fumiko Yonezawa and Kazuo Morigaki. Coherent Potential Approximation. Basic concepts and applications. *Progress of Theoretical Physics Supplement*, 53:1–76, 01 1973.

[71] P. E. A. Turchi, M. Sluiter, F. J. Pinski, D. D. Johnson, D. M. Nicholson, G. M. Stocks, and J. B. Staunton. First-principles study of phase stability in cu-zn substitutional alloys. *Phys. Rev. Lett.*, 68:418–418, Jan 1992.

[72] Ellad B Tadmor, Frédéric Legoll, WK Kim, LM Dupuy, and Ronald E Miller. Finite-temperature quasi-continuum. *Applied Mechanics Reviews*, 65(1), 2013.

[73] S Qu, V Shastry, WA Curtin, and Ronald E Miller. A finite-temperature dynamic coupled atomistic/discrete dislocation method. *Modelling and simulation in materials science and engineering*, 13(7):1101, 2005.

[74] Yashashree Kulkarni, Jaroslaw Knap, and Michael Ortiz. A variational approach to coarse graining of equilibrium and non-equilibrium atomistic description at finite temperature. *Journal of the Mechanics and Physics of Solids*, 56(4):1417–1449, 2008.

[75] J Marian, G Venturini, BL Hansen, J Knap, M Ortiz, and GH Campbell. Finite-temperature extension of the quasicontinuum method using langevin dynamics: entropy losses and analysis of errors. *Modelling and Simulation in Materials Science and Engineering*, 18(1):015003, 2009.

[76] Jeffrey S Amelang and Dennis M Kochmann. Surface effects in nanoscale structures investigated by a fully-nonlocal energy-based quasicontinuum method. *Mechanics of Materials*, 90:166–184, 2015.

[77] Wolfram Georg Nöhring and William Arthur Curtin. Thermodynamic properties of average-atom interatomic potentials for alloys. *Modelling and Simulation in Materials Science and Engineering*, 24(4):045017, 2016.

[78] Giovanni Bonny, Dmitry Terentyev, RC Pasianot, Samuel Poncé, and Alexander Bakaev. Interatomic potential to study plasticity in stainless steels: the FeNiCr model alloy. *Modelling and simulation in materials science and engineering*, 19(8):085008, 2011.

[79] Till Junge. Cadd mesher https://c4science.ch/diffusion/CADDMESH/, 2016.

[80] Xiang-Yang Liu, PP Ohotnicky, JB Adams, C Lane Rohrer, and RW Jr Hyland. Anisotropic surface segregation in Al-Mg alloys. *Surface science*, 373(2-3):357–370, 1997.

[81] GP Purja Pun and Y Mishin. Development of an interatomic potential for the ni-al system. *Philosophical Magazine*, 89(34-36):3245–3267, 2009.

[82] G Thomas. The effect of short-range order on stacking fault energy and dislocation arrangements in fcc solid solutions. *Acta Metallurgica*, 11(12):1369–1371.

[83] NR Dudova, RO Kaibyshev, and VA Valitov. Short-range ordering and the abnormal mechanical properties of a ni-20% cr alloy. *The Physics of Metals and Metallography*, 108(6):625, 2009.

[84] Soumyadipta Maiti and Walter Steurer. Structural-disorder and its effect on mechanical properties in single-phase TaNbHfZr high-entropy alloy. *Acta Materialia*, 106:87–97, 2016.

[85] Wenqiang Feng, Yang Qi, and Shaoqing Wang. Effects of short-range order on the magnetic and mechanical properties of FeCoNi(AlSi)$_x$ high entropy alloys. *Metals*, 7(11):482, 2017.

[86] PC Gehlen and JB Cohen. Computer simulation of the structure associated with local order in alloys. *Physical Review*, 139(3A):A844, 1965.

[87] Gui-Sheng Wang, Erna Krisztina Delczeg-Czirjak, Qing-Miao Hu, Kalevi Kokko, Börje Johansson, and Levente Vitos. The effect of long-range order on the elastic properties of cu3au. *Journal of physics: Condensed matter*, 25(8):085401, 2013.

[88] Ishan Tembhekar, Jeffrey S Amelang, L Munk, and Dennis M Kochmann. Automatic adaptivity in the fully nonlocal quasicontinuum method for coarse-grained atomistic simulations. *International Journal for Numerical Methods in Engineering*, 110(9):878–900, 2017.

[89] Duancheng Ma, Martin Friák, Johann von Pezold, Dierk Raabe, and Jörg Neugebauer. Computationally efficient and quantitatively accurate multiscale simulation of solid-solution strengthening by ab initio calculation. *Acta Materialia*, 85:53–66, 2015.

[90] Rea Labusch. A statistical theory of solid solution hardening. *physica status solidi (b)*, 41(2):659–669, 1970.

[91] R Labusch. Statistische theorien der mischkristallhärtung. *Acta metallurgica*, 20(7):917–927, 1972.

[92] David Rodney, L Ventelon, E Clouet, L Pizzagalli, and F Willaime. Ab initio modeling of dislocation core properties in metals and semiconductors. *Acta Materialia*, 124:633–659, 2017.

[93] Allan Bower. *Applied mechanics of solids*. CRC press, 2009.

[94] Joseph A Yasi, Louis G Hector Jr, and Dallas R Trinkle. First-principles data for solid-solution strengthening of magnesium: From geometry and chemistry to properties. *Acta Materialia*, 58(17):5704–5713, 2010.

[95] Emmanuel Clouet. The vacancy–edge dislocation interaction in fcc metals: A comparison between atomic simulations and elasticity theory. *Acta materialia*, 54(13):3543–3552, 2006.

[96] Emmanuel Clouet, Sébastien Garruchet, Hoang Nguyen, Michel Perez, and Charlotte S Becquart. Dislocation interaction with c in α-fe: A comparison between atomic simulations and elasticity theory. *Acta Materialia*, 56(14):3450–3460, 2008.

[97] A Tehranchi, B Yin, and WA Curtin. Softening and hardening of yield stress by hydrogen–solute interactions. *Philosophical Magazine*, 97(6):400–418, 2017.

[98] AN Stroh. Dislocations and cracks in anisotropic elasticity. *Philosophical magazine*, 3(30):625–646, 1958.

[99] Woldemar Voigt et al. *Lehrbuch der kristallphysik*, volume 962. Teubner Leipzig, 1928.

[100] András Reuß. Berechnung der fließgrenze von mischkristallen auf grund der plastizitätsbedingung für einkristalle. *ZAMM-Journal of Applied Mathematics and Mechanics/Zeitschrift für Angewandte Mathematik und Mechanik*, 9(1):49–58, 1929.

[101] Richard Hill. The elastic behaviour of a crystalline aggregate. *Proceedings of the Physical Society. Section A*, 65(5):349, 1952.

[102] Vasily V Bulatov, Vasily Bulatov, and Wei Cai. *Computer simulations of dislocations*, volume 3. Oxford University Press on Demand, 2006.

[103] BA Szajewski, F Pavia, and WA Curtin. Robust atomistic calculation of dislocation line tension. *Modelling and Simulation in Materials Science and Engineering*, 23(8):085008, 2015.

[104] DM Barnett, RJ Asaro, SD Gavazza, DJ Bacon, and RO Scattergood. The effects of elastic anisotropy on dislocation line tension in metals. *Journal of Physics F: Metal Physics*, 2(5):854, 1972.

[105] DY Li and JA Szpunar. Determination of single crystals' elastic constants from the measurement of ultrasonic velocity in the polycrystalline material. *Acta metallurgica et materialia*, 40(12):3277–3283, 1992.

[106] CJ Howard and EH Kisi. Measurement of single-crystal elastic constants by neutron diffraction from polycrystals. *Journal of applied crystallography*, 32(4):624–633, 1999.

[107] Xinpeng Du and Ji-Cheng Zhao. Facile measurement of single-crystal elastic constants from polycrystalline samples. *npj Computational Materials*, 3(1):1–8, 2017.

[108] J Bandyopadhyay and KP Gupta. Low temperature lattice parameter of nickel and some nickel-cobalt alloys and grüneisen parameter of nickel. *Cryogenics*, 17(6):345–347, 1977.

[109] Francesco Maresca and William A Curtin. Mechanistic origin of high strength in refractory bcc high entropy alloys up to 1900k. *Acta Materialia*, 182:235–249, 2020.

[110] Céline Varvenne and William A Curtin. Predicting yield strengths of noble metal high entropy alloys. *Scripta Materialia*, 142:92–95, 2018.

[111] Norihiko L Okamoto, Shu Fujimoto, Yuki Kambara, Marino Kawamura, Zhenghao MT Chen, Hirotaka Matsunoshita, Katsushi Tanaka, Haruyuki Inui, and Easo P George. Size effect, critical resolved shear stress, stacking fault energy, and solid solution strengthening in the crmnfeconi high-entropy alloy. *Scientific reports*, 6:35863, 2016.

[112] G Laplanche, A Kostka, C Reinhart, J Hunfeld, G Eggeler, and EP George. Reasons for the superior mechanical properties of medium-entropy CrCoNi compared to high-entropy CrMnFeCoNi. *Acta Materialia*, 128:292–303, 2017.

[113] Frederik Otto, A Dlouhỳ, Ch Somsen, Hongbin Bei, G Eggeler, and Easo P George. The influences of temperature and microstructure on the tensile properties of a CoCrFeMnNi high-entropy alloy. *Acta Materialia*, 61(15):5743–5755, 2013.

[114] Takeshi Teramoto, Kazuki Yamada, Ryo Ito, and Katsushi Tanaka. Monocrystalline elastic constants and their temperature dependences for equi-atomic CrMnFeCoNi high-entropy alloy with the face-centered cubic structure. *Journal of Alloys and Compounds*, 777:1313–1318, 2019.

[115] G Laplanche, P Gadaud, O Horst, F Otto, G Eggeler, and EP George. Temperature dependencies of the elastic moduli and thermal expansion coefficient of an equiatomic, single-phase CoCrFeMnNi high-entropy alloy. *Journal of Alloys and Compounds*, 623:348–353, 2015.

[116] Amanda Haglund, Michael Koehler, Dhiraj Catoor, Easo P George, and Veerle Keppens. Polycrystalline elastic moduli of a high-entropy alloy at cryogenic temperatures. *Intermetallics*, 58:62–64, 2015.

[117] Zhenggang Wu, Hongbin Bei, George M Pharr, and Easo P George. Temperature dependence of the mechanical properties of equiatomic solid solution alloys with face-centered cubic crystal structures. *Acta Materialia*, 81:428–441, 2014.

[118] SL Shang, A Saengdeejing, ZG Mei, DE Kim, Hui Zhang, S Ganeshan, Yi Wang, and ZK Liu. First-principles calculations of pure elements: Equations of state and elastic stiffness constants. *Computational Materials Science*, 48(4):813–826, 2010.

[119] Gerard Paul M Leyson, LG Hector Jr, and William A Curtin. First-principles prediction of yield stress for basal slip in Mg-Al alloys. *Acta materialia*, 60(13-14):5197–5203, 2012.

[120] Shankha Nag, Céline Varvenne, and William A Curtin. Solute-strengthening in elastically anisotropic fcc alloys. *Modelling and Simulation in Materials Science and Engineering*, 28(2):025007, 2020.

[121] Binglun Yin, Francesco Maresca, and WA Curtin. Vanadium is an optimal element for strengthening in both fcc and bcc high-entropy alloys. *Acta Materialia*, 188:486–491, 2020.

[122] M Claudia Troparevsky, James R Morris, Paul RC Kent, Andrew R Lupini, and G Malcolm Stocks. Criteria for predicting the formation of single-phase high-entropy alloys. *Physical Review X*, 5(1):011041, 2015.

[123] Andrei V Ruban, Sam Shallcross, SI Simak, and Hans Lomholt Skriver. Atomic and magnetic configurational energetics by the generalized perturbation method. *Physical review B*, 70(12):125115, 2004.

[124] Travis E Oliphant. *A guide to NumPy*, volume 1. Trelgol Publishing USA, 2006.

[125] XW Zhou, RA Johnson, and HNG Wadley. Misfit-energy-increasing dislocations in vapor-deposited cofe/nife multilayers. *Physical Review B*, 69(14):144113, 2004.

[126] De-Ye Lin, SS Wang, DL Peng, M Li, and XD Hui. An n-body potential for a zr–nb system based on the embedded-atom method. *Journal of Physics: Condensed Matter*, 25(10):105404, 2013.

[127] S. I. Rao. Unpublished research.

[128] Received via private communication from W. Nöhring, (wolfram.noehring@imtek.uni-freiburg.de).

[129] Yuri Mishin. Atomistic modeling of the γ and γ'-phases of the ni–al system. *Acta Materialia*, 52(6):1451–1467, 2004.

[130] Gene Simons and H Wang. Single crystal elastic constants and calculated aggregate properties. *J. Grand. Res. Center.-1965.-34*, (1):269, 1977.

[131] E Antillon, C Woodward, SI Rao, B Akdim, and TA Parthasarathy. A molecular dynamics technique for determining energy landscapes as a dislocation percolates through a field of solutes. *Acta Materialia*, 166:658–676, 2019.

[132] Michael Zaiser. Dislocation motion in a random solid solution. *Philosophical Magazine A*, 82(15):2869–2883, 2002.

[133] L Proville and S Patinet. Atomic-scale models for hardening in fcc solid solutions. *Physical Review B*, 82(5):054115, 2010.

[134] Wu-Rong Jian, Zhuocheng Xie, Shuozhi Xu, Yanqing Su, Xiaohu Yao, and Irene J Beyerlein. Effects of lattice distortion and chemical short-range order on the mechanisms of deformation in medium entropy alloy cocrni. *Acta Materialia*, 2020.

[135] Andrea Fantin, Giovanni Orazio Lepore, Anna M Manzoni, Sergey Kasatikov, Tobias Scherb, Thomas Huthwelker, Francesco d'Acapito, and Gerhard Schumacher. Short-range chemical order and local lattice distortion in a compositionally complex alloy. *Acta Materialia*, 2020.

[136] Ruopeng Zhang, Shiteng Zhao, Jun Ding, Yan Chong, Tao Jia, Colin Ophus, Mark Asta, Robert O Ritchie, and Andrew M Minor. Short-range order and its impact on the crconi medium-entropy alloy. *Nature*, 581(7808):283–287, 2020.

[137] LR Owen, HY Playford, HJ Stone, and MG Tucker. Analysis of short-range order in cu3au using x-ray pair distribution functions. *Acta Materialia*, 125:15–26, 2017.

[138] LR Owen, HY Playford, HJ Stone, and MG Tucker. A new approach to the analysis of short-range order in alloys using total scattering. *Acta Materialia*, 115:155–166, 2016.

[139] Ruopeng Zhang, Shiteng Zhao, Colin Ophus, Yu Deng, Shraddha J Vachhani, Burak Ozdol, Rachel Traylor, Karen C Bustillo, JW Morris, Daryl C Chrzan, et al. Direct imaging of short-range order and its impact on deformation in ti-6al. *Science advances*, 5(12):eaax2799, 2019.

[140] YJ Zhang, D Han, and Xiao Wu Li. A unique two-stage strength-ductility match in low solid-solution hardening ni-cr alloys: decisive role of short range ordering. *Scripta Materialia*, 178:269–273, 2020.

[141] D Han, ZY Wang, Y Yan, F Shi, and XW Li. A good strength-ductility match in cu-mn alloys with high stacking fault energies: Determinant effect of short range ordering. *Scripta Materialia*, 133:59–64, 2017.

[142] JM Cowley. An approximate theory of order in alloys. *Physical Review*, 77(5):669, 1950.

[143] JM Cowley. Short-range order and long-range order parameters. *Physical Review*, 138(5A):A1384, 1965.

[144] JH Harris, WA Curtin, and L Schultz. Hydrogen storage characteristics of mechanically alloyed amorphous metals. *Journal of Materials Research*, 3(5):872–883, 1988.

[145] WA Curtin, VS Deshpande, A Needleman, E Van der Giessen, and Mathias Wallin. Hybrid discrete dislocation models for fatigue crack growth. *International journal of fatigue*, 32(9):1511–1520, 2010.

[146] Kristopher Learion Baker and DH Warner. An atomistic investigation into the nature of near threshold fatigue crack growth in aluminum alloys. *Engineering Fracture Mechanics*, 115:111–121, 2014.

[147] F Thiel, D Utt, A Kauffmann, K Nielsch, K Albe, M Heilmaier, and J Freudenberger. Breakdown of varvenne scaling in (aunipdpt) 1- xcux high-entropy alloys. *Scripta Materialia*, 181:15–18, 2020.

[148] BA Szajewski, A Hunter, DJ Luscher, and IJ Beyerlein. The influence of anisotropy on the core structure of shockley partial dislocations within fcc materials. *Modelling and Simulation in Materials Science and Engineering*, 26(1):015010, 2017.

[149] Y Mishin, Diana Farkas, MJ Mehl, and DA Papaconstantopoulos. Interatomic potentials for monoatomic metals from experimental data and ab initio calculations. *Physical Review B*, 59(5):3393, 1999.

[150] Yu Mishin, MJ Mehl, DA Papaconstantopoulos, AF Voter, and JD Kress. Structural stability and lattice defects in copper: Ab initio, tight-binding, and embedded-atom calculations. *Physical Review B*, 63(22):224106, 2001.

Shankha Nag

CONTACT INFORMATION

PhD Student
Laboratory for Multiscale Mechanics Modeling
Institute of Mechanical Engineering
École Polytechnique Fédérale de Lausanne
Lausanne, 1015, Switzerland

e-mail: `shankha.nag@epfl.ch`
ORCID: `0000-0001-9309-8366`
Google Scholar: `KVZq8YOAAAAJ`

RESEARCH INTERESTS

Computational material science, high-entropy alloys, dislocation mechanics, atomistic simulation, statistical mechanics of complex alloys.

EDUCATION

École Polytechnique Fédérale de Lausanne
PhD in Materials Science and Engineering 2015–2020

PhD thesis: Concurrent multiscale modeling and theory of solute-strengthening for dilute and complex concentrated alloys
Thesis advisor: William A. Curtin

Indian Institute of Science Bangalore
M.Tech in Materials Engineering 2013–2015

Cumulative Performance Index - **7.9** (on a scale of 8)
M.Tech thesis: Micromechanics and deformation behaviour of amorphous systems.
Thesis advisor: Upadrasta Ramamurty

National Institute of Technology Durgapur
B.Tech. in Metallurgical and Materials Engineering 2009–2013

Cumulative Performance Index - **9.27** (on a scale of 10)
B.Tech thesis: Correlation between ferrite grain size, microstructure and tensile properties of low carbon steels.
Thesis advisor: Dipak Kumar Mondal

PUBLICATIONS

S. Nag, W. A. Curtin, *Solute-strengthening in alloys with short-range order* (*In preparation*)

S. Nag, W. A. Curtin, *Effect of Solute-Solute Interactions on Strengthening of Random Alloys from Dilute to High Entropy Alloys*, Acta Materialia 200, 659–673 (*2020*)

S. Nag, R. L. Narayan, J. Jang, C. Mukhopadhyay, U. Ramamurty, *Statistical nature of the incipient plasticity in amorphous alloys*, Scripta Materialia 187, 360–365 (*2020*).

S. Nag, C. Varvenne, W. A. Curtin, *Solute-strengthening in elastically anisotropic fcc alloys*, Modelling Simul. Mater. Sci. Eng. 28, 025007 (*2020*).

S. Nag, T. Junge, W. A. Curtin, *Atomistic-Continuum Coupling of random alloys*, Modelling Simul. Mater. Sci. Eng. 27, 075004 (*2019*).

S. Nag, P. Sardar, A. Jain, A. Himanshu, D. K. Mondal, *Correlation between ferrite grain size, microstructure and tensile properties of 0.17wt% carbon steel with traces of microalloying elements*, Materials Science and Engineering: A 597, 253 – 263 (*2014*).

PRESENTATIONS

S. Nag, W. A. Curtin, "Force-based Atomistic-Continuum Coupling of Random Alloys", *16th European Mechanics of Materials Conference* (*2018*), Nantes, France.

S. Nag, W. A. Curtin, "Force-based Atomistic-Continuum Coupling of Random Alloys", *13th World Congress in Computational Mechanics* (*2018*), New York, USA.

S. Nag, W. A. Curtin, "Solute strengthening in High-Entropy Alloys", *Euromat* (*2019*), Stockholm, Sweden.

Scholastic Achievements

Masters degree with distinction (ranked 1^{st})

All-India Rank 5 in Graduate Aptitude Test in Engineering (GATE) 2013

Bachelors degree with distinction (ranked 2^{nd})

Travel Award for WCCM, 2018, New York

Teaching Experiences

Teaching Assistant, EPFL

- Introduction to Structural Mechanics — Spring Semester 2019
- Metallography practicals — Spring Semester 2018
- Linear Algebra and Geometry, Cours de mise à niveau — Spring Semester 2017

Internship

Beam and Radiation Monitoring (BRM) group, CMS Unit, May–July, 2012
European Organization of Nuclear Research (CERN), Geneva, Switzerland

Project: Choice of Material for a Directional Muon Halo Detector and the Study of the Directionality and Measurement of Scintillation in Fused Quartz Bar.

Project supervisor: Dr. Anne E. Dabrowski and Dr. Marina Giunta

Technical Skills

Programming Languages - Python, C++, Matlab.

Software - LAMMPS, Ovito, LaTeX, Mathematica.

Experimental - SEM examinations, optical microscopy, mechanical testing.

Frequentist inference - Maximum likelihood estimation, EM-algorithm, model selection.

Referee service

Reviewed manuscripts for *Acta Materialia* and *Scripta Materialia*.

Selected Coursework

- Materials at multiscales: theory, modeling and simulation
- Scientific programming for engineers
- Defects in Materials
- Thermodynamics and kinetics
- Phase transformations
- Stucture and characterization of materials
- Electron Microscopy in Materials Characterization
- Statistical methods in atomistic computer simulations
- Modeling and Simulation in Materials Engineering
- Mechanical behaviour of Materials
- Finite element method
- Diffusion in solids
- Fracture
- Laboratory Experiments in Metallurgy

References

Prof. William A. Curtin, EPFL (email: *william.curtin@epfl.ch*)

Prof. Upadrasta Ramamurty, IISc Bangalore (email: *uram@ntu.edu.sg*)

Dr. Céline Varvenne, CINaM, Aix-Marseille University (email: *varvenne@cinam.univ-mrs.fr*)